Systematics of Giant Impacts in Late-Stage Planet Formation

and

Active Neutron Experiments on the Surface of Mars

by

Travis Saint James Gabriel

A Dissertation Presented in Partial Fulfillment
of the Requirements for the Degree
Doctor of Philosophy

Approved July, 1 2019 by the
Graduate Supervisory Committee:

Craig Hardgrove, Co-Chair
Erik I. Asphaug, Co-Chair
Thomas Sharp
Mikhail Zolotov
Patrick Young

ARIZONA STATE UNIVERSITY

August 2019

ABSTRACT

Part I – I analyze a database of Smoothed Particle Hydrodynamics (SPH) simulations of collisions between planetary bodies and use the data to define semi-empirical models that reproduce remant masses. These models may be leveraged when detailed, time-dependent aspects of the collision are not paramount, but analytical intuition or a rapid solution is required, *e.g.* in 'N-body simulations'. I find that the stratification of the planet is a non-negligible control on accretion efficiency. I also show that the absolute scale (total mass) of the collision may affect the accretion efficiency, with larger bodies more efficiently disrupting, as a function of gravitational binding energy. This is potentially due to impact velocities above the sound speed. The interplay of these dependencies implies that planet formation, depending on the dynamical environment, may be separated into stages marked by differentiation and the growth of planets more massive than the Moon.

Part II – I examine time-resolved neutron data from the Dynamic Albedo of Neutrons (DAN) instrument on the Mars Science Laboratory (MSL) Curiosity rover. I personally and independently developed a data analysis routine (described in the supplementary material in Chapter 2) that utilizes spectra from Monte Carlo N-Particle Transport models of the experiment and the Markov-chain Monte Carlo method to estimate bulk soil/rock properties. The method also identifies cross-correlation and degeneracies. I use data from two measurement campaigns that I targeted during remote operations at ASU. I find that alteration zones of a sandstone unit in Gale crater are markedly elevated in H content from the parent rock, consistent with the presence of amorphous silica. I posit that these deposits were formed by the most recent aqueous alteration events in the crater, since subsequent events would have produced matured forms of silica that were not observed. I also find that active dunes

in Gale crater contain minimal water and I developed a Monte Carlo phase analysis routine to understand the amorphous materials in the dunes.

All three chapters are either published, in-review, or will be submitted in a short time; I refer the reader to their published forms for the most up-to-date and peer-reviewed versions.

DEDICATION

To my parents, friends, colleagues, and strangers alike who have guided me, even in the smallest of ways, towards a better future; it is time now for me to pay it forward.

ACKNOWLEDGMENTS

I foremost thank my mother and father who lent me their ear any time. I attribute the temperament, creativity, and work ethic required to get through many tough moments in gradschool to the examples they set.

Professionally, there were mentors and colleagues that helped me get to where I am now. First, I would like to thank Joseph Harrington and Csaba Palotai for taking me on as a research assistant and involving me in all aspects of the scientific process at such an early point in my career. Joe's unwaivering moral compass and ethics are attributes anyone should strive to emulate and I will continue asking myself, "What would Joe do?" I would like to thank Alan Stern for extending to me an opportunity in Orlando, Florida when, unbeknownst to him, I was facing some unfortunate circumstances. His gesture lead to rewarding outreach work with Jaydeep Mukherjee, a fantastic mentor to me and a resource to the state of Florida. I am considerably appreciative of Erik Asphaug, who served as a great advisor for nearly my entire academic career and is a source of countless stimulating conversations that have flourished into rewarding scientific endeavours; they will undoubtedly continue to do so for years to come. I thank Craig Hardgrove for an exciting adventure in broadening horizons and developing new expertise in neutron spectroscopy; his attentiveness to students and genuine care for their goals is appreciated. I thank Professor Zuhair Nashed for his endless mathematical insight and superb teachings at the University of Central Florida that laid a foundation early in my education. I also want to thank Sarah Stewart-Mukhopadhyay for conversations over the years about the progress and future of the field of planetary collisions.

Many friends near and far have also had a positive influence through the years. Things wouldn't have been the same without the mind blowing hikes with Enrique

and Eric. I thank Ian for his sense of humor and for being like a brother at times. I thank Sean Czarnecki for countless hours of interesting conversations and I have enjoyed being a sounding board for each other's ideas; at some point we'll figure out how the universe works! I thank Ed Garnero for being a fantastic friend, and, most importantly, a fellow bass guitar fanatic; I will always appreciate his perspectives any topic, especially over a cup of joe. Anna, I want to thank you for your unending patience and support. I also want to thank Krysten Villalon, for your enduring friendship, Anthony, Diana, and my new goddaughter, for being more than family, Cherie Achilles, for more things than I can list here, Francois Tissot, for our shared perspectives on many topics, Stephen Dibb, for your friendship and great attitude, Helene Piet, for your friendship and willingness to teach a top roper to lead climb, Tane and James, for being there during the good and bad, Jack Lightholder, for fun collaboration and antics, Megan Hufford, for brightening everyone's day, Ernest Cisneros, for being part of the bedrock of SESE, and to my Dissertation Committee, Hannah Kerner, Stephen "Stevie Wonder" Schwartz, Kevin Hubbard, the LROC team, Dan Scheeres, Philip Armitage, Nicola Baresi, Stefaan van Waal, and others at UCF, CU Boulder, and ASU for your friendships through the years; "It takes a village."

TABLE OF CONTENTS

CHAPTER Page

LIST OF TABLES

LIST OF FIGURES

Chapter 1

EMPIRICAL MODEL FOR MASS OF REMNANTS IN GRAVITY-DOMINATED COLLISIONS WITH TREATMENT FOR 'HIT AND RUN' AND DENSITY STRATIFICATION

Travis S. J. Gabriel,[1*†] Alan P. Jackson,[2] Erik Asphaug,[3] Andreas Reufer,[4] Martin Jutzi,[4] and Willy Benz[4]

[1]School of Earth and Space Exploration, Arizona State University, Tempe, AZ 85287, USA.

[2]Centre for Planetary Sciences, University of Toronto, Toronto, Ontario M1C 1A4, Canada.

[3]Lunar and Planetary Laboratory, University of Arizona, Tucson, AZ 85721, USA.

[4]Physikalisches Institut, University of Bern, Bern, Switzerland.

[*]Corresponding author: Travis.Gabriel@asu.edu

[†]Present address: 781 E Terrace Mall, ISTB4, Room 795, Tempe, AZ 85287-6004, USA.

Citation: T. S. J. Gabriel, A. P. Jackson, E. Asphaug, A. Reufer, M. Jutzi, and W. Benz

(2019). Empirical model for mass of remnants in gravity-dominated collisions with treatment for 'hit and run' and density stratification. In review in *The Astrophysical Journal*.

Abstract

We develop empirical relationships for the accretion and erosion of colliding gravity-dominated bodies under conditions expected in late-stage solar system formation. These are fast, easily-coded relationships based on a large database of smoothed particle hydrodynamics (SPH) simulations of collisions between bodies of different compositions, including those that are water-rich. We illustrate the paucity of disruptive collisions between major bodies, as compared to the collisions between less massive planetesimals in late-stage planet formation, and

thus focus on more probable, low-velocity collisions. We also pay particular attention to the transition zone between merging collisions and those where the impactor does not merge with the target, but continues downrange, a 'hit-and-run' collision. We find that hit-and-run collisions occur more often in density-stratified bodies and across a wider range of impact angles than suggested by the most commonly-used analytic approximation. We also identify a possible transitional zone in gravity-dominated collisions where larger bodies may undergo more disruptive collisions when the impact velocity exceeds the sound speed. Our results are contrary to the commonly-assumed invariance of total mass (scale), density structure, and material composition on the largest remnants of giant impacts. We provide an algorithm for adopting our model into N-body planet formation simulations, so that the mass of growing planets and debris can be tracked.

1.1 Introduction

Planet-scale collisions gained prominence in the context of terrestrial planet formation in the post-Apollo era (e.g. Hartmann and Davis, 1975; Wetherill, 1985). A large body of subsequent work has led to the widely-accepted prediction that the final phases of the growth of small, non-gaseous planets is dominated by chaotic collisions between planetary embryos (e.g. Kenyon and Bromley, 2006; Raymond et al., 2009; Kokubo and Genda, 2010). Giant impacts between planetary embryos are also a key feature within the newly-introduced planet formation framework 'pebble accretion' (e.g. Morbidelli et al., 2015), which features the swift accretion of planetary embryos from small components. There is substantial evidence for the occurrence of these giant, planetary-scale impacts on the terrestrial planets in our own Solar system, with

such impacts implicated in the origin of the Moon (e.g. Cameron and Ward, 1976; Benz et al., 1986; Canup and Asphaug, 2001; Canup, 2004), the formation of Mercury (e.g. Benz et al., 2007; Asphaug and Reufer, 2014), and the genesis of the Martian Hemispheric dichotomy/Borealis basin (Wilhelms and Squyres, 1984; Marinova et al., 2008; Marinova et al., 2011). In the particular case of the Moon, not only do we have evidence in the existence of the Moon itself, but also potentially from signatures left by subsequent collisions between debris released by the impact and the asteroid belt (Bottke et al., 2015). Indeed the only one of the terrestrial planets for which we do not currently have direct evidence of a giant impact event is Venus and it is likely not a coincidence that Venus is the planet about whose surface we know the least. Planetary-scale collisions are by no means limited to the inner regions of the Solar system. In the Kuiper belt the Pluto-Charon binary system is believed to have formed in an impact much like that which formed our own Moon (e.g. Canup, 2005; S. A. Stern et al., 2006; Canup, 2011). The Haumea collisional family (Brown et al., 2007; Leinhardt et al., 2010) also likely has its origin in a giant impact and the saturnian satellites are theorized as remnants of the giant impact accretion of Titan (e.g. Asphaug and Reufer, 2013).

We are also accruing evidence for the occurrence of giant impacts in other planetary systems. The strongest candidate is probably the HD172555 system, for which the mid-infrared spectrum shows the presence of copious quantities of amorphous silica dust in the terrestrial region of this 12 Myr-old A5V star (Lisse et al., 2009). Since amorphous silica is produced by the fast quenching of molten material, this points to the dust being generated by a recent collision at >10 km/s, equivalent to planetary escape velocities, between two massive proto-planets which would produce large volumes of melt (Lisse et al., 2009). Another candidate is the A-star Beta Pictoris. Observations

by Telesco et al. (2005) revealed a large brightness asymmetry in the mid-infrared at a projected separation of about 50 AU from the star. More recent observations with the Atacama Large Millimetre Array (ALMA) by Dent et al. (2014) reveal co-located asymmetries in the sub-mm continuum and in CO gas. One explanation for the origin of this asymmetry in the Beta Pictoris debris disk is a recent (in the last million years) collision between two icy proto-planets (Dent et al., 2014; Jackson et al., 2014). As members of the Beta Pictoris moving group (29 pc and 19.44 pc distant respectively), HD172555 and Beta Pictoris are two of the nearest young A-stars to the Solar system. Taken together they provide potential nearby analogues of the giant impacts that have been inferred for our own inner and outer Solar system.

Alongside these observational considerations, theoretical work has shown that properly accounting for the outcomes of giant impacts during the chaotic phase of terrestrial planet formation is likely essential to accurately model the final planetary system. Earlier N-body planet formation simulations such as Chambers (2004) or Kenyon and Bromley (2006) used a perfect-merger model for the outcome of collisions, where two colliding bodies will *always* result in a single body with mass equal to the sum of the two. In contrast, detailed modelling of individual impacts using hydrocode simulations, such as that of C. Agnor and Asphaug (2004) and Asphaug et al. (2006), showed that the perfect-merger model is not realistic. In particular, hydrocode simulations of off-axis collisions between similarly-sized bodies have shown that the class of 'hit-and-run' collisions, in which the bodies collide without significant accretion or disruption, is important, especially with regards to the fate of the impactor that continues on a deflected heliocentric orbit. For typical velocities in a dynamical system of self-stirred bodies, hit-and-run collisions appear to happen as frequently as effective mergers (e.g. C. Agnor and Asphaug, 2004). Furthermore, the impactor that

deflects downrange can reimpact the same target, at timescales $\sim 10^3 - 10^5$ years on average at 1 AU, or collide with another body (Emsenhuber and Asphaug, 2019). In either case, subsequent collisions may also be hit and run (Emsenhuber and Asphaug, 2019), serving as an efficient transport mechanism between growing planetary bodies.

It is clear that incorporating a more realistic accretion model into N-body simulations is highly desirable; however modelling of individual giant impacts shows that they can result in a wide variety of outcomes (e.g. Asphaug, 2010). Attempts have been made (Genda et al., 2011) to construct hybrid methods in which an N-body simulation spawns a Smoothed-Particle Hydrodynamics (SPH) simulation when a collision is detected. The N-body simulation is temporarily halted, then resumed once it is provided the output of the SPH simulation. This is exceptionally computationally expensive since the N-body code integrates for millions of years (months of wall-clock time), each SPH simulation integrates for hours (days of wall clock time), and hundreds of such collisions between large bodies will occur in N-body models of late-stage planet formation. Thus far no such scheme has successfully been demonstrated in the literature. With a true hybrid method beyond reach, at least in the near term, efforts have focused instead on characterizing the parameter space of giant impact outcomes and constructing empirical relationships to link the pre-impact parameters to the post-impact outcomes in analytical models that serve as a surrogate for SPH. Fully data-drive methods are also possible such as interpolation or machine learning (Cambioni et al., 2019), which don't rely on underlying assumptions of human-derived analytical forms. Ideally the models apply to a large range of conditions and scales (*i.e.* total colliding mass). The most comprehensive effort to date to conduct such a characterization of the outcomes of giant impacts through physically-motivated analytical forms ('scaling laws') is that of Leinhardt and Stewart (2012) and Stewart

and Leinhardt (2012), and their model has now begun to be directly incorporated into the next generation of N-body models (e.g. Chambers, 2013; Leinhardt et al., 2015).

Previous efforts at characterizing the outcomes of giant impacts have drawn on the wealth of existing laboratory-scale impact data and literature for impacts and asteroids, with catastrophic disruption of the target (the impact energy that produces a largest remnant that is half of the total colliding mass) used as the key point of comparison, since disruption is readily achieved in small bodies in the laboratory and in the asteroid belt; though note that there are issues with the definition of catastrophic disruption for off-axis collisions between similar-sized bodies, as we discuss in Section 1.2. In a dynamical system of self-stirred bodies, such as a population of planetary embryos, impact velocities are at most a few times the escape velocity which is well below the catastrophic disruption threshold, as we discuss further in Section 1.2.1. In contrast, small bodies embedded within a population of larger bodies, such as asteroids in the present day Solar system, will collide at similar absolute velocities to the larger bodies, and thus at much larger multiples of their escape velocity such that collisions between the small bodies will be largely disruptive.

In this work we focus on collisions of planetary embryos whose impact outcomes, namely the mass of remnants, are dominated by gravity. Collisions of this scale are relevant to the collisions between interacting particles in modern N-body codes, (e.g. Chambers, 2013). We begin by providing an overview of the landscape of giant impact parameters and outcomes, particularly as it applies to terrestrial planet formation, in Section 1.2. Then we review past efforts at constructing scaling laws used to predict giant impact outcomes in Section 1.3. We describe our methodology in Section 2.3 before presenting our results in Section 1.5. In Section 1.6 we compare our results with previous work and discuss the applicability of our empirical relationships to the range

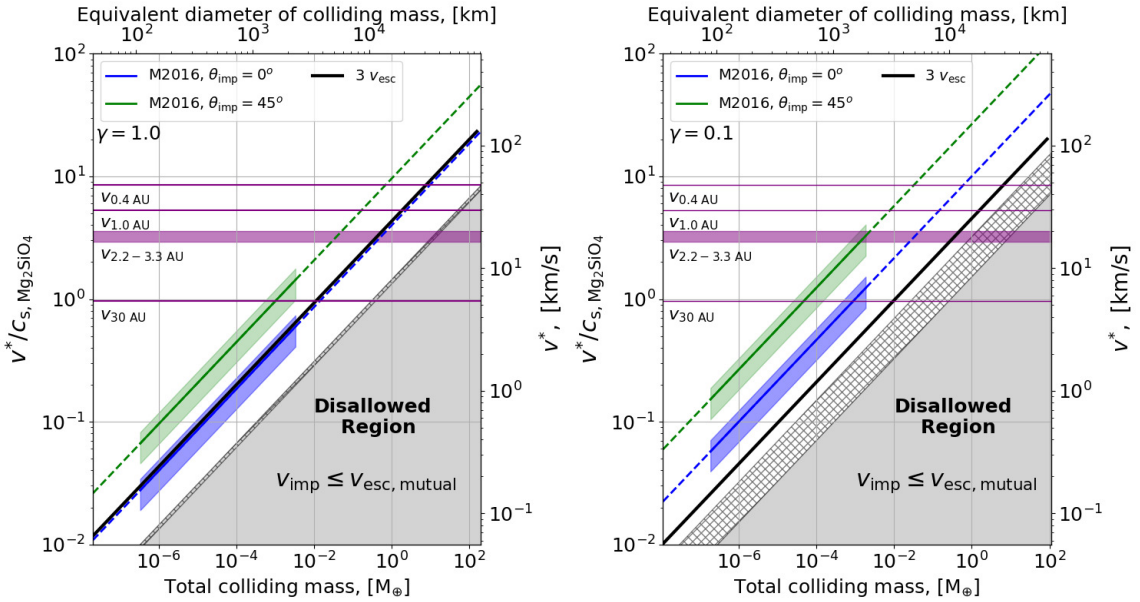

Figure 1.1. Comparison between collision velocities to disruption thresholds. The blue and green lines represent catastrophic disruption velocities from Movshovitz et al. (2016) for head-on and $\theta_{\rm imp} = 45°$ collisions, with the shaded bands showing their uncertainties. Velocity in the left hand y axis is scaled by the sound speed of forsterite at 0 °C and 1 atm (~ 5.6 km/s) (Suzuki et al., 1983). The grey zone represents velocities less than $v_{\rm esc}$, which are disallowed for 2-body interactions, and the hatched zone represents impact energy less than half the mutual gravitational binding energy. The purple horizontal lines indicate circular velocities at different radial positions in the solar system. Chambers (2013) finds all embryo-embryo impacts occur below 3 $v_{\rm esc}$ (black dotted line) in terrestrial solar system formation. Mutual escape velocity $v_{\rm esc,mutual}$ was computed assuming $\rho_{\rm bulk} = 3000$ kg m^{-3} and an impactor-to-target mass ratio of $\gamma = M_{\rm imp}/M_{\rm tar} = 1$ (left) and $\gamma = 0.1$ (right).

of gravity-dominated collisions. A key product of our work is a simple prescription for incorporating giant impact outcomes into N-body codes, which we present in Section 1.7. Finally we summarize our conclusions in Section 1.8. The Appendix provides a description of the Markov chain Monte Carlo (MCMC) optimization routine used to globally reduce the residuals of our analytical model across the database of simulations.

1.2 The Landscape of Giant Impacts

Unlike in the cratering of planetary surfaces, collisions between similar-sized bodies feature an impactor whose mass is not negligible by definition. Typically, giant impacts do not result in long lasting surface morphologies resembling classical impact craters and any surface deformation is often erased within a few gravitational timescales. A possible exception is the Borealis basin impact hypothesis for the origin of the hemispheric dichotomy on Mars (Marinova et al., 2008; Marinova et al., 2011). We note however that the impactor-to-target mass ratio in that case is small, $\sim$0.01, and thus this basin-forming collision can be thought of as being in the transition between cratering and similar-sized collisions.

A key parameter of giant impacts is the two-body escape velocity of the target and impactor,

$$v_{\rm esc} = \left(2\mathcal{G} \frac{M_{\rm tar} + M_{\rm imp}}{R_{\rm tar} + R_{\rm imp}} \right)^{\frac{1}{2}}, \tag{1.1}$$

where $M_{\rm tar}$, $R_{\rm tar}$ is the mass and radius of the target respectively and $M_{\rm imp}$, $R_{\rm imp}$ is the mass and radius of the impactor respectively. Equation 1.1 is an adjustment from the single-body form, $v_{\rm esc} = \sqrt{2\mathcal{G}M_{\rm tar}/R_{\rm tar}}$, to account for the comparable mass of the impactor with respect to the target. The impactor-to-target mass ratio is defined by:

$$\gamma = M_{\rm imp}/M_{\rm tar}, \tag{1.2}$$

so $0 < \gamma \leq 1$ and, depending on the bulk densities of the bodies, it is still possible that $R_{\rm imp} > R_{\rm tar}$, a scenario simulated in Movshovitz et al. (2016).

Another key parameter is the impact angle, $\theta_{\rm imp}$, which we define as 0 for a head-on collision and 90° for a perfectly-grazing geometry. The familiar result of Shoemaker (1961) applies equally to giant impacts as it does to cratering projectiles: that the probability distribution of impact angles goes according to $P(\theta_{\rm imp}) = \sin(2\theta_{\rm imp})$, which has a modal value of 45°. In collisions of similar-sized bodies there is not a lot of material overlap for angles greater than around 30°, *and 75% of collisions occur at angles greater than 30°*. Even moderate-velocity giant impacts can be 'hit-and-run' (Asphaug et al., 2006), with a sizable portion of the impactor continuing downrange, a phenomenon first reported in C. Agnor and Asphaug (2004).

1.2.1 Paucity of Disruptive Collisions

A common tool used to understand giant impact outcomes and to develop predictions for the mass of the largest remnant has been the catastrophic disruption threshold. This represents the energy, Q^*, at which the mass of the largest remnant is equal to half of the colliding mass, $M_{\rm LR} = 0.5M_{\rm tot} = 0.5(M_{\rm tar} + M_{\rm imp})$. In the case where the projectile is much smaller than the target, specific impact energy takes on the familiar form

$$Q = \frac{1}{2}\frac{M_{\rm imp}v_{\rm imp}^2}{M_{\rm tar}}, \tag{1.3}$$

where $M_{\rm imp}$, $M_{\rm tar}$, and $v_{\rm imp}$ is the impactor mass, target mass, and impact velocity respectively. Since the impact velocities of growing planets are governed by the mutual escape velocities of the bodies, giant impacts span a range of impact velocities which we can compare to disruption velocities (derived from Q^*) reported in the literature

In Figure 1.1 we compare the disruption threshold velocity to impact velocities in

which collisions between gravity-dominated bodies will take place, for an impactor-to-target mass ratio of $\gamma = 1$ on the left and $\gamma = 0.1$ on the right. The horizontal purple lines mark the circular orbital velocities at roughly the locations of Mercury, Earth, the asteroid belt, and Neptune and thus represent indicative boundaries on the maximum possible impact velocity at these locations[1]. The blue and green diagonal lines meanwhile show the disruption thresholds from Movshovitz et al. (2016) for head-on and $\theta_{\rm imp} = 45°$ collisions respectively, both calculated for the appropriate value of γ, since a less massive impactor must travel faster to have the same kinetic energy. We can readily see that it is highly implausible for a body larger than $\sim$1 $M_\oplus$ to be disrupted at an orbital distance of 1 AU since the maximum impact velocity is lower than the blue and green disruption lines at those masses. In the main belt-region it is nearly impossible for $\sim$1 $M_\oplus$, $\gamma = 0.1$ collisions to result in disruption since impact energies are strictly in the hatched zone in Figure 1.1 (right). Larger bodies can be disrupted at smaller orbital distances, but at larger orbital distances our analysis becomes even more stringent - *beyond the orbit of Uranus even lunar mass bodies ($\sim 10^{-2} M_\oplus$) cannot collide destructively.*

At $\sim$30 AU the circular velocity (5.4 km/s) is close to the bulk sound speed of forsterite at 0°C and 1 atm, $\sim$5.6 km/s (Suzuki et al., 1983). The sound speed of water is lower at 0°C and 1 atm: $\sim$1.4 km/s in liquid phase (e.g. Smith and Lawson, 1954) and $\sim$2.1 km/s in solid (Ih) phase (e.g. Vogt et al., 2008), so the onset of shock-producing collisions occurs at lower velocities for outer Solar system bodies[2]

[1] A *strict* boundary would be twice the orbital velocity to account for perfectly-in-plane retrograde orbits, however this is exceedingly unlikely. For most systems, the keplerian boundaries are rather conservative as collision velocities are on the order of $\sim ev_{\rm keplerian}$ and thus often a small fraction of the Keplerian velocity.

[2] This sound speed normalization should be used as a rough guideline as sound speed is temperature, pressure, and phase dependent. In SPH simulations, the manifestation of the transition would be

In the absence of damping forces like gas drag, two bodies must always collide at speeds greater than their mutual escape velocity, and thus the grey region, where $v_{\rm imp} < v_{\rm esc}$, is disallowed. The hatched and grey zone together is the region where the impact kinetic energy is less than half the mutual gravitational binding energy and disruptive outcomes have not been observed in this regime. As such, collisions between equal-sized bodies with $M_{\rm tar} \approx 0.2 M_\oplus$ will always be super-sonic, since even in the lowest-velocity collisions possible ($\sim$1 $v_{\rm esc}$) the sound speed is exceeded. Note that in regions where $v_{\rm esc}$ exceeds the orbital velocity (purple lines), our analysis implies that collisions are not possible; in this region the outcome of scattering events is dominated by the ejection of one of the bodies from the system rather than by collisions (e.g. Wyatt et al., 2017).

Alongside the indicative boundaries provided by the orbital velocity and the escape velocity we also show black diagonal lines at 3 $v_{\rm esc}$. These correspond to the results of terrestrial planet formation simulations from Chambers (2013) that show all embryo-embryo impacts[3] occur at less than 3 $v_{\rm esc}$ (see Figure S1.2 for the full distribution of impact velocities) while planetesimal-embryo impacts occur at up to at most 20 $v_{\rm esc}$. Though their results apply strictly to embryos larger than 0.093 $M_\oplus$, the initial embryo mass in their simulations, we note that it is expected from theory that embryo-embryo collisions should take place at low velocities, a few times $v_{\rm esc}$, due to dynamical friction with planetesimals (e.g. Goldreich et al., 2004). As we can see, this implies that disruptive collisions between embryos should be very rare since

dependent on the accuracy of the equation of state. For comparison, at 0°C and 1 atm ANEOS provides $c_{\rm s}$ = 1.49 km/s and 6.29 km/s for water and forsterite respectively.

[3]In fact, the largest embryo-embryo impact velocity in those simulations is somewhat lower than $3 v_{\rm esc}$; however, since there are very few high-velocity collisions (poor statistics) we use 3 $v_{\rm esc}$ as a conservative estimate.

even in the more disruptive case of a head-on impact with an impactor-to-target mass ratio of 1 (left panel of Figure 1.1) the disruption criterion of Movshovitz et al. (2016) (blue line) lies along the highest embryo-embryo collision velocities of Chambers (2013) (black line).

We emphasize that the blue disruption line shown in the left-hand panel of Figure 1.1 is the most favourable possible case. While this appears to show that it is possible to disrupt an Earth-mass body at 1 AU this would require a head-on impact with another Earth-mass object at an impact velocity equal to Earth's orbital velocity (*e.g.* an eccentricity ≈ 1). This is an extremely unlikely impact configuration. Head-on impacts are strongly disfavoured geometrically, as compared to grazing angles, and equal mass collisions are also less likely than unequal mass collisions. Similarly an impact at close to the orbital velocity is very difficult to arrange since it requires an impactor that is plunging through the entire planetary system (Jackson et al., 2018). More typically one would be considering disruption in terms of the green line in the right-hand panel - an unequal mass collision at a glancing angle and we can see that this lies far above the highest embryo-embryo collision velocities found by Chambers (2013). It is also notable that a large range of embryo-embryo collisions with $\gamma = 0.1$ occur at impact energies less than half the gravitational binding energy (hatched zone, Figure 1.1 right).

In contrast we can expect that planetesimal-planetesimal collisions will occur at similar *absolute* velocities as planetesimal-embryo collisions. The velocity dispersion in the planetesimals governs the collision velocities, and thus they occur at significantly higher values of $v_{\rm imp}/v_{\rm esc}$ since $v_{\rm esc}$ for a planetesimal will be substantially smaller. Put in other terms, $v_{\rm esc}$ is proportional to the mass of the colliding planetesimals (which are small), but $v_{\rm imp}$ is proportional to the mass of the largest bodies in

the dynamical 'neighborhood' (which are comparatively much larger). As such planetesimal-planetesimal collisions should generally be destructive and act to shut off planetesimal growth when the embryos are growing chaotically through giant impacts, as is generally assumed (e.g. Kenyon and Bromley, 2016). However, the difference in size scale between asteroids and planetary embryos does not allow for them to be modeled explicitly in an N-body simulation of planet formation, instead the full population of asteroids and small bodies are modeled as fewer 'super particles' that represent the much larger distribution.

In sum, giant impact scaling laws must account for complexities, distinct from their classical cratering-physics counterparts, in both geometry and the energetics of the collision in order to make accurate predictions which are necessary and relevant for N-body planetary evolution codes. In the following section, we review the landscape of literature on giant impact scaling laws, and the collision regimes for which they are appropriate, in order to provide the context for our contribution to the subject.

1.3 Existing Scaling Laws

Since we are studying giant impacts in the context of the final assembly of planets, it is clear that the mass of the largest body that emerges from the impact event, and perhaps the second, are important properties. A number of authors have developed scaling laws to predict remnant masses from pre-impact conditions. Housen and Holsapple (1990) provides a framework that most giant impact scaling law literature is constructed upon, where catastrophic disruption threshold for laboratory-scale to planetary-scale collisions is described in terms of a combination of the momentum and/or the energy of the collision. However, as discussed by Movshovitz et al. (2016)

(see their Appendix) the scaling laws are not appropriate for similar-sized collisions and, at least for the gravity regime, simple energy scaling is adequate. In particular, we highlight that the dimensional analysis approach used by Housen and Holsapple (1990) to develop their framework relies on a point-source approximation. This is a similar approximation in scaling relations for cratering, the development of which is well described by Holsapple (1993). Similar-sized collisions are, in stark contrast, not point-source interactions and as such we should not expect that a framework derived in the point-source limit will continue to apply. Thus, scaling laws continue to evolve from early adaptations in the literature.

1.3.1 Benz and Asphaug (1999)

Benz and Asphaug (1999) focused on the catastrophic disruption threshold, in the context of collisions in the asteroid belt. They examined the transition from small-scale collisions (centimeters to meters in size), where the disruption outcome is governed by the material strength of the bodies, to large-scale collisions (kilometers in size), where the disruption outcome is dominated by self-gravity. To do so, they employed the SPH method with self-gravity and a model for dynamical fracture of brittle material (Benz and Asphaug, 1994) to simulate collisions into targets ranging from 1 cm – 100 km in diameter. They employed the Tillotson equation of state to model both basalt and water-ice targets.

Importantly, Benz and Asphaug (1999) discuss the distinction between what constitutes the 'largest remnant' produced by strength-dominated collisions and gravity-dominated collisions. The largest remnant in strength-dominated collisions is the largest monolithic rock at the top of a size-distribution of other fragments. In

contrast, the largest remnant in gravity-dominated collisions is an accumulation of an array of gravitationally-bound materials: intact monolithic fragments, fluidized debris, vapor-rich disk, *et cetera*.

Benz and Asphaug (1999) were focused primarily on the conditions of the asteroid belt where the velocity dispersion of the swarm of small bodies can be well constrained, thus impact velocity was held constant. For a given target mass they determined the disruption thresholds by holding both the impact angle and velocity constant while allowing the impactor size to vary, effectively probing different ranges of impact energy; because of this methodology the impactor-to-target mass ratio (Equation 1.2) required to disrupt the target was larger than 1 in some cases (Benz and Asphaug, 1999). They limited their study to 3 and 5 km/s for basalt, and 0.5 and 3 km/s for ice.

They find that gravity-dominated bodies tend to become weaker as they decrease in size, with the weakest bodies being ∼300 m in diameter, whereas bodies smaller than this become more resistant to disruption as the effects of material strength (tensile strength in their model) dominate. The scaling law they develop for both regimes is used widely and takes on the following form:

$$Q^*_{\rm D} = Q_0 \left(R_{\rm tar}\right)^a + B\rho \left(R_{\rm tar}\right)^b , \tag{1.4}$$

where Q_0, a, B, and b are fitted parameters. However, the fitted parameters are relevant for specific disruption velocities which were held constant, thus we caution the use of this scaling law outside of its intended context, for example to solve for the disruption velocity given constant $M_{\rm tar}$ and $M_{\rm imp}$ or to apply the relation to planet-scale collisions.

In Figure 1.2 we compare the scaling law of Benz and Asphaug (1999) against

the mutual binding energy of two colliding bodies. The slope of the gravity-regime term in Equation 1.4 (right hand side) is shallower than that of the gravitational binding energy. This demonstrates that there exists a transitional regime, we denote as 'mixed', where the collision outcome is dominated by both gravity and strength, and the slope must evolve from ∼1.2-1.4 to 2 so as to not predict disruptive collisions with impact energies well below the gravitational binding energy. Since Benz and Asphaug (1999) include a strength model in their SPH simulations they implicitly allow for the existence of such a mixed regime. In comparison it is no surprise that scaling laws in the gravity-only domain, explicitly excluding material strength, (e.g. Movshovitz et al., 2016, and our work), report scaling laws proportional to R^2. The slopes of the disruption thresholds in the mixed region have been recently explored as a function of different strength models; the inclusion of dissipation by friction, for example, has shown there are measurable differences in the catastrophic disruption threshold at sizes up to ∼100 km (e.g. Jutzi, 2015).

Benz and Asphaug (1999) also introduced a functional relationship for the mass of the largest remnant in a giant impact,

$$\frac{M_{\rm LR}}{M_{\rm tar}} = -s\left(\frac{Q}{Q^*} - 1\right) + 0.5, \tag{1.5}$$

which was an important basis on which future scaling laws for remnant masses were based. Owing to the simplicity of this relation and Equation 1.4 they are used in numerous numerical studies of planet formation, and frequently well outside the parameter space that was studied.

Although our work is primarily focused on the collisions of gravity-dominated bodies, as is relevant to late-stage planet formation, understanding collisional outcomes in the transitional regime between strength- and gravity-dominated collisions is an

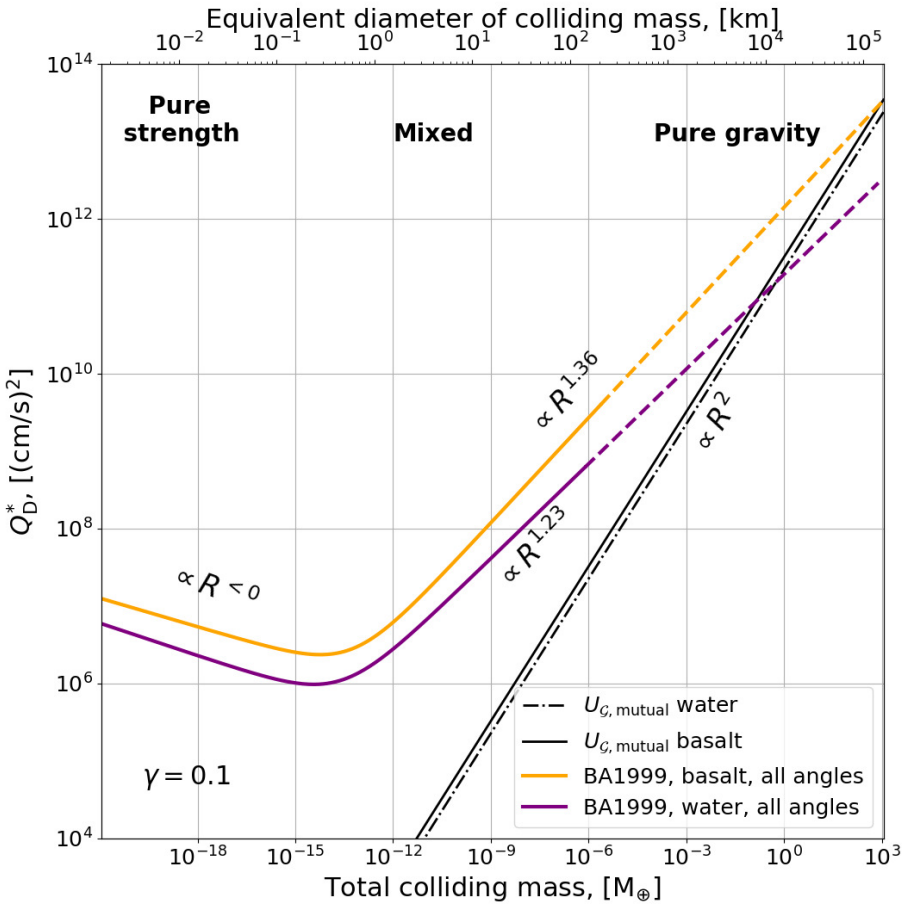

Figure 1.2. The catastrophic disruption threshold energy from Benz and Asphaug (1999) compared to the mutual gravitational binding energy for the colliding bodies with $\gamma = 0.1$. Dark red and orange lines are water ice and basalt collisions that included a strength model and self gravity, averaged over data for several angles and impact velocities. The black solid and dot-dashed lines show the mutual gravitational binding energy for basalt ($\rho = 3000$ kg/m^3) and water ($\rho = 1000$ kg/m^3) bodies. Collisions with impact energy below the black lines cannot result in appreciable disruption, but the true disruption threshold likely lies above them.

area of important ongoing work. Collisions at the kilometer to tens of kilometers scale is critical in understanding in the formation of small bodies, such as Vesta (e.g. Jutzi et al., 2013), irregularly-shaped comets (e.g. Jutzi and Asphaug, 2015), and asteroid collisional families (e.g. Jutzi et al., 2010; Jutzi et al., 2018). However, incorporating collisions of billions of small bodies and remnants in planet formation codes is still out of reach for even the most sophisticated N-body schemes.

1.3.2 Stewart and Leinhardt (2009)

Stewart and Leinhardt (2009) developed scaling laws to predict the mass of the largest remnant and focused on the catastrophic disruption threshold. They simulated low-velocity collisions between gravitationally-bound granular aggregates (rubble piles) using the N-body code PKDGrav (e.g. Leinhardt et al., 2000; Richardson et al., 2000; Stadel, 2001). The particles are indestructible and undeformable, and the contact physics were governed by restitution. Thus the bodies are gravity-dominated with no inter-granular cohesion, no calculation of impact shock physics, and no measurable or evolvable thermodynamic states.

Stewart and Leinhardt (2009) studied aggregates with diameters D=2, 20, 100 km undergoing head-on collisions at sub-sound speed velocities (1-300 m/s) and used two impactor-to-target mass ratios, $\gamma = 0.03$ and $\gamma = 1$. Disruption threshold data from several other studies were also used to fit scaling laws in Stewart and Leinhardt (2009), including simulations of strength-dominated collisions and laboratory studies of the disruption of $\sim$cm-sized targets.

To account for scenarios that involve collisions of objects with disparate densities

they developed a 'normalized radius',

$$R_{C1} = \left(\frac{3}{4\pi} \frac{M_{\rm tot}}{1 \text{ g/cm}^3} \right)^{1/3}, \tag{1.6}$$

which represents an uncompressed sphere of water with mass $M_{\rm tot} = M_{\rm tar} + M_{\rm imp}$. Since giant impacts involve impactors comparable in size to the target, which is not the case in classical cratering, the reduced mass kinetic energy (scaled by the total mass) was introduced,

$$Q_{\rm R} = \frac{1}{2} \frac{\mu v_{\rm imp}^2}{M_{\rm tot}}, \tag{1.7}$$

where μ is the reduced mass,

$$\mu = \frac{M_{\rm tar} M_{\rm imp}}{M_{\rm tot}}, \tag{1.8}$$

and $v_{\rm imp}$ is the impact velocity. Like Equation 1.3, the units of $Q_{\rm R}$ are in specific energy, but using a different normalization; $Q_R \propto \gamma/(1+\gamma)^2$, whereas $Q \propto \gamma$.

Under their scheme, the disruption threshold energy, $Q^*_{\rm RD}$, for a given set of colliding bodies is $Q^*_{\rm RD} = Q_{\rm R}$ when $M_{\rm LR} = \frac{1}{2} M_{\rm tar}$. Based on the framework of Housen and Holsapple (1990), who developed disruption criteria for bodies in the strength and gravity-dominated regime, Stewart and Leinhardt (2009) reported a velocity-dependent relationship for $Q^*_{\rm RD}$,

$$Q^*_{\rm RD} = q_{\rm s} R_{C1}^{9\bar{\mu}/(3-2\phi)} v_{\rm imp}^{(2-3\bar{\mu})} + q_g R_{C1}^{3\bar{\mu}} v_{\rm imp}^{2-3\bar{\mu}}, \tag{1.9}$$

where in this case, $\bar{\mu}$ is a fitted material parameter between $1/3 \leq \bar{\mu} \leq 2/3$ (with $\bar{\mu} = 1/3$ representing pure 'momentum scaling' and $\bar{\mu} = 2/3$ representing pure 'energy

scaling') and ϕ is a flaw distribution parameter that ranges from 6 to 9 depending on the material. The first term of Equation 1.9 has a negative slope, as appropriate for the strength regime (see Figure 1.2) and the second has a positive slope, as appropriate for the gravity regime. They find that $\bar{\mu}$=0.4, $q_{\rm s} = 500$ and $q_g = 10^{-4}$ provides a good fit to simulations of gravity-dominated collisions (these values require $v_{\rm imp}$ and R_{C1} to be in cgs units). Different constants were fit for laboratory experiments in the strength regime, $q_{\rm s} = 7 \times 10^4$, $q_g = 10^{-4}$, $\bar{\mu} = 0.5$, and $\phi = 8$. Stewart and Leinhardt (2009) also reports their catastrophic disruption threshold $Q^*_{\rm RD}$ (Equation 1.9) for the gravity regime assuming pure-energy scaling ($\bar{\mu} = 2/3$),

$$Q^*_{\rm RD} = aR^2_{\rm C1}, \tag{1.10}$$

where $a = (1.7 \pm 0.3) \times 10^{-6}$ and $(5.3 \pm 1.8) \times 10^{-6}$ for equal mass projectiles and small projectiles respectively; the velocity-dependent term drops out and the relation is proportional to $R^2_{\rm C1}$, as appropriate for the gravity regime (See black lines in Figure 1.2). Moreover, Stewart and Leinhardt (2009) provided a scaling law for the mass of the largest remnant $M_{\rm LR}$, similar to Equation 1.5 developed in Benz and Asphaug (1999),

$$M_{\rm LR}/M_{\rm tot} = 1 - 0.5 Q_{\rm R}/Q^*_{\rm RD}, \tag{1.11}$$

that holds well for impact energies with $Q_{\rm R}/Q^*_{\rm RD} < 2$.

Although Stewart and Leinhardt (2009) demonstrates this disruption criteria is robust for low-velocity collisions of self-gravitating aggregates, Equation 1.9 does not include dependence on impact angle. To that end, they note that $Q^*_{\rm RD}$ values seem to decrease by $\sim$10% when $\theta_{\rm imp} = 45^\circ$.

1.3.3 Leinhardt and Stewart (2012)

Leinhardt and Stewart (2012) developed scaling laws with parameters that were fit independently for small bodies (with and without strength) and large, hydrodynamic (strengthless) bodies, some of which included differentiated bodies (Leinhardt and Stewart, 2012, Figure 12 and Table 3 therein). Their scaling law fit to small bodies included new simulations of sub-sonic collisions that used target bodies 10 km in radius with four different impactor masses, all with a bulk density of 1 g/cm^3. They expanded on the work of Stewart and Leinhardt (2009) by simulating impacts at four different impact angles, $\theta_{\rm imp} = 0^\circ,\ 22.8^\circ,\ 49.4^\circ,\ 71.3^\circ$.

Leinhardt and Stewart (2012) introduced the concept of 'interacting mass' to resolve the fact that in grazing collisions some of the impactor (if it is large enough) may interact only minimally, or not at all, with the target body. The interacting mass is constructed to represent only the portion of the impactor that directly intersects the target (see Figure 2 of Leinhardt and Stewart 2012). It is important to note however that the kinetic energy of the interacting mass is reported differently between Leinhardt and Stewart (2012, Equation 12) and the full derivation reported in Movshovitz et al. (2016, Equation 20). Though we do not examine the origin of this discrepancy since, as described later, we choose to eschew the concept of the interacting mass altogether. Nevertheless, we demonstrate the discrepancy in the supplement for posterity.

The catastrophic disruption threshold in Leinhardt and Stewart (2012) includes a dependence on the impactor-to-target mass ratio, γ, and $\bar{\mu}$,

$$Q^*_{\rm RD} = Q^*_{{\rm RD},\gamma=1} \left(\frac{1}{4} \frac{(\gamma+1)^2}{\gamma} \right)^{((2/3\bar{\mu})-1)}, \tag{1.12}$$

where $Q^*_{{\rm RD},\gamma=1}$ is the catastrophic disruption threshold for a head-on collision between

equal-mass bodies. However, Movshovitz et al. (2016) demonstrated that this correction produces inaccuracies for small values of γ. In the case of off-axis collisions, a correction for the interacting mass is applied (Leinhardt and Stewart, 2012, Equation 15). The catastrophic disruption threshold term takes on a form similar to that of Equation 1.10,

$$Q^*_{\mathrm{RD},\gamma=1} = c^* \frac{4}{5} \pi \rho_1 \mathcal{G} R^2_{\mathrm{C1}}, \tag{1.13}$$

where c^* is a fitted parameter and $\rho_1 = 1$ g/cm^3. Using these relations, in conjunction with Equation 1.11, Leinhardt and Stewart (2012) reports that the mass of the largest remnant can be predicted for a variety of types of bodies (*e.g.* hydrodynamic or granular) with adjustments to the fit parameters. For hydrodynamic bodies, $c^* = 1.9 \pm 0.3$ and for small bodies $c^* = 5 \pm 2$ (in cgs units); a difference of about a factor of 2 with some overlap.

The mass of the second largest remnant is computed in two different ways, under Leinhardt and Stewart (2012), depending on the scenario. In a relatively head-on scenario, the second largest remnant is merely the largest body in the cascade of impact debris, *i.e.* the second largest remnant is the top of the debris size distribution often modeled with a power law. In a hit-and-run scenario, the second largest remnant is the eroded impactor that continues downrange along with debris that can be described by a size distribution. At the top of the debris size distribution lies the *third* largest remnant. To determine the mass of the second largest remnant in a hit-and-run collision per Leinhardt and Stewart (2012), the catastrophic disruption of criteria of the 'reverse' impact is computed. Note that in this case the interacting mass for the reverse collision is intended to exclude the mass of the *target* that does not directly

intersect the impactor. The scaling law of Equation 1.11 is then used to determine the mass of the second largest remnant for any impact energy.

1.3.4 Movshovitz et al. (2016)

Movshovitz et al. (2016) pay particular attention to the catastrophic disruption threshold and determine the appropriate scaling law variables for the gravity-dominated regime to predict disruption. They simulate collisions at high energy which allows for a direct interpolation of the catastrophic disruption threshold energy, providing an overall more accurate prediction than extrapolative methods. They find that simply the reduced mass impact energy, $K = Q_{\mathrm{R}} M_{\mathrm{tot}}$, is an ideal variable for scaling catastrophic disruption in the gravity regime (pure energy scaling). Their disruption threshold K^* is a multiple of the gravitational binding energy of the 2-body system at the point of collision, $U_{\mathcal{G},\mathrm{mutual}}$; we introduce $U_{\mathcal{G},\mathrm{mutual}}$ formally later. Moreover, as stated in the previous section, Movshovitz et al. (2016) use a correction factor which removes the non-interacting mass of the collision from the computation of K; once the correction factor is applied the kinetic energy is denoted as K_α and the catastrophic disruption data under this definition more tightly follow a power law. However, even when using this correction factor they still found that the prefactor on K^* is a function of θ_{imp}, so additional empirical functionality is needed. Thus we utilize the scaling parameters of Movshovitz et al. (2016) and replace the interaction mass correction by an empirical relationship.

1.4 Methodology

To understand how the outcomes of giant impacts vary under a variety of pre-impact conditions we simulated collisions of similar-sized bodies using the 3D smoothed-particle hydrodynamics (SPH) code SPHLATCH (Reufer, 2011). This code was designed specifically for handling giant impacts using a Barnes-Hut tree based self-gravity calculation and can use the ANEOS, M-ANEOS, and TILLOTSON equations of state. SPHLATCH has been well tested against standard test problems, such as the blast tube test (Sod, 1978), and used in previous planet formation studies (Reufer et al., 2012; Asphaug and Reufer, 2013; Asphaug and Reufer, 2014; Emsenhuber et al., 2018), producing similar outcomes to other SPH codes when applied to standard scenarios such as Moon-formation. Since we are focused on predicting the mass of remnants in the gravity regime of giant impacts, we assume a fluid rheology and self-gravity in our SPH simulations; however, SPHLATCH has recently been updated to include material strength as well (Emsenhuber et al., 2018). We use the common form of artificial viscosity (Monaghan, 1992) with no artificial viscosity 'switches' (e.g. Balsara, 1995); these switches are used to combat erroneous activation of artificial viscosity, but can introduce other non-physical effects (see Raskin and Owen (2016) for the effects of these switches on a test problem most relevant to planetary problems). We also use the standard SPH formulation which is based on the differentiability of density. We recognize the fact that in the case of the post-impact disc in the Moon-forming collision, density-independent formulations (which rely on the differentiability of pressure) provide different results from standard SPH and can better resolve static features of planetary problems such as the density discontinuity at the core-mantle boundary (Hosono et al., 2016). However, additional corrections must be employed to

accurately resolve shocks in density-independent schemes (Saitoh and Makino, 2013) and the effect of this formulation on the masses of the largest remnants generated through collisions with strong shocks is unclear at this time. Nevertheless, it is important to point out that the outcome of SPH simulations of different numerical variety can vary, sometimes significantly, for planetary problems. Hosono et al. (e.g. 2019), for example, finds that their density-independent SPH formulation shows a *significant* discrepancy in the amount of Earth material incorporated in the post-impact disc in the Moon-forming collision; this result effectively upends the high level of misplaced confidence in planetary SPH simulations on the topic and is an important cautionary tale. Thus we caution the over interpretation of model results below the few to $\sim$10% level, depending on the detailed nature of the impact outcome of interest. We use a cubic spline kernel and the smoothing length is adjusted to an optimum number of 50 neighbors. Sensitivity to the choice of artificial viscosity, SPH flavor, or spline on the mass of the largest remnants is outside of the scope of this work and thus we find it appropriate to use the most common forms. The methodology for determining the mass of remnants and bound clumps from SPH simulation output is described in Emsenhuber and Asphaug (2019). Data for each simulated collision is also provided as supplementary text files; the supplementary text files 'Table1.txt', 'Table2.txt', and 'Table3.txt' provide $M_{\rm LR}$, $M_{\rm 2LR}$, and $M_{\rm esc}$ for the pure SiO_2, SiO_2-Fe, and H_2O-SiO_2-Fe bodies respectively, as a function of all pre-impact initial conditions (see column descriptions in the header).

1.4.1 Parameter Space

A number of variables influence the outcome of a giant impact. These parameters include the impact scale (total mass of the colliding bodies ; $M_{\rm tot}$), mass ratio between the target and the impactor ($\gamma = M_{\rm imp}/M_{\rm tar}$), impact angle ($\theta_{\rm imp}$), impact velocity ($v_{\rm imp}$), material composition, thermal state, material strength, and pre-impact rotational states. As such, the complete parameter space is inherently very large and it is beneficial to identify the range of conditions probable in the late-stages of planet formation, while others are held constant.

'Composition' in itself hides a multitude of different avenues for variation. For example, two bodies may have a similar bulk geochemistry but differ in mineralogy due to differentiation or their thermal state. Colliding bodies that originated from different dynamical zones may have entirely different geochemical compositions as well. Moreover, few material equations of state exist for the range of mineralogy found in primitive and evolved planets, and even fewer SPH codes implement a large range of equations of state. In this study we choose to examine bodies composed of three materials: quartz (an analogue for mantle/crust silicates), iron (an analogue for nickel-iron core material), and water. Quartz was chosen in particular since its equation of state is most up-to-date (Melosh, 2007) and it has been used extensively in giant impact studies (e.g., Canup and Asphaug, 2001; Marcus et al., 2009; Asphaug and Reufer, 2014). We simulate pairs of colliding planets with three material categories: homogeneous SiO_2, 2-layer SiO_2-Fe and 3-layer H_2O-SiO_2-Fe; thermodynamic information is sourced from a tabularization of the ANEOS and M-ANEOS equation of state (Reufer, 2011). The SiO_2-Fe component in both cases is in 'chondritic' abundance, 70wt% SiO_2 and 30wt% Fe. The 3-layer planets are 50wt% H_2O. The water-rich planet composition is

the same composition as used by Asphaug and Reufer (2013) and dissimilar to that of Marcus et al. (2010) who used a 50wt% H_2O, 50wt% Serpentine composition; both used the ANEOS equation of state. The difference between the bodies used by these studies is a good example of the influence of assumptions regarding differentiation. The Marcus et al. (2010) bodies represent a partially-differentiated state, whereas ours and those of Asphaug and Reufer (2013) are more analogous to a fully-differentiated state.

Collisions between bodies with non-zero rotation, either inherited from the disk or from a previous off-axis impact (C. B. Agnor et al., 1999), are an inevitable phenomenon in late-stage planet formation. First demonstrated by Canup (2008) in simulations of the Moon-forming collision, pre-impact rotation of the colliding bodies can fundamentally change disruption and accretion dynamics. Properly examining pre-impact rotation requires the consideration of six independent parameters, the spin rates of the target and impactor, alongside four angles to describe the orientation of the spin axes relative to each other and the impact plane. As such, considering pre-impact rotation inherently comes with a large computational cost, requiring that other parameters are held constant (as was done in Canup (2008) and Rufu et al. (2017)). To allow consideration of a larger number of other parameters we thus choose to ignore pre-impact rotation and reserve this topic for future study.

As discussed in Section 1.2, N-body simulations of late-stage formation of the terrestrial Solar system demonstrate that planetary embryos collide at typically 1-2 $v_{\rm esc}$. Thus we conducted simulations across 1–4 $v_{\rm esc}$ to capture rare, higher impact velocity events, with finer resolution in the most probable 1–2 $v_{\rm esc}$ range. We simulated collisions between bodies with a range of impactor-to-target mass ratios from $\gamma = 0.1$ to 0.7, depending on the material. Our database spans several decades of $M_{\rm tot}$, from

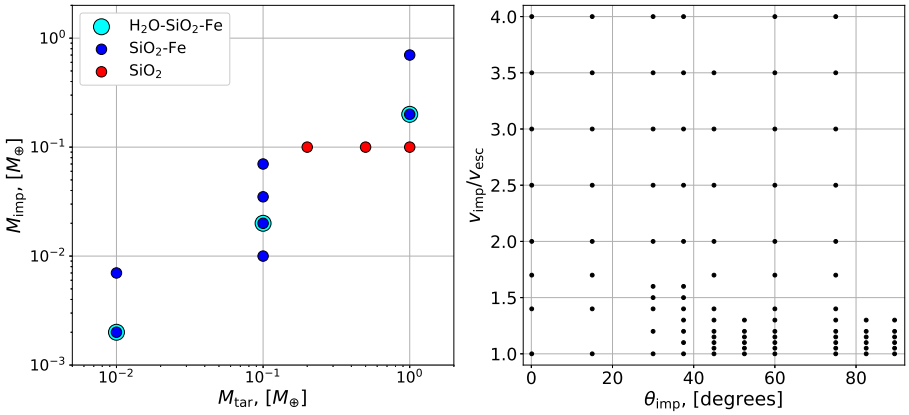

Figure 1.3. The parameter space of our giant impact simulations in terms of the major input variables. The target mass ($M_{\rm tar}$) and impactor mass ($M_{\rm imp}$) combinations are shown in the left hand panel. Red points indicate collisions between SiO_2 bodies, blue points indicate collisions between SiO_2-Fe bodies, and cyan points indicate collisions between H_2O-SiO_2-Fe bodies. At each point in the left hand panel, simulations cover the full grid of impact angle ($\theta_{\rm imp}$) and impact velocity normalized by the 2-body escape velocity (Equation 1.1) $v_{\rm imp}/v_{\rm esc}$ shown in the right hand panel.

10^{-2}-1 $M_\oplus$, which spans escape velocities from a few to over 10 km/s. We cover the entire range of possible impact angles from $\theta_{\rm imp} = 0.1^o$ to 89.5^o. Our simulations have a resolution of $\sim 10^5$ particles in the target body[4], as is widely used in giant impact studies (e.g. Marcus et al., 2009; Marcus et al., 2010; Canup, 2011; Asphaug and Reufer, 2013). Note that the 10^4 particle N-body simulations performed by Leinhardt and Stewart (2012) are somewhat similar to 10^5 particle SPH simulations due to the differences between the numerical schemes[5]. The parameter space spanned by our simulations is depicted in Figure 1.3.

[4]The impactor is composed of $\sim \gamma 10^5$ particles.

[5]Asphaug (2010) describes the differences in resolving power of granular codes (*e.g.* PKDGRAV) and SPH codes.

1.5 Our Scaling Laws

The aim of scaling laws is to reduce the input and outcome spaces, composed of thousands of particle positions, velocities, thermal states, etc., to a few fundamental parameters, allowing for the broad outcome of the simulation to be predicted by simple functions of a small set of input and output parameters. Previous works have approached this from somewhat different perspectives, using different fundamental variables. Movshovitz et al. (2016) demonstrated the superiority of pure-energy scaling for gravity-dominated collisions and we find their structure to be intuitive, so we begin in a similar way. However, unlike Movshovitz et al. (2016) we aim to provide a set of predictive relationships for remnant and debris masses for use in N-body simulations and do not focus on constructing the most appropriate physical scaling law variables. To globally optimize our empirical model we employ a Markov-chain Monte Carlo (MCMC) routine (Foreman-Mackey et al., 2013). The setup of the optimization scheme is reported in the Supplementary Material. This scheme was chosen as it allows for a set of several empirical equations and associated parameters to be globally optimized across multiple outputs in our database (largest remnant and runner mass in this case). The output of the scheme also allows for the assessment of degeneracy and correlation of empirical fit parameters which provides important feedback in the development of empirical relationships.

The first parameter we use is the impact energy, which acts to disrupt the bodies in a collision,

$$K = \frac{1}{2}\mu v_{\rm imp}^2, \tag{1.14}$$

where μ is the reduced mass of the two bodies,

$$\mu = \frac{M_{\rm tar} M_{\rm imp}}{M_{\rm tar} + M_{\rm imp}}, \tag{1.15}$$

and $v_{\rm imp}$ is the impact velocity of the two bodies. Note that we do not use the concept of 'interacting mass' introduced by Leinhardt and Stewart (2012), and also used by Movshovitz et al. (2016).

1.5.1 Gravitational Binding Energy

For collisions between large bodies the total gravitational potential energy $U_{\mathcal{G}}$ is the dominant contributor to the overall binding energy of the bodies (e.g. Benz and Asphaug, 1999). The binding energy is thus described by,

$$U_{\mathcal{G}} = -\mathcal{G} \int_0^R M(r) m(r) \frac{dr}{r}, \tag{1.16}$$

where $m(r)$ is the mass of a shell of size dr, $M(r)$ is the mass interior to the shell, and R is the radius of the planet. Assuming a constant density throughout the body, the equation simplifies to

$$U_{\mathcal{G}} = \frac{3}{5} \frac{\mathcal{G} M^2}{R}, \tag{1.17}$$

where M is the total mass of the body and we use the convention that the binding energy is positive.

The binding energy of the *system* of impacting bodies must account for their

separation at impact (e.g. Movshovitz et al., 2016),

$$U_{\mathcal{G}} = U_{\mathcal{G},\mathrm{tar}} + U_{\mathcal{G},\mathrm{imp}} + \mathcal{G}\frac{M_{\mathrm{tar}}M_{\mathrm{imp}}}{R_{\mathrm{tar}} + R_{\mathrm{imp}}}, \tag{1.18}$$

where the binding energy of the target and impactor, $U_{\mathcal{G},\mathrm{tar}}$ and $U_{\mathcal{G},\mathrm{imp}}$ respectively, can be computed either analytically (Equation 1.17) or by integrating Equation 1.16, but the offset factor is an approximation.

1.5.1.1 Compression and Density Stratification

The assumption of constant density yields a lower limit for the actual gravitational binding energy. As a planet increases in mass, the internal pressures rise and the materials begin to compress, resulting in density gradients even within layers of constant bulk composition. In the simulations of Movshovitz et al. (2016) and PKDGRAV simulations of small bodies in Stewart and Leinhardt (2009) and Leinhardt and Stewart (2012), the bodies are small and compression is negligible. Here, however we study bodies covering several orders of magnitude in mass and even our smallest bodies are larger than the largest bodies used by Movshovitz et al. (2016). Combined with the three different compositions, two of which are layered, our simulations thus span a range of degrees of density stratification that may influence impact outcomes.

To quantify the degree of density stratification of the two bodies involved in the collision in a simple 1-dimensional measure, we introduce the ratio of the analytical and numerical values of the gravitational binding energy of the two bodies,

$$\Lambda = \frac{U_{\mathcal{G},a,tar} + U_{\mathcal{G},a,imp}}{U_{\mathcal{G},n,tar} + U_{\mathcal{G},n,imp}}, \tag{1.19}$$

where the analytical value, $U_{\mathcal{G},a}$, is calculated using the constant density approximation (Equation 1.17). For individual bodies the ratio of the analytic and numerical values, $U_{\mathcal{G},a}/U_{\mathcal{G},n}$, can reach $\sim$85%. The bodies used in our study and their physical parameters are reported in Table S1.2. The value of Λ is smaller for more massive bodies as increased central pressures result in greater compression and transitions to high-pressure polymorphs. Note that even in the pure SiO_2 bodies, compression under gravity and a solid-state phase transition results in a density gradient toward the center of the body. This produces minor discrepancies between $U_{\mathcal{G},\,\mathrm{a}}$ and $U_{\mathcal{G},\mathrm{n}}$.

We show the values of Λ for bodies in our study in Figure 1.4. Compression and density stratification cause deviations from the analytical binding energy, especially for the layered bodies, as expected. As we discuss in later sections we find that certain aspects of the impact outcome are dependent on this ratio, particularly in predicting hit-and-run collisions. We note that there is degeneracy in this formulation. Bodies of different compositions may yield similar values of Λ, but so long as the onset of hit and run depends solely on mass distribution, the utility of this parameter is likely to hold reasonably well.

1.5.2 Predicting Hit-and-Run

Many studies (e.g. C. Agnor and Asphaug, 2004; Asphaug et al., 2006; Kokubo and Genda, 2010; Stewart and Leinhardt, 2012) have shown that a substantial region of pre-impact conditions of similar-sized collisions result in hit and run. It is natural then that N-body studies have shown that such hit-and-run outcomes are common, accounting for around half of all giant impacts in many cases (e.g. Kokubo and Genda,

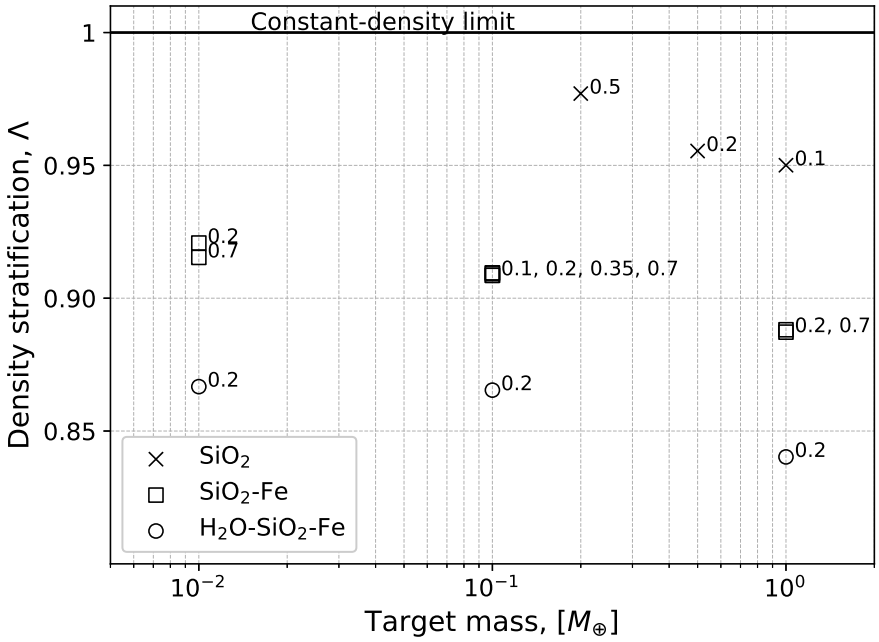

Figure 1.4. The ratio of the analytically- and numerically-determined binding energy of the target and impactor, Λ. This ratio represents the degree of density stratification of the two bodies involved in the collision, with $\Lambda = 1$ being the uncompressed, homogeneous density limit. The 'x', square, and circle symbols represent the homogeneous SiO_2, 2-layer SiO_2-Fe, and 3-layer H_2O-SiO_2-Fe bodies respectively. The impactor-to-target mass ratio is reported next to each point. The homogeneous silicate bodies approach the constant-density limit for small enough masses, however we note that these planets still include a solid-state phase transition and demonstrate minor levels of stratification.

2010; Chambers, 2013). Delineating the transition between the merging/erosive and hit-and-run regime is thus clearly important.

Here we define the hit-and-run transition as the point in which the impactor continues down range, largely unscathed. This transition presents itself as a step discontinuity, $\xi_{\rm jump}$, in the accretion efficiency parameter developed by Asphaug (2010):

$$\xi = \frac{M_{\rm LR} - M_{\rm tar}}{M_{\rm imp}}. \tag{1.20}$$

In a perfect merger, when the mass of the largest remnant $M_{\rm LR}$ is equal to the total

mass of the colliding bodies, $M_{\rm LR} = M_{\rm tar} + M_{\rm imp}$ and $\xi = 1$. If the impact is a merger that produces escaping debris, with mass $M_{\rm esc} = M_{\rm imp}$, then $M_{\rm LR} = M_{\rm tar}$ and $\xi = 0$. Similarly, in a clean hit-and-run collision, where the impactor continues downrange unscathed, $M_{\rm LR} = M_{\rm tar}$ and thus $\xi = 0$ as well. As such, taken on its own, accretion efficiency is degenerate with respect to hit-and-run and erosive collisions, *i.e.* the fate of the 'runner'. Without knowledge of the second largest remnant mass, an erosive collision and a hit-and-run collision cannot be distinguished by ξ alone.

1.5.2.1 The Impact Angle Threshold

At low impact angles and low velocities the colliding bodies merge and produce minimal mass (a few percent of the total mass) to debris, so $\xi \approx 1$. At low angles the accretion efficiency also smoothly declines as a function of impact velocity, since more escaping debris is produced (See Figure 1.5, top panel). In contrast, at some threshold angle a sharp, step-like discontinuity in ξ occurs (see Figure 1.5, second from top panel). This marks the point at which a large portion of the impactor mass does not accrete onto the target, but is dispersed downrange, either as a debris field ('impactor disruption') or as a relatively intact mass (hit and run). At larger angles, a majority of the parameter space between 1–4 $v_{\rm esc}$ is dominated by hit and run of a cleaner variety. However, as discussed in Section 1.5.2, a value of $\xi \approx 0$ alone does not alone predict hit and run. For example, from Figure 1.5 we can see that at $\theta_{\rm imp} = 22.5^\circ$ and $v_{\rm imp} = 2v_{\rm esc}$, a value of $\xi \approx 0$ is found, yet the hit and run discontinuity is not shown. Figures 1.14, 1.15, and 1.16 (see Appendix) show accretion efficiency across the entire database of SPH simulations and they demonstrate that the degeneracy

exists for all combinations of γ and $M_{\rm tar}$; values of $\xi \approx 0$ are present both in erosive (more head-on) collisions and hit-and-run (more glancing) collisions.

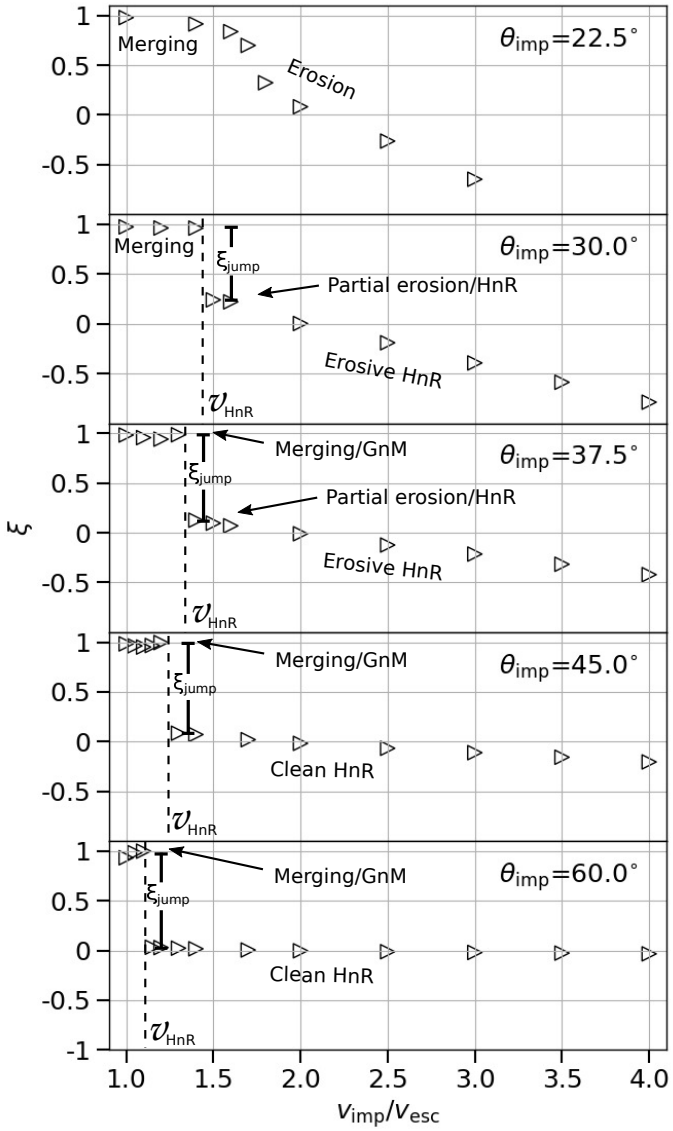

Figure 1.5. Accretion efficiency for simulations of rock-iron planets with $M_{\rm tar} = 0.2M_{\oplus}$ and $M_{\rm imp} = 0.1M_{\oplus}$ impacting at $\theta_{\rm imp} = 22.5°$, 30°, 45°, and 60°. The step discontinuity of ξ due to hit-and-run is evident for $\theta_{\rm imp} > 22.5°$. For this combination of $M_{\rm tar}$, γ, and material type, the geometric threshold for hit-and-run has the bounds: $22.5° < \theta_{\rm HnR} \leq 30°$. The dashed line indicates the velocity threshold for hit-and-run, which is inversely related to $\theta_{\rm imp}$. The step discontinuity in accretion efficiency that marks the onset of runner disruption/hit and run is labeled $\xi_{\rm jump}$.

We show only one value of impactor-to-target mass ratio in Figure 1.5, however, the hit-and-run angle, $\theta_{\rm HnR}$ can vary depending on the impactor-to-target mass ratio. For similar-sized collisions Asphaug (2010) defined the grazing angle, θ_b, that represents the impact geometry at which the velocity vector drawn through the center of the impactor does not intersect the target,

$$\theta_b = \sin^{-1}\left(\frac{R_{\rm tar}}{R_{\rm imp} + R_{\rm tar}}\right). \tag{1.21}$$

For cases with $\gamma << 1$ the impactor is colliding with what can be approximated as an infinite plane, whereas in a giant impact the target is comparable in size to the projectile. This makes it common for the projectile core to miss the target core entirely in a typical giant impact, plowing instead through its less-dense mantle.

Due to the lack of a recipe for hit-and-run angle in the literature, several authors have implemented the grazing criterion (Equation 1.21) to represent the angular threshold beyond which all collisions are considered hit-and-run (Chambers, 2013; Quintana et al., 2016, e.g.)[6]; that is, any collision that satisfies $\theta_{\rm imp} > \theta_{\rm b}$, regardless of the impact velocities, is hit and run. However, Figure 1.5 demonstrates that the velocity at which hit and run occurs varies with impact angle. The grazing criterion simplification will over-estimate hit-and-run collisions in the case of events that would actually be low velocity graze-and-merge events; for example, the canonical Moon-forming giant impact would be hit and run according to that rule. Conversely it will under-estimate hit-and-run collisions in the case of high impact velocity; some collisions as steep as 15-20°, close to head-on, can be hit and run under certain conditions (we demonstrate this later). Leinhardt and Stewart (2012) uses Equation 1.21 in the

[6]In Chambers (2013) $\theta_{\rm graz}$ is equal to $\theta_{\rm b}$ defined in Asphaug (2010)

construction of their scaling laws, alongside the velocity threshold criterion to account for this behavior.

Our study includes a reasonably high-resolution sampling of $\theta_{\rm imp}$, enabling us to directly estimate $\theta_{\rm HnR}$ for the first time. For example, as shown in Figure 1.5, by having a fine resolution in $\theta_{\rm imp}$ and $v_{\rm imp}$ we are able to find that the angle at which hit-and-run may occur for this pair of bodies is between $22.5^\circ < \theta_{\rm HnR} \leq 30^\circ$, whereas Equation 1.21 would predict it to occur at 42.5°. However, determining the hit and run angle must take into account the mass of the second largest remnant (runner) since hit and run is described as when the impactor continues downrange somewhat unscathed. We estimated the hit-and-run angle across the database of simulations, assuming hit and run is defined by: 1. a discontinuity in ξ, and 2. a relatively-intact second largest remnant ($M_{\rm 2LR} \geq 0.5 M_{\rm imp}$). Using this criteria we show the relationship of $\theta_{\rm HnR}$ with respect to pre-impact parameters in Figure 1.6. It is first immediately clear that the hit-and-run angle decreases as a function of γ, as predicted by Equation 1.21. This effect is recognized in Figures 1.14, 1.15, and 1.16; the transition from merging to hit and run ($\xi \approx 1$ to $\xi \approx 0$) occurs at lower angles for larger γ.

In Figure 1.6 the hit-and-run thresholds are also observed to differ for the three material compositions, or equivalently density-stratifications. This is most noticeable at $\gamma = 0.2$, where there are data for all three compositions. Homogeneous bodies transition to hit-and-run at systematically-larger angles than the rock-iron bodies, which hit-and-run at larger angles than the water-rich 3-layer bodies. The merging regime ($\xi \approx 1$) is larger, encompassing higher velocity collisions, in the less stratified bodies. Less stratified bodies also tend to undergo disruption of the impactor into a string of remnants that are subsequently accumulated gravitationally downrange. For example, simulations at $\gamma = 0.2$ between pure SiO_2 bodies show $M_{\rm 2LR} \approx 0.5 M_{\rm imp}$

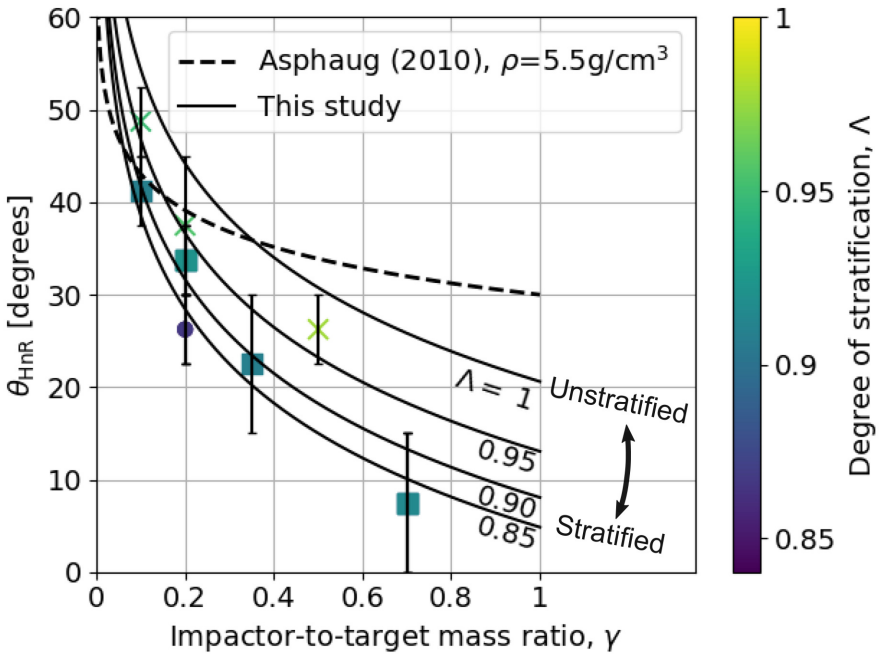

Figure 1.6. Angles at which collisions can transition from merging to hit-and-run as a function of impactor-to-target mass ratio, γ. The Asphaug (2010) grazing criterion is the dashed line (Equation 1.21). The 'x', square, and circle symbols represent the homogeneous SiO_2, 2-layer SiO_2-Fe, and 3-layer H_2O-SiO_2-Fe bodies respectively. Error bars extend from the angle at which hit-and-run does not occur (lower bound) to the angle at which it does (upper bound). Color represents the degree of density stratification. Planets with greater density stratification can hit-and-run at lower angles (closer to head-on geometry) as evidenced by the hit-and-run transition of the icy bodies (blue circle) for $\gamma = 0.2$, whereas uncompressed, homogeneous bodies require a more glancing geometry.

at $\theta_{\rm imp} = 37.5°$ for a slim set of impact velocities; however, the runner is largely gravitationally-accumulated debris. We can understand the origin of this trend physically since a more centrally-condensed impactor can more easily suffer a collision and partial stripping of some of the outer layers while still retaining the bulk of its mass as a bound entity.

To account for the dependence of the hit-and-run angle on density stratification we introduce the parameter Λ, defined in Section 1.5.1, in our empirical prediction of

θ_{HnR}:

$$\theta_{\mathrm{HnR}} = a \ \log_{10}(\gamma) + b\Lambda^{c}, \tag{1.22}$$

where $a = -33.8$, $b = 20.6$, $c = 8.9$, and θ_{HnR} is in degrees. We note that the data in Figure 1.6 is illustrative; our model was optimized to $M_{\mathrm{LR}/M_{\mathrm{tot}}}$ & $M_{\mathrm{2LR}/M_{\mathrm{imp}}}$ via a weighted MCMC scheme, thus the scheme is agnostic to whether or not the impactor remained 'relatively intact' throughout the collision or was gravitationally reaccumulated downrange. The optimization finds dependence on stratification as demonstrated by the values of b and c (See Figure S1.3 for the posterior distributions of the fit parameters). It is also immediately apparent that hit and run generally occurs at lower angles than predicted by models that assume $\theta_{\mathrm{HnR}} = \theta_b$, particularly for larger values of γ and for stratified planets.

We note that Equation 1.22 can only be accurate to $\pm 15^{\circ}$, since this is the angular resolution of our database and is close to the variation between the material types. Moreover, the transition to hit-and-run is not binary; instead, collisions transition from 'impactor disruption' to hit and run semi-smoothly, depending on density stratification; this transition is also on the order of $\sim 15^{\circ}$. Future work involving a larger number of different density stratifications, particularly at large values of γ, would be needed to better characterize the functionality of this effect.

We acknowledge the possibility that the effect may be due, at least in part, to thermodynamic effects; the different density stratifications in this study are produced by combinations of different materials, with different equations of state. For example, the most stratified planets are also the most volatile (water) rich, providing a different thermodynamic circumstance in the collision than the pure SiO_2 or SiO_2-Fe bodies.

1.5.2.2 The Impact Velocity Threshold

The criterion of $\theta_{\rm imp} > \theta_{\rm HnR}$ is a necessary, but not sufficient condition to define the transition to hit and run. For example, in the free-fall velocity limit ($v_{\rm imp} = v_{\rm esc,mutual}$) the impactor is bound and is thus guaranteed to merge with the target regardless of impact angle. The dashed lines in Figure 1.5 demonstrate that the hit-and-run velocity threshold decreases at glancing geometries due to less of the impactor being involved in the collisional interaction. Kokubo and Genda (2010) fit a hit-and-run criterion (their Equation 16) as a function of both $\theta_{\rm imp}$ and γ,

$$\frac{v_{\rm HnR}}{v_{\rm esc}} = 2.43\Gamma\Theta^{5/2} - 0.0408\Gamma + 1.86\Theta^{5/2} + 1.04, \tag{1.23}$$

where $\Gamma = (1-\gamma)/(1+\gamma) = (M_{\rm tar} - M_{\rm imp})/M_{\rm tar}$ and $\Theta = 1 - \sin(\theta_{\rm imp})$. We found limited evidence for dependence of the impact velocity threshold on the impactor to target mass ratio (γ) and so use the γ-free formulation:

$$\frac{v_{\rm HnR}}{v_{\rm esc}} = d\left(1 - \sin\left(\theta_{\rm imp}\right)\right)^{5/2} + e, \tag{1.24}$$

where $d = 1.88$ and $e = 1.13$, and e represents the hit-and-run velocity in the limit of $\theta_{\rm imp} \to 90°$. Both Equation 1.23 and 1.24 resolve the hit-and-run velocity threshold with similar accuracy. However, using Equation 1.23 without a geometric threshold would allow for near-head-on hit-and-run collisions if impact velocity is high; these conditions are more likely to lead to the disruption of the impactor than hit and run. For similar reasons described in Section 1.11 in the Appendix, we rule out the angular momentum criterion of Jutzi and Asphaug (2015) as a standalone predictor of hit and run across all angles and velocities. We also examined the extent to which the

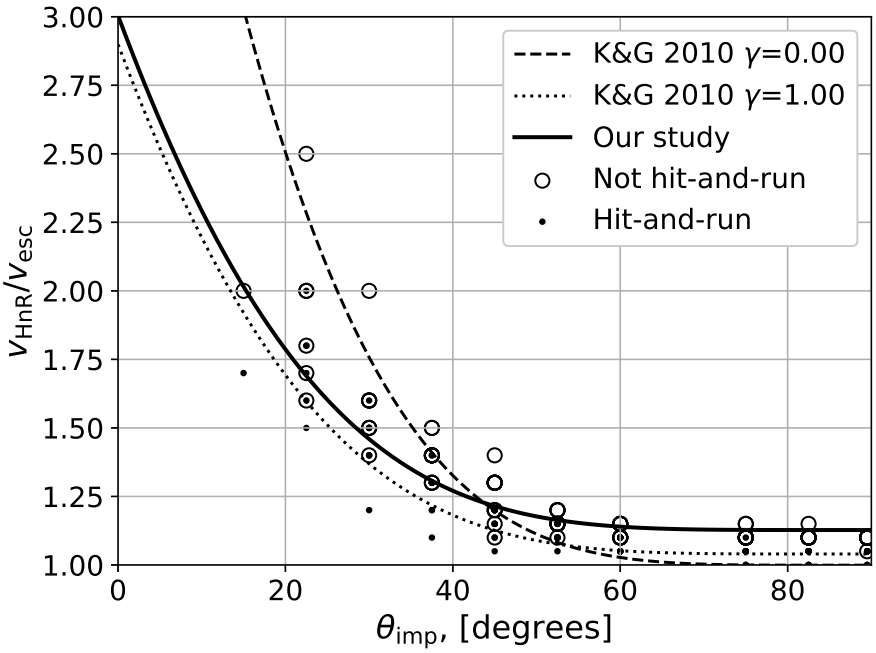

Figure 1.7. The relationship between $\theta_{\rm imp}$ and $v_{\rm HnR}$. Closed circles represent the highest impact velocity at which hit-and-run does not occur and open circles represent the lowest impact velocity at which hit-and-run occurs for each combination of $\theta_{\rm imp}$, material type, γ, and $M_{\rm tar}$. The dashed curves are the velocity criteria of Kokubo and Genda (2010) (Equation 1.23) for the end-member scenarios of γ=0.1 and 1.0. The solid curve is our γ-independent relation (Equation 1.24).

velocity transition to hit and run may be dependent on impact scale, *i.e.* whether Equation 1.24 requires dependence on $M_{\rm tot}$. To do so, we leverage the fact that the H_2O-SiO_2-Fe simulations span three orders of magnitude in total mass and use a constant γ. We find that the onset of hit and run is potentially variable at the $\pm$0.05-0.1 $v_{\rm esc}$ level (just at the resolution of our database) and is thus minimal. We also find that the velocity criterion is similarly insensitive to Λ, which was checked by examining H_2O-SiO_2-Fe and SiO_2-Fe simulations at $\gamma = 0.2$.

1.5.3 On the Nuances of Graze-and-Merge

Graze and merge is a phenomenon observed in the study of the giant impact formation of the Moon (e.g. Cameron, 2001) and in some models of the Haumea system (e.g. Leinhardt et al., 2010). In a giant impact, although the impactor may have sufficient energy to escape the 2-body system, the relatively minor collisional interaction in a grazing collision can reduce the kinetic energy sufficiently such that the impactor becomes bound to the target. The net effect is that graze-and-merge collisions involve two separate collisions, one with $v_{\rm imp}/v_{\rm esc} \gtrapprox 1$ and another, occurring soon after or days later, with $v_{\rm imp}/v_{\rm esc} < 1$ (C. Agnor and Asphaug, 2004). Comparatively, the classical 2-body problem in close approach does not exhibit this phenomena, unless energy is dissipated during the close approach, *e.g.* by tidal dissipation.

Physically, graze and merge itself manifests in several ways. The two bodies can remain relatively near one another, in a series of tidal-collisional interactions or the impactor can continue downrange as a *temporary* runner, only to reaccrete some time later. Since graze-and-merge collisions exist on a slim phase boundary whose outcome is critically dependent on the brief, minor interactions between small amounts of mass (and thus few SPH particles), they are the outcome regime most sensitive to numerical aspects (rounding error, timestepping schemes, SPH smoothing kernels, etc.) and initial conditions (density stratification, initial setup of the orbits, equation of state, etc.). Indeed, Genda et al. (2012) finds that different initial thermal states can change the transition between merging and hit-and-run. Due to the more drawn out process of a graze-and-merge collision it is also important that the simulation is allowed to run for long enough or the outcome may not be converged. We do not attempt to provide empirical laws regarding graze-and-merge collisions since empirical

relationships for graze-and-merge are likely to be an outcome very discrepant from one SPH implementation to another; this was similarly avoided in Leinhardt and Stewart (2012). However, since the graze-and-merge regime occurs at impact angles and velocities common in embryo-embryo collisions, it is an important area of study that requires detailed comparisons of SPH formulations and consideration for initial thermodynamic conditions.

1.5.4 Hit-and-Run Efficiency

In a 'clean' hit-and-run, the target and impactor are both minimally disrupted, i.e. $M_{\rm LR} \approx M_{\rm tar}$ and $M_{\rm run} \approx M_{\rm imp}$, where $M_{\rm run}$ is the mass of the second largest remnant in hit and run. From Equation 1.20 it follows that $\xi = 0$ in this case. However, as shown in the 30° case in Figure 1.5 and in Asphaug (2010, Figure 8), the target can be partially eroded in a in a hit-and-run collision, so $\xi > 0$ is achievable. This is labeled 'Partial erosion/HnR', however for a slim range of geometries near $\theta_{\rm imp} \approx \theta_{\rm HnR}$ the impactor may be disrupted, potentially to be reaccumulated downrange. As the impact angle increases, the hit and run outcome becomes more 'clean' and the target retains a greater amount of its pre-impact mass. Simultaneously, in terms of the runner, as impact angle increases it is disrupted to a lesser extent.

To account for the behavior of the efficiency of hit and run we fit an empirical model that predicts the discontinuity in accretion efficiency, $\xi_{\rm jump}$, seen by the example in Figure 1.5. As shown in Figure 1.8, we find the jump in accretion efficiency between merge/graze and merge and hit and run is described with reasonable accuracy by the

following function:

$$\xi_{\rm jump} = 1 - 0.5 \left(\frac{\theta_{\rm HnR}(90^\circ - \theta_{\rm imp})}{\theta_{\rm imp}(90^\circ - \theta_{\rm HnR})} \right)^f , \tag{1.25}$$

where f=1.42, $\theta_{\rm HnR}$ is described by Equation 1.22, and angles are in degrees. We find that collisions of large impactor-to-target mass ratio tend to have 'cleaner', more efficient hit-and-run transitions, *i.e.* $\xi_{\rm jump} \sim 1$ for a large range of angles. This is likely due to two reasons, 1. for a fixed impact geometry, smaller impactors have a greater fraction of their own mass interacting in the collision and 2. the discrepancy between the gravitational binding energies is greatest for small-γ scenarios, so the impactor is less robust against the strong tidal interaction. Figures 1.14 and 1.15 illustrate this effect, where the hit-and-run transition is increasingly diffuse for disparately-sized bodies (small-γ collisions).

To obtain a fit that produces a smooth transition in ξ shown in Figures 1.14, 1.15, and 1.16, a feature that would be provided by purely data-driven methods, the optimization would need to be performed with the prefactor (currently 0.5) as a free parameter. However, our model is designed to differentiate the occurrence of a runner from simply the largest remnant in a debris cascade, which is an important distinction or 'switch' for N-body implementations, as the runner and the debris field are dynamically, morphologically, and thermodynamically distinct objects.

1.5.5 Maximum Mass of Remnants

In the non-hit-and-run regime, the maximum achievable mass of the largest remnant is $M^*_{\rm LR} = M_{\rm tot}$, although we note that all simulations, even those near $v_{\rm imp}/v_{\rm esc} \sim 1$, involve some amount of escaping debris. In the hit-and-run regime the maximum

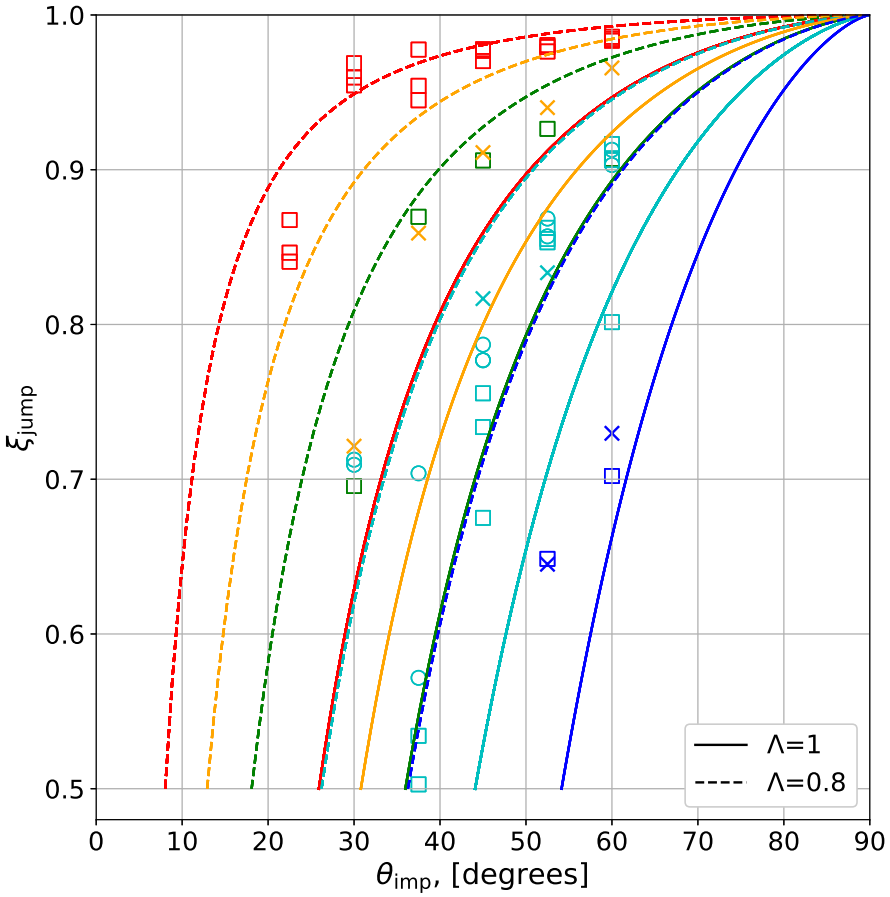

Figure 1.8. The jumps in accretion efficiency that occurs in the transition from merge/graze and merge to hit and run. Red, orange, green, cyan, and blue symbols represent jumps determined by hand for our γ=0.7, 0.5, 0.35, 0.2, and 0.1 simulations. The 'x', square, and circle symbols represent the homogeneous SiO_2, 2-layer SiO_2-Fe, and 3-layer H_2O-SiO_2-Fe bodies respectively. Values were computed 'by hand' from the data and high angle data was excluded as it suffers from stochastic effects from graze-and-merge. Plotted data is shown for illustration purposes; the lines indicate the MCMC optimization of Equation 1.25 to data of M_{LR} and M_{2LR} across the entire database of SPH simulations.

achievable mass of the largest remnant is $M^*_{\rm LR} = M_{\rm tot} - \xi_{\rm jump} M_{\rm imp}$, where $\xi_{\rm jump}$ is provided by Equation 1.25. It follows that $M^*_{\rm LR}$ is a piece-wise function, dependent on whether or not the collision is a hit-and-run:

$$M^*_{\rm LR} = \begin{cases} M_{\rm tot} & \text{not HnR} \\ M_{\rm tot} - \xi_{\rm jump} M_{\rm imp} & \text{HnR} \end{cases} \tag{1.26}$$

We find the following scaling law is sufficient for predicting the mass of the largest remnant:

$$M_{\rm LR} = M^*_{\rm LR} \left(1 - \frac{K}{K^*}\right) \tag{1.27}$$

where K is computed using Equation 1.14 and $K^* = \alpha U_{\mathcal{G}}$, where α is a fitted parameter. The largest remnant will be half of its maximum mass once $K = \alpha U_{\mathcal{G}}/2$. The value of $M_{\rm LR}/M_{\rm tot}$ should be zero where Equation 1.27 predicts negative values, though as discussed in Section 1.2.1, highly-disruptive scenarios are not common in late-stage planet formation.

We found the behavior of α is best described as an exponential function of $\theta_{\rm imp}$,

$$\alpha = g\theta^h_{\rm imp} + \alpha_0, \tag{1.28}$$

where $g = 10^{-4.90}$, $h = 3.72$, and $\alpha_0 = 3.75$. We point out that α has very large values at glancing angles (see Figure 1.9); for example, α differs by roughly a factor of five for collisions between $\theta_{\rm imp} = 0°$ and $45°$. Thus, to disrupt the target to the same amount with respect to its maximum achievable mass M^*, collisions at $\theta_{\rm imp} = 45°$ require roughly five times more energy, or around 2.2 times the impact velocity as those at $\theta_{\rm imp} = 0°$ (since $E_{\rm kin} \propto v^2_{\rm imp}$). This result is intuitive since glancing angles

poorly couple the impact energy to the target and so this relation, at least in part, may be accounting for effects due to the interacting mass, albeit empirically. We do not explicitly model disruptive collisions at glancing angles, so the disruption threshold for glancing collisions, dictated by α, is often an extrapolation. Since embryo-embryo collisions beyond $v_{\rm imp}/v_{\rm esc} \sim 4$ are rare the fact that α is not precise for larger impact angles is not critical for modeling collisions in late-stage planet formation; the more salient point is that disruption simply does not occur in large angle collisions under the conditions found in typical late stage planet formation scenarios. It is important to acknowledge that Genda et al. (2015) finds the disruption threshold is not a converged quantity at resolutions beyond the state-of-the-art in the literature ($\sim 10^6$ SPH particles). Although they do not reach convergence at their highest resolution simulations, they find that the criterion is inversely proportional to the resolution in the target body, $K^* \propto n_{\rm tar}^{-1/3}$; our simulations which have a range of target resolutions of 1-2 $\times 10^5$ particles are thus ∼50-60% higher than the expected value. In Figure 1.9, we show the 50% correction to the α relation and an additional correction for subsonic collisions, which we discuss in Section 1.6.3.

In a hit-and-run collision the mass is divided into three parcels: largest remnant, runner (the impactor after a hit-and-run collision), and debris. To compute the mass of the runner we first compute the maximum achievable mass of the runner,

$$M^*_{\rm run} = \begin{cases} 0 & \text{not HnR} \\ M_{\rm tot} - M^*_{\rm LR} \equiv \xi_{\rm jump} M_{\rm imp} & \text{HnR,} \end{cases} \tag{1.29}$$

where $M^*_{\rm LR}$ is described by Equation 1.26. This formulation assumes the amount of escaping debris just before the jump is equal to the amount of escaping debris just after the jump, at the onset of hit-and-run. The mass of the runner can be determined

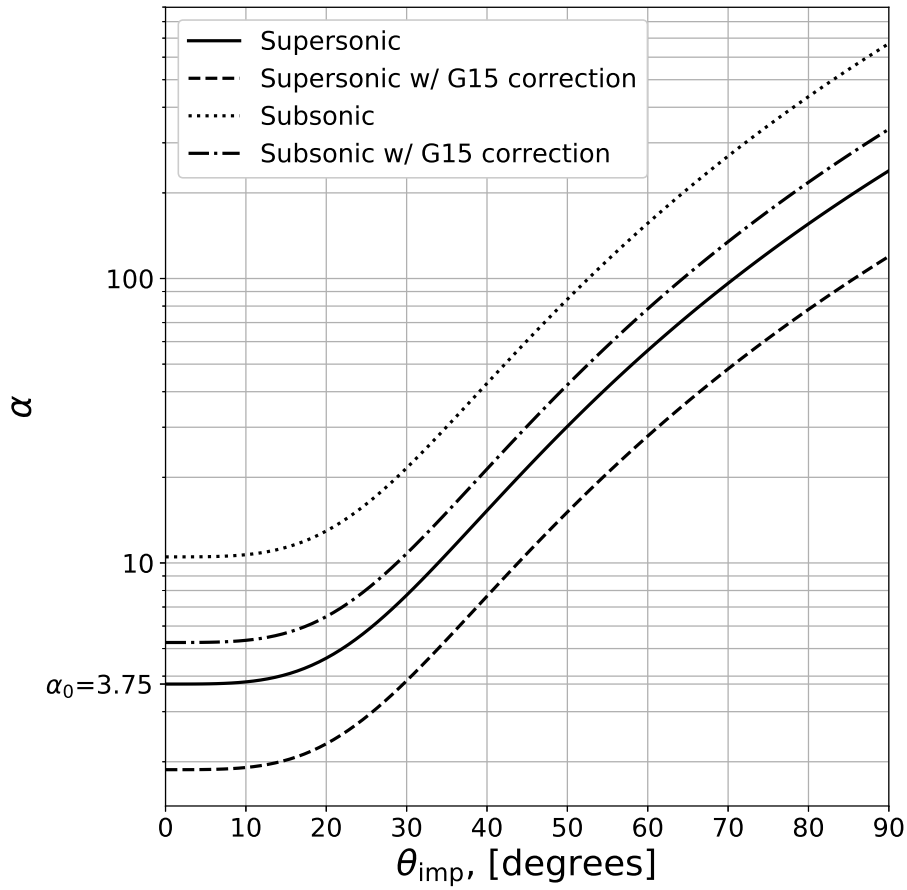

Figure 1.9. The behavior of α (Equation 1.28) as a function of impact angle. We show a 50% correction due to the unconverged nature of disruption thresholds in SPH simulations, labeled 'G15' (Genda et al., 2015). A correction of 2α is also shown to account for the fact that subsonic collisions, common between small similar-sized bodies, may be more robust against disruption.

using a form similar to that of Equation 1.27,

$$M_{\text{run}} = M^*_{\text{run}} \left(1 - \frac{K}{K^*}\right). \tag{1.30}$$

We find that the value of α (See Equation 1.28) fit for the disruption of the largest remnant provides a good fit to the mass of the runner for most cases. The mass of

the escaping debris is computed using mass conservation:

$$M_{\rm esc} = \begin{cases} M_{\rm tot} - M_{\rm LR} & \text{not HnR} \\ M_{\rm tot} - M_{\rm LR} - M_{\rm run} & \text{HnR.} \end{cases} \tag{1.31}$$

The residuals between the optimized model and the underlying dataset for $M_{\rm LR}$, $M_{\rm run}$, and $M_{\rm esc}$ are shown in Figures S1.7-1.15.

1.6 Discussion

It is prudent to examine our model in the context of existing literature on the subject and describe its applicability to collisions outside the range of parameter space covered by our database. Since catastrophic disruption is a widely-used concept in the giant impact literature, this is a useful point in drawing comparisons. For the most complete scaling law for the mass of remnants in the literature, that of Leinhardt and Stewart (2012), we can also perform a complete comparison across our entire database.

1.6.1 Catastrophic Disruption Terminology

The term 'catastrophic disruption' and its definition, as applied to giant impacts, is problematic and misleading. A clean (glancing) hit-and-run collision between two near-equal-mass bodies satisfies the $M_{\rm LR} = M_{\rm tot}/2$ condition for catastrophic disruption, however the target and impactor are somewhat intact. In this case, $M_{\rm LR} = M_{\rm tar}/2$ more appropriately represents a 'catastrophic' outcome, since in a clean hit and run the target and impactor mass are almost entirely decoupled to begin with. Instead, we

caution the use of 'catastrophic disruption' terminology altogether, because of the risk of interpreting the threshold as one that is physical in nature, which is not the case in collisions of similar-sized bodies at probable impact geometries (grazing). However, we recognize its wide use as a benchmark across various studies and it remains useful in head-on cases for similar-sized collisions.

1.6.2 Comparison of Catastrophic Disruption for Head-on, Equal-Mass Collisions

Catastrophic disruption is only reached in our near head-on collisions. For comparison to other work this is convenient since hit and run does not occur in head-on ($\theta_{\rm imp} = 0$) collisions; whether a scaling law predicts the onset of hit and run correctly or not is irrelevant here. We first consider collisions with $\gamma = 1$.

1.6.2.1 Movshovitz et al. (2016)

For Movshovitz et al. (2016) the comparison is straightforward since they use similar variables. They report that catastrophic disruption occurs at $K = (5.5 \pm 2.9) U_{\mathcal{G}}$. In our case for head-on collisions $\alpha = \alpha_0$ and catastrophic disruption occurs at $K_{\rm dis} = \frac{1}{2}\alpha_0 U_{\mathcal{G}}$. From the MCMC optimization we find $K_{\rm dis} = 1.9 U_{\mathcal{G}}$, however the individual values[7] of $\frac{1}{2}\alpha_0$ span $\sim 1.6 - 2.5$. The catastrophic disruption energy found by Movshovitz et al. (2016) is thus about a factor of 2–3 higher than ours, with the upper and lower ranges being comparable, and the results are compared in Figure 1.10. For equal-sized collisions (left panel) our head-on disruption energy is lower than the embryo collision

[7]We directly interpolate the values of α_0 where possible and use linear extrapolation with the two highest velocity datapoints otherwise.

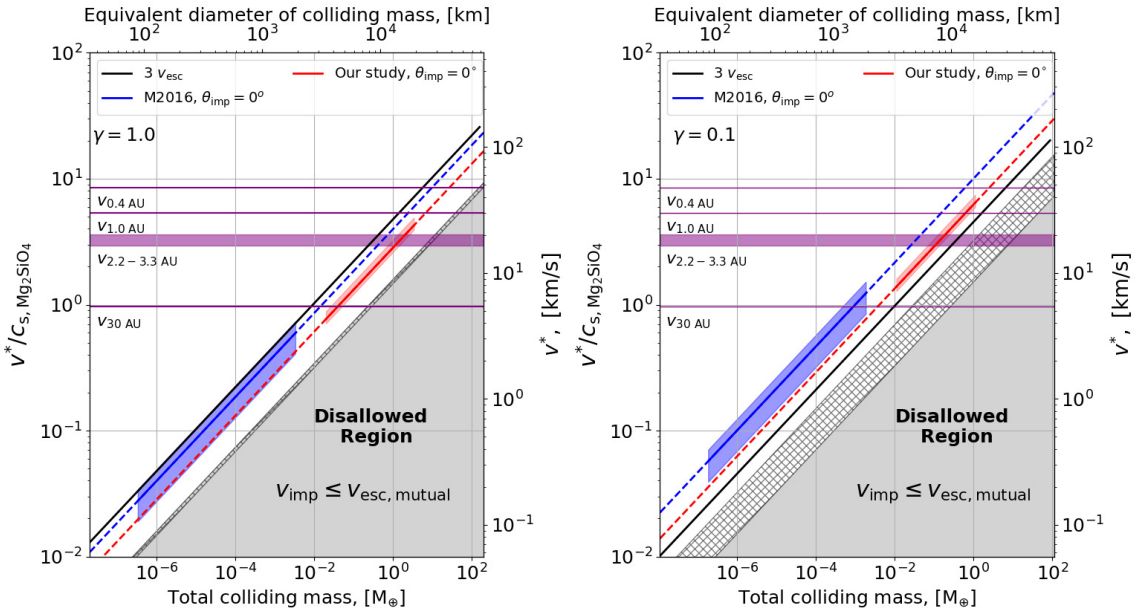

Figure 1.10. The same as Figure 1.1, but now includes our result for the disruption criteria for head-on collisions (red line). The red shaded band represents the entire range of disruption energies in our data; thered line represents the optimized value ($\alpha_0/2 = 1.9$). The blue line and shaded regions represents the range reported in Movshovitz et al. (2016). The transition to supersonic impact velocities occurs roughly at the boundary between the study of Movshovitz et al. (2016) and our study.

velocities from Chambers (2013) (black dotted line), thus it is possible for large, equal-sized embryos to undergo some level of disruption, predicated on those collisions being near head-on, which is a low-probability geometry (Shoemaker, 1961). Even though our prediction is somewhat lower than that of Movshovitz et al. (2016), it is still very unlikely for collisions with $M_{\rm tot} \approx 1 M_\oplus$ and $\gamma = 0.1$ (right panel) to result in disruption at 1 AU. Note also that Movshovitz et al. (2016) used significantly smaller bodies than our study, a point we consider further in Section 1.6.3.

1.6.2.2 Leinhardt and Stewart (2009)

The comparison to Stewart and Leinhardt (2009) is somewhat more complicated since they use different variables, necessitating a conversion. In a head-on collision, $Q^*_{\rm RD}$ is the impact energy at catastrophic disruption, normalized by total mass, $K_{\rm dis}/M_{\rm tot}$, so:

$$Q^*_{\rm RD} = \frac{1}{2}\frac{K^*}{M_{\rm tot}}, \tag{1.32}$$

since $K_{\rm dis} = K^*/2$. Using $Q^*_{\rm RD}$ from Stewart and Leinhardt (2009) for equal-sized collisions (Equation 1.10) we obtain:

$$aR^2_{\rm C1} = \frac{1}{2}\frac{K^*}{M_{\rm tot}} = \frac{1}{2}\frac{\alpha U_{\mathcal{G}}}{M_{\rm tot}}. \tag{1.33}$$

The value of α simplifies in the case of $\theta_{\rm imp} = 0$ (Equation 1.28):

$$aR^2_{\rm C1} = \frac{1}{2}\frac{\alpha_0 U_{\mathcal{G}}}{M_{\rm tot}}, \tag{1.34}$$

where $U_{\mathcal{G}}$ is the numerically-calculated binding energy of the whole system, since we use the numerical value to fit α. In the case of $\gamma = 1$ each body has a mass $\frac{1}{2}M_{\rm tot}$, and thus each has the same binding energy, $U_{\mathcal{G},\rm tar} = U_{\mathcal{G},\rm imp}$. Using the definition of Λ (Equation 1.19), the total binding energy computed numerically, including the adjustment to account for the separation of the bodies (Equation 1.18), is thus:

$$U_{\mathcal{G},\rm num} = -\left(\frac{1}{8} + \frac{3}{10\Lambda}\right)\frac{GM^2_{\rm tot}}{R}, \tag{1.35}$$

where R is the radius of the target and impactor. For the small bodies of Stewart and Leinhardt (2009) we can reasonably assume that $\Lambda = 1$, and thus $U_{\mathcal{G}} = \frac{17}{40} G M_{\rm tot}^2 / R$. Note that for our SiO_2-Fe bodies Λ is typically around 0.91, which would make the prefactor closer to $\frac{18}{40}$. It then follows that

$$aR_{\rm C1}^2 = \frac{17}{60}\alpha_0 \pi R^2 \rho_{\rm bulk} \mathcal{G}, \tag{1.36}$$

where $\rho_{\rm bulk}$ is the bulk density of the body, which ranges from 500-3000 kg m^{-3} for the bodies in Stewart and Leinhardt (2009), and around 3000-5000 kg m^{-3} for our larger planets. Using the definition for $R_{\rm C1}$ we obtain:

$$a(\frac{3}{4\pi}\frac{M_{\rm tot}}{\rho_{\rm H_2O}})^{2/3} = \frac{17}{60}\alpha_0 \pi R^2 \rho_{\rm bulk} \mathcal{G} \tag{1.37}$$

and the value of a can be solved for,

$$a = \frac{17}{60}\alpha_0 \pi \mathcal{G} \rho_{\rm bulk}^{1/3} \rho_{\rm H_2O}^{2/3}. \tag{1.38}$$

Assuming a bulk density of 500-3000 kg m^{-3}, as used by Stewart and Leinhardt (2009), and $\alpha_0 \approx 3.75$ this gives $a \approx (1.7-3.2)\times 10^{-8}$ m kg$^{-1/3}$ s^{-2}. For densities more relevant to our planets, $\sim$3000-5000 kg m^{-3}, the range is $a \approx (3.2 - 3.8) \times 10^{-8}$ m kg$^{-1/3}$ s^{-2}. In the cgs units used by Stewart and Leinhardt (2009) these ranges become $a \approx (1.7 - 3.2) \times 10^{-7}$ cm g$^{-1/3}$ s^{-2} and $a \approx (3.2 - 3.8) \times 10^{-7}$ cm g$^{-1/3}$ s^{-2}. Thus, our value is within a factor of 3-10 of the $a = (1.7 \pm 0.3) \times 10^{-6}$ cm^2 g$^{-2/3}$ s^{-2} reported by Stewart and Leinhardt (2009). In this case, our disruption criterion is lower, however Stewart and Leinhardt (2009) used much smaller bodies than our study; again, this is a point we consider further in Section 1.6.3.

1.6.2.3 Leinhardt and Stewart (2012)

As done for Stewart and Leinhardt (2009), we must convert to the different formulation used by Leinhardt and Stewart (2012). We begin by again equating $Q^*_{\rm RD}$ and $K_{\rm dis}/(2M_{\rm tot})$, this time using the relation for catastrophic disruption of Leinhardt and Stewart (2012) at $\gamma = 1$ (Equation 1.13), from which we obtain:

$$c^* \frac{4}{5} \pi \rho_{\rm H_2O} G R^2_{\rm RC1} = \frac{1}{2} \frac{\alpha_0 U_{\mathcal{G}} M_{\rm tot}}{R}. \tag{1.39}$$

As above we then use $U_{\mathcal{G}} = \frac{17}{40} G M^2_{\rm tot}/R$, which gives us

$$c^* R^2_{C1} = \frac{17}{48} \alpha_0 R^2 \frac{\rho_{\rm bulk}}{\rho_{\rm H_2O}}, \tag{1.40}$$

and substituting in for R_{C1},

$$c^* = \frac{17}{48} \alpha_0 \left(\frac{\rho_{\rm bulk}}{\rho_{\rm H_2O}} \right)^{\frac{1}{3}}. \tag{1.41}$$

In this case $c^* \approx 1.9 - 2.3$ for bulk densities of 3000-5000 kg m^{-3} and if $\alpha_0 = 3.75$. Leinhardt and Stewart (2012) reports two values of c^*, the relevant one being that which was fit to collisions between hydrodynamic planets in the literature, $c^* = 1.9 \pm 0.3$, which is very close to our value. A value of $c^* = (5 \pm 2)$ was also reported for smaller bodies, some of which were modeled with strength while others only featured self-gravity. Nevertheless, this number is close to the values found by Stewart and Leinhardt (2009) and Movshovitz et al. (2016) implying there may exist some dependence of the catastrophic disruption threshold on the scale (total mass) of the collision.

1.6.3 Scale Dependence

Gravity-dominated collisions modeled in our study and in previous work span several orders of magnitude in $M_{\rm tot}$, from Earth-mass planets down to bodies tens of kilometers in size. So it is prudent to address whether scale effects exists *within* the pure-gravity regime. As described in Asphaug (2010) and discussed in Leinhardt and Stewart (2012), detailed impact outcomes, such as the irreversible increases in entropy due to shock heating, production of vapor, *et cetera*, will undoubtedly depend on the scale and thus absolute velocity of the collision. For example, Burger et al. (2017) finds vapor production to be strongly governed by the scale (absolute velocity) of the collision. However, here we are concerned with whether these thermodynamic effects may be driving changes in the *bulk* outcomes (mass of remnants) which are assumed to be invariant of scale in the literature thus far. We also distinguish scale dependence in the gravity regime from those that are well-documented near the strength regime (at smaller scales), which is discussed in Section 1.3.1.

We noted in Section 1.6.2 that our value for the catastrophic disruption energy for a head-on, $\gamma = 1$ collision matched well with what Leinhardt and Stewart (2012) found for large, hydrodynamic planets. However, the values found by Stewart and Leinhardt (2009) and Movshovitz et al. (2016) for smaller gravity-dominated bodies were consistently higher. For example, Movshovitz et al. (2016) used hydrodynamic bodies (modeled with the Tillotson equation of state) with masses of $10^{-6} - 10^{-3}$ $M_{\oplus}$, 1 to 4 orders of magnitude smaller in mass than ours. The fitted relation from Stewart and Leinhardt (2009) for subsonic collisions between gravity-dominated rubble-pile aggregates, the relation we examine herein (Equation 1.10), involved even less massive bodies. This suggests that some amount of scale dependence may exist, where smaller

gravity-dominated bodies require more energy to disrupt, relative to their binding energy, than bodies greater than $\sim 10^{-3} - 10^{2} M_{\oplus}$.

A possible source for the difference in scaling laws in the pure-gravity regime is the transition from sub-sonic to super-sonic collisions. In Figure 1.10 we show the scaling laws of Movshovitz et al. (2016) and ours, with the solid lines representing the range of bodies simulated in the respective works. The $v_{30\ \mathrm{AU}}$ line indicates roughly the threshold for subsonic to super-sonic collisions ($v^*/c_{\mathrm{s,Mg_2SiO_4}} \approx 1$). It is particularly striking that this transition occurs roughly at the boundary between our study and that of Movshovitz et al. (2016), indicating potential scale-dependent effects *within* the pure gravity regime due to the onset of shock-generating collisions. This result would be counter to the classical argument, developed for the context of cratering collisions, that supersonic collisions less efficiently translate impace energy into kinetic energy (or excavation) of the target medium due to the production of 'waste heat' (Holsapple, 1993).

It is important to note that numerical effects also play a role in the estimation of the disruption energy (Genda et al., 2015). The disruption threshold is artificially greater in lower resolution simulations and results at lower resolutions can be scaled according to the target resolution $K_{\mathrm{dis}} \propto n_{\mathrm{tar}}^{1/3}$ (Genda et al., 2015). Thus, the $5{\times}10^4$ particle simulations in Movshovitz et al. (2016) should have a disruption threshold $\sim$25% lower at an equivalent resolution to our simulations performed at $n_{\mathrm{tar}} = 1\ {\times}10^5$ particle resolution, shrinking the discrepancy between the two studies, but not resolving it entirely. Whether $U_{\mathcal{G}}$ is computed numerically or analytically (using the constant-density approximation) is also an important consideration, particularly when the colliding bodies have differentiated structures or are large in scale. Due to these

effects the difference between the true value and the approximation is ∼1-20% (see Table S1.2), enhancing the discrepancy between the two studies.

We must also bear in mind our limited ability to directly compare differences in thermodynamically-driven effects between studies in the literature that use different numerical schemes, different equations of state that may not be thermodynamically consistent, *e.g.* Tillotson in Movshovitz et al. (2016), or initial thermal conditions. We also emphasize the weakness of this dependence, if it is present: for example, our smallest targets are 10^7 times more massive than the targets used by Stewart and Leinhardt (2009) and yet the difference in the disruption criterion for their small bodies is a factor of ∼3-10. In order to address whether scale dependence exists (in terms of remnant masses) due to transition to supersonic impact velocities, one must carefully consider the equation of state in use across the different studies, as the thermodynamic response of materials in the giant impact literature are not directly comparable. For these reasons, evidence for scale dependence is limited at this time and not absolutely conclusive.

1.6.4 Comparison of catastrophic disruption in the limit of small impactors

It is also prudent to examine our empirical model in the limit of small impactors ($\gamma \to 0$), in comparison with those of previous work. Note that we do not encourage the use of any giant impact scaling laws in the cratering regime ($\gamma \to 0$ with impact energies well below disruption) and accuracy cannot be guaranteed in $\gamma \to 0$ cases generally, since the physics of the former scenario are of a different scale than the SPH simulations used in giant impact literature. Nonetheless this limit is still useful for examining the behaviour of the scaling relationships.

Per Equation 1.28, as $\gamma \to 0$, $\theta_{\rm imp}$ dependence on the disruption energy vanishes and $\alpha \to \alpha_0 = 3.75\alpha_0 = 3.82$. This implies that as $\gamma \to 0$ the efficiency with which the impact energy is coupled into the target is independent of of $\theta_{\rm imp}$, but is not entirely independent of γ since $U_{\mathcal{G}}$ includes a contribution from the impactor (see Equation 1.18). Physically, the disappearance of dependence on $\theta_{\rm imp}$ at very small γ is somewhat intuitive; over the range of $\theta_{\rm imp}$, either all of the impactor will strike the target or all of the impactor will miss the target. Furthermore, at very small γ, impacts with energies significantly lower than required for disruption can be well modelled as striking an infinite plane. However, it is also reasonable to expect that impact energy will be more poorly coupled to the target in off-axis collisions, such as in the case of scouring collisions (e.g. Schultz and Wrobel, 2011), however this regime is not covered in our simulations of giant impacts.

The indirect dependence of γ in Movshovitz et al. (2016), due to the interacting mass, disappears for head-on collisions since the interacting mass is equal to the total mass in that case. Their scaling law thus similarly trends to a constant value as $\gamma \to 0$. This is significant as their collisions includes a large range of impactor-to-target mass ratios, from $\gamma = 1$ to $\gamma \approx 0.01$.

Differing from the others, Leinhardt and Stewart (2012) cast their scaling laws in terms of a fit for $Q^*_{\rm RD}$ at $\gamma = 1$ with a correction for scenarios with $\gamma < 1$,

$$Q^*_{\rm RD} = Q^*_{{\rm RD},\gamma=1} \left(\frac{1}{4} \frac{(\gamma+1)^2}{\gamma} \right)^{2/3\bar{\mu}-1} . \tag{1.42}$$

They fit $\bar{\mu} = 0.35$, such that the index $2/(3\bar{\mu}) - 1 \approx 0.9$, and thus in the limit $\gamma \to 0$, $Q^*_{\rm RD} \to \infty$. This implies that very small impactors cannot disrupt the target, regardless of impact energy, which we find unphysical.

Benz and Asphaug (1999) demonstrate that the disruption threshold for off-axis

collisions is systematically higher across the entire study, however at each angle a new impactor size (or equivalently γ) was determined. Since γ was not held constant or reported, the dependence of $Q^*_{\rm D}$ on γ is unclear and indeed Equation 1.4 does not have direct dependence on γ. However, given that $Q^*_{\rm D}$ is clearly dependent on $\theta_{\rm imp}$ across their study, it may be the case that in the strength-dominated regime, dependence on $\theta_{\rm imp}$ in the limit of $\gamma \to 0$ exists.

1.6.5 Full Comparison to Leinhardt and Stewart (2012) Formalism

We can also perform a comparison to the full scaling law formalism of Leinhardt and Stewart (2012), which is the most extensive of previous scaling law efforts for giant impacts. We use the value of $c^* = 1.9 \pm 0.3$ suggested by Leinhardt and Stewart (2012) for large hydrodynamic planets. We first performed several tests to ensure our implementation of their model is accurate considering the many steps involved. This includes ensuring the value of the specific impact energy and interacting mass fraction reported in their Table 1 matches our implementation. When using their catastrophic disruption energy Q'^*_{RD} the masses of the largest and second largest remnants agrees between our implementation and their Table 1.

As shown in Figure 1.11, both our predictions and those of Leinhardt and Stewart (2012) match our data well at $\gamma = 0.1$. For larger impactor-to-target mass ratios, the predictions of Leinhardt and Stewart (2012) do not accurately predict the transition to hit-and-run. This is illustrated in the right-hand panels of Figure 1.11 for the $\theta_{\rm imp} = 22.5°$ and $30°$ cases. At $\theta_{\rm imp} = 37.5°$, Leinhardt and Stewart (2012) correctly predicts that hit and run occurs; however it predicts the onset of hit and run at lower velocity than seen in our simulation data and predicts a constant largest remnant

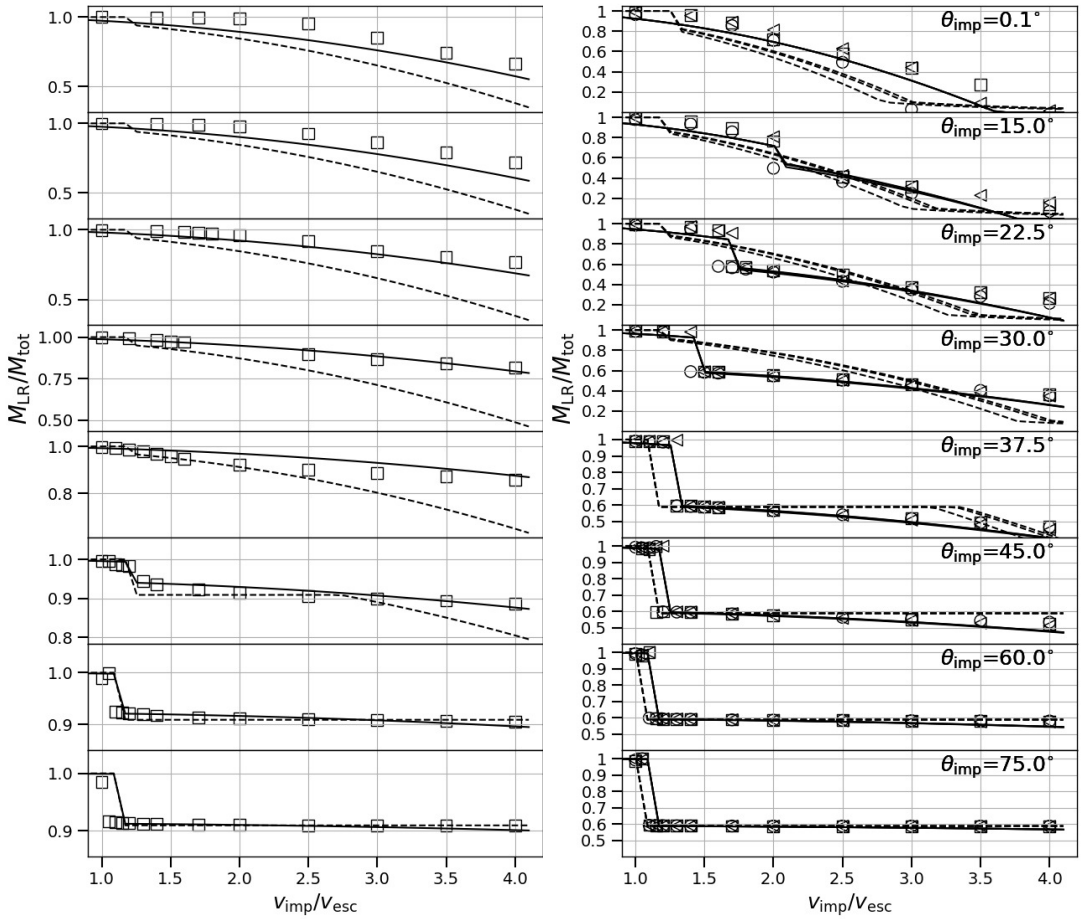

Figure 1.11. The largest remnant mass, normalized by the total mass, for the giant impact simulations of differentiated, 2-layer, SiO_2-Fe planets with an impactor-to-target mass ratio of $\gamma = 0.1$ (left) with $M_{tar} = 0.1M_{\oplus}$ and $\gamma = 0.7$ (right) with $M_{tar} = 1.0M_{\oplus}$, $0.1M_{\oplus}$, and $0.01M_{\oplus}$. Circle, square, and triangle symbols represent data for $M_{tar} = 1.0M_{\oplus}$, $0.1M_{\oplus}$, and $0.01M_{\oplus}$ respectively. The blue solid line represents the prediction from our scaling laws and the dashed line represents that of Leinhardt and Stewart (2012). Both scaling laws predict the hit-and-run transition in the $\gamma = 0.1$ case, which is demonstrated by the discontinuity at $\theta_{imp} = 45°$. At larger γ (right), the grazing criterion (Asphaug, 2010) implemented by Leinhardt and Stewart (2012), does not predict the existence of hit-and-run collisions at v_{imp} approaching 2 seen in the $\theta_{imp} = 22.5°$ and 30° data.

mass until the onset of erosion at $v_{imp} \sim 3.25 v_{esc}$, whereas our representation includes the erosion of the target in hit-and-run scenarios.

The prediction of hit and run at lower angles in our work is expected as generally our geometric criterion for hit and run (Equation 1.22) is lower than the grazing

angle condition, which was not intended to be a hit and run criterion Asphaug (2010). Moreover, this underprediction of hit-and-run in models that implement the simple grazing angle criterion from Asphaug (2010) grows for collisions between bodies of greater density stratification. This suggests that the number of hit-and-run collisions reported by Chambers (2013) ($\sim$42% for embryo-embryo collisions) and by Kokubo and Genda (2010) ($\sim$49% in simulations that involved strictly embryos) are lower bounds on the prevalence of hit and run, but may be over-estimates for the lowest velocity collisions. However, because the impact parameters (particularly γ for each of the collisions) in those N-body studies are not reported, we cannot estimate the fraction of merging or erosive collisions that would be predicted as hit and run by our model. Furthermore, as demonstrated in Chambers (2013) and Emsenhuber and Asphaug (2019), a sequence of multiple hit-and-run collisions between two bodies can occur, so it is reasonable to expect many more hit-and-run collisions from N-body codes that implement our geometric criterion..

In terms of the mass of the runner, we generally find both scaling laws have issues for hit-and-run collisions at low γ. For example, in the left-hand panel of Figure 1.12 both scaling laws predict hit-and-run for $\theta_{\rm imp} = 45^\circ$, but the scaling law of Leinhardt and Stewart (2012) overpredicts the amount of erosion of the projectile (smaller runner) whereas our relation underpredicts the erosion of the runner. However, we find that at larger angles our scaling law agrees well with the simulation data, as seen in the $\theta_{\rm imp} = 60^\circ$ case. At larger γ (See right-hand panel of Figure 1.12) we find the scaling laws of Leinhardt and Stewart (2012) significantly overpredict the level of erosion in the runner at $v_{\rm imp} > 2v_{\rm esc}$, as can be seen in the $\theta_{\rm imp} = 37.5^\circ$ and 45° cases, however this discrepancy diminishes at higher (more grazing) angles.

Under our formalism the runner is always less massive than the projectile since

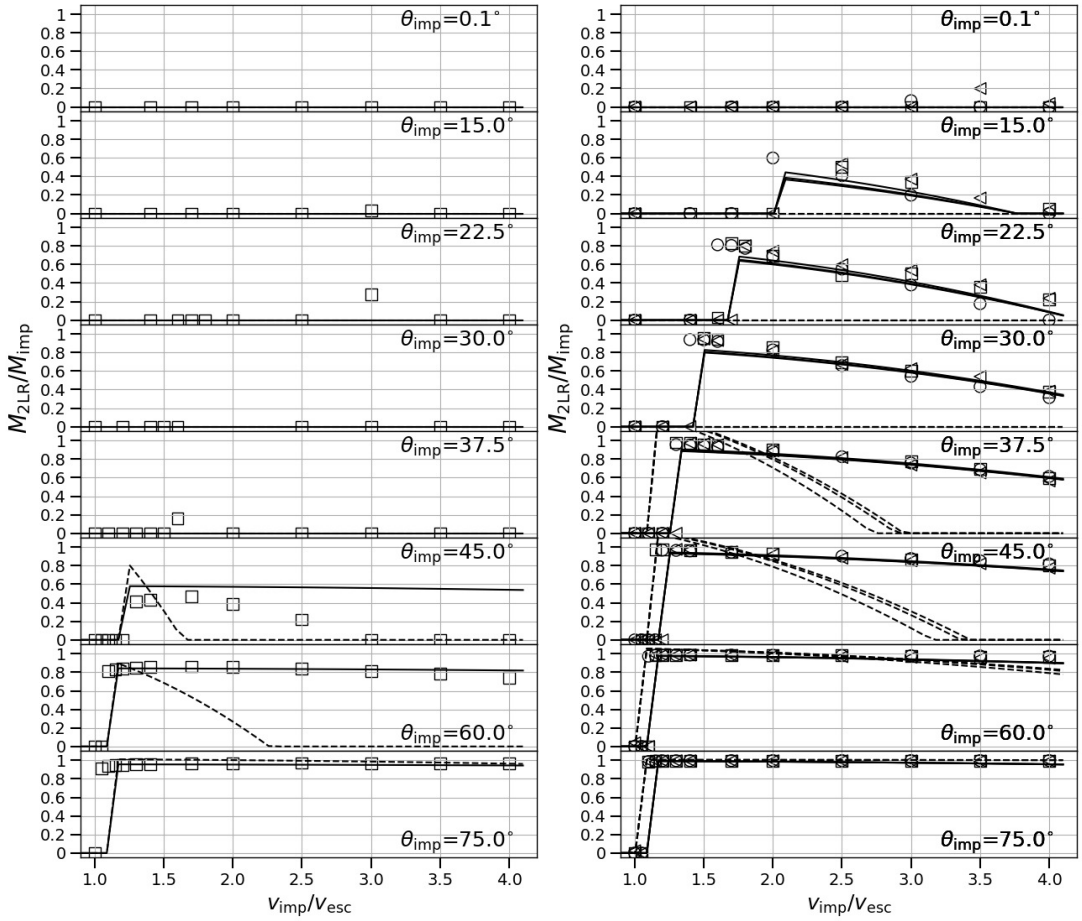

Figure 1.12. The second largest remnant mass, normalized by the impactor mass, for the giant impact simulations of differentiated, 2-layer, SiO_2-Fe planets with an impactor-to-target mass ratio of γ=0.1 (left) with $M_{\rm tar} = 0.1M_\oplus$ and $\gamma = 0.7$ (right) with $M_{\rm tar} = 1.0M_\oplus$, $0.1M_\oplus$, and $0.01M_\oplus$. Circle, square, and triangle symbols represent data for $M_{\rm tar} = 1.0M_\oplus$, $0.1M_\oplus$, and $0.01M_\oplus$ respectively. The blue solid line represents the prediction from our scaling laws and the dashed line represents that of Leinhardt and Stewart (2012).

$\xi_{\rm jump}$ is less than 1 (See Equation 1.25). This is not always the case in the formalism of Leinhardt and Stewart (2012), where at low velocities the runner can be more massive than the projectile[8], a phenomenon not observed in our simulations. As for the prediction of escaping mass, in both our framework and that of Leinhardt and Stewart (2012) mass is conserved such that $M_{\rm tot} = M_{\rm LR} + M_{\rm esc}$ for non-hit-and-run collisions or $M_{\rm tot} = M_{\rm LR} + M_{\rm run} + M_{\rm esc}$ in the case of hit-and-run, where $M_{\rm run}$ is the mass of the impactor after the collision. Therefore, where there is a discrepancy in the prediction of the mass of the largest remnants, there is also a discrepancy in the predicted escaping mass (see Figure 1.13).

In Section 1.17 we provide a comparison of the prediction of $M_{\rm LR}$ between the two models against three distinct datasets: the disruptive collisions in Movshovitz et al. (2016), the dataset herein, and the PKDGRAV simulation data from Leinhardt and Stewart (2012) (their Table 4). Note that in our model we do not attempt to describe the size distribution of smaller remnants. This is not resolved in SPH simulations of giant impacts at our resolution, which is why we have limited this analysis to target, runner, and debris. Users of our algorithm in the next section should refer to Leinhardt and Stewart (2012) and others if they require estimates for the size-frequency distribution of debris.

For the realms of giant impacts we have considered, we find that our model and that of Leinhardt and Stewart (2012) show residuals centered about zero with minimal systematic bias and a low mean-squared error (MSE), which is a measure of the accuracy of the model across the dataset. Our model has, at worst, an MSE of

[8]Predicting the mass of the runner in the Leinhardt and Stewart (2012) formalism requires computing the interacting mass of the 'reverse impact'; however, $M_{\rm interact}$ for the reverse impact, as defined in Equation 48 of Leinhardt and Stewart (2012), has units of volume rather than mass. To obtain a mass we thus multiplied the volume obtained using their Equation 48 by the bulk density of the target.

$\sim$0.08. This corresponds to an expected residual in $M_{\rm LR}$ values of 0.28 $M_{\rm tot}$ for 'super-catastrophic' scenarios, and an expected residual of 0.07 $M_{\rm tot}$ across our database which emphasizes the range of collision velocities and geometries expected in late-stage planet formation. We find that the MSE of the Leinhardt and Stewart (2012) model is several times greater, and in most cases the discrepancy increases when adjusting for the probability distribution of impact angles ($P(\theta_{\rm imp}) = \sin(2\theta_{\rm imp})$. As noted, some of this discrepancy is due to the underprediction of hit and run when using the Asphaug (2010) grazing criterion.

1.7 Prescription for N-body Codes

We provide a step-by-step methodology for estimating the outcome of a gravity-dominated collision in an N-body environment.

1. Determine $M_{\rm tar}$, $M_{\rm imp}$ such that $M_{\rm tar} \geq M_{\rm imp}$. Determine $\theta_{\rm imp}$ and $v_{\rm imp}$ from the relative position and velocity vectors, and compute $M_{\rm tot} = M_{\rm tar} + M_{\rm imp}$, $\mu = M_{\rm tar}M_{\rm imp}/M_{\rm tot}$, $\gamma = M_{\rm imp}/M_{\rm tar}$, $v_{\rm esc} = \sqrt{2\mathcal{G}M_{\rm tot}/(R_{\rm imp} + R_{\rm tar})}$, and $K = \frac{1}{2}\mu v_{\rm imp}^2$
2. Compute the gravitational binding energy analytically (Equation 1.17 and 1.18) and numerically to determine Λ (Equation 1.19). If the density structure is not tracked, use $\Lambda \approx 0.88$ and 0.95 for differentiated water-rich and rocky planets respectively. For stripped cores (homogeneous bodies) use $\sim$0.98. In the limit of small homogeneous bodies use $\Lambda = 1$.
3. Determine if $\theta_{\rm imp} > \theta_{\rm HnR}$ and $v_{\rm imp}/v_{\rm esc} > v_{\rm HnR}$, where $\theta_{\rm HnR} = -33.8\log_{10}(\gamma) + 20.6\Lambda^{8.9}$ and $v_{\rm HnR} = 1.88\left(1 - \sin(\theta_{\rm imp})\right)^{5/2} + 1.13$.
    a) If not, the collision is not hit and run and $M_{\rm LR}^* = M_{\rm tot}$.

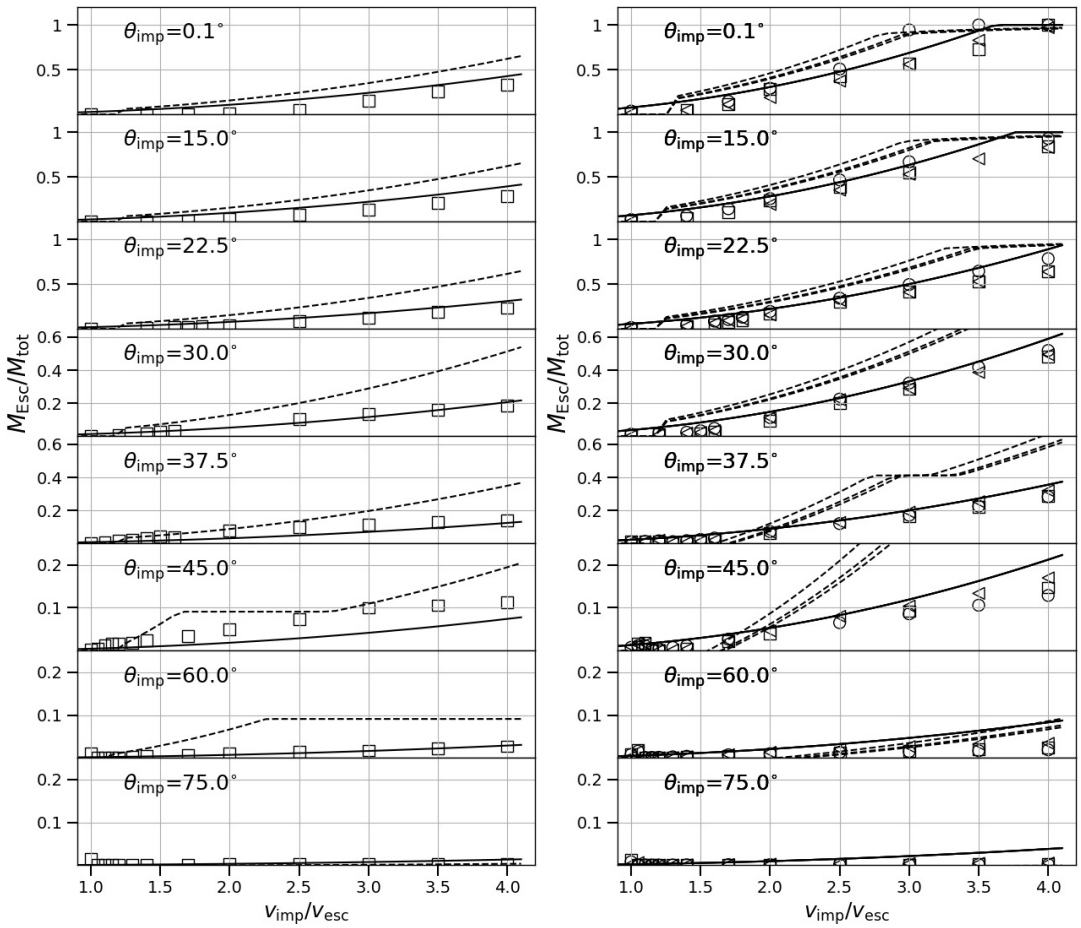

Figure 1.13. The escaping mass, normalized by the total colliding mass, for the giant impact simulations of differentiated, 2-layer, SiO_2-Fe planets with an impactor-to-target mass ratio of γ=0.1 (left) with $M_{\rm tar} = 0.1M_\oplus$ and 0.7 (right) with $M_{\rm tar} = 1.0M_\oplus$, $0.1M_\oplus$, and $0.01M_\oplus$. Circle, square, and triangle symbols represent data for $M_{\rm tar} = 1.0M_\oplus$, $0.1M_\oplus$, and $0.01M_\oplus$ respectively. The blue solid line represents the prediction from our scaling laws and the dashed line represents that of Leinhardt and Stewart (2012).

b) If so, compute $\xi_{\rm jump} = 1 - \frac{1}{2}\left(\frac{\theta_{\rm HnR}(90^\circ - \theta_{\rm imp})}{\theta_{\rm imp}(90^\circ - \theta_{\rm HnR})}\right)^{1.42}$, then compute the maximum-achievable mass of the largest remnant for the hit-and-run case: $M^*_{\rm LR} = M_{\rm tot} - \xi_{\rm jump} M_{\rm imp}$.

4. Compute $\alpha = 10^{-4.90}\theta_{\rm imp}^{3.72} + 3.75$. If the total mass is less than $0.01 M_\oplus$ then $\sim 2.0\alpha$ may be used to account for subsonic impacts. To approximate the *true* erosion expected in a collision, reduce the value of α by 50% (Genda et al., 2015).
5. Compute mass of the largest remnant: $M_{\rm LR} = {\rm MAX}(0,\ M^*_{\rm LR}\,(1 - K/K^*))$, where $K^* = \alpha U_{\mathcal{G}}$
6. If collision was hit-and-run, compute $M^*_{\rm run} = \xi_{\rm jump} M_{\rm imp}$, then compute the mass of the runner: $M_{\rm run} = {\rm MAX}(0,\ M^*_{\rm run}\,(1 - K/K^*))$.
7. Compute $M_{\rm esc} = M_{\rm tot} - M_{\rm LR} - M_{\rm run}$

1.8 Conclusions

We have developed a model that accurately predicts the mass of remnants in giant impacts between gravity-dominated bodies and can be easily adopted into N-body methods. Using a MCMC method, the model was optimized to results from over $\sim$1400 SPH simulations that span the most relevant conditions expected in late stages of planet formation. A weighted MCMC scheme was used to globally optimize the empirical model to the entire dataset and account for imbalances in the simulated impact conditions.

Since roughly half of the time a population of self-stirred bodies are expected to produce hit-and-run events, where only a portion of the impactor and target directly intersect, and the impactor continues downrange in a deflected trajectory (e.g. C.

Agnor and Asphaug, 2004), we pay particular attention to this regime. The transition of collisions from merging to hit and run occurs as a fairly sharp boundary in the pre-impact parameter space, namely at low velocities and grazing angles, so we finely sampled the parameter space in these regions. This allowed for the development of a greatly improved hit-and-run criterion and thus a more accurate prediction of the masses of remnants compared to the prevailing models in the literature.

By modeling planets of variable composition we found that the density stratification of the colliding bodies leads to hit-and-run collisions at lower angles than suggested by using the grazing rule (Asphaug, 2010). Considering this, we expect that primitive (undifferentiated) bodies early in the formation process and stripped cores late in the formation process (or in dynamically stirred regions) tend to undergo hit and run least often. Collisions between differentiated bodies will be hit and run more often, increasing the accretion timescale. This effect demonstrates that the accretion dynamics and timescales are contingent on the internal structure of the planets in the dynamical environment, an aspect not currently accounted for in state-of-the-art N-body planet formation codes. We also demonstrate that hit-and-run collisions do not result in the target and impactor emerging unscathed, with no erosion of either body, but rather exhibit a range of accretion efficiency that is dependent on the impactor-to-target mass ratio and impact angle (e.g. C. Agnor and Asphaug, 2004), a behavior we fit empirically.

We also report a potential transition within the pure gravity regime that violates the commonly-assumed scale invariance assumption for giant impacts. We posit that erosion may be enhanced in collisions where the impact velocity is supersonic, which occurs in a self-stirred system of planetary embryos with masses $\sim 10^{-3} - 10^{-2} M_{\oplus}$. In light of our results it is also reasonable to expect that a complicated interplay of

thermodynamic effects and density stratification governs the onset of hit and run and other impact outcomes. The onset of differentiation, which occurs early on due to heating from ^{26}Al heating, and the occurrence of supersonic collisions between self-stirred embryos, which occurs later when embryos reach masses roughly that of Earth's Moon, mark two new potential transitions in the process of planet formation.

We argue that the commonly-used definition of the catastrophic disruption threshold energy, the impact energy at which the largest remnant has half of the total mass after collision, is inappropriate in the case of collisions between similar-sized bodies of any scale. A hit-and-run scenario between two equal-mass bodies produces a largest remnant that has half the total mass after collision (satisfying the catastrophic disruption criteria), but it may be minimally disrupted. In this case, the morphological result of the collision would not reflect the disruption of either body and certainly could not be described as 'catastrophic'. We insist that catastrophic disruption generally does not describe the outcome of collisions between major bodies during terrestrial planet formation and is a metric that is useful only when the bodies are disparately sized or in head-on scenarios.

Finally, our empirical model for estimating giant impact outcomes is readily implemented into N-body codes, allowing them to track the mass (and by mass loss or gain, the composition) of large remnants and debris after a collision in the purely gravity-dominated regime. We provide adjustments for the possible phenomenon of scale-dependence in the gravity regime as well as numerical convergence effects expected from the resolution of our simulations.

1.9 Acknowledgements

This work was supported by the NASA Earth and Space Science Exploration Fellowship award 18-PLANET18R-0036 (Parameterizing the Aftermath of Giant Impacts) and the NASA Nexus for Exoplanet System Science (NEXSS) award at Arizona State University. The first author would like to personally thank Sarah Stewart-Mukhopadhyay for insightful conversations that have positively shaped aspects of the manuscript.

1.10 Appendix: Accretion Efficiency Data

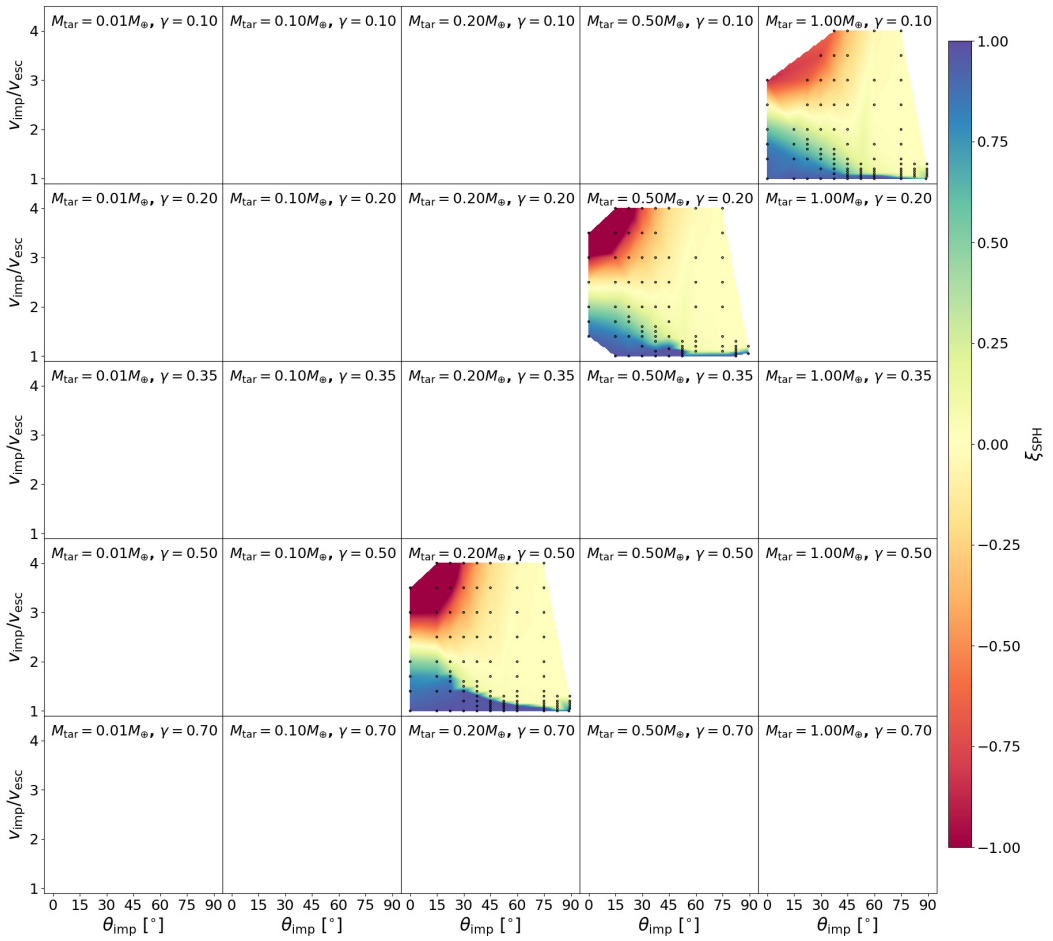

Figure 1.14. The accretion efficiency for the pure SiO_2 bodies as a function of impact angle ($\theta_{\rm imp}$; x axis) and impact velocity normalized by the mutual escape velocity ($v_{\rm imp}/v_{\rm esc}$; y axis). Linear interpolation was used to produce the heat map. Each panel represents a unique combination of impactor-to-target mass ratio (γ; rows) and target mass ($M_{\rm tar}$; columns). Cool colors represent erosive outcomes whereas warm colors represent accretionary outcomes.

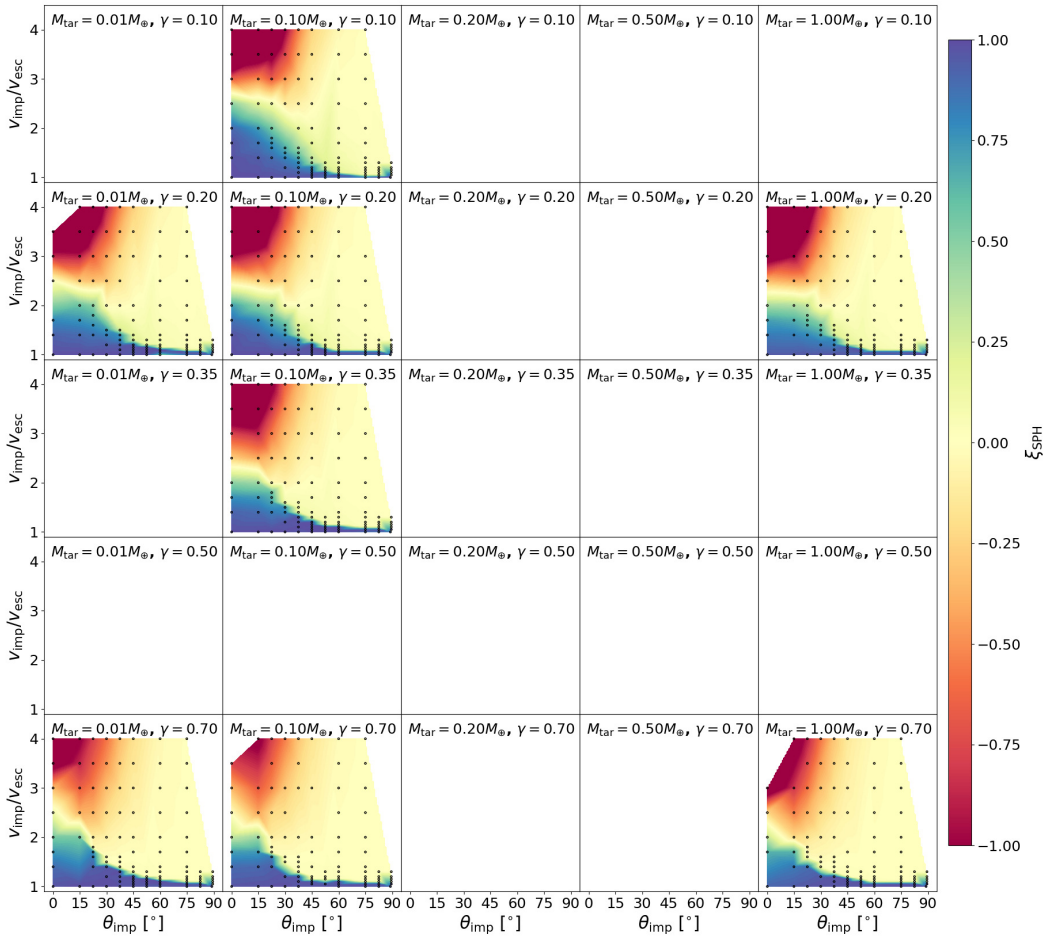

Figure 1.15. The accretion efficiency for the SiO_2-Fe bodies. Axes are the same as Figure 1.14.

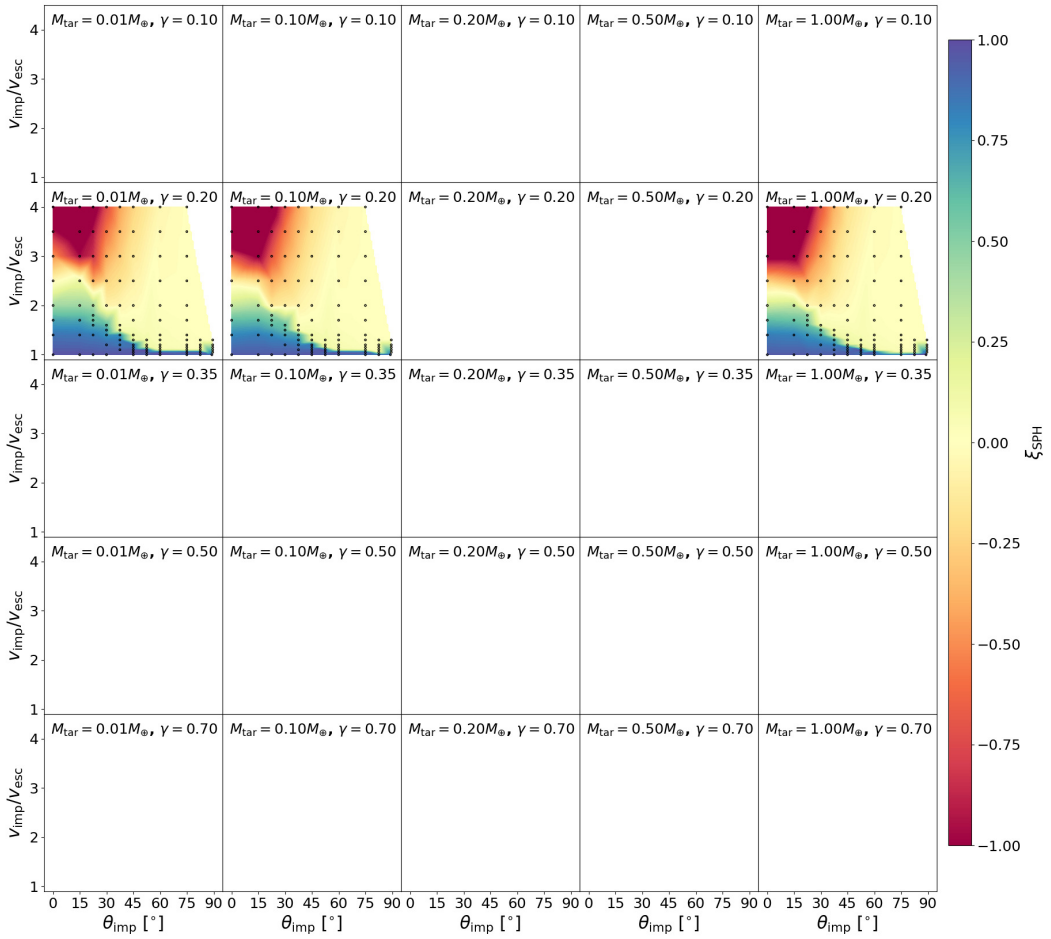

Figure 1.16. The accretion efficiency for the H_2O-SiO_2-Fe bodies. Axes are the same as Figure 1.14.

1.11 Angular Momentum as a Hit-and-Run Criterion

As we have designed our hit-and-run criteria based on both a geometric threshold and a velocity threshold it is reasonable to examine whether an angular momentum criterion may singularly encapsulate the behavior of the two. For example, Jutzi and Asphaug (2015) found that the onset of hit-and-run occurred when the angular momentum of the colliding bodies, $L = \sin(\theta_{\rm imp}) M_{\rm imp} v_{\rm imp} (R_{\rm imp} + R_{\rm tar})$, reached $\sim$1.4 times the 'reference' angular momentum. This is the angular momentum of the bodies colliding at $v_{\rm imp} = v_{\rm esc}$ and $\theta_{\rm imp} = 45°$. As shown in Figure **??**, at high angles the criterion from Jutzi and Asphaug (2015) predicts hit-and-run collisions at $\sim 1 v_{\rm esc}$. For lower angles their prediction diverges rapidly from our velocity criterion (Equation 1.24) and our data. We generally find it to predict hit and run at systematically higher velocities at low angles. It is important to note that the scale, composition, and rheology of the colliding bodies are vastly different, which is a reasonable source of the discrepancy. Nevertheless, at near head-on collisions, the model of Jutzi and Asphaug (2015) predicts hit and run if the impact velocity is sufficiently high. At these impact energies the outcome would be catastrophic, not hit and run. Adjusting the prefactor to be lower than 1.4 allows it to fit at intermediate angles, but this would then predict hit and run at velocities less than $v_{\rm esc}$ at high angles. Thus a single critical angular momentum cannot explain the onset of hit-and-run and additional functionality, beyond adjusting the prefactor, is required.

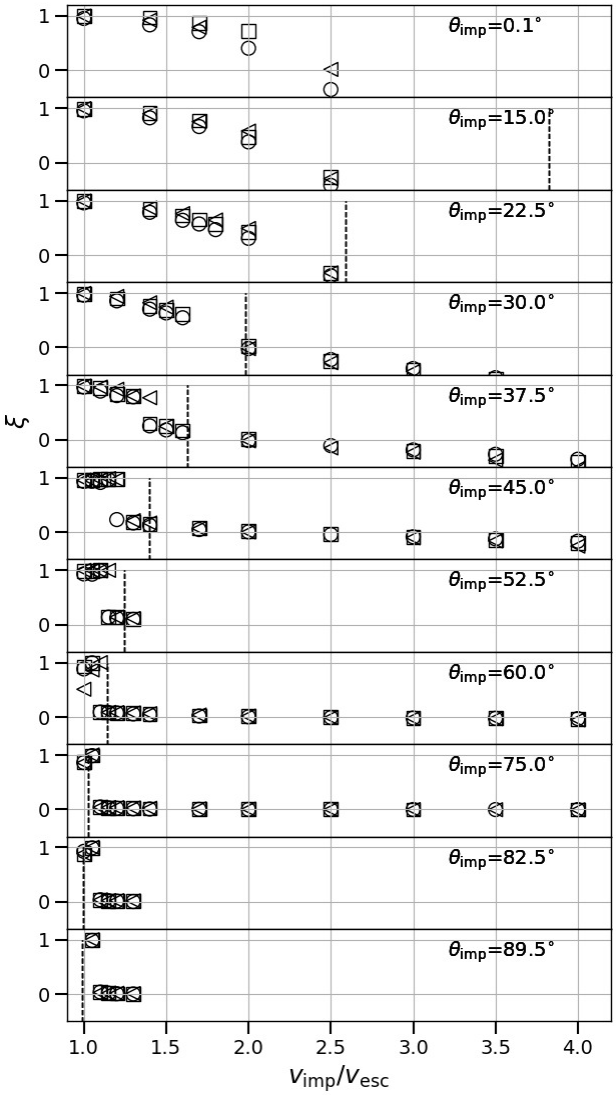

Figure S1.1. The hit-and-run threshold from Jutzi and Asphaug (2015) (dashed line) as a function of impact velocity, compared to the accretion efficiency data from the SiO_2-Fe simulations in our study. Circle, square, and triangle symbols represent data for $M_{\rm tar} = 1.0M_{\oplus}$, $0.1M_{\oplus}$, and $0.01M_{\oplus}$ respectively.

1.12 Markov-Chain Monte Carlo Analysis

We utilize the MCMC method to minimize the uncertainties between the M_{LR} and $M_{2\mathrm{LR}}$ predicted by our empirical model developed in Section 5 and the values of M_{LR} and $M_{2\mathrm{LR}}$ in the $\sim$1400 simulations depicted in Figure 1.3. Specifically, we use the emcee package (Foreman-Mackey et al., 2013) for the Python Programming Language and implement the affine-invariant ensemble sampler (Goodman and Weare, 2010). The model developed utilizes 9 optimized parameters, a, b, and c from Equation 1.22, d and e from Equation 1.24, f from Equation 1.25, and g, h, and α_0 from Equation 1/28. We posited in Section 5.1.1 that the density stratification parameter Λ is adequate for describing the difference in mass distribution between the bodies of different materials. From Figure 1.4 it is apparent that the database of simulations is imbalanced in terms of the distribution of Λ and γ, *e.g.* there are many more $\gamma = 0.2$ simulations than $\gamma = 0.35$ and there are many more $\Lambda \approx 0.9$ simulations than there are $\Lambda \approx 0.85$. Furthermore, the database includes sampling in θ_{imp} that is not commensurate with the true probability distribution of impact angles from a randomized direction ($P(\theta) = \sin(2\theta)$) (Shoemaker, 1961). As such, we maximize a weighted version of the log of the likelihood function in the MCMC routine to optimize the fit parameters,

$$\begin{aligned}\mathcal{L}(a, b, ..., \alpha_0) &= \\ &- \frac{1}{2}\sum_{i}^{N} w_i \left\{ \frac{\left[M_{\mathrm{LR,data},i} - M_{\mathrm{LR,model},i}(a, b, ..., \alpha_0)\right]^2}{\sigma^2_{\mathrm{LR},i}} + ln\left(2\pi\sigma^2_{\mathrm{LR},i}\right) \right\} \\ &- \frac{1}{2}\sum_{i}^{N} w_i \left\{ \frac{\left[M_{\mathrm{run,data},i} - M_{\mathrm{run,model},i}(a, b, ..., \alpha_0)\right]^2}{\sigma^2_{\mathrm{run},i}} + ln\left(2\pi\sigma^2_{\mathrm{run},i}\right) \right\}\end{aligned} \tag{S1.1}$$

where the weight, w_i, for any given data point, $\xi_{\mathrm{data},i}$, in the grid of simulations is computed as the multiplication of several weights constructed to account for the imbalances of the simulation grid.

$$w_i = w_{\gamma,i} \times w_{\theta_{\mathrm{imp}},i} \times w_{\sin 2\theta,i} \times w_{\Lambda,i} \tag{S1.2}$$

The weights $w_{\gamma,i}$ and $w_{\theta_{\mathrm{imp}}}$ account for the difference in the grid density of γ and θ_{imp}. We divide the width of a band of the parameter, which is $0 < \gamma < 0.15$ for the first band of γ, by the product of the total number of simulations in the band and the total range of the parameter (1 for γ and 90 for θ_{imp}). The same is performed for θ_{imp} since we do not evenly sample θ_{imp}, *e.g.* we do not have simulations in the range of $0° < \theta_{\mathrm{imp}} < 15°$, but we have simulations in less than 15° increments at higher angles. To account for the probability distribution of impact angles we then multiply this weight by $w_{\sin 2\theta,i} = \sin(2\theta_{\mathrm{imp}})$. The weight $w_{\Lambda,i}$ is required since each set of materials in the database have similar values of Λ (See Figure 1.4). It is computed by taking the inverse of the product of the number of simulations with the same database and the number of databases (3). Effectively, this final weighting factor assumes the database covers three values of Λ, which is generally the case, but this is indeed a simplification. The impact velocity distribution of the database of simulations is weighted towards lower velocities, with approximately 60% of the simulations lying below 1.5 v_{esc}. The true distribution of impact velocities for embryo-embryo collisions may be even more heavily weighted towards lower velocities, for example in Chambers (2013) ∼95% of the impacts occurring below ∼1.6 v_{esc} (see Figure S1.2). We tested rebalancing the weights across the impact velocity parameter and weighting according to the distribution in Figure S1.2, but find that while the optimized parameters in that case provide tight fits to the low velocity data they produce vastly poorer results for high

velocity data, as might be expected. We choose not to implement a velocity weighting scheme beyond that resulting from the structure of the database, particularly because doing so provides well-balanced residuals across the parameter space, allowing for wide applicability of the optimized model. We also note that the impact velocity distribution is dependent on the dynamical system and the impact accretion/erosion model used in the N-body simulation, and within any system/model is likely to be a function of time and/or radial location. This contrasts with the impact angle distribution which is theoretically derived and not expected to vary between systems.

The weighting scheme can be qualitatively understood by examining the set of grid-based figures. In Figures S1.4–S1.6 we show the weights w_i to demonstrate they are commensurate with the intended behavior. For example, they demonstrate that near head-on ($\theta_{\rm imp} \approx 0$) or highly off-axis $\theta_{\rm imp} \approx 90^\circ$ collisions have a lower weight across the entire database due to accounting for the probability distribution of impact angles, $P(\theta_{\rm imp}) = \sin(2\theta_{\rm imp})$. The SiO_2 data generally shows higher weights due the fact that there are much fewer simulations for that range of Λ; the SiO_2-Fe is most numerous and the H_2O-SiO_2-Fe data exists only for $\gamma = 0.2$ where sampling is greatest, and thus both are weighted less compared to other datasets and γ values, respectively.

The MCMC routine was initialized with a number of walkers that was 8 times the number of free parameters (72 walkers in this case) and the routine was allowed to iterate for 100,000 steps. The last 5,000 steps were used to compute *a priori* for a 'production' run of 20,000 iterations. However, rapid convergence was observed; *i.e.*, the median values of the parameters did not change substantially after 20,000-30,000 iterations in the extensive burn-in stage. We assume constant values of uncertainty, $\sigma_{\rm LR} = (0.05/(1+\gamma))\, M_{\rm LR}$ and $\sigma_{\rm 2LR} = (0.05/\gamma) M_{\rm 2LR}$, to account for numerical errors in the clump finding algorithm which is used to compute the mass of remnants. This

choice effectively increases the overall weight of deviations in M_{LR} over those in M_{2LR}, and we consider this a reasonable approach given that the second largest remnant encompasses less mass in the simulation and is thus less dependable. The posterior distribution of the optimized parameters are shown in Figure S1.3 and the median values are reported in Table S1.1.

Figures S1.7–S1.9 show the deviations in $M_{\mathrm{LR}}/M_{\mathrm{tot}}$ between the MCMC-optimized model and the simulated data. Deviations are generally less than $0.1M_{\mathrm{tot}}$, except in the $\gamma = 0.7$ data for the SiO_2-Fe bodies; however the region of higher deviations in that data is along a thin margin where v_{HnR} is slightly overestimated or underestimated. Figures S1.10–S1.12 show the deviations in $M_{\mathrm{run}}/M_{\mathrm{imp}}$ between the MCMC-optimized model and the simulated data. Figures S1.13–S1.15 show the deviations in $M_{\mathrm{esc}}/M_{\mathrm{tot}}$ between the MCMC-optimized model and the simulated data. Our model is shown to reproduce the underlying dataset to within roughly $\pm 0.1M_{\mathrm{tot}}$ for the largest remnant mass; localized errors can be higher in regions where the transition to hit and run is not exactly predicted (see lower-right panel of Figure S1.8). For the runner mass our model tends to overestimate the mass of the runner in the runner-distruption regime, *i.e.* for large velocities and at semi-glancing angles ($\theta_{\mathrm{imp}} \approx 30°$). Where the transition to hit and run is not exactly predicted the mass of the runner is naturally underpredicted, resulting in the slim blue regions at low velocities of Figures S1.10–S1.12. In terms of escapting debris mass, the conservation of mass assumption provides accuracy to within roughly $\pm 0.1M_{\mathrm{tot}}$. Locally, however, the residuals may reach higher values.

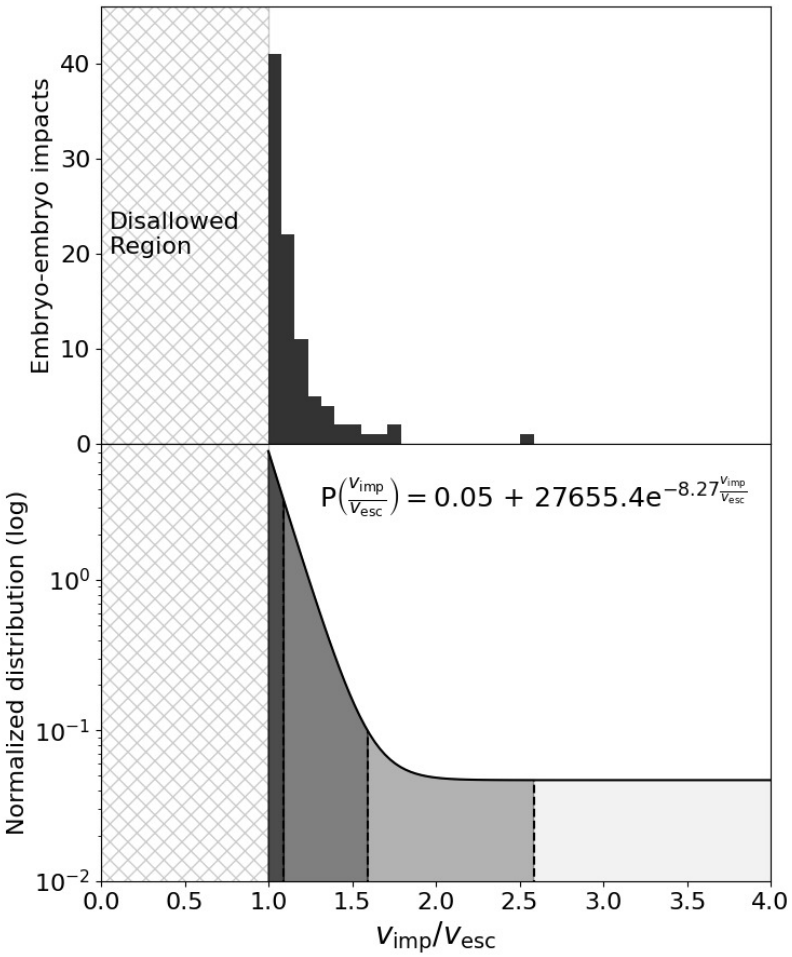

Figure S1.2. Impact velocity distribution for embryo-embryo collisions in (Chambers, 2013) (their Figure 6). The top panel shows a histogram of the raw values and the bottom panel shows a fitted probability distribution that is truncated at 4 $v_{\rm esc}$ and normalized to an area of unity. The three shaded domains represent the 50, 95, and 99 percentiles.

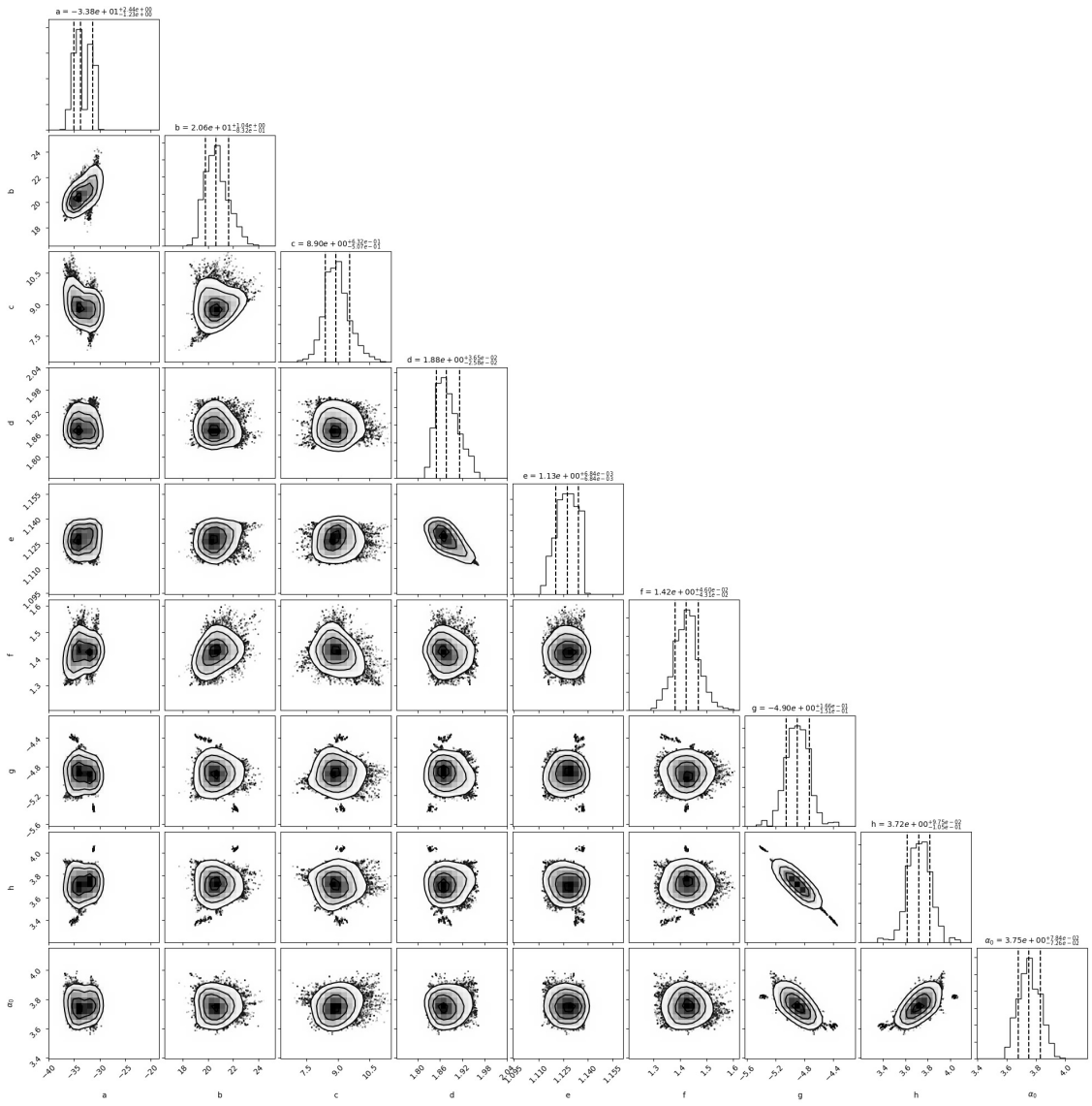

Figure S1.3. The posterior distributions of the optimized parameters in a series of 1-dimensional and 2-dimensional histograms (Foreman-Mackey, 2016). The scatter density plots in the off-diagonal frames are 2-dimensional projections of the posterior distributions; these frames illustrate the covariance of each possible pair of the fitted parameters. Diagonal frames show the 1-dimensional marginalized likelihood for each parameter. In each diagonal frame the 16%, 50%, and 84% quantiles are shown; between the 8% and 84% quantile lies 67% of the likelihood distribution.

Table S1.1. Reported values of the fit parameters provided by MCMC optimization of accretion efficiency (ξ). The values are the 50th percentile of the posterior distributions of the fit parameters (See the diagonal in Figure S1.3). The last column lists the equation number in the main manuscript where the parameter is introduced.

Parameter	Value	Equation
a	-33.8	22
b	20.6	22
c	8.9	22
d	1.88	23
e	1.13	23
f	1.42	25
g	$10^{-4.9}$	28
h	3.72	28
$^{\dagger}\alpha_0^*$	3.75	28

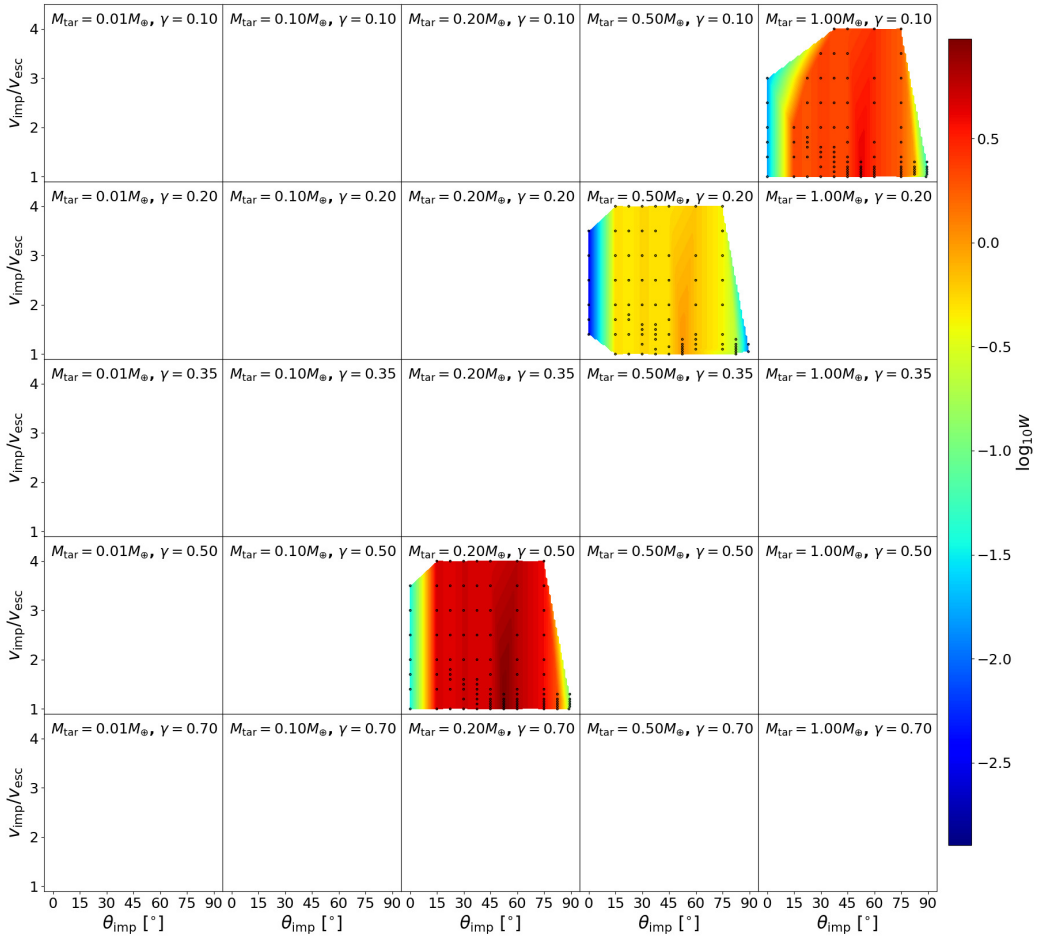

Figure S1.4. The log of the weights w_i used in the MCMC routine for the pure SiO_2 bodies. Each panel represents a unique combination of impactor-to-target mass ratio (γ; rows) and target mass (M_{tar}; columns). Cooler colors represent lower weights.

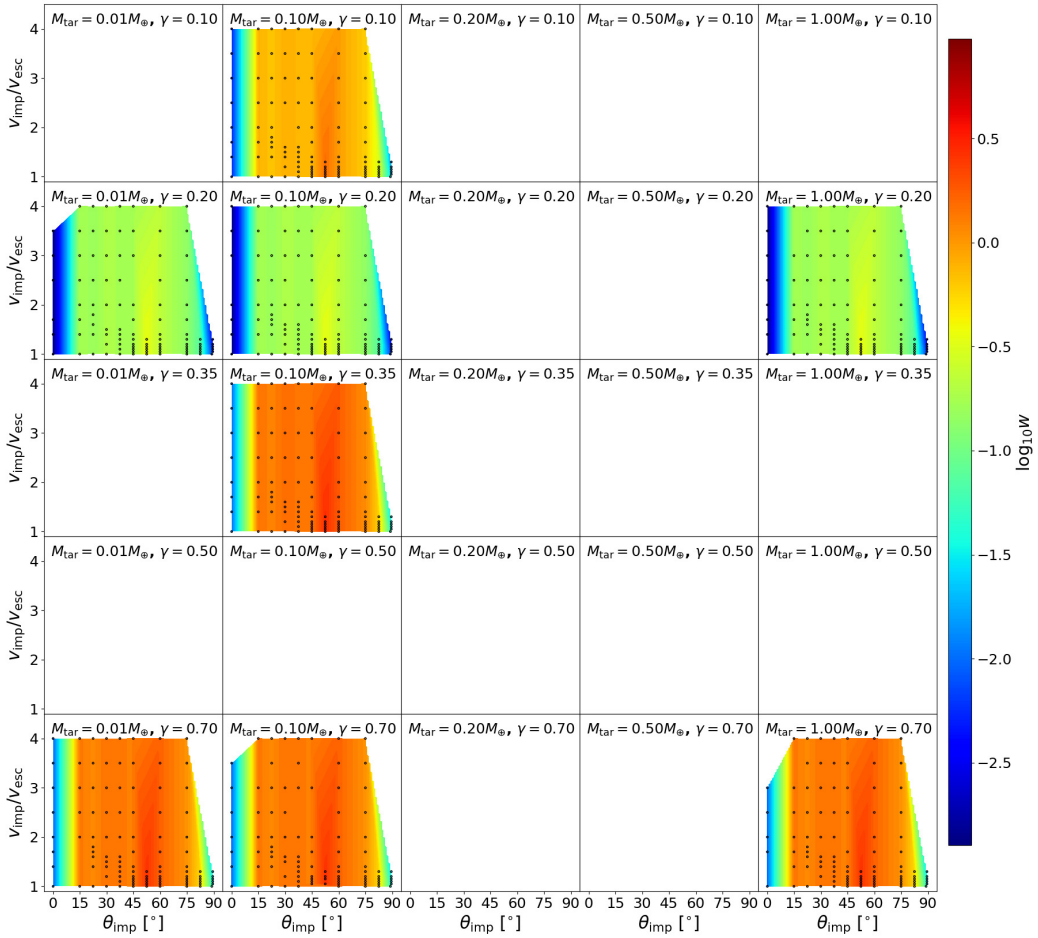

Figure S1.5. The log of the weights w_i used in the MCMC routine for the SiO_2-Fe bodies. The plot configuration is the same as Figure S1.4.

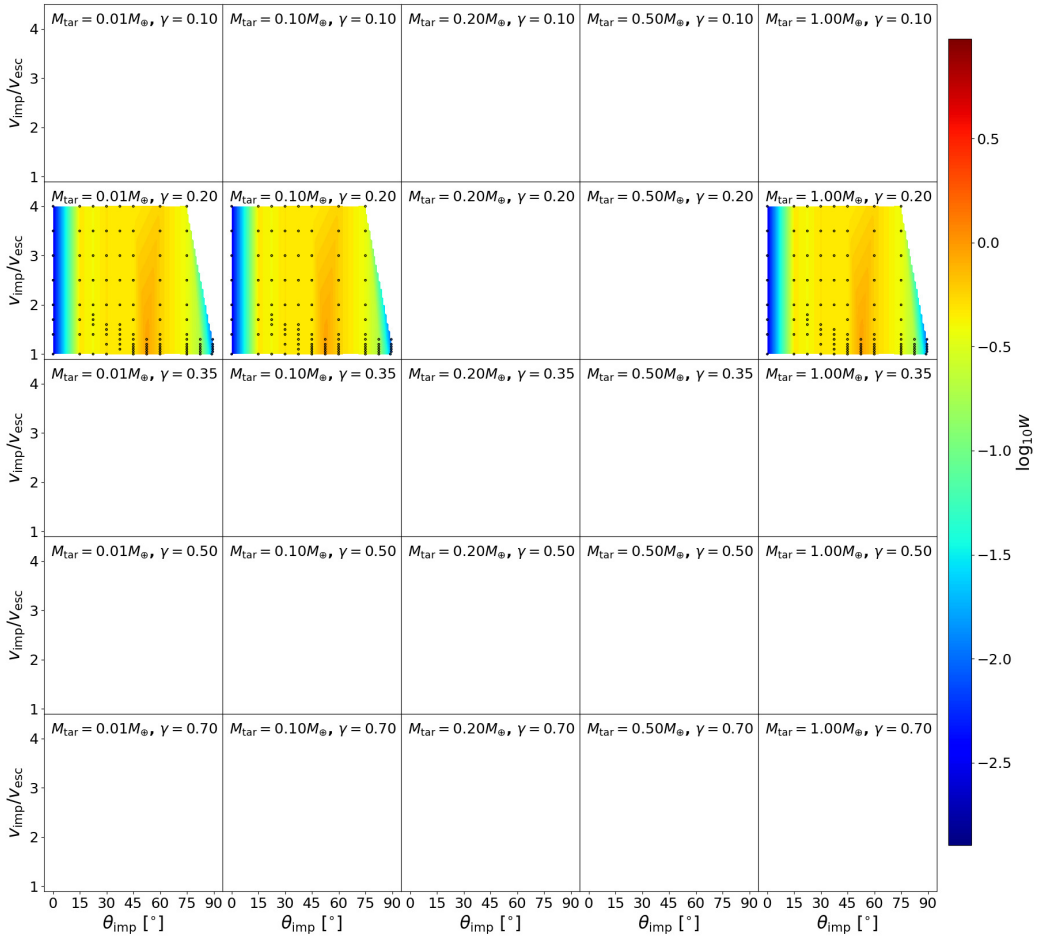

Figure S1.6. The log of the weights w_i used in the MCMC routine for the H_2O-SiO_2-Fe bodies. The plot configuration is the same as Figure S1.4.

1.13 Deviations in Largest Remnant Mass for the Best-Fit MCMC Model

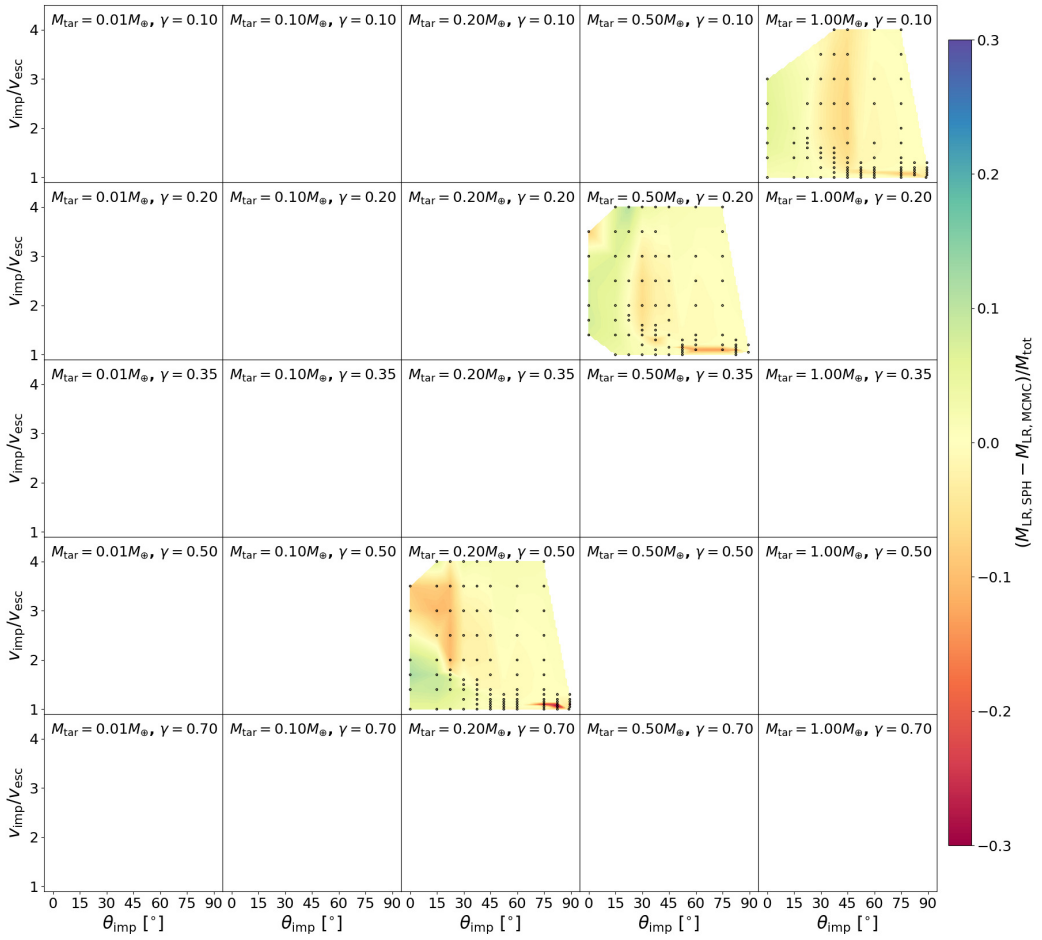

Figure S1.7. The deviations in $M_{\rm LR}/M_{\rm tot}$ for the pure SiO_2 bodies between the prediction of the best-fit model provided by the MCMC method herein and the simulated data on which the model was fit. Each panel represents a unique combination of impactor-to-target mass ratio (γ; rows) and target mass ($M_{\rm tar}$; columns). Lighter colors represent minimal deviation of the MCMC-optimized model from the SPH collision data.

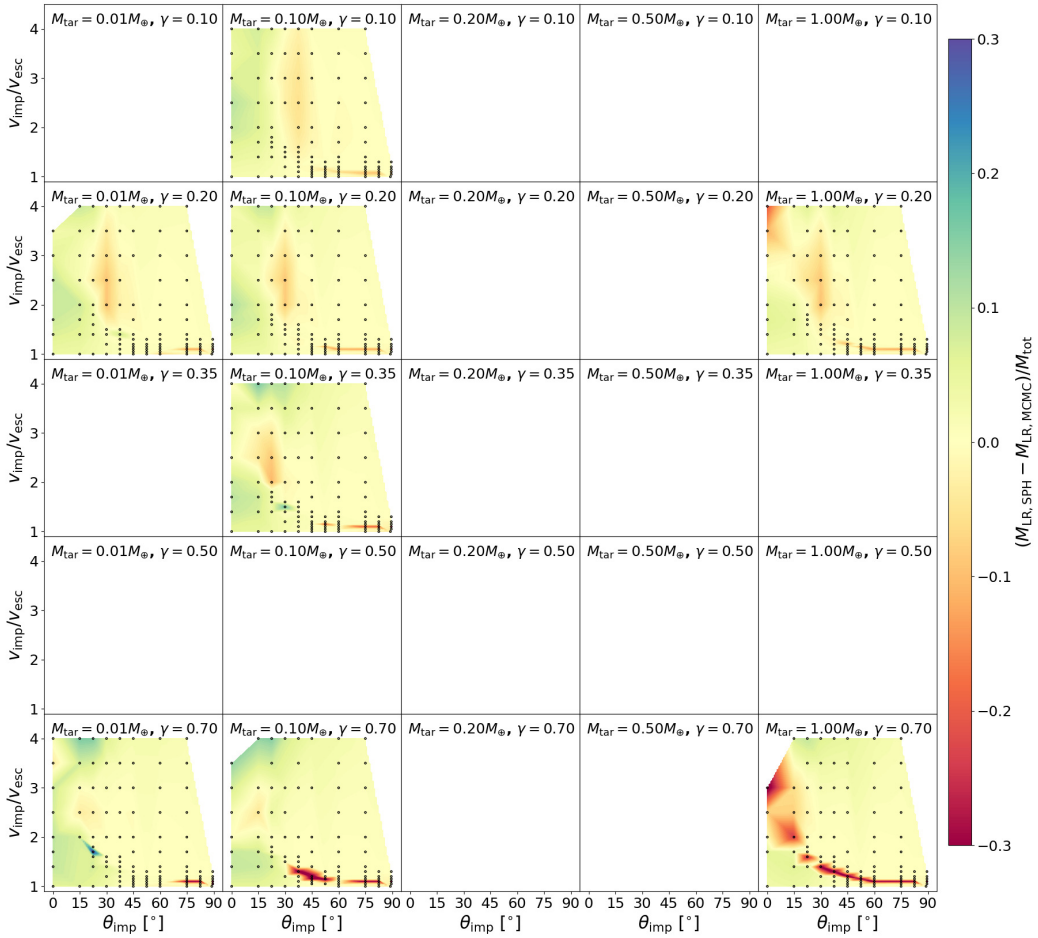

Figure S1.8. The deviations in $M_{\rm LR}/M_{\rm tot}$ for the SiO_2-Fe bodies between the prediction of the best-fit model provided by the MCMC method herein and the simulated data on which the model was fit. The plot configuration is the same as Figure S1.7.

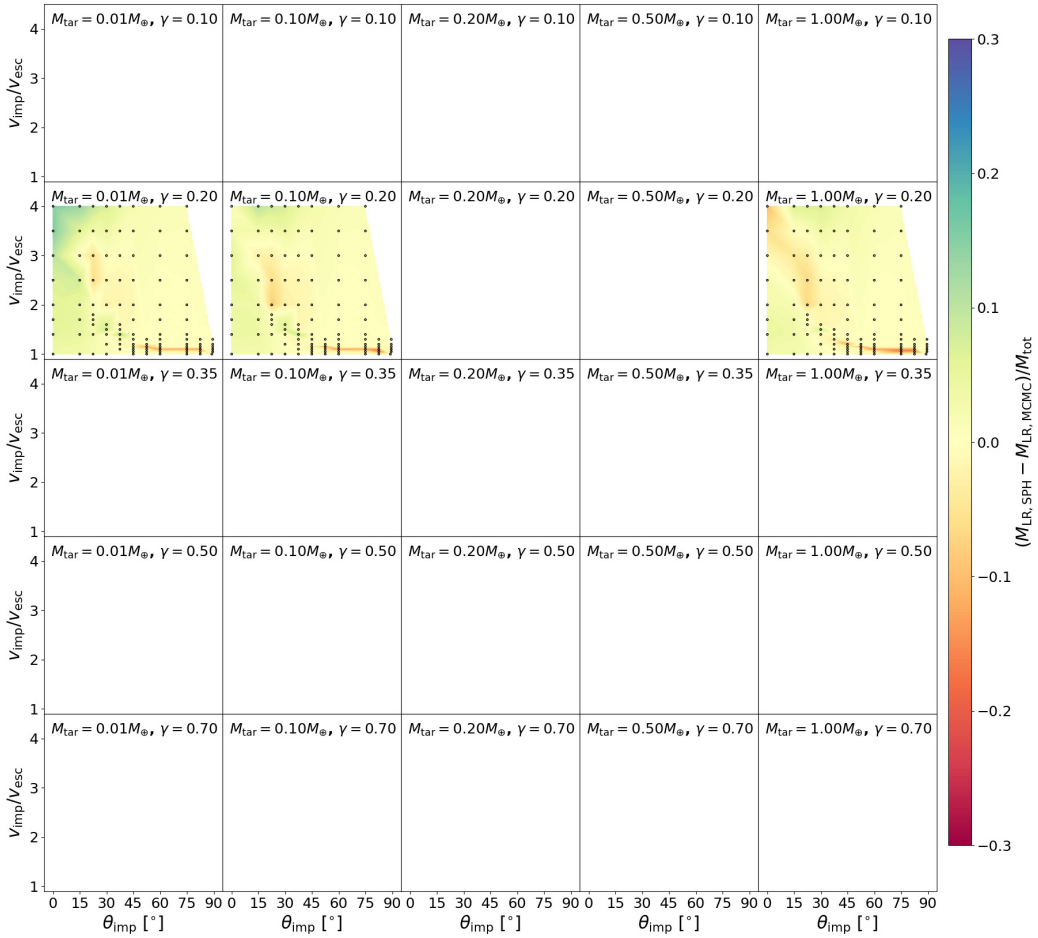

Figure S1.9. The deviations in $M_{\rm LR}/M_{\rm tot}$ for the H_2O-SiO_2-Fe bodies between the prediction of the best-fit model provided by the MCMC method herein and the simulated data on which the model was fit. The plot configuration is the same as Figure S1.7.

1.14 Deviations in Runner Mass for the Best-Rit MCMC Model

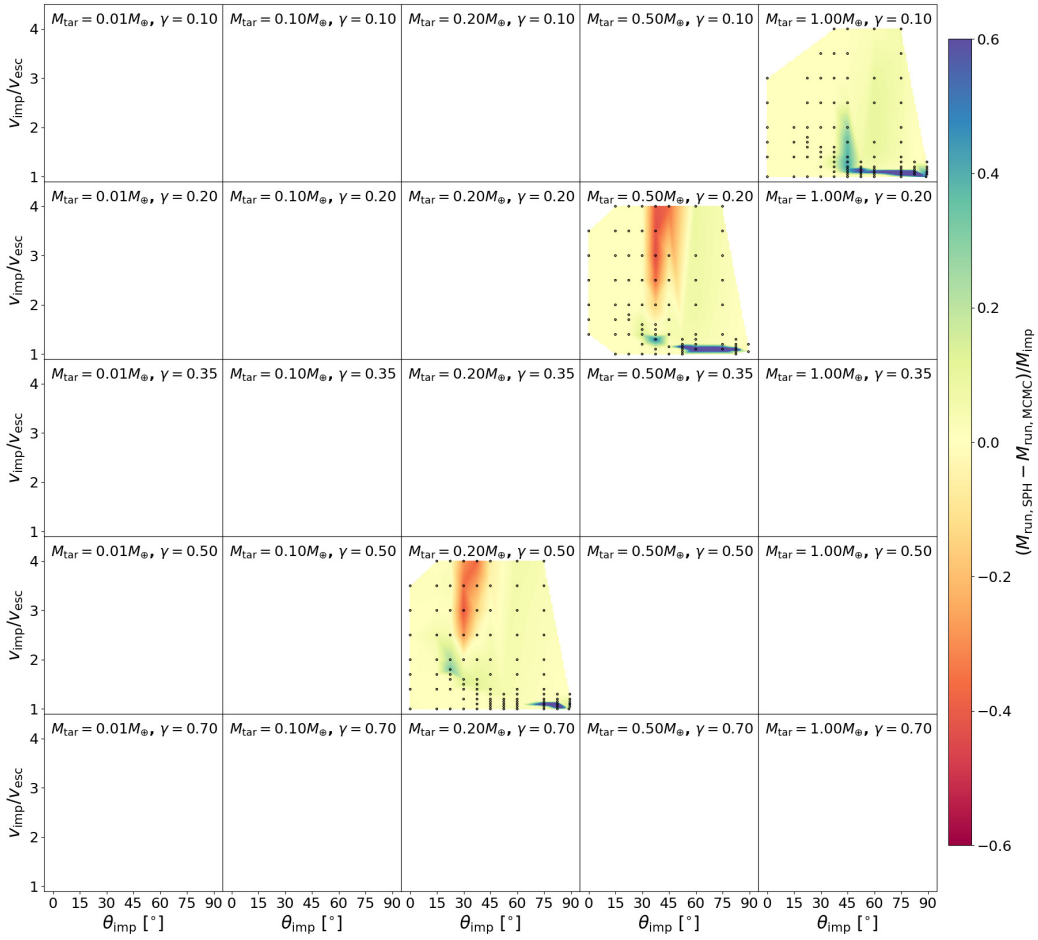

Figure S1.10. The deviations in M_{run}/M_{imp} for the pure SiO_2 bodies between the prediction of the best-fit model provided by the MCMC method herein and the simulated data on which the model was fit. Each panel represents a unique combination of impactor-to-target mass ratio (γ; rows) and target mass (M_{tar}; columns). Lighter colors represent minimal deviation of the MCMC-optimized model from the SPH collision data.

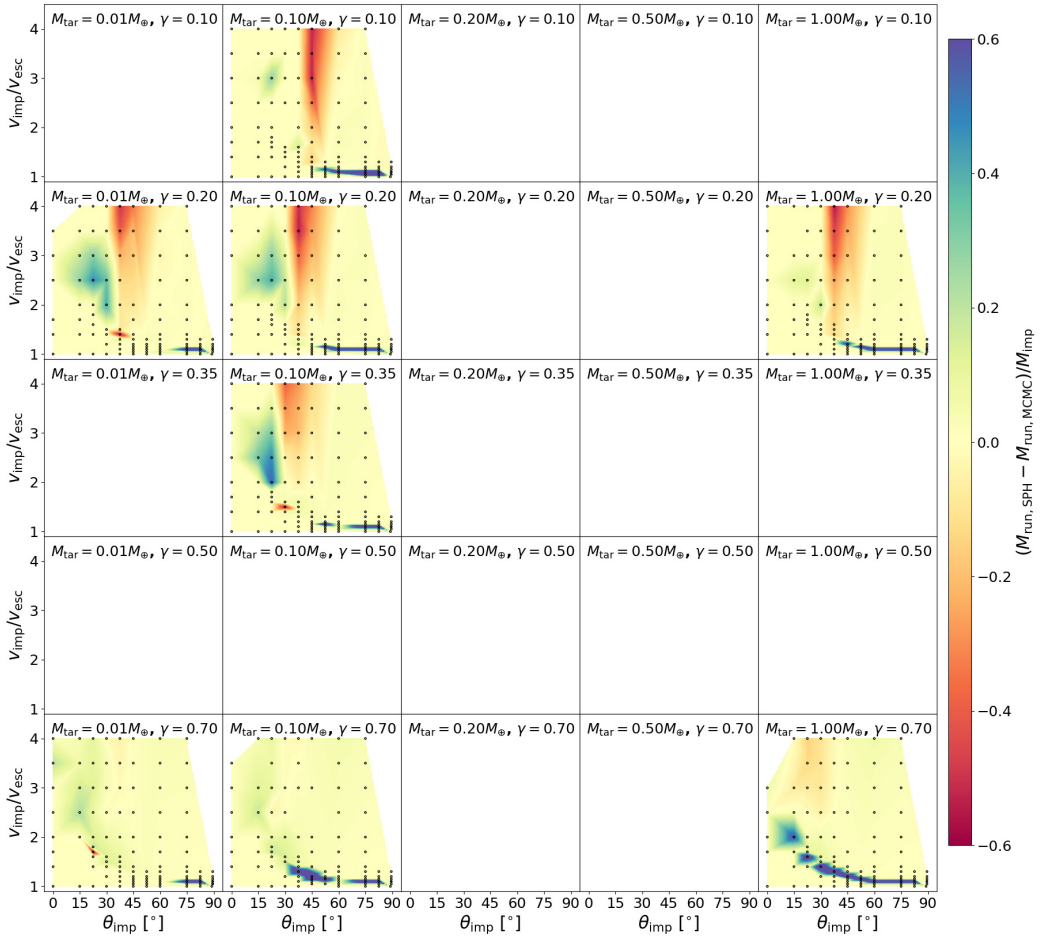

Figure S1.11. The deviations in $M_{\rm run}/M_{\rm imp}$ for the SiO_2-Fe bodies between the prediction of the best-fit model provided by the MCMC method herein and the simulated data on which the model was fit. The plot configuration is the same as Figure S1.10.

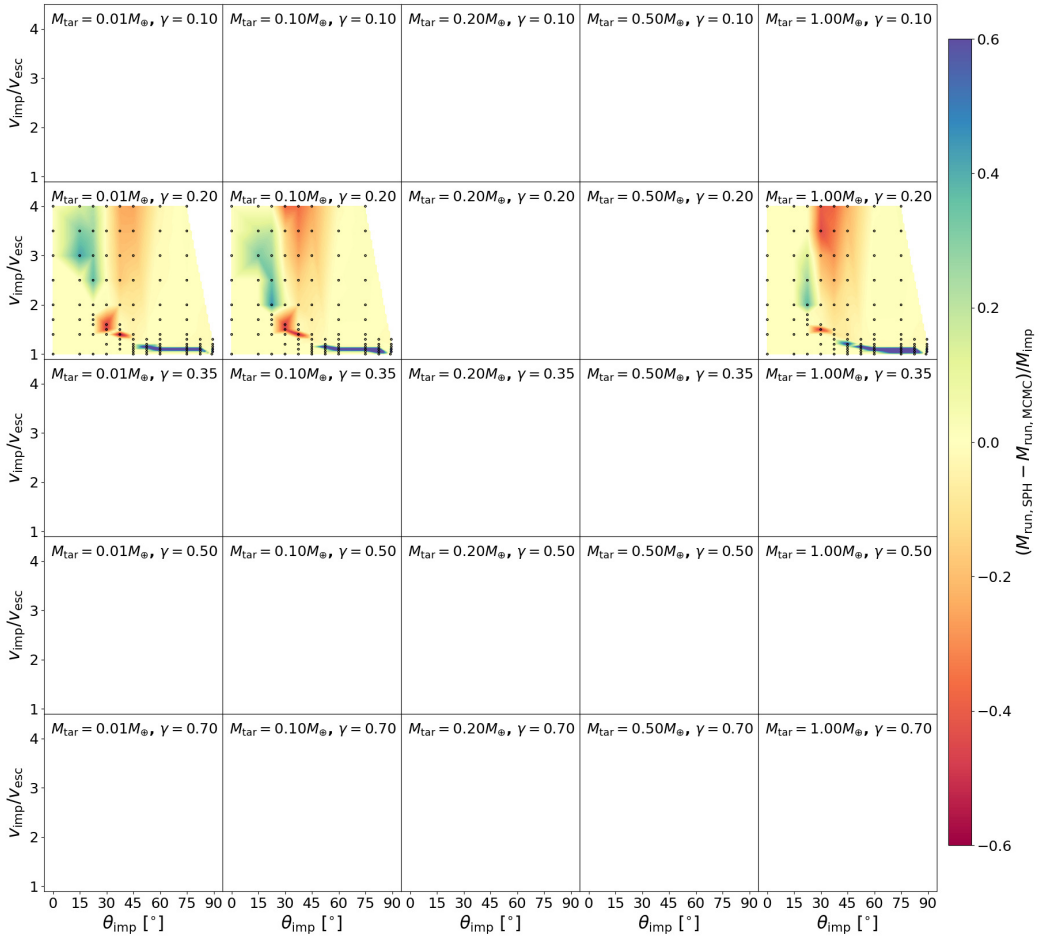

Figure S1.12. The deviations in $M_{\rm run}/M_{\rm imp}$ for the H_2O-SiO_2-Fe bodies between the prediction of the best-fit model provided by the MCMC method herein and the simulated data on which the model was fit. The plot configuration is the same as Figure S1.10.

1.15 Deviations in Escaping Mass for the Best-Rit MCMC Model

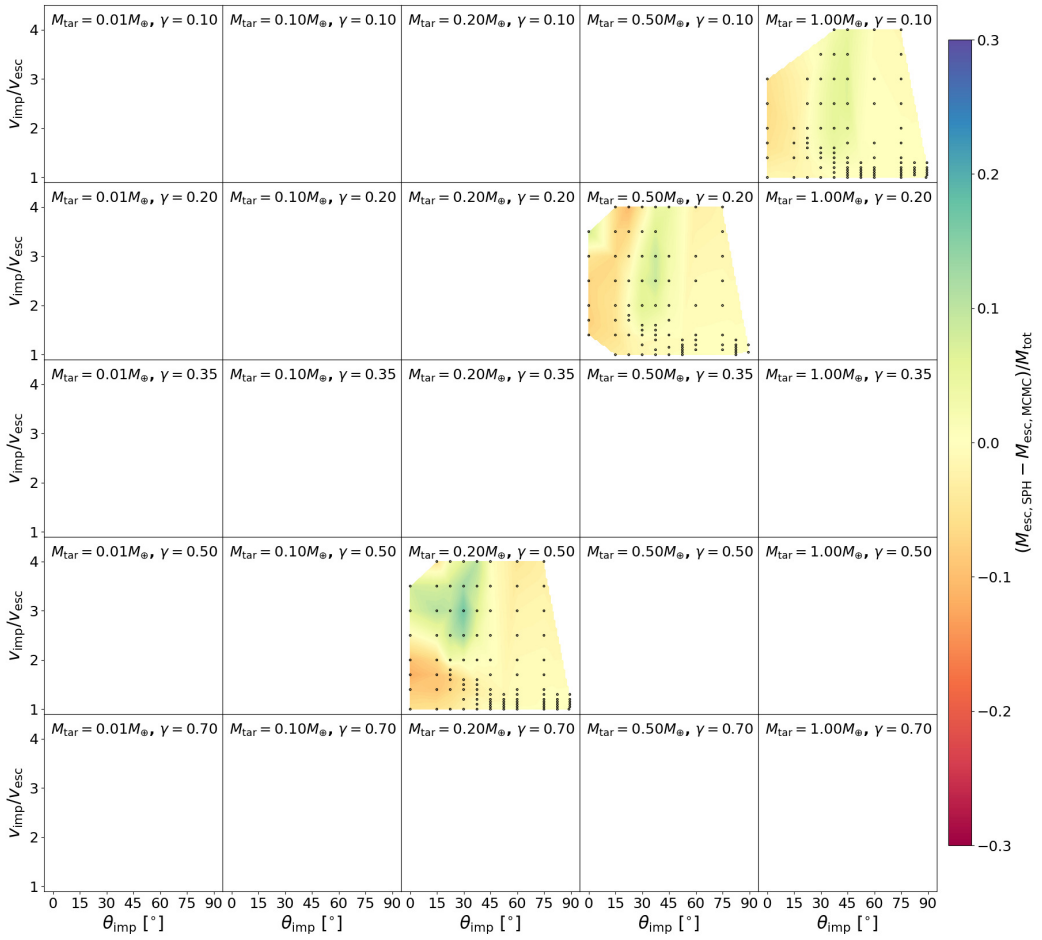

Figure S1.13. The deviations in M_{esc}/M_{tot} for the pure SiO_2 bodies between the prediction of the best-fit model provided by the MCMC method herein and the simulated data on which the model was fit. Each panel represents a unique combination of impactor-to-target mass ratio (γ; rows) and target mass (M_{tar}; columns). Lighter colors represent minimal deviation of the MCMC-optimized model from the SPH collision data.

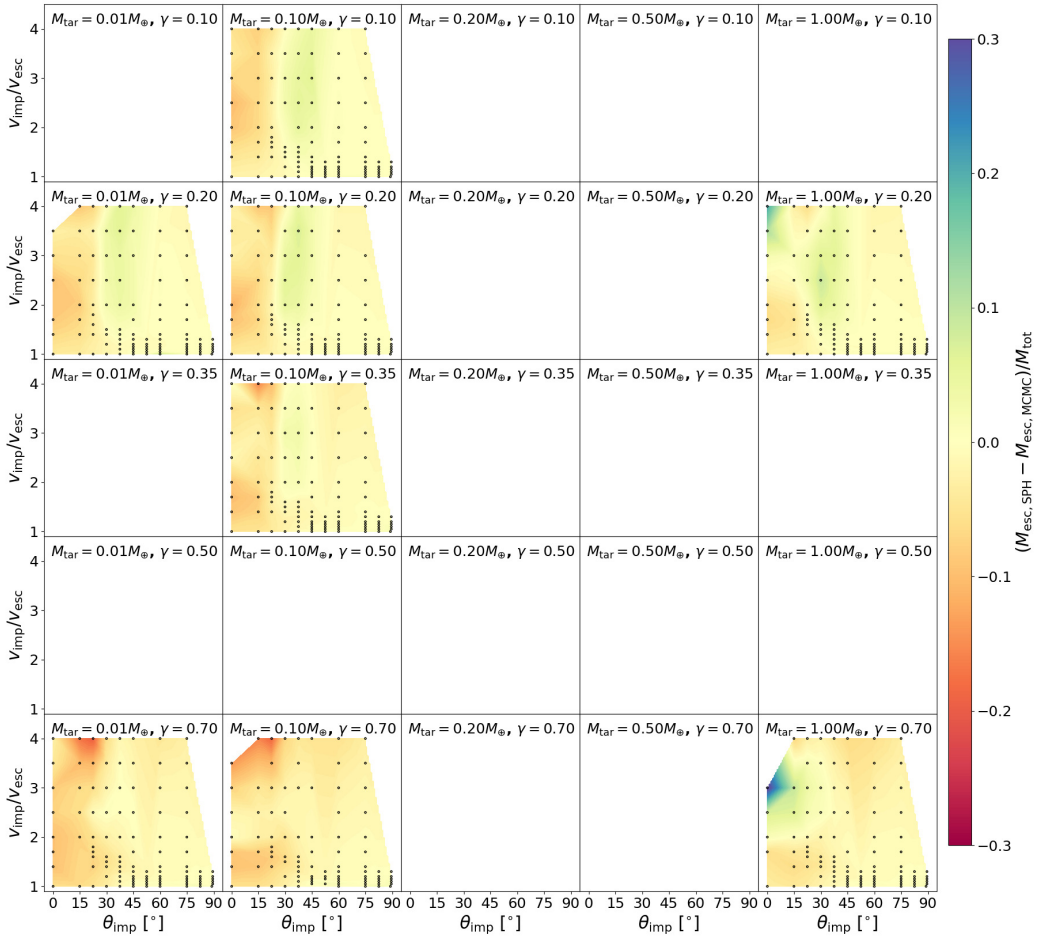

Figure S1.14. The deviations in M_{esc}/M_{tot} for the SiO_2-Fe bodies between the prediction of the best-fit model provided by the MCMC method herein and the simulated data on which the model was fit. The plot configuration is the same as Figure S1.13.

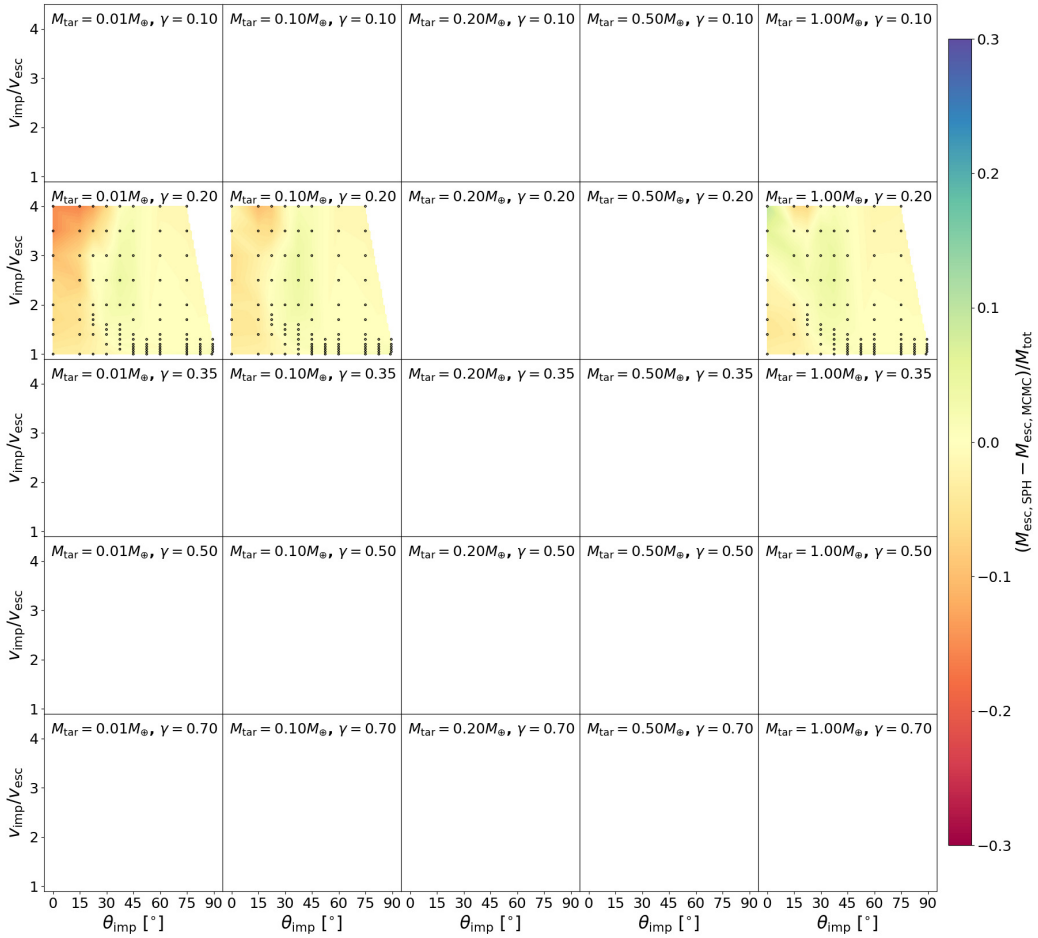

Figure S1.15. The deviations in M_{esc}/M_{tot} for the H_2O-SiO_2-Fe bodies between the prediction of the best-fit model provided by the MCMC method herein and the simulated data on which the model was fit. The plot configuration is the same as Figure S1.13.

Table S1.2. The parameters of the SPH bodies used in the simulations herein, each with a unique identifier in the first column. Radii are measured after the bodies are relaxed in SPH for several times the free-fall timescale. The columns under $U_{\mathcal{G}}$ represent various values of the gravitational binding energy, from numerical integration or from the analytic solution (Equation 1.17). The ratio of the numerical and analytic values demonstrates the degree of density stratification in each of the planets; i.e. smaller ratios means mass is more centrally concentrated in the body. In this study, we use the numerical value of the two colliding planets to compute the binding energy of the collision using Equation 1.18.

				$U_{\mathcal{G}}$, [ergs]			
Planet number	Material	M, $[M_\oplus]$	R, $[R_\oplus]^a$	Numerical^b	Analytic	Ratio	Nodes $[10^3]^c$
P01	H_2O-SiO_2-Fe	1.002	1.258	2.125×10^{39}	1.790×10^{39}	0.842	100
P02	H_2O-SiO_2-Fe	0.100	0.646	4.012×10^{37}	3.477×10^{37}	0.866	100
P03	H_2O-SiO_2-Fe	0.010	0.317	8.170×10^{35}	7.079×10^{35}	0.866	100
P04	H_2O-SiO_2-Fe	0.200	0.795	1.316×10^{38}	1.128×10^{38}	0.857	20
P05	H_2O-SiO_2-Fe	0.020	0.395	2.633×10^{36}	2.281×10^{36}	0.866	20
P06	H_2O-SiO_2-Fe	0.002	0.189	5.428×10^{34}	4.719×10^{34}	0.869	20
P12	SiO_2-Fe	1.002	1.021	2.478×10^{39}	2.201×10^{39}	0.888	100
P14	SiO_2-Fe	0.100	0.534	4.625×10^{37}	4.203×10^{37}	0.909	100
P15	SiO_2-Fe	0.010	0.257	9.465×10^{35}	8.703×10^{35}	0.920	100
P16	SiO_2-Fe	0.700	0.925	1.334×10^{39}	1.186×10^{39}	0.890	70
P17	SiO_2-Fe	0.200	0.657	1.524×10^{38}	1.368×10^{38}	0.897	20
P18	SiO_2-Fe	0.070	0.479	2.517×10^{37}	2.292×10^{37}	0.911	70
P19	SiO_2-Fe	0.020	0.323	3.043×10^{36}	2.788×10^{36}	0.916	20
P20	SiO_2-Fe	0.010	0.256	9.482×10^{35}	8.755×10^{35}	0.923	10
P21	SiO_2-Fe	0.035	0.385	7.792×10^{36}	7.128×10^{36}	0.915	35
P22	SiO_2-Fe	0.007	0.229	5.198×10^{35}	4.784×10^{35}	0.920	70
P23	SiO_2-Fe	0.002	0.151	6.433×10^{34}	5.950×10^{34}	0.925	20
P24	SiO_2	1.000	1.117	2.116×10^{39}	2.007×10^{39}	0.949	250
P25	SiO_2	0.500	0.912	6.451×10^{38}	6.141×10^{38}	0.952	250
P26	SiO_2	0.200	0.704	1.310×10^{38}	1.273×10^{38}	0.972	100
P27	SiO_2	0.100	0.570	3.974×10^{37}	3.926×10^{37}	0.988	50
P28	SiO_2	0.100	0.569	3.975×10^{37}	3.939×10^{37}	0.991	25

1.16 Comparison to Data from Movshovitz et al. (2016)

Movshovitz et al. (2016) provides an independent dataset of high-velocity, disruptive collisions that we can utilize to make an independent comparison of the remnant mass estimates. In Figure S1.16 we compare the residuals between our model and SPH simulation data from Movshovitz et al. (2016), as well as residuals between the model of Leinhardt and Stewart (2012) and the SPH simulation data from Movshovitz et al. (2016). Residuals are shown as a function of impact parameters, with underpredictions lying to the left of the zero line and overpredictions to the right. Importantly, both models are roughly centered near a zero residual, however there are notable differences and biases. The general spread of residuals is larger in Leinhardt and Stewart (2012) (see top panel), with a cluster of underpredictions in dissimilar-sized bodies and off-axis geometries (see third and fifth panel from the top). Our model tends to overpredict the mass of the larger remnant, likely due to the uncertainty involved in the sound speed correction factor. Our model also shows systematic bias with respect to the total mass, with underpredictions for lower total mass and overpredictions at higher total mass. We do not attempt to compare $M_{\rm run}$ predictions to data reported by Movshovitz et al. (2016); the second-largest remnant in their high-energy, disruptive collisions is more likely to be representative of a debris fragment, which would be considered part of a size distribution of debris encompassed by $M_{\rm esc}$ in our SPH simulations, rather than an intact runner. Overall we find the mean-squared error (MSE) is several times larger in the Leinhardt and Stewart (2012) model (MSE=0.29 $M_{\rm tot}$) than ours (MSE=0.04 $M_{\rm tot}$); adjusting the fit values for the Leinhardt and Stewart (2012) model to the 'hydrodynamic body' values ($\bar{\mu} = 0.36$ and $c^* = 5$) produces a similar MSE and introduces a greater degree of bias towards underpredictions. It

is also important to note that the residuals are not normalized for the probability distribution of impact angles ($P(\theta_{\rm imp}) = \sin(2\theta)$). When normalizing for this effect, the ratio of the mean-squared error (MSE) between the two models grows by ∼2-3 times.

1.17 Comparison to our Data

We also compare our model and that of Leinhardt and Stewart (2012) to our dataset of SPH simulations. In Figures S1.17–S1.20 we show the residuals for the SiO_2, SiO_2-Fe, and H_2O-SiO_2-Fe bodies respectively. Both models are observed to provide a tight fit to zero residual, with minimal systematic overprediction or underprediction and minimal MSE. For the pure SiO_2 ($\Lambda \approx 1$, homogeneous bodies), where the prediction of the hit-and-run angle is similar in both models, there is minimal systematic bias with respect to impact geometry (fifth panel of Figure S1.17). Instead, both models tend to show slight underpredictions at low angles and overpredictions at high angle; this is likely due to the shared assumption of both models with respect to the shape of the principal disruption curve (*e.g.* Equations 1.5, 1.11, and 1.30). There are some notable biases, particularly in the datasets with stratified planets. The Leinhardt and Stewart (2012) model exhibits increased scatter at low impact velocities (second panel of Figure S1.18) and low-to-mid impact angles (fifth panel), which is likely due to the underestimation of the hit and run criterion from Asphaug (2010). Importantly, for angles larger than about 45°, both models agree and tightly cluster around the zero line; the only exception being the few outliers due to imperfect prediction of the hit-and-run velocity transition. When normalizing for the probability distribution of

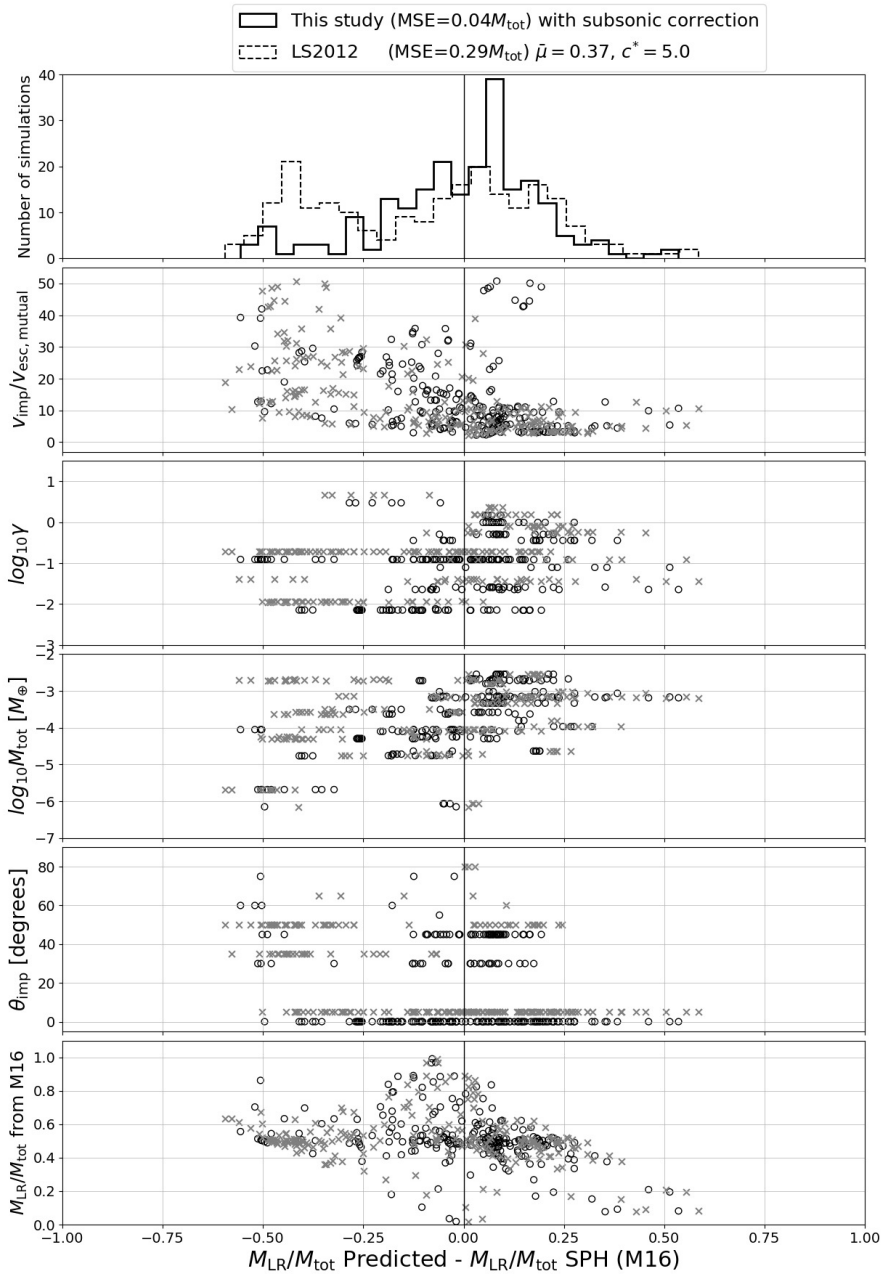

Figure S1.16. Shown are the residuals of $M_{\rm LR}/M_{\rm tot}$ between giant impact models and simulation results from Movshovitz et al. (2016, Supplementary Table 3 therein). We assumed c^* and $\bar{\mu}$ values appropriate for small bodies in the Leinhardt and Stewart (2012) model. The top panel shows the cumulative distribution of residuals. The four consecutive panels present the residuals as a function of impact parameters to examine potential model biases. The last panel presents the residuals as a function of the true value of $M_{\rm LR}/M_{\rm tot}$. Impactor-to-target mass ratio (γ) and impact angle ($\theta_{\rm imp}$) values have been artificially offset by $+0.05$ and $+5^o$ in the Leinhardt and Stewart (2012) residuals for clarity.

impact angles, as was similarly done in the previous section, the ratio of the MSE between the two studies grows only by a few tens of percent.

1.18 Comparison to Leinhardt and Stewart (2012) Data

We also compare the residuals of the two models computed for the data from the subsonic collision data from Leinhardt and Stewart (2012) (their Table 4). Both models show the mode of the residuals is at zero, however there is a tail of underestimated values in both cases. The bias towards underestimated remnant mass lies primarily in impact velocity, indicating that the two models are not predicting the catastrophic and supercatstrophic scenarios. This point is also reflected in the final panel, where the residuals lie on a 1-to-1 line with the SPH results from Leinhardt and Stewart (2012) indicating the models predict a zero value at those points. Slight bias towards underestimation of remnant masses for small γ is also seen. We generally conclude that both models do not resolve the supercatastrophic simulation data from Leinhardt and Stewart (2012) and may require refitting to resolve that regime. In terms of the global accuracy, the MSE in our model is lower however the discrepancy decreases slightly when correcting for the probability distribution of impact angles.

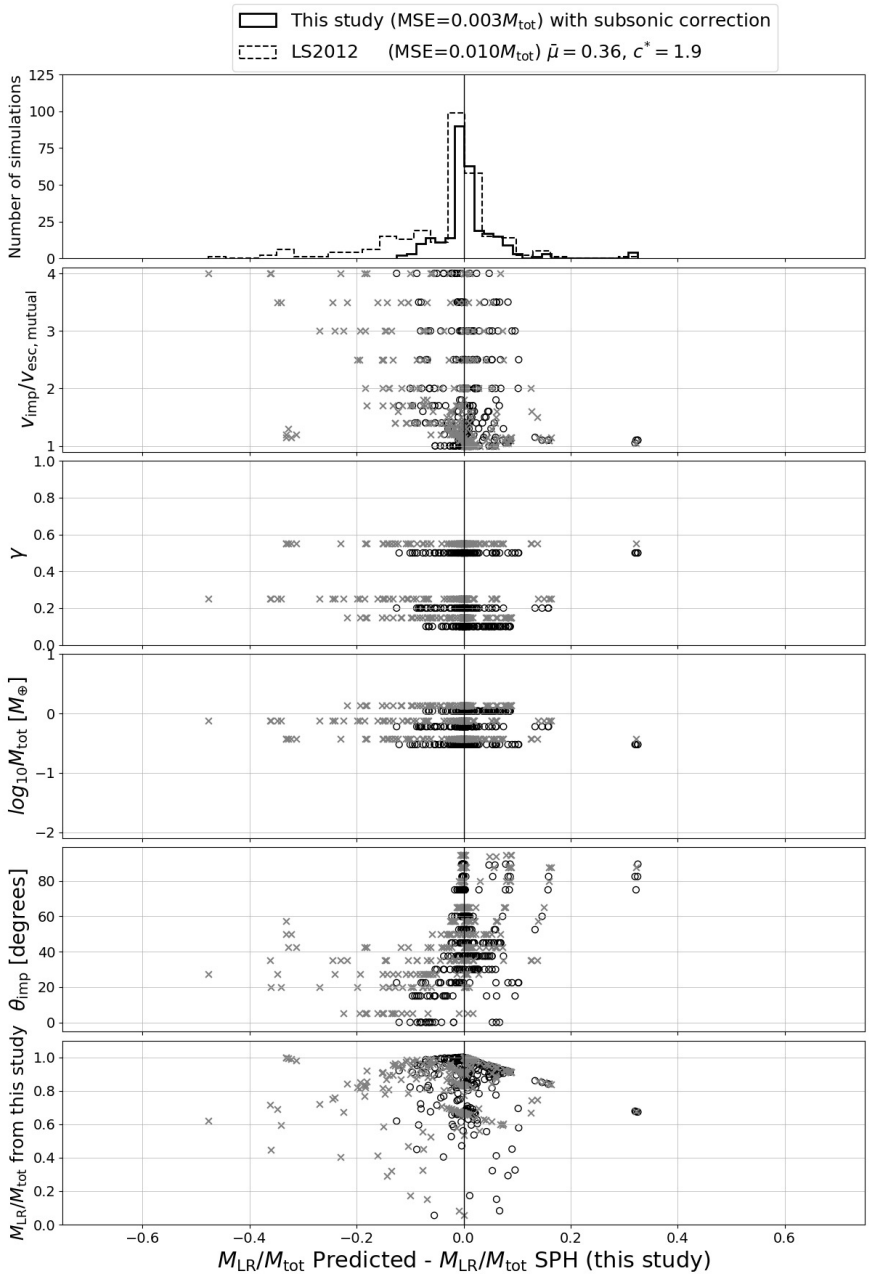

Figure S1.17. Shown are the residuals of $M_{\rm LR}/M_{\rm tot}$ between giant impact models and simulation results from this work (pure SiO_2 bodies). We assumed the $\bar{\mu}$ and c^* values appropriate for hydrodynamic bodies in the Leinhardt and Stewart (2012) model. The top panel shows the cumulative distribution of residuals with mean-squared error (residual) reported in the legend. The four consecutive panels present the residuals as a function of an impact parameter to examine potential systematic bias in both models. The last panel presents the residuals as a function of the true value of $M_{\rm LR}/M_{\rm tot}$. Impactor-to-target mass ratio (γ), total mass ($M_{\rm tot}$), and impact angle ($\theta_{\rm imp}$) values for the Leinhardt and Stewart (2012) model residuals have been artificially offset by +0.05, 0.1 $M_{\rm tot}$, and $+5^o$ for clarity.

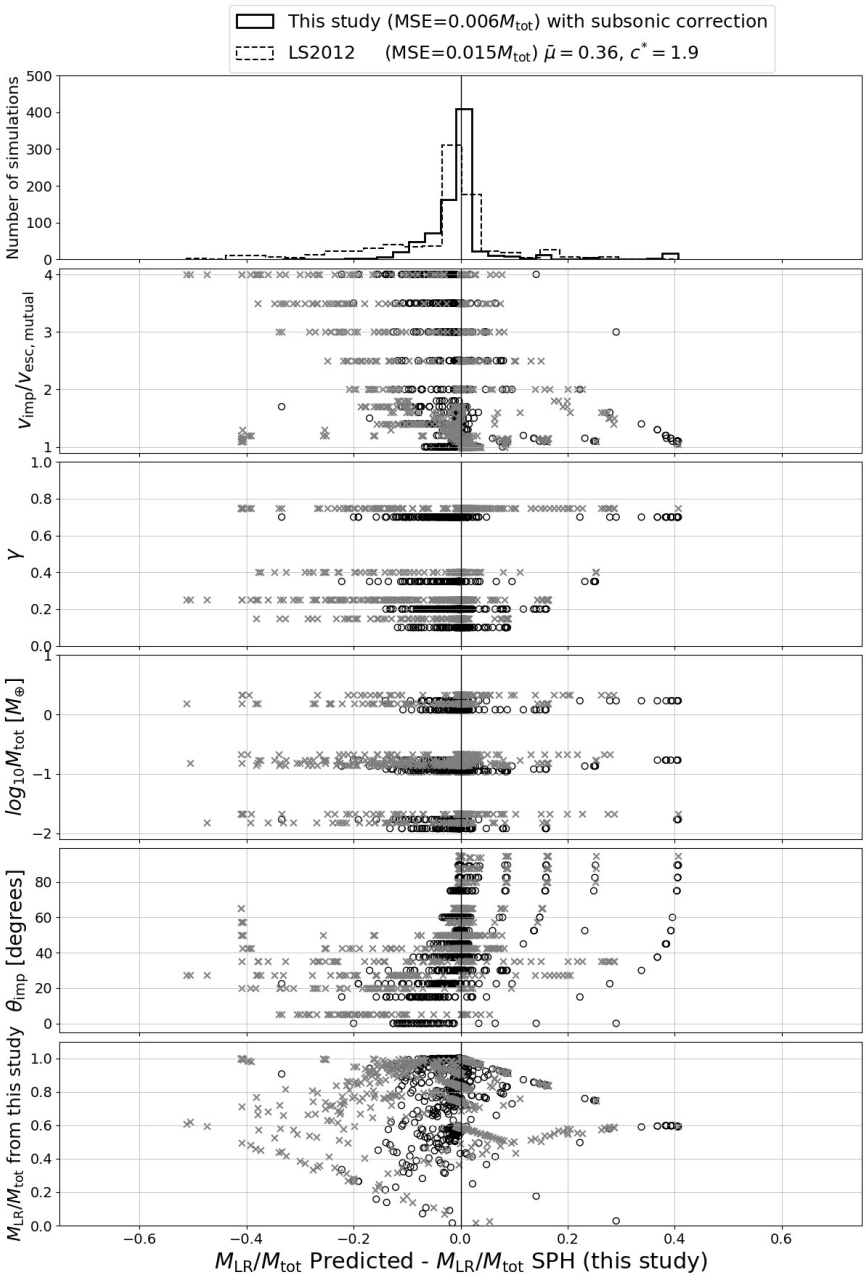

Figure S1.18. Same as Figure S1.17 for SiO_2-Fe bodies.

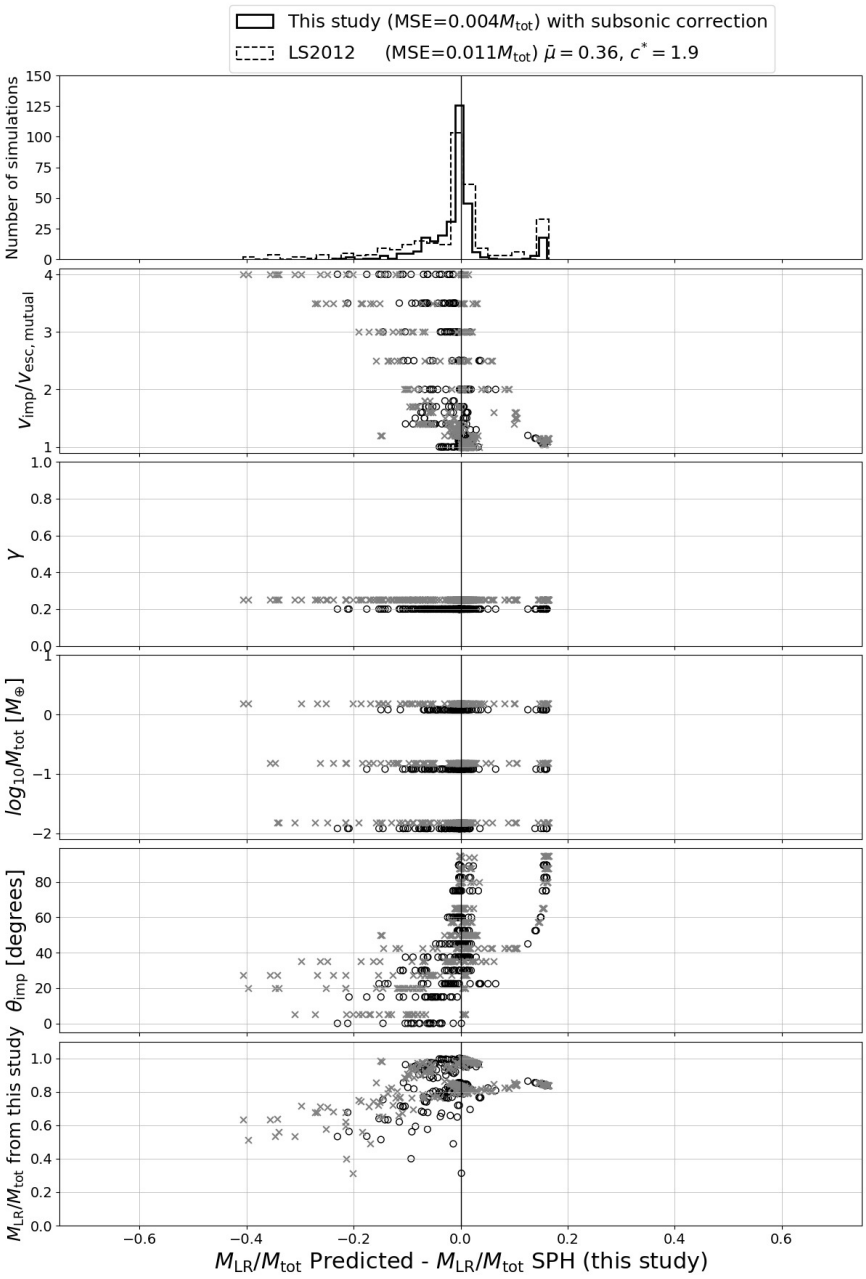

Figure S1.19. Same as Figure S1.17 for SiO_2-Fe bodies.

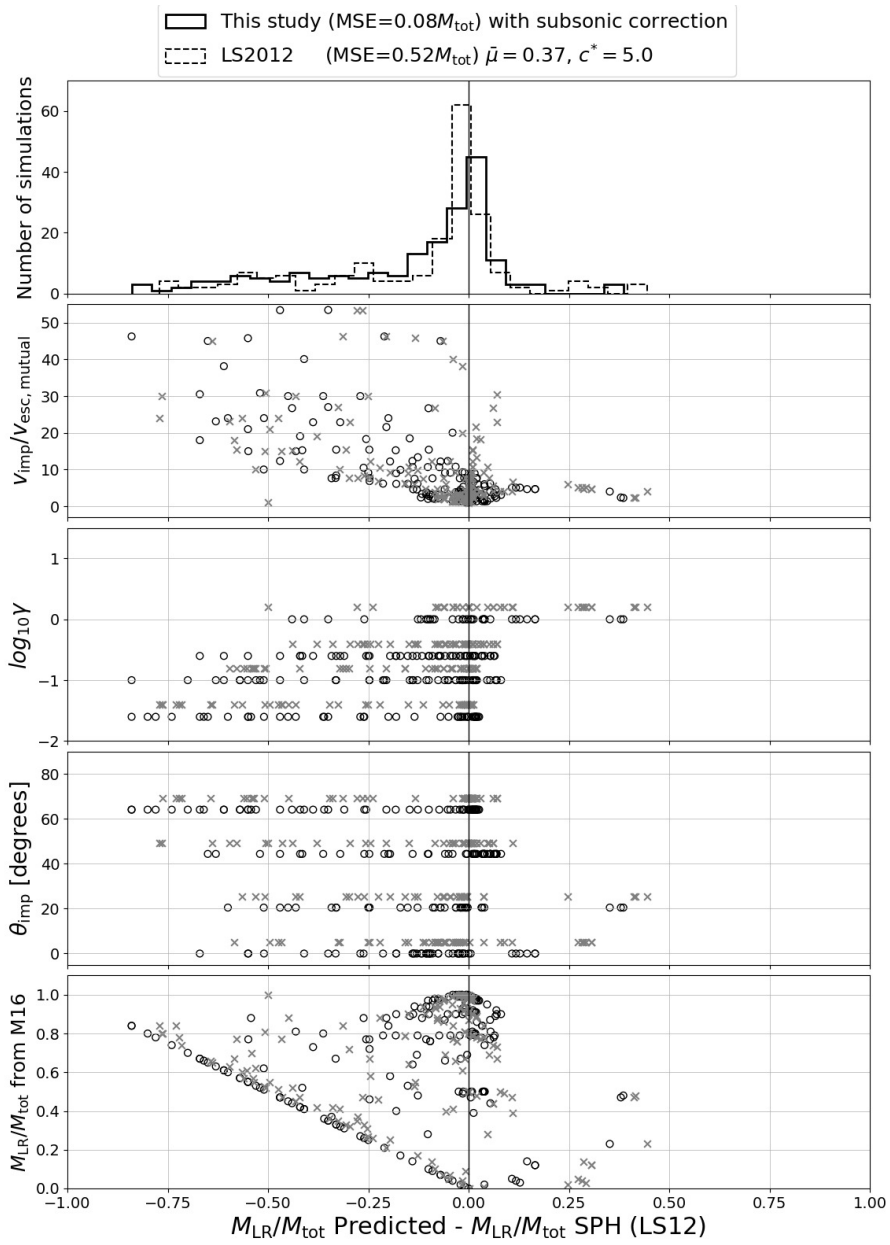

Figure S1.20. Shown are the residuals of $M_{\rm LR}/M_{\rm tot}$ between giant impact models and simulation results from Leinhardt and Stewart (2012) (their Table 4). We assumed the $\bar{\mu}$ and c^* values appropriate for small bodies in the Leinhardt and Stewart (2012) model. The top panel shows the cumulative distribution of residuals with mean-squared error (residual) reported in the legend. The three consecutive panels present the residuals as a function of an impact parameter to examine potential systematic bias in both models. The last panel presents the residuals as a function of the true value of $M_{\rm LR}/M_{\rm tot}$. Impactor-to-target mass ratio (γ) and impact angle ($\theta_{\rm imp}$) values for the Leinhardt and Stewart (2012) model residuals have been artificially offset by $+0.05$ and $+5^o$ for clarity.

References

Agnor, C. B., R. M. Canup, and H. F. Levison (Nov. 1999). On the Character and Consequences of Large Impacts in the Late Stage of Terrestrial Planet Formation. *Icarus* 142, pp. 219–237.

Agnor, C. and E. Asphaug (Oct. 2004). Accretion Efficiency during Planetary Collisions. *Astrophysical Journal Letters* 613, pp. L157–L160.

Asphaug, E. (2010). Similar-sized collisions and the diversity of planets. *Chemie der Erde / Geochemistry* 70, pp. 199–219.

Asphaug, E., C. B. Agnor, and Q. Williams (Jan. 2006). Hit-and-run planetary collisions. *Nature* 439, pp. 155–160.

Asphaug, E. and A. Reufer (Mar. 2013). Late origin of the Saturn system. *Icarus* 223, pp. 544–565.

Asphaug, E. and A. Reufer (Aug. 2014). Mercury and other iron-rich planetary bodies as relics of inefficient accretion. *Nature Geoscience* 7, pp. 564–568.

Balsara, D. S. (1995). von Neumann stability analysis of smoothed particle hydrodynamics—suggestions for optimal algorithms. *Journal of Computational Physics* 121 (2), pp. 357–372.

Benz, W., A. Anic, J. Horner, and J. A. Whitby (Oct. 2007). The Origin of Mercury. *Space Science Reviews* 132, pp. 189–202.

Benz, W. and E. Asphaug (Jan. 1994). Impact simulations with fracture. I - Method and tests. *Icarus* 107, p. 98.

Benz, W. and E. Asphaug (1999). Catastrophic disruptions revisited. *Icarus* 142 (1), pp. 5–20.

Benz, W., W. L. Slattery, and A. G. W. Cameron (June 1986). The origin of the moon and the single-impact hypothesis. I. *Icarus* 66, pp. 515–535.

Bottke, W. F., D. Vokrouhlický, S. Marchi, T. Swindle, E. R. D. Scott, J. R. Weirich, and H. Levison (Apr. 2015). Dating the Moon-forming impact event with asteroidal meteorites. *Science* 348, pp. 321–323.

Brown, M. E., K. M. Barkume, D. Ragozzine, and E. L. Schaller (Mar. 2007). A collisional family of icy objects in the Kuiper belt. *Nature* 446, pp. 294–296.

Burger, C., T. I. Maindl, and C. M. Schäfer (Dec. 2017). Transfer, loss and physical processing of water in hit-and-run collisions of planetary embryos. *Celestial Mechanics and Dynamical Astronomy* 130 (1), p. 2.

Cambioni, S., E. Asphaug, A. Emsenhuber, T. S. J. Gabriel, R. Furfaro, and S. R. Schwartz (Mar. 2019). Realistic On-The-Fly Outcomes of Planetary Collisions: Machine Learning Applied to Simulations of Giant Impacts, arXiv:1903.04507, arXiv:1903.04507. eprint: 1903.04507.

Cameron, A. G. W. (2001). From interstellar gas to the Earth-Moon system. *Meteoritics & Planetary Science* 36 (1), pp. 9–22.

Cameron, A. G. W. and W. R. Ward (Mar. 1976). The Origin of the Moon. *Lunar and Planetary Science Conference*. 7. Lunar and Planetary Science Conference.

Canup, R. M. (2004). Simulations of a late lunar-forming impact. *Icarus* 168 (2), pp. 433–456.

Canup, R. M. (Jan. 2005). A Giant Impact Origin of Pluto-Charon. *Science* 307, pp. 546–550.

Canup, R. M. (2008). Lunar-forming collisions with pre-impact rotation. *Icarus* 196 (2). Mars Polar Science IV, pp. 518–538.

Canup, R. M. (Feb. 2011). On a Giant Impact Origin of Charon, Nix, and Hydra. *Astronomical Journal* 141, 35, p. 35.

Canup, R. M. and E. Asphaug (Aug. 2001). Origin of the Moon in a giant impact near the end of the Earth's formation. *Nature* 412 (6848), pp. 708–712.

Chambers, J. E. (July 2004). Planetary accretion in the inner Solar System. *Earth and Planetary Science Letters* 223, pp. 241–252.

Chambers, J. E. (May 2013). Late-stage planetary accretion including hit-and-run collisions and fragmentation. *Icarus* 224, pp. 43–56.

Dent, W. R. F. et al. (Mar. 2014). Molecular Gas Clumps from the Destruction of Icy Bodies in the β Pictoris Debris Disk. *Science* 343, pp. 1490–1492. eprint: 1404.1380.

Emsenhuber, A. and E. Asphaug (Apr. 2019). Fate of the Runner in Hit-and-run Collisions. *The Astrophysical Journal* 875 (2), p. 95.

Emsenhuber, A., M. Jutzi, and W. Benz (2018). SPH calculations of Mars-scale collisions: The role of the equation of state, material rheologies, and numerical effects. *Icarus* 301, pp. 247–257. eprint: 1710.03245.

Foreman-Mackey, D. (2016). corner.py: Scatterplot matrices in Python. *The Journal of Open Source Software* 24.

Foreman-Mackey, D., D. W. Hogg, D. Lang, and J. Goodman (Mar. 2013). emcee: The MCMC Hammer. *Publications of the Astronomical Society of the Pacific* 125, p. 306. arXiv: 1202.3665.

Genda, H., T. Fujita, H. Kobayashi, H. Tanaka, and Y. Abe (2015). Resolution dependence of disruptive collisions between planetesimals in the gravity regime. *Icarus* 262, pp. 58–66.

Genda, H., E. Kokubo, and S. Ida (Mar. 2011). Giant Impacts and Terrestrial Planet Formation. *Lunar and Planetary Science Conference*. 42. Lunar and Planetary Science Conference, p. 2090.

Genda, H., E. Kokubo, and S. Ida (Jan. 2012). Merging Criteria for Giant Impacts of Protoplanets. *Astrophysical Journal* 744, 137, p. 137. eprint: 1109.4330.

Goldreich, P., Y. Lithwick, and R. Sari (Sept. 2004). Planet Formation by Coagulation: A Focus on Uranus and Neptune. *Annual Review of Astronomy and Astrophysics* 42, pp. 549–601. eprint: astro-ph/0405215.

Goodman, J. and J. Weare (2010). Ensemble samplers with affine invariance. *Communications in Applied Mathematics and Computational Science* 5, pp. 65–80.

Hartmann, W. K. and D. R. Davis (1975). Satellite-sized planetesimals and lunar origin. *Icarus* 24 (4), pp. 504–515.

Holsapple, K. A. (1993). The scaling of impact processes in planetary sciences. *Annual Review of Earth and Planetary Sciences* 21, pp. 333–373.

Hosono, N., K. Shun-ichiro, M. Junichiro, and T. R. Saitoh (Dec. 2019). Terrestrial magma ocean origin of the Moon. *Nature Geoscience*.

Hosono, N., T. R. Saitoh, J. Makino, H. Genda, and S. Ida (June 2016). The giant impact simulations with density independent smoothed particle hydrodynamics. *Icarus* 271, pp. 131–157. eprint: 1602.00843.

Housen, K. R. and K. A. Holsapple (Mar. 1990). On the fragmentation of asteroids and planetary satellites. *Icarus* 84, pp. 226–253.

Jackson, A. P., T. S. J. Gabriel, and E. I. Asphaug (Mar. 2018). Constraints on the pre-impact orbits of Solar system giant impactors. *Monthly Notices of the Royal Astronomical Society* 474, pp. 2924–2936.

Jackson, A. P., M. C. Wyatt, A. Bonsor, and D. Veras (June 2014). Debris froms giant impacts between planetary embryos at large orbital radii. *Montly Notices of the Royal Astronomical Society* 440, pp. 3757–3777.

Jutzi, M. (2015). SPH calculations of asteroid disruptions: The role of pressure dependent failure models. *Planetary and Space Science* 107. VIII Workshop on Catastrophic Disruption in the Solar System, pp. 3–9.

Jutzi, M. and E. Asphaug (June 2015). The shape and structure of cometary nuclei as a result of low-velocity accretion. *Science* 348, pp. 1355–1358.

Jutzi, M., E. Asphaug, P. Gillet, J.-A. Barrat, and W. Benz (Feb. 2013). The structure of the asteroid 4 Vesta as revealed by models of planet-scale collisions. *Nature* 494, pp. 207–210.

Jutzi, M., P. Michel, W. Benz, and D. C. Richardson (May 2010). Fragment properties at the catastrophic disruption threshold: The effect of the parent bodys internal structure. *Icarus* 207, pp. 54–65.

Jutzi, M., P. Michel, and D. C. Richardson (Aug. 2018). Fragment properties from large-scale asteroid collisions: I: Results from SPH/N-body simulations using porous parent bodies and improved material models. *ArXiv e-prints*.

Kenyon, S. J. and B. C. Bromley (Mar. 2006). Terrestrial Planet Formation. I. The Transition from Oligarchic Growth to Chaotic Growth. *Astronomical Journal* 131, pp. 1837–1850. eprint: arXiv:astro-ph/0503568.

Kenyon, S. J. and B. C. Bromley (Jan. 2016). Variations on Debris Disks III. Collisional Cascades and Giant Impacts in the Terrestrial Zones of Solar-type Stars. *The Astrophysical Journal* 817, 51, p. 51.

Kokubo, E. and H. Genda (May 2010). Formation of Terrestrial Planets from Protoplanets Under a Realistic Accretion Condition. *Astrophysical Journal Letters* 714, pp. L21–L25. eprint: 1003.4384.

Leinhardt, Z. M., J. Dobinson, P. J. Carter, and S. Lines (June 2015). Numerically Predicted Indirect Signatures of Terrestrial Planet Formation. *The Astrophysical Journal* 806, 23, p. 23. arXiv: 1506.05233.

Leinhardt, Z. M., R. A. Marcus, and S. T. Stewart (May 2010). The Formation of the Collisional Family Around the Dwarf Planet Haumea. *Astrophysical Journal* 714, pp. 1789–1799.

Leinhardt, Z. M., D. C. Richardson, and T. Quinn (June 2000). Direct N-body Simulations of Rubble Pile Collisions. *Icarus* 146, pp. 133–151. eprint: astro-ph/9908221.

Leinhardt, Z. M. and S. T. Stewart (Jan. 2012). Collisions between Gravity-dominated Bodies. I. Outcome Regimes and Scaling Laws. *The Astrophysical Journal* 745, 79, p. 79.

Lisse, C. M., C. H. Chen, M. C. Wyatt, A. Morlok, I. Song, G. Bryden, and P. Sheehan (Aug. 2009). Abundant Circumstellar Silica Dust and SiO Gas Created by a Giant Hypervelocity Collision in the ˜12 Myr HD172555 System. *The Astrophysical Journal* 701, pp. 2019–2032.

Marcus, R. A., D. Sasselov, S. T. Stewart, and L. Hernquist (Aug. 2010). Water/Icy Super-Earths: Giant Impacts and Maximum Water Content. *Astrophysical Journal Letters* 719, pp. L45–L49.

Marcus, R. A., S. T. Stewart, D. Sasselov, and L. Hernquist (Aug. 2009). Collisional Stripping and Disruption of Super-Earths. *Astrophysical Journal Letters* 700, pp. L118–L122.

Marinova, M. M., O. Aharonson, and E. Asphaug (Feb. 2011). Geophysical consequences of planetary-scale impacts into a Mars-like planet. *Icarus* 211, pp. 960–985.

Marinova, M. M., O. Aharonson, and E. Asphaug (June 2008). Mega-impact formation of the Mars hemispheric dichotomy. *Nature* 453 (7199).

Melosh, H. J. (2007). A hydrocode equation of state for SiO2. *Meteoritics and Planetary Science* 42, pp. 2079–2098.

Monaghan, J. J. (1992). Smoothed particle hydrodynamics. *Annual Review of Astronomy and Astrophysics* 30, pp. 543–574.

Morbidelli, A., M. Lambrechts, S. Jacobson, and B. Bitsch (2015). The great dichotomy of the Solar System: Small terrestrial embryos and massive giant planet cores. *Icarus* 258, pp. 418–429. eprint: 1506.01666.

Movshovitz, N., F. Nimmo, D. G. Korycansky, E. Asphaug, and J. M. Owen (Nov. 2016). Impact disruption of gravity-dominated bodies: New simulation data and scaling. *Icarus* 275, pp. 85–96.

Quintana, E. V., T. Barclay, W. J. Borucki, J. F. Rowe, and J. E. Chambers (Apr. 2016). The Frequency of Giant Impacts on Earth-like Worlds. *Astrophysical Journal* 821, 126, p. 126. eprint: 1511.03663.

Raskin, C. and J. M. Owen (Nov. 2016). Examining the Accuracy of Astrophysical Disk Simulations with a Generalized Hydrodynamical Test Problem. *The Astrophysical Journal* 831 (1), 26, p. 26. arXiv: 1607.04293.

Raymond, S. N., D. P. O'Brien, A. Morbidelli, and N. A. Kaib (Oct. 2009). Building the terrestrial planets: Constrained accretion in the inner Solar System. *Icarus* 203, pp. 644–662.

Reufer, A. (2011). Collisions in planetary systems. PhD thesis. Universiät Bern.

Reufer, A., M. M. M. Meier, W. Benz, and R. Wieler (Sept. 2012). A hit-and-run giant impact scenario. *Icarus* 221, pp. 296–299.

Richardson, D. C., T. Quinn, J. Stadel, and G. Lake (Jan. 2000). Direct Large-Scale N-Body Simulations of Planetesimal Dynamics. *Icarus* 143, pp. 45–59.

Rufu, R., O. Aharonson, and H. B. Perets (2017). A multiple-impact origin for the Moon. *Nature Geoscience* 10 (2), pp. 89–94.

Saitoh, T. R. and J. Makino (Apr. 2013). A density-independent formulation of smoothed particle hydrodynamics. *The Astrophysical Journal* 768 (1), p. 44.

Schultz, P. H. and K. E. Wrobel (2011). The oblique impact Hale and its consequences on Mars. *Journal of Geophysical Research: Planets* 117 (E4).

Shoemaker, E. (1961). *Interpretation of Lunar Craters*, pp. 283–359.

Smith, A. H. and A. W. Lawson (1954). The Velocity of Sound in Water as a Function of Temperature and Pressure. *The Journal of Chemical Physics* 22 (3), pp. 351–359.

Sod, G. A. (Apr. 1978). A survey of several finite difference methods for systems of nonlinear hyperbolic conservation laws. *Journal of Computational Physics* 27, pp. 1–31.

Stadel, J. G. (2001). Cosmological N-body simulations and their analysis. PhD thesis. University of Washington.

Stern, S. A., H. A. Weaver, A. J. Steffl, M. J. Mutchler, W. J. Merline, M. W. Buie, E. F. Young, L. A. Young, and J. R. Spencer (Feb. 2006). A giant impact origin for Pluto's small moons and satellite multiplicity in the Kuiper belt. *Nature* 439, pp. 946–948.

Stewart, S. T. and Z. M. Leinhardt (2009). Velocity-Dependent Catastrophic Disruption Criteria for Planetesimals. *The Astrophysical Journal* 691 (2), pp. L133–L137.

Stewart, S. T. and Z. M. Leinhardt (May 2012). Collisions between Gravity-dominated Bodies. II. The Diversity of Impact Outcomes during the End Stage of Planet Formation. *Astrophysical Journal* 751, 32, p. 32. eprint: 1109.4588.

Suzuki, I., O. L. Anderson, and Y. Sumino (Jan. 1983). Elastic properties of a single-crystal forsterite Mg2SiO4, up to 1,200 K. *Physics and Chemistry of Minerals* 10 (1), pp. 38–46.

Telesco, C. M. et al. (Jan. 2005). Mid-infrared images of Beta Pictoris and the possible role of planetesimal collisions in the central disk. *Nature* 433, pp. 133–136.

Vogt, C., K. Laihem, and C. Wiebusch (2008). Speed of sound in bubble-free ice. *The Journal of the Acoustical Society of America* 124 (6), pp. 3613–3618.

Wetherill, G. W. (May 1985). Occurrence of giant impacts during the growth of the terrestrial planets. *Science* 228, pp. 877–879.

Wilhelms, D. E. and S. W. Squyres (May 1984). The martian hemispheric dichotomy may be due to a giant impact. *Nature* 309, pp. 138–140.

Wyatt, M. C., A. Bonsor, A. P. Jackson, S. Marino, and A. Shannon (Jan. 2017). How to design a planetary system for different scattering outcomes: giant impact sweet spot, maximizing exocomets, scattered discs. *Monthly Notices of the Royal Astronomical Society* 464, pp. 3385–3407. eprint: 1610.00714.

Chapter 2

WATER ABUNDANCE OF DUNES IN GALE CRATER, MARS FROM ACTIVE NEUTRON EXPERIMENTS & IMPLICATIONS FOR AMORPHOUS PHASES

Travis S. S. Gabriel,[1*†] Craig Hardgrove,[1†] Sean Czarnecki,[1†] Elizabeth Rampe,[2] William Rapin,[3] Cherie N. Achilles,[4] Daniel Sullivan,[1†] Suzanne Nowicki,[5] Lucy Thompson,[6] Maxim Litvak,[7] Igor Mitrofanov,[7] Robert T. Downs[8]

[1]School of Earth and Space Exploration, Arizona State University, Tempe, AZ 85287, USA.

[2]NASA Johnson Space Center, Houston, TX 77058, USA

[3]California Institute of Technology, Pasadena, CA 91125, USA

[4]NASA Goddard Spaceflight Center, Goddard, MD 20771, USA

[5]Los Alamos National Laboratory, Los Alamos, NM 87545, USA

[6]Planetary and Space Science Centre, University of New Brunswick, Fredericton, NB E3B 5A3, Canada

[7]Institute for Space Research, Russian Academy of Sciences, Moscow, Russia

[8]Department of Geosciences, University of Arizona, Tucson, AZ 85721, USA

[*]Corresponding author: Travis.Gabriel@asu.edu

[†]Present address: 781 E Terrace Mall, ISTB4, Room 795, Tempe, AZ 85287-6004, USA.

Citation: T. S. J. Gabriel, C. Hardgrove, S. Czarnecki, E. Rampe, W. Rapin, C. N. Achilles, D. Sullivan, S. Nowicki, L. Thompson, M. Litvak, I. Mitrofanov, and R. T. Downs (2018). Water abundance of dunes in Gale crater, Mars from active neutron experiments & implications for amorphous phases. *Geophysical Research Letters*, 45(23).

2.1 Abstract

We report the water abundance of Bagnold Dune sand in Gale crater, Mars by analyzing active neutron experiments using the Dynamic Albedo of Neutrons (DAN) instrument. We report a bulk water-equivalent-hydrogen abundance of 0.68 ± 0.15 wt%, which is similar to measurements several kilometers away and from those taken of the dune surface. Thus, the dune is likely dehydrated throughout.Furthermore, we use geochemical constraints, including bulk water content, to develop compositional models of the amorphous fraction for which little information is known. We find the amorphous fraction contains ∼26-64 wt% basaltic glass and up to ∼24 wt% rhyolitic glass, suggesting at least one volcanic source for the dune material. We also find a range of hydrated phases may be present in appreciable abundances, either from the incorporation of eroded aqueously-altered sediments or the direct alteration of the dune sand.

2.2 Introduction

The Mars Science Laboratory (MSL), Curiosity rover conducted two campaigns to study the composition and morphology of active sand dunes that are found on nearly all sides of the central peak of Gale crater (Mount Sharp). Both campaigns were conducted at the Bagnold Dune Field on the northwest flank of Mount Sharp. Bridges and Ehlmann (2017) provided an overview of the Bagnold phase 1 campaign (sol 1162–1254) and Lapotre and E. B. Rampe (2018) provides an overview of the Bagnold phase 2 campaign (sol 1602–1660), the subject of this special issue. The crystalline component of the Bagnold Dunes is primarily mafic; analogous to globally-distributed

dune sands on Mars (E. B. Rampe et al., 2018). X-ray amorphous material constitutes ∼40 wt% of Bagnold sand and, by combining results from x-ray spectrometry (for bulk geochemical abundances) and x-ray diffraction (for mineralogical abundances), the abundance of major rock-forming elements of the amorphous fraction has been constrained (Achilles et al., 2017; E. B. Rampe et al., 2018). However, specific amorphous phase abundances have not been constrained using those geochemical estimates. Amorphous materials can range from relatively unaltered, water-poor materials, *e.g.* glasses, to water-rich materials formed in an aqueous environment, thus, understanding the amorphous fraction of the dune is critical in constraining the alteration history of the sand and its source region, for which there are several candidate locales (Ehlmann et al., 2017). Herein we place constraints on the range of phase abundances in the amorphous fraction and demonstrate that the water content of the material plays an important role. To determine the water content of Bagnold dune sand, we performed in-situ active neutron experiments using the Dynamic Albedo of Neutrons (DAN) instrument at the dune. We also compare our results to those of Bagnold phase 1 to examine whether the dunes exhibit compositional variability with depth, lateral distance, and morphology.

The Bagnold Dune Field consists primarily of barchan and linear dunes that are spaced ∼150-200 m apart and reach heights up to ∼10 m (Silvestro et al., 2013). The dune field is active, migrating ∼0.4 meters per Earth year primarily driven by winds blowing from NE to SW (Bridges et al., 2014; Newman et al., 2017; Silvestro et al., 2013). Near-surface, low-wind-speed, eolian activity is the dominant driver of Bagnold Dune morphology (e.g. Ehlmann et al., 2017; Newman et al., 2017; Sullivan and Kok, 2017). The highly-active Namib Dune, studied in Bagnold phase 1, with ripple migration rates of ∼1.7 m per Earth year, shows no silt size or finer grains

(Ehlmann et al., 2017; Silvestro et al., 2016), likely due to the preferential lofting of smaller grains through eolian activity. Namib Dune has among the lowest water abundances measured along the Curiosity rover's traverse, $\sim 0.9 \pm 0.3$ wt% H_2O as measured by the Sample Analysis at Mars instrument (SAM) Evolved Gas Analysis (EGA) experiments of surficial dune material (Sutter et al., 2017) and 0.8 wt% water equivalent hydrogen (WEH) by active DAN experiments (no reported uncertainty) which are sensitive to $\sim$60 cm depth (Ehlmann et al., 2017). The fact that the dune hydrogen abundance is similarly dehydrated both surficially (J. C. Stern et al., 2018; Sutter et al., 2017) and at depth (Ehlmann et al., 2017), and that fine-grained material is considered to be the predominant carrier of hydration in unconsolidated soils (e.g. Ehlmann et al., 2017), suggests that Bagnold dunes lack the fine-grained reservoir throughout (at depth). We note that SAM EGA experiments report H_2S and H_2 as well, however they are in minimal abundance ($\sim 10^{-2}$ wt%).

The Bagnold Dunes are olivine-rich basaltic sand (Achilles et al., 2017; E. B. Rampe et al., 2018) with geochemistry similar to the nearby Stimson eolian sandstone formation (Ehlmann et al., 2017; O'Connell-Cooper et al., 2017); however, the Stimson does not contain olivine (Ehlmann et al., 2017). Ehlmann et al. (2017) finds Bagnold sands are geochemically distinct from other unconsolidated materials in Gale Crater and from materials measured by the Mars Exploration Rovers (MER). The SAM and DAN instruments indeed found the hydrogen in the active dunes to be depleted with respect to local bedrock (Cousin et al., 2017; Ehlmann et al., 2017; Sutter et al., 2017). Our work herein and EGA experiments further corroborate the dehydrated state of the dunes.

Ehlmann et al. (2017) finds there are two reservoirs of water in unconsolidated Martian soils: (1) sand-sized amorphous clasts with bound water, and (2) silt-sized

amorphous materials primarily with adsorbed and/or loosely-bound water. Bagnold dunes in particular, lack the dust/silt component which indicates that the sand-sized amorphous clasts are the dominant volatile reservoir in Bagnold sand. In fact, Ehlmann et al. (2017) reports over 90% of the water in the 'Gobabeb sample', as part of SAM EGA experiments in the Bagnold phase I campaign (Sutter et al., 2017) was not adsorbed, but was from hydroxylated phases or fluid inclusions.

The amorphous fraction of Bagnold Dunes is 40 ± 15 wt% (Achilles et al., 2017; E. B. Rampe et al., 2018), yet its water content is markedly low compared to regions of high amorphous content observed along the traverse such as the silica-rich regions in the Murray and Stimson formations. The 'Lubango' target, an opal-rich fracture halo in the Stimson formation, for example, features an amorphous fraction of ∼73% and a corresponding water content of 4.0 ± 1.2 WEH (Rapin et al., 2018). This suggests a markedly different inventory and/or hydration state of amorphous phases in active sands. Since amorphous materials can range from water-poor glasses to water-rich products of aqueous alteration, we compute the range of possible phases present in Bagnold Dune sands to complement our understanding of the material as provided by mineralogy. The presence or absence of certain amorphous phases can also be used to help identify the source region for active dune sands in Gale crater.

2.2.1 Amorphous Material

Amorphous phases lack long-range crystallographic structure, so they do not produce a diagnostic set of peaks in powder X-ray diffraction (XRD) patterns, unlike minerals. X-ray amorphous phases produce broad 'humps' that can vary in breadth, position, and number according to chemical composition and the presence of

short-range crystallographic ordering. Bish et al. (2013) suggested basaltic glass and allophane were appropriate matches to the amorphous hump found in inactive dune sand at the Rocknest target. However, libraries of available X-ray amorphous phases to compare to CheMin data are not comprehensive. Ongoing work to build spectral libraries (Achilles et al., 2018) will broaden the catalogue of materials to be modeled in the future. Despite the current limitations in fitting the amorphous XRD hump, geochemical constraints of amorphous materials can be computed by subtracting the mineralogic contribution determined from CheMin XRD from bulk-rock geochemical abundances provided by Alpha Particle X-ray Spectroscopy (APXS) analysis. Using this method, Blake et al. (2013) and Achilles et al. (2017) identified candidate amorphous phases in the Rocknest (static dune sample) and Gobabeb targets respectively. However, a detailed assessment of the abundances of X-ray amorphous phases in Gale crater sands has not been performed until this study.

2.3 Methodology

We constrain the amorphous composition of Bagnold Dunes by combining two distinct methodologies: (1) active DAN analysis to determine the water content of the bulk subsurface dune material, and (2) amorphous phase analysis using a Monte Carlo method to determine the range of amorphous compositions that satisfy the geochemical constraints derived from APXS, CheMin, and DAN. First, we analyze neutron experiments at Ogunquit Beach (see map, Figure S2.1, in the Supplementary Materials) to determine the bulk water content of the dune by fitting modeled spectra to measured spectra using a Markov Chain Monte Carlo method. Since hydrous phases in Bagnold Dune sands are hosted predominantly in the amorphous fraction,

we translate the bulk water content into that of the amorphous fraction. Finally, we randomly-generate mixtures of 11 candidate amorphous phases and report those that satisfy all geochemical constraints on the amorphous fraction, including the DAN-derived water content.

2.3.1 DAN Measurements

DAN is located at the aft of the Curiosity rover and consists of a pulse neutron generator (PNG) and two He^3 detectors. In 'passive' mode, DAN detects neutrons produced in the Mars surface by cosmic-ray bombardment, at energies of 0.001 eV – 1 keV and 0.4 eV – 1 keV in the two He^3 detectors respectively. In 'active' mode, the PNG produces 14.1 MeV neutrons via the $^2\mathrm{D} + {}^3\mathrm{T} \rightarrow n\ (14.1\mathrm{MeV}) + {}^4\mathrm{He}\ (3.5 MeV)$ reaction, for a pulse duration of 1–2 μs/pulse. The detectors then measure the moderated neutron flux returning from the subsurface for a 0.1 second window after the pulse, divided into 64 log-normal time bins; the process is repeated for ∼12,000 pulses in a standard measurement, each result coadded to produce a smooth neutron response profile. A more in-depth description of the instrument is provided by Mitrofanov et al. (2012). The shapes of die-away curves depend on the abundance of subsurface elemental hydrogen and neutron absorbers (primarily Cl and Fe (e.g. Hardgrove et al., 2011; Sears, 1992)), the distribution of these elements in the DAN field-of-view (Mitrofanov et al., 2014), and subsurface bulk density (Mitrofanov et al., 2016). An active DAN surface footprint is ∼2 m in diameter and extends to a depth of ∼60 cm (Sanin et al., 2015). Thus, DAN complements APXS and the Chemistry and Camera (ChemCam) instrument, which are sensitive to depths of a few μm.

Active DAN experiments were performed at Mount Desert Island, a dune in

the Bagnold field that overlies bedrock of the Sutton Island member of the Murray formation. The rover was backed over the dune on sol 1659 and two ∼12,000 pulse measurements were performed with the instrument surface footprint encompassed completely by dune sand. The water content of the underlying bedrock, which is also in the DAN field-of-view, was unknown. We determined the water content of the bedrock using co-added data from experiments on sols 1669 and 1671 over a nearby Murray bedrock exposure (see Figure S2.2).

2.3.1.1 DAN Modeling and Input Parameters

DAN experiments are compared to the results of neutron transport models using the Monte Carlo N-Particle 6 code (MCNP6) developed by Los Alamos National Laboratory (McKinney et al., 2006; Pelowitz, 2008). We used an updated input file template, developed by Jun et al. (2013), that implements major rover components and the DAN instrument; the file was tested against pre-flight, calibration spectra generated at the Jet Propulsion Laboratory. In contrast, the methods of Sanin et al. (2015) do not include rover components, but instead only model an array (ring) of detectors above the Martian surface and corrections are applied to account for neutron scattering by the rover. The model employed herein is more computationally expensive since neutron-rover interactions are modeled explicitly and only one set of DAN detectors are modeled (reducing the speed at which the simulation reaches convergence); however, this methodology does not require correction factors.

We modeled the martian subsurface as two layers: a lower-density (1.6 g/cm^3) dune overlying higher density (1.8 g/cm^3) bedrock between 29 and 69 cm deep. We used measured abundances for the major rock-forming elements of both layers; the

lower layer composition sourced from the Sebina bedrock drill target, representative of the Sutton Island member, and the upper layer composition from the Gobabeb target (O'Connell-Cooper et al., 2017) (See Table S2.1). Oxide abundances were converted to elemental abundances, and then to isotopes using terrestrial abundances (Berglund and Wieser, 2011), as required by MCNP6. Implicit in this modeling setup is the assumption that the water content of both the bedrock and Bagnold Dune sand is homogeneously distributed and that both are well-represented by homogeneously-distributed Sebina and Gobabeb-like geochemistries. Our data-to-model comparison routine, which depends on uncertainty estimation using the MCMC method is described further in the Supplementary Materials (Foreman-Mackey et al., 2013).

2.3.2 Amorphous Phase Modeling

Amorphous phases used in the Monte Carlo model were selected based on FULLPAT analysis of amorphous materials in CheMin data from Ogunquit Beach (E. B. Rampe et al., 2018), the geochemistry of the X-ray amorphous component calculated from CheMin and APXS results (E. B. Rampe et al., 2018), and X-ray amorphous materials that are common in volcanic terrains on Earth. Basaltic glass, rhyolitic glasses, and ferrihydrite were selected because FULLPAT models of CheMin data from Ogunquit Beach suggest their presence in the sample. Furthermore, volcanic glasses are commonly found in subaerial volcanic rocks, and ferrihydrite is a common incipient weathering product of basalt. We used a Gusev basaltic glass composition (Filiberto et al., 2008) and a rhyolitic glass composition from a glass-bearing inclusion in the Chassigny meteorite (Varela et al., 2000). We assumed a purely Fe-bearing ferrihydrite composition (e.g., no Si substitution or adsorbed ionic complexes). Opal-A

was selected because it is a common weathering product in volcanic terrains (e.g. Black and Hynek, 2018; Ehlmann et al., 2012) and was identified on Mars from orbit and *in situ* within samples from Gale crater (Morris et al., 2016; E. B. Rampe et al., 2017; Yen et al., 2017) and Gusev crater (e.g. Ruff et al., 2011; Squyres et al., 2008). We assumed a purely Si-bearing opal-A. Hisingerite and allophane were selected (e.g. Burns, 1986; E. Rampe et al., 2012) they are common incipient weathering products in volcanic terrains, where hisingerite generally forms in mafic volcanic rocks (Whelan and Goldich, 1961) and allophane forms in glassy deposits (e.g. Wada, 1990). To account for the phosphorus in the amorphous component, amorphous Ca-phosphate was selected because of the observation of apatite in CheMin data from mudstone samples from the Murray formation (E. B. Rampe et al., 2017) and the precipitation of a Ca-phosphate phase in acid-sulfate alteration experiments to mimic the phosphate-rich martian soil Paso Robles (Hausrath et al., 2013). We selected Fe- and Mg-sulfates because SAM SO_2 release data indicate their presence in Ogunquit Beach (J. C. Stern et al., 2018). We assumed ferric, rather than ferrous, sulfate is present because of the observation of the crystalline ferric sulfate jarosite in some samples from the Murray formation (E. B. Rampe et al., 2017). We selected K- and Na-sulfate to account for K_2O and Na_2O in the amorphous component. We note that phosphate and sulfate can be chemisorbed onto nanophase weathering products (e.g. E. B. Rampe et al., 2016), but we assumed they were present as discrete phases.

2.3.3 Water Content of Amorphous Phases

Water contents for each phase were determined from thermogravimetric (TG) analyses under SAM-like instrument conditions (e.g., carrier gas, pressure, temperature

range, ramp rate) of synthetic amorphous phases or from values reported in the literature. Water contents for ferrihydrite, allophane, and hisingerite were 4 wt%, 6.5 wt%, and 2.6 wt%, respectively, as measured by TG of synthetic phases (E. B. Rampe et al., 2016); hisingerite data are from follow-on experiments from E. B. Rampe et al. (2016). SAM data from Ogunquit Beach and Gobabeb suggest Bagnold sands are nearly devoid of adsorbed water; as such, we used H_2O released from 300-850° C for the water contents for ferrihydrite, allophane, and hisingerite to exclude adsorbed water from our calculations (Sutter et al., 2017). We assumed 0.1 wt% H_2O in both the basaltic and rhyolitic glasses since the parent magma of martian meteorites have <0.3 wt% H_2O (Filiberto and Treiman, 2009). For opal-A, different water contents may be considered as it is known to vary significantly among opals. At Gale crater, opal was identified within silica-rich light-toned alteration halos, and with an average opal water content of 6.3 wt% determined from the hydrogen signal in the ChemCam instrument (Rapin et al., 2017a; Rapin et al., 2018). However, the SAM instrument yielded a water content of 1.1 ± 0.4 wt% for the same rock (Rapin et al., 2018). This difference is interpreted as an effect of sample grinding and preheating which significantly decreases the dehydration temperature of opal (Thomas et al., 2007). Therefore water content of opal in Bagnold dunes, being a loose powder transported and exposed to the atmosphere, is likely closer the SAM result; thus, we used 2.0 wt% H_2O for the opal-A, as computed from the SAM bulk water content as was similarly done in Rapin et al. (2018). We assumed 22 wt% H_2O in amorphous Mg-sulfate based on TG measurements of amorphous Mg-sulfate synthesized to investigate the fate of Mg-sulfate phases on Mars (Vaniman et al., 2004). We assumed 21.26 wt% H_2O in amorphous ferric sulfate based on TG measurements of synthetic amorphous ferric sulfate prepared by vacuum dehydration (Sklute et al., 2015), but the samples were

not allowed a similar amount of time to equilibrate in martian conditions as were those of Vaniman et al. (2004). We assumed K-sulfate, Na-sulfate, and Ca-phosphate were anhydrous because, although water can adsorb to the surfaces of crystalline K-sulfate and Na-sulfate (e.g. Balic-zunic et al., 2016; Herrero et al., 2015) and synthetic amorphous Ca-phosphate (e.g. Li et al., 2007), SAM data suggest active sands in Gale crater generally lack adsorbed water (J. C. Stern et al., 2018). The geochemical abundances of the modeled amorphous phases are summarized in Table S2.2.

2.4 Results

2.4.1 Bulk Dune Hydration Analysis

Our analysis of the underlying Murray bedrock indicates a bulk water content of 4.2 ± 0.51 WEH (1σ) (see Figure S2.4). This relatively high water content is due to the presence of clays (∼19 wt%), jarosite (∼0.9 wt%), and amorphous material (∼51 wt%) seen in the Sebina drill sample of the Murray (Bristow et al., 2018). Using this result to inform our two-layer models which feature the dune sand and underlying bedrock, we find a bulk water content of 0.68 ± 0.15 WEH (1σ) for the dune sand at Ogunquit Beach (see Figure 2.1), which agrees well with SAM results at the same location (0.8 ± 0.3 wt% H_2O). These results also agree with active DAN results during Bagnold phase 1 that found 0.8 WEH (no reported uncertainty) (Ehlmann et al., 2017) and SAM results at the same location (0.9 ± 0.3 wt% H_2O). The low water content of the dune compared to other unconsolidated sediments in Gale crater is also consistent with the hydrogen signal measured by ChemCam Laser-Induced Breakdown Spectroscopy experiments (LIBS) (see Figure S2.5) (Rapin et al., 2017b; Rapin et al.,

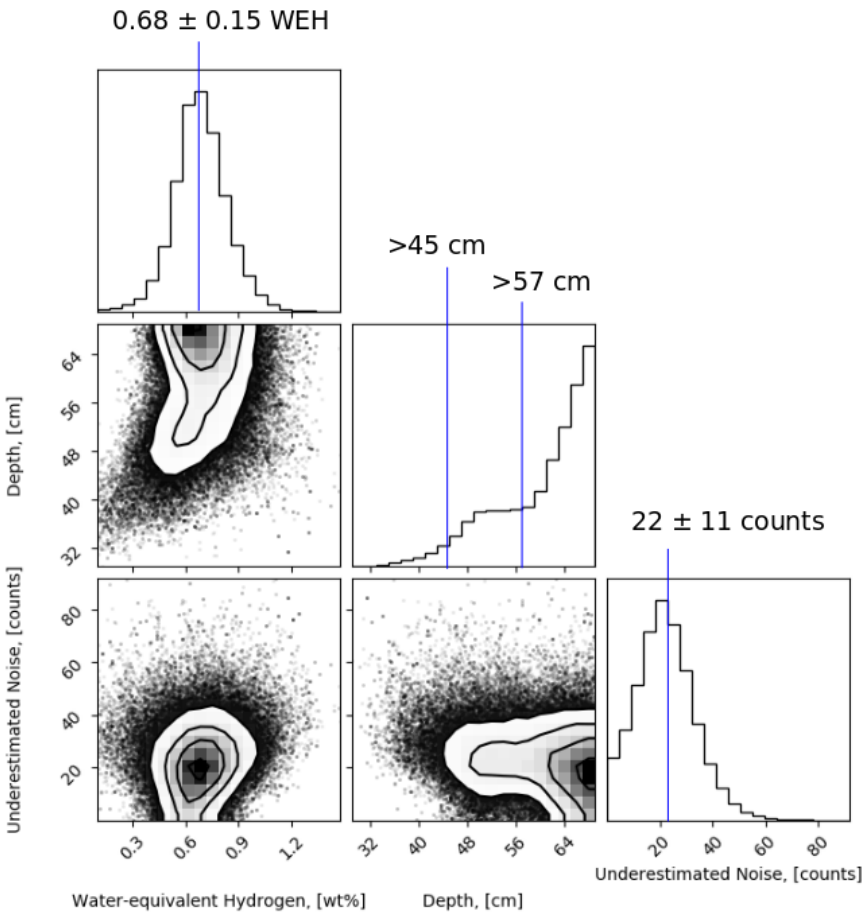

Figure 2.1. Shown are the *a posteriori* distributions of the fitted parameters determined from analysis of the active DAN experiment at Bagnold phase 2. The marginalized probability of parameters is projected into a histogram likelihood is shown as histograms along the diagonal. The mean and standard deviation of the water content of the top layer (dune) is 0.68 ± 0.15 WEH, and the underestimated uncertainty is f=22 ± 11 counts, with a correlation coefficient of 0.14 between the two parameters. Depths ≥57 cm encompass 68% of the likelihood (1σ) and depths of ≥45 cm encompass 95% (2σ).

2018). It shows qualitatively that active dunes measured during Bagnold phase 1 and 2 have the same hydration signature, lower than fine-grained soils encountered along the traverse (Cousin et al., 2014; Cousin et al., 2017; Forni et al., 2013).

2.4.2 Amorphous Component Analysis

To constrain the range of amorphous phases in the Bagnold Dunes, we perform a Monte Carlo procedure to randomly generate mixtures of 11 candidate amorphous phases. The geochemical abundances of each mixture are compared to measured abundances from CheMin XRD and APXS analysis determined for the amorphous fraction (O'Connell-Cooper et al., 2017; E. B. Rampe et al., 2018) (See Table S2.3 for the geochemical constraints). Figure 2.2 shows the range of models that fit all geochemical constraints (colored points), compared to those that do not fit the water content constraint (grey points). We find that the abundance of basaltic glass in the amorphous material is at least 23.9 wt%, but up to 64.0 wt%, with up to 23.7 wt% rhyolitic glass. Opal, allophane, hisingerite, and ferrihydrite can be present in the amorphous fraction up to 28.0 wt%, 10.6 wt%, 40.5 wt%, and 19.7 wt% respectively (see Figure 2.2.

We find the good-fit models constrained by geochemical abundances provided from APXS and CheMin experiments span a range ∼1.0–5.0 wt% H_2O. A smaller range of allowable water abundance is provided by the active DAN results herein. We first assume water is primarily in the amorphous fraction since hydrated crystalline minerals were below CheMin detection limits at Bagnold phase 1 (Achilles et al., 2017). The Ogunquit Beach sample is similarly devoid of hydrated crystalline phases; a ∼7 wt% phyllosilicate feature in the X-ray diffraction pattern is likely due to contamination from a previous sample (E. B. Rampe et al., 2018). The oxide abundance constraints for the amorphous fraction used herein have been renormalized to account for the contamination (E. B. Rampe et al., 2018). To translate our water abundance of the bulk into that of the amorphous material, we require an estimate of the amophous

fraction. The minimum abundance of X-ray amorphous material is 33 wt% at Ogunquit Beach (E. B. Rampe et al., 2018), as constrained from a combination of APXS and CheMin analysis. The maximum abundance is constrained by FULLPAT analysis of the X-ray amorphous hump and E. B. Rampe et al. (2018) finds a best fit value of 40 ± 15 wt%. Thus, at Ogunquit Beach, we assume the amorphous fraction ranges from 33 wt% (constrained by APXS & CheMin) to 55 wt% (constrained by CheMin FULLPAT analysis), with a mean of 44 wt%. This allows the water abundance measured in the *bulk* sand to be translated to the abundance of the amorphous fraction, (0.68 ± 0.15 WEH)/(44 ± 11 wt% (3σ)) = 1.55 ± 0.36 WEH (1σ). We note that decreasing the bulk density assumption of the dune sand in our MCNP6 models by 0.2 g/cm^3 produces best-fit water estimates that are ∼0.15 WEH lower.

2.5 Discussion

Active neutron experiments at Bagnold phase 1 (Ehlmann et al., 2017) indicated that Bagnold Dunes are depleted in water (∼0.8 WEH) compared to all materials examined by active neutron experiments in Gale Crater to-date (Litvak et al., 2016; Mitrofanov et al., 2014); however, Sutter et al. (2017, see supplementary material) reported a water content of 1.1 ± 0.5 WEH. The upper end of this range is similar to the abundance in bedrock targets reported therein and in Mitrofanov et al. (2014). Our results at Bagnold phase 2 confirm that Bagnold sands indeed contain depleted levels of water (0.68 ± 0.15 WEH). This is consistent with SAM EGA results at Bagnold phase 2 (0.8 ± 0.3 WEH) and with refinements of the Bagnold phase 1 measurements (0.9 ± 0.3 WEH) (J. C. Stern et al., 2018). ChemCam LIBS hydrogen peaks are also systematically lower for active dune sands than those of inactive

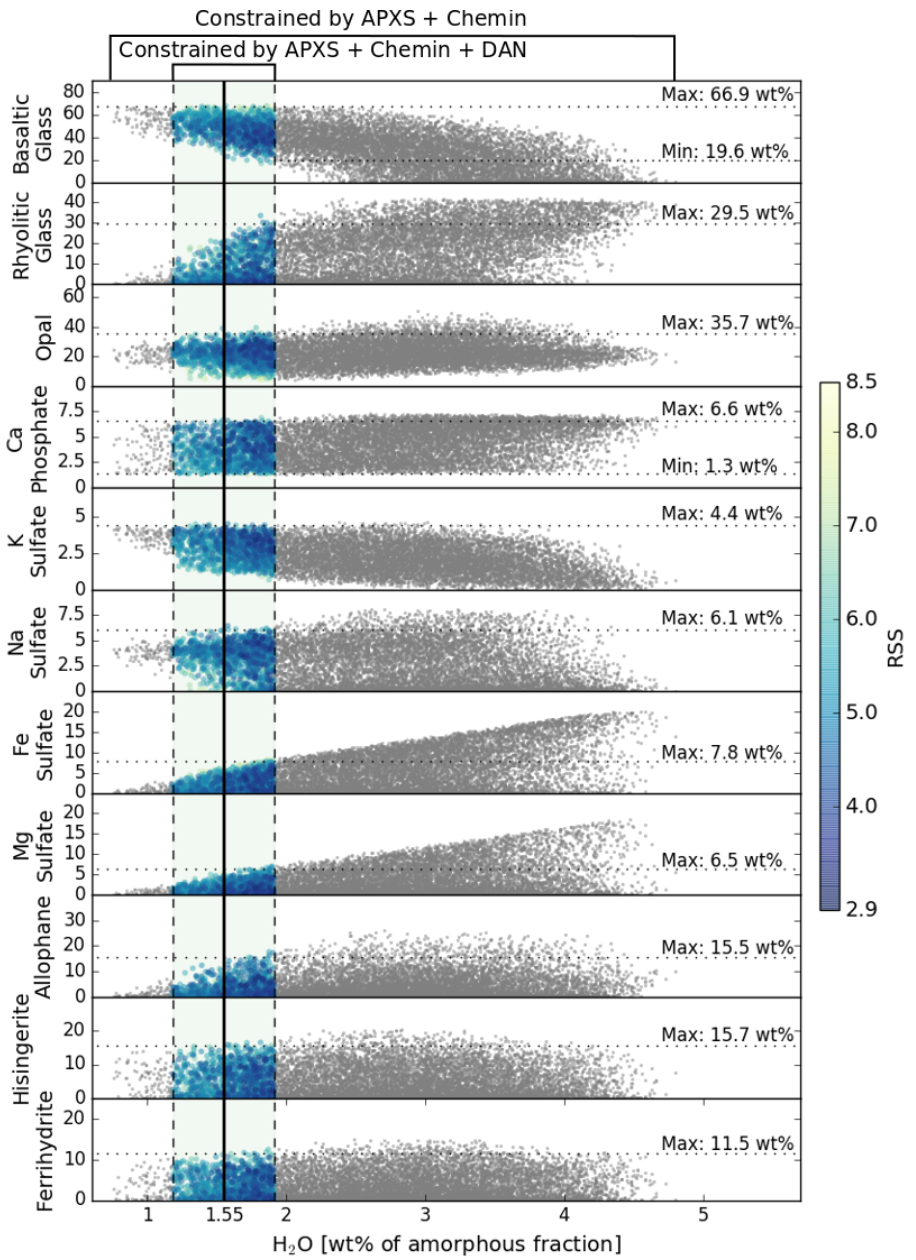

Figure 2.2. Shown are 10,000 randomly-generated models that satisfy oxide constraints on the amorphous fraction of Bagnold sands. Each model is represented by a single point in each panel. The y-axis is the abundance of a particular amorphous phase in wt% and the x axis is the water content of the models. The vertical dashed lines represent the allowed range of water content, as measured by DAN. Colors represent the root of the sum of squares of the deviations of the models from the target, or 'RSS.' Darker colors are models with lower deviations from oxide constraints. The reported minima and maxima are 3σ estimates computed using a bootstrap resampling (10^5 samples).

bedforms with a greater fraction of fine-grained components. Since the sensing area of active DAN experiments reaches to depths of ∼60 cm (Sanin et al., 2015) and SAM EGA experiments are sensitive to scooped samples from the dune surface, our results indicate the water distribution, or equivalently, the distribution of hydrated amorphous reservoirs, are likely homogeneous with depth. This finding suggests eolian activity efficiently mixes grains in the active dunes over time, potentially through the entirety of the dune body.

Since Bagnold Dune sands lack appreciable hydrated minerals (Achilles et al., 2017; E. B. Rampe et al., 2018), the amorphous fraction (44 ± 11 wt%) is the primary source of the measured water content. Water in Bagnold sands is suggested to be sourced from a coarse-grained ($\gtrapprox$150 μm), silica-rich reservoir with partially hydroxylated products of alteration, bound water/OH in glass, or both, in contrast to the source for inactive dunes: a fine-grained ($\lessapprox$150 μm), silica-poor reservoir with mostly loosely-bound and adsorbed water (Ehlmann et al., 2017). Indeed, SAM EGA experiments of Bagnold Dune sand find that the temperature of peak water release is at >300 °C (J. C. Stern et al., 2018; Sutter et al., 2017), which indicates an absence of significant amounts of adsorbed water. Thus, the water abundance derived for the amorphous content herein, 1.55 ± 0.36 WEH is an in-situ measurement of the water content in the coarse-grained reservoir.

Using constraints from the DAN analysis, in addition to constraints from CheMin (E. B. Rampe et al., 2018) and APXS (O'Connell-Cooper et al., 2018), we find basaltic glass composes at least 23.9 wt% of the amorphous fraction, necessitating a volcanic source for Bagnold Dune sand. Good-fit models (Figure 2.2) also allow for significant abundances of rhyolitic glass, opal, and hisingerite; however, these phases are the predominant carriers of silica which leads to model solutions consistent with

anticorrelated abundances of these phases. For example, as shown in Figure S2.6, models with high abundances of opal have correspondingly low abundances of rhyolitic glass (anticorrelation). However, opal is correlated with ferrihydrite to compensate for the losses in Fe in opal-rich geochemistries.

Our result is consistent with Achilles et al. (2017) that found the X-ray amorphous hump pattern can be modeled with a mixture of basaltic and rhyolitic glass; however, it is likely that hydrated phases are present, motivating the development of additional X-ray spectral libraries for amorphous materials. We find that each of the modeled sulfates are limited to abundances less than $\sim$7 wt% of the amorphous fraction, but their presence in good-fit models is consistent with SAM EGA experiments of the Ogunquit Beach sample that indicate the existence of these phases from high SO_2 release temperatures (500-800 ^{o}C) (J. C. Stern et al., 2018).

We predict the source region of Bagnold Dunes should contain water contents no less than 0.68 $\pm$ 0.15 wt% H_2O since Bagnold sands have had ample opportunity to equilibrate with the martian low vapor pressure atmosphere and thus are likely dehydrated with respect to their source. The presence of basaltic glass indicates that Bagnold sands include contributions from at least one volcanic source for the dune sand, but the presence of rhyolitic glass in good-fit models also indicates that Bagnold sands potentially include contributions from a silicic volcanic source. A single source for both volcanic glasses is also possible, however this would require eruptions of an evolving magmatic body. Products of aqueous alteration, namely opal, allophane, hisingerite, and ferrihydrite are also possible in appreciable abundances in Bagnold dunes. It is thus possible that aqueously-altered sediments contributed to the Bagnold Dune sand or that the sand was directly altered.

2.6 Conclusion

We find that hydrated phases in the Bagnold Dune Field are likely homogeneously distributed at depth and laterally, across kilometer scales. Specifically, we find the dune sand to have a bulk water content of 0.68 ± 0.15 WEH near Ogunquit Beach, which is consistent with similar active neutron measurements by the DAN instrument near Gobabeb (∼0.8 WEH) (Ehlmann et al., 2017), located several km north in the same dune field. SAM EGA experiments show that sand scooped from the dune surface has 0.8 ± 0.3 WEH at Ogunquit Beach and 0.9 ± 0.3 WEH at Gobabeb (J. C. Stern et al., 2018), which agrees well with our results. Considering that DAN is sensitive to the top ∼60 cm (Sanin et al., 2015) and that SAM is sensitive to the shallow, scooped dune material, we conclude that the distribution of water and the associated amorphous reservoirs are homogeneous throughout the Bagnold Dunes.

Since hydrated crystalline phases were not observed above CheMin detection limits and >90% of the water is bound (non-adsorbed) water (Achilles et al., 2018; Ehlmann et al., 2017; E. B. Rampe et al., 2018), the Bagnold Dune sands provide the unique opportunity to directly measure the hydration state of the bound water in the amorphous fraction. Using the DAN-derived water content, in addition to APXS and CheMin analysis, we constrained the maximum and minimum abundances of 11 candidate amorphous phases for Bagnold Dune sands. Specifically, we find that the Bagnold Dunes likely contain ∼11–28 wt% basaltic glass in the bulk. However, our results do not preclude the the possibility that the Bagnold Dunes contain material sourced from silica-rich volcanic complexes since the composition of rhyolitic glass can be in abundances of ∼0–10 wt% in the bulk. Future work will involve the fitting of these models to the amorphous 'hump' in XRD patterns to further constrain the

amorphous composition, testing the range of abundances derived. We conclude that the amorphous composition of the Bagnold Dune sand necessitates a complex history, that includes one or more volcanic sources. It is also possible that Bagnold Dune sand was directly altered or that aqueously-altered bedrock sediment contributed to the dune sand.

2.7 Supplementary Materials

This Supplementary Information includes two distinct materials: (1) a description of the data processing pipeline for active DAN measurements and (2) supporting figures and tables for the main manuscript. All data products for the DAN instrument used in the preparation of this manuscript are hosted publicly on the Planetary Data System (PDS) (www.pds.nasa.gov). Tools for preprocessing of binary data products to (raw) active DAN count data are also available as part of the PDS.

2.7.1 Active DAN Data Analysis

Measured data from the CTN and CETN detectors, $\mathbf{D}^{\mathrm{CTN}}$ and $\mathbf{D}^{\mathrm{CETN}}$ respectively, are compared to those provided by MCNP6 models of the experiment, $\mathbf{M}^{\mathrm{CTN}}$ and $\mathbf{M}^{\mathrm{CETN}}$ respectively. Using the Monte Carlo N-Particle 6 (MCNP6) transfer code, the DAN active experiment will be modeled several times, each model will vary some aspect of the geochemistry of the martian subsurface. Often the hydrogen content will be varied, while all other elemental abundances and rover components are kept constant. The abundance of other major rock-forming elements are sourced from APXS experiments (see Table S2.1). A set of models, with variable hydrogen and

other free parameters, are then compared to the measurement in order to find a 'best-fit' model (e.g. Mitrofanov et al., 2014; Sanin et al., 2015).

Unlike in the MCNP6 models for active DAN experiments, where the PNG is the only source of neutrons, the actual active DAN experiment on Mars is subject to background signal. This signal is due to both cosmic-ray bombardment that produces thermalized neutrons and the alpha decay of 238-plutonium from the Multi-Mission Radioisotope Thermoelectric Generator (MMRTG) which is the primary power source for the Curiosity Rover. This background signal is constant over the course of a ∼20-minute active DAN experiment and can be directly computed from neutron die-away curves by taking advantage of the design of the detector integration time (Sanin et al., 2015); after the decay of thermal neutrons returning from the subsurface after a single pulse, the detectors remain on for some time to detect the background signal. Although Sanin et al. (2015) describes the correction of background used herein, we outline these steps for completeness. Long after the peak arrival of thermalized neutrons, the DAN detectors continue integrating for a total time of 100,000 μs in 64 time bins. These late time bins can be used to compute a background count rate which can then be subtracted from the spectra (Sanin et al., 2015). Using the time bins from Sanin et al. (2015), b_i^{BG}=48 and b_f^{BG}=63 (counting from 1, with endpoints included), we first compute the total number of counts in late time bins in both detectors,

$$\begin{aligned} C_{\mathrm{BG}}^{\mathrm{CTN}} &= \sum_{b_i^{\mathrm{BG}}}^{b_f^{\mathrm{BG}}} \mathbf{D}^{\mathrm{CTN}} \\ C_{\mathrm{BG}}^{\mathrm{CETN}} &= \sum_{b_i^{\mathrm{BG}}}^{b_f^{\mathrm{BG}}} \mathbf{D}^{\mathrm{CETN}}, \end{aligned}$$

and divide the count number by the total elapsed time from bin 48 to 63, Δt_{BG} =

54278.7 μs,

$$\begin{aligned}\dot{C}_{\mathrm{BG}}^{\mathrm{CTN}} &= \frac{C_{\mathrm{BG}}^{\mathrm{CTN}}}{\Delta t_{\mathrm{BG}}} \\ \dot{C}_{\mathrm{BG}}^{\mathrm{CETN}} &= \frac{C_{\mathrm{BG}}^{\mathrm{CETN}}}{\Delta t_{\mathrm{BG}}}.\end{aligned}$$

The uncertainty in the background count rate is also computed,

$$\begin{aligned}\delta_{\mathrm{BG}}^{\mathrm{CTN}} &= \frac{1}{\Delta t_{\mathrm{BG}}}\sqrt{\sum_{b_i^{\mathrm{BG}}}^{b_f^{\mathrm{BG}}}\left(\delta_{\mathbf{D}^{\mathrm{CTN}}}\right)^2} \\ \delta_{\mathrm{BG}}^{\mathrm{CETN}} &= \frac{1}{\Delta t_{\mathrm{BG}}}\sqrt{\sum_{b_i^{\mathrm{BG}}}^{b_f^{\mathrm{BG}}}\left(\delta_{\mathbf{D}^{\mathrm{CETN}}}\right)^2},\end{aligned}$$

where $\delta_{\mathbf{D}}$ is the 1σ uncertainty in the DAN count data $\mathbf{D}$. We assume the count data follows the Poisson distribution, *i.e.* $\delta_{\mathbf{D}} = \sqrt{\mathbf{D}}$.

Then the contribution of background is removed from each bin according to the background count rate for the particular detector and the time elapsed in each bin, *i.e.* the width of the corresponding time bin,

$$\begin{aligned}\mathbf{D}'^{\mathrm{CTN}} &= \mathbf{D}^{\mathrm{CTN}} - \dot{C}_{\mathrm{BG}}^{\mathrm{CTN}}\Delta\mathbf{t} \\ \mathbf{D}'^{\mathrm{CETN}} &= \mathbf{D}^{\mathrm{CETN}} - \dot{C}_{\mathrm{BG}}^{\mathrm{CETN}}\Delta\mathbf{t}.\end{aligned}$$

The uncertainty in this computation is also propagated for each time bin,

$$\begin{aligned}\delta'_{\mathbf{D}^{\mathrm{CTN}}} &= \sqrt{\left(\delta_{\mathbf{D}^{\mathrm{CTN}}}\right)^2 + \left(\delta_{\mathrm{BG}}^{\mathrm{CTN}}\Delta\mathbf{t}\right)^2} \\ \delta'_{\mathbf{D}^{\mathrm{CETN}}} &= \sqrt{\left(\delta_{\mathbf{D}^{\mathrm{CETN}}}\right)^2 + \left(\delta_{\mathrm{BG}}^{\mathrm{CETN}}\Delta\mathbf{t}\right)^2}\end{aligned}$$

and the effect of background subtraction is demonstrated in Figure S2.3.

Since the overall shape of neutron die-away curves are indicative of subsurface geochemistry (Hardgrove et al., 2011) we compare the shape of die-away curves for the time bins that demonstrate the most dynamic range with respect to changing subsurface geochemistry (Sanin et al., 2015). The time bins used herein are similar to those in Sanin et al. (2015), b_i^{CTN}=18 and b_f^{CTN}=34 in the CTN detector, and b_i^{CETN}=13 and b_f^{CETN}=17 in the CETN detector (counting from 1). We first normalize the MCNP6 count tally data to that of the DAN data in the time bins of interest, effectively translating the model tally data into count space. First, we compute a sum of the detector data separately for both detectors,

$$\begin{aligned} U^{\mathrm{CTN}} &= \sum_{b_i^{\mathrm{CTN}}}^{b_f^{\mathrm{CTN}}} \mathbf{D}'^{\mathrm{CTN}} \\ U^{\mathrm{CETN}} &= \sum_{b_i^{\mathrm{CETN}}}^{b_f^{\mathrm{CETN}}} \mathbf{D}'^{\mathrm{CETN}}. \end{aligned}$$

The uncertainty of the sum is also computed,

$$\begin{aligned} \delta_{U^{\mathrm{CTN}}} &= \sqrt{\sum_{b_i^{\mathrm{CTN}}}^{b_f^{\mathrm{CTN}}} \left(\delta'_{\mathbf{D}^{\mathrm{CTN}}}\right)^2} \\ \delta_{U^{\mathrm{CETN}}} &= \sqrt{\sum_{b_i^{\mathrm{CETN}}}^{b_f^{\mathrm{CETN}}} \left(\delta'_{\mathbf{D}^{\mathrm{CETN}}}\right)^2}. \end{aligned}$$

Then, we compute the same sum of the *model* data, separately for both detectors,

$$V^{\mathrm{CTN}} = \sum_{b_i^{\mathrm{CTN}}}^{b_f^{\mathrm{CTN}}} \mathbf{M}^{\mathrm{CTN}}$$

$$V^{\mathrm{CETN}} = \sum_{b_i^{\mathrm{CETN}}}^{b_f^{\mathrm{CETN}}} \mathbf{M}^{\mathrm{CETN}}.$$

The uncertainty of the sum is also computed,

$$\delta_{V^{\mathrm{CTN}}} = \sqrt{\sum_{b_i^{\mathrm{CTN}}}^{b_f^{\mathrm{CTN}}} \left(\delta_{\mathbf{M}^{\mathrm{CTN}}}\right)^2}$$
$$\delta_{V^{\mathrm{CETN}}} = \sqrt{\sum_{b_i^{\mathrm{CETN}}}^{b_f^{\mathrm{CETN}}} \left(\delta_{\mathbf{M}^{\mathrm{CETN}}}\right)^2}.$$

By dividing both sums, U and V, we arrive at the conversion factor X that converts tally data to count space,

$$X^{\mathrm{CTN}} = \frac{U^{\mathrm{CTN}}}{V^{\mathrm{CTN}}},$$
$$X^{\mathrm{CETN}} = \frac{U^{\mathrm{CETN}}}{V^{\mathrm{CETN}}},$$

with error propagated as such:

$$\delta_{X^{\mathrm{CTN}}} = \frac{U^{\mathrm{CTN}}}{V^{\mathrm{CTN}}} \sqrt{\left(\frac{\delta_{U^{\mathrm{CTN}}}}{U^{\mathrm{CTN}}}\right)^2 + \left(\frac{\delta_{V^{\mathrm{CTN}}}}{V^{\mathrm{CTN}}}\right)^2}$$
$$\delta_{X^{\mathrm{CETN}}} = \frac{U^{\mathrm{CETN}}}{V^{\mathrm{CETN}}} \sqrt{\left(\frac{\delta_{U^{\mathrm{CETN}}}}{U^{\mathrm{CETN}}}\right)^2 + \left(\frac{\delta_{V^{\mathrm{CETN}}}}{V^{\mathrm{CETN}}}\right)^2}.$$

Then the tally data from MCNP6 models are normalized,

$$\mathbf{M}'^{\mathrm{CTN}} = \mathbf{M}^{\mathrm{CTN}} X^{\mathrm{CTN}}$$
$$\mathbf{M}'^{\mathrm{CETN}} = \mathbf{M}^{\mathrm{CETN}} X^{\mathrm{CETN}}$$

and the error is propagated,

$$\begin{aligned}
\delta'^{\mathrm{CTN}}_{\mathbf{M}} &= \mathbf{M}^{\mathrm{CTN}} X^{\mathrm{CTN}} \sqrt{\left(\frac{\delta_{\mathbf{M}^{\mathrm{CTN}}}}{\mathbf{M}^{\mathrm{CTN}}}\right)^2 + \left(\frac{\delta_{X^{\mathrm{CTN}}}}{X^{\mathrm{CTN}}}\right)^2} \\
\delta'^{\mathrm{CETN}}_{\mathbf{M}} &= \mathbf{M}^{\mathrm{CETN}} X^{\mathrm{CETN}} \sqrt{\left(\frac{\delta_{\mathbf{M}^{\mathrm{CETN}}}}{\mathbf{M}^{\mathrm{CETN}}}\right)^2 + \left(\frac{\delta_{X^{\mathrm{CETN}}}}{X^{\mathrm{CETN}}}\right)^2}.
\end{aligned}$$

At this point, the normalized model data, $\mathbf{M}'$, can be compared to background subtracted data, $\mathbf{D}'$, from an active DAN experiment.

Instead of minimizing the χ^2 parameter as a means of finding a best-fit model, as is performed in Mitrofanov et al. (2014) and Sanin et al. (2015), we employ a Markov Chain Monte Carlo (MCMC) method (Foreman-Mackey et al., 2013) to maximize the likelihood function, or more specifically minimize the negative log of the likelihood function:

$$\mathcal{L} = -\frac{1}{2}\sum_{i}^{N}\left(\frac{(C_i - \mathcal{M}_i(p_0, p_1, ..., p_N)}{\sigma_i^2} + ln(2\pi\sigma_i^2)\right),$$

where C_i is the measurement data, $\mathcal{M}_i$ an interpolant of the modeled data as a function of the free parameters, *e.g.* H abundance, and the sum is taken over the range of time bins in the CTN detector shown in Figure S2.2. We have found that the CETN detector is not diagnostic, *i.e.* lacks dynamic range over the parameters of this study, and thus it is excluded from this analysis. The variance of the data and the model in each time bin is captured by the σ_i^2 term,

$$\sigma_i^2 = \delta C_i^2 + \delta\mathcal{M}_i^2(p_0, p_1, ..., p_N) + f^2,$$

where δC_i is the uncertainty of DAN data and $\delta\mathcal{M}_i$ is the uncertainty in the modeled

spectra. Our MCNP6 models simulate 2.5e9 particles which provides <<5% relative error in modeled spectra for the time bins of interest. We conservatively set $\delta\mathcal{M}_i$ to be a constant 5% relative error. A new free parameter has been introduced, f, which represents the underestimation of the count uncertainty. Larger values of this parameter indicate either poor statistical convergence in the model, poor statistical convergence in the measurement, and/or a poor overall fit of the model to the data, *i.e.* inaccurate model assumptions; however, in our study we find reasonable values of f, *i.e.* f is less than a few percent of the counts in DAN spectra. In sum, the MCMC routine will find the combination of hydrogen abundance and other free parameters, *e.g.* depth, that best fits the observed spectra, while also accounting for underestimated uncertainties.

The computational resources to generate a synthetic model of active DAN spectra using the MCNP6 code is not insignificant, on the order of several hours per model on ∼100 core compute clusters and on the order of days on modern desktops. Thus the generation of model data cannot occur 'in line' with the MCMC routine, but rather a 'grid' of models are generated beforehand. A model grid is composed of models that vary the free parameters, $p_0, p_1, ..., p_N$, to discrete values for which we are trying to find a non-discrete 'best-fit' value of the free parameters. In the case of DAN, examples of free parameters include hydrogen content, depth of a geochemically-distinct top layer, bulk density, etc. In the analysis to determine the water content of the local (Murray formation) bedrock performed herein, we allowed only hydrogen content to vary, from 1 WEH to 6 WEH in increments of 0.2 WEH.

Once a model grid is simulated, an interpolant is generated, $\mathcal{M}(p_0, p_1, ..., p_N)$, which allows the MCMC routine to produce modeled active DAN spectra at non-discrete parameter values. We choose to employ a linear interpolant, which assumes

the behavior of the count rate as a function of the free parameter is linear, for a given bin, between discrete increments of the parameters. This assumption is appropriate when the free parameters have sufficient resolution; we find a resolution of 0.2-0.4 WEH is an appropriate sampling resolution for bulk water content and 5-10 cm is an appropriate sampling resolution for depth.

Before comparing the model grid to data, the MCMC routine requires an *a priori* 'guess' of the free parameters for each walker. We found the results of this study are rather insensitive to the initial conditions, provided the MCMC routine is allowed sufficient iterations. The *a priori* (mean and 1 standard deviation) for the water content of the bedrock in the homogeneous model was 3.0 $\pm$ 0.3 WEH. For the two-layer models, the *a priori* for the dune hydrogen was 1.0 $\pm$ 0.3 WEH and the *a priori* for the depth was 40 $\pm$ 10 cm. In both cases the *a priori* for the parameter f was 40 $\pm$ 10 counts. We simulated $8N_p$ walkers, where N_p is the number of free parameters; $N_p = 1$ in the case of the bedrock model analysis (variable hydrogen in a single layer) and $N_p = 2$ in the case of the dune analysis (variable hydrogen in the top layer, variable thickness of the top layer). We allowed the walkers to perform 10,000 steps (iterations) in the parameter space before the routine is halted. The mean and standard deviation of the free parameters are determined using the last 9,000 positions of each of the $8N_p$ walkers. The *a posteriori* distribution of the free parameters, which is composed of the 9,000 walker positions, is shown in a series of projections in Figures 1 and S4.

2.7.2 Supplementary Tables

Table S2.1. Shown are the H-free elemental abundances[a] in wt% for drill targets. Values were converted from oxide abundances provided by APXS experiments of drill tailing piles. The geochemistries of active dune sands are within 2 standard deviations in macroscopic absorption cross section, resulting in similar signatures in DAN spectra. Compositions were renormalized to include the water content of the simulation.

	Drill Sites			
Element	*Sebina*	*Gobabeb* Dump Pile B	*Ogunquit Beach*	σ_{abs} [barns][b]
Cl	1.06	0.498	0.530	33.5
Mn	0.124	0.333	0.318	13.3
Br	0.0104	0.00810	0.00310	6.90
Ti	0.659	0.408	0.558	6.10
Ni	0.102	0.0696	0.0488	4.49
Cr	0.205	0.166	0.349	3.05
Fe	14.2	15.4	15.3	2.56
K	0.689	0.334	0.382	2.10
Zn	0.0814	0.0152	0.0241	1.11
Na	1.49	1.28	1.91	0.53
S	3.66	1.17	1.38	0.53
Ca	5.10	4.77	5.15	0.43
Al	4.59	4.17	4.98	0.231
P	0.266	0.343	0.327	0.172
Si	21.6	21.6	21.1	0.171
Mg	2.56	6.93	5.30	0.063
O (remainder)[c]	43.6	42.5	42.340	0.00019

[a] Isotopic abundances of each element, required for the MCNP6 input file, are computed assuming terrestrial abundances (Berglund and Wieser, 2011).

[b] σ_{abs} is the absorption cross section of an element (assuming terrestrial isotopic abundances) and is provided by Sears (1992) for 2,200 m/s neutrons.

[c] Since APXS provides all major rock-forming elements, we assume the remaining species is oxygen.

Table S2.2. Shown are the amorphous phases used in the modeling herein and their associated geochemical abundances in wt%. The chemical formula represents the dehydrated form of each phase from which the water-free abundances were computed. The abundances of each phase are renormalized to account for the water content listed in the last column.

Amorphous phase	Formula	SiO_2	TiO_2	Al_2O_3	FeO_T	MnO	MgO	CaO	Na_2O	K_2O	P_2O_5	SO_3	H_2O
Basaltic glass[a]	N/A	46.91	0.56	10.92	19.21	0.42	10.64	8.01	2.56	0.10	0.57	-	0.10[c]
Rhyolitic glass[b]	N/A	71.06	0.30	16.87	1.02	-	-	0.34	8.38	1.94	-	-	0.10[c]
Opal	SiO_2	98.50	-	-	-	-	-	-	-	-	-	-	2.0[d]
Ca phosphate	$Ca_3(PO_4)_2$	-	-	-	-	-	-	54.24	-	-	45.76	-	-
K sulfate	K_2SO_4	-	-	-	-	-	-	-	-	54.06	-	45.94	-
Na sulfate	Na_2SO_4	-	-	-	-	-	-	-	43.64	-	-	56.36	-
Fe sulfate	$Fe_2(SO_4)_3$	-	-	-	31.44	-	-	-	-	-	-	47.29	21.27
Mg sulfate	$MgSO_4$	-	-	-	-	-	26.12	-	-	-	-	51.88	22.00
Allophane	$Al_2O_3(SiO_2)_{1.5}$	49.63	-	43.87	-	-	-	-	-	-	-	-	6.50[e]
Hisingerite	$Fe_2O_3SiO_2$	26.63	-	-	70.77	-	-	-	-	-	-	-	2.60[f]
Ferrihydrite	Fe_2O_3	-	-	-	96.00	-	-	-	-	-	-	-	4.00[e]

[a] Water-free abundances sourced from Filiberto et al. (2008) [b] Water-free abundances sourced from Varela et al. (2000) [c] Water abundance sourced from Filiberto and Treiman (2009) that estimated parent magmas of martian meteorites to have <0.3 wt% H_2O [d] Water abundance computed from bulk water content reported by *in situ* EGA experiments of primarily opaline material in Gale crater (Rapin et al., 2018) [e] Water abundance sourced from E. B. Rampe et al. (2016) [f] Water abundance sourced from follow-on experiments from E. B. Rampe et al. (2016)

Table S2.3. Shown are the Cl- and Cr-free oxide abundances estimated for the amorphous component of the *Ogunquit Beach* sand[a]. Compositions were calculated for the minimum, 33 wt%, and maximum, 55 wt%, estimates of the X-ray amorphous material in the sample (E. B. Rampe et al., 2018). Deriving geochemical abundances for the amorphous fraction requires assumptions about the geochemistry of crystalline phases, *e.g.* assuming an Mg content of pyroxene, and an assumption on the amorphous fraction, *e.g.* assuming amorphous material composes 33 wt% of the bulk (e.g. E. B. Rampe et al., 2018). However, we do not attempt to address the effects of varying the former, but reserve that for future study. As such, the range of abundances reported in the table represent the minimum range of oxide abundances. To account for this, 'good fit' models fall within 2 times the range of the oxides reported for the minimum and maximum amorphous fraction assumptions (*e.g.*, the SiO_2 range is 43.58 wt% – 49.63 wt%). These constraints are not applied to Mn and Ti since olivine and pyroxene compositions, reported as Fe-Mg and Fe-Mg-Ca solid solutions in E. B. Rampe et al. (2018), do not account for the presence of trace elements possible in the mineral structures. Furthermore, minerals in abundance of <1 wt% are below the CheMin instrument detection limit. Thus, trace elements in major crystalline phases and those comprising undetectable crystalline phases are included in the calculated amorphous composition.

	Amorphous fraction	
Oxide	33 %	55 %
SiO_2	**46.00**	47.21
TiO_2	2.90	**1.73**
Al_2O_3	**5.10**	8.38
FeO	25.80	**20.86**
MnO	1.12	**0.67**
MgO	**0.00**	4.58
CaO	**4.06**	5.96
Na_2O	3.02	**2.94**
K_2O	1.84	**1.09**
P_2O_5	2.37	**1.41**
SO_3	7.78	**5.18**

[a] Crystalline phase compositions are reported in (E. B. Rampe et al., 2018).

2.7.3 Supplementary Figures

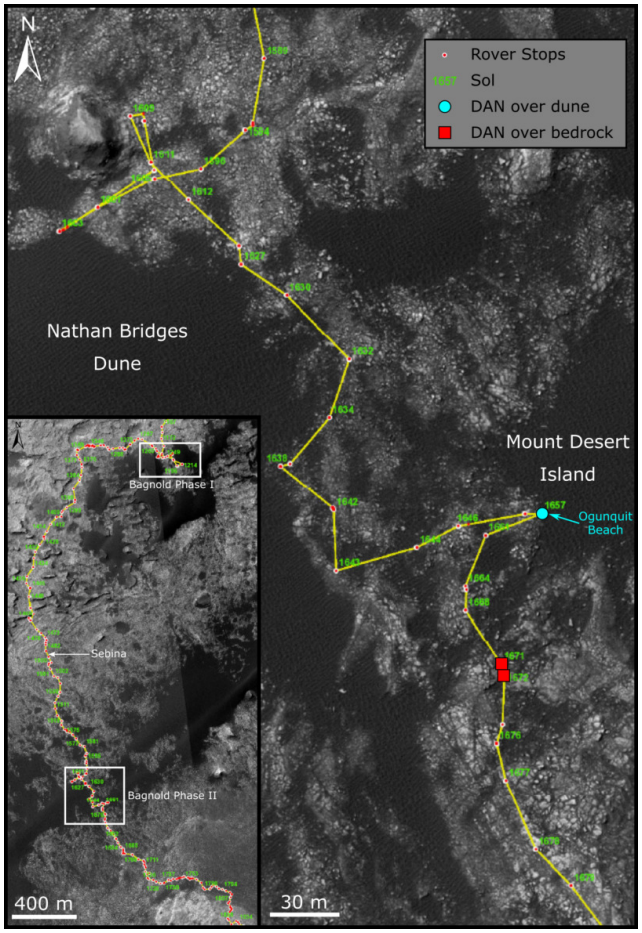

Figure S2.1. Shown is a map of the Bagnold campaign; dark material is part of the larger Bagnold Dunes. The active DAN dune measurement at Mount Desert Island is shown as a blue circle; this is the location of the *Ogunquit Beach* target. Locations of DAN measurements used to determine the water abundance of the local bedrock are shown as red squares. The inset shows phase 1 in context with phase 2 and the *Sebina* drill target. Rover stops and associated sols are shown as red circles and green text respectively.

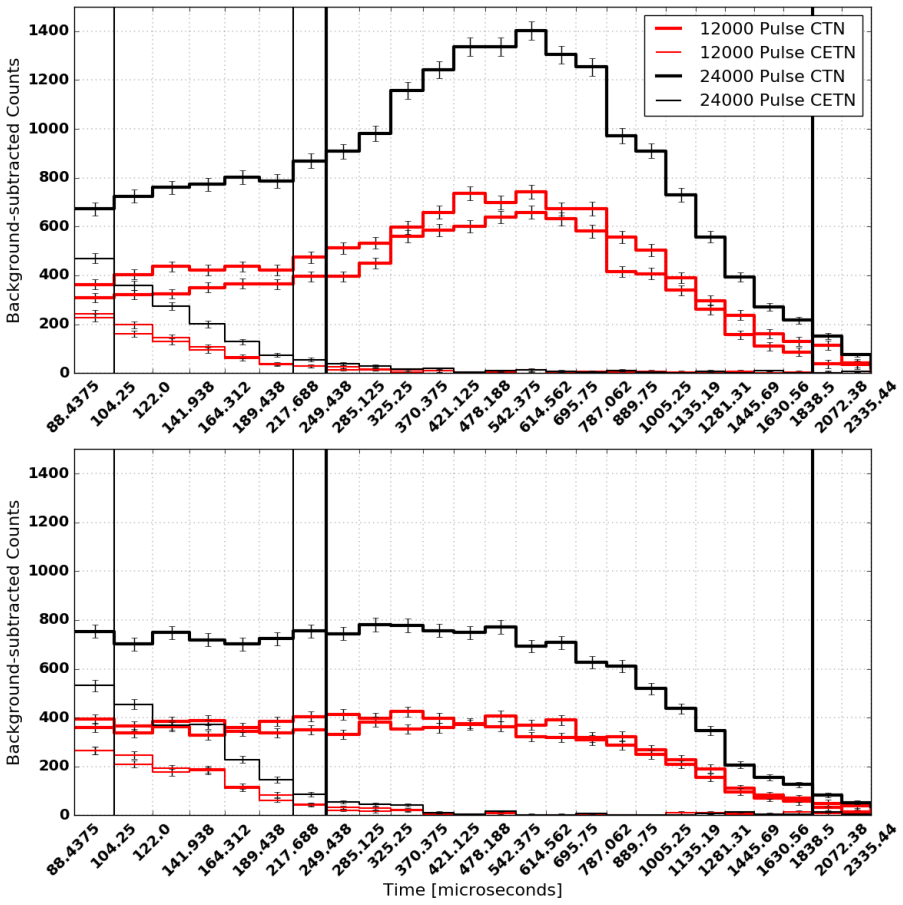

Figure S2.2. Shown are plots of background-subtracted active DAN data. Thin and thick lines represent data from the CETN and CTN detector, respectively. (Top) Neutron die-away curves from bedrock measurements at the same location on sols 1669 and 1671 (red lines) were coadded to produce a more statistically converged curve (black lines). (Bottom) The same coadding process was performed for the two dune measurements at Mount Desert Island on sol 1659. The peak of thermal neutrons in the CTN detector for the off-dune measurement (top) is not featured in the on-dune measurement (bottom), indicating the on-dune measurement detected less H. The thin and thick vertical lines mark the bounds of the time bin ranges used in data-to-model comparative analyses of the CETN and CTN detectors, respectively.

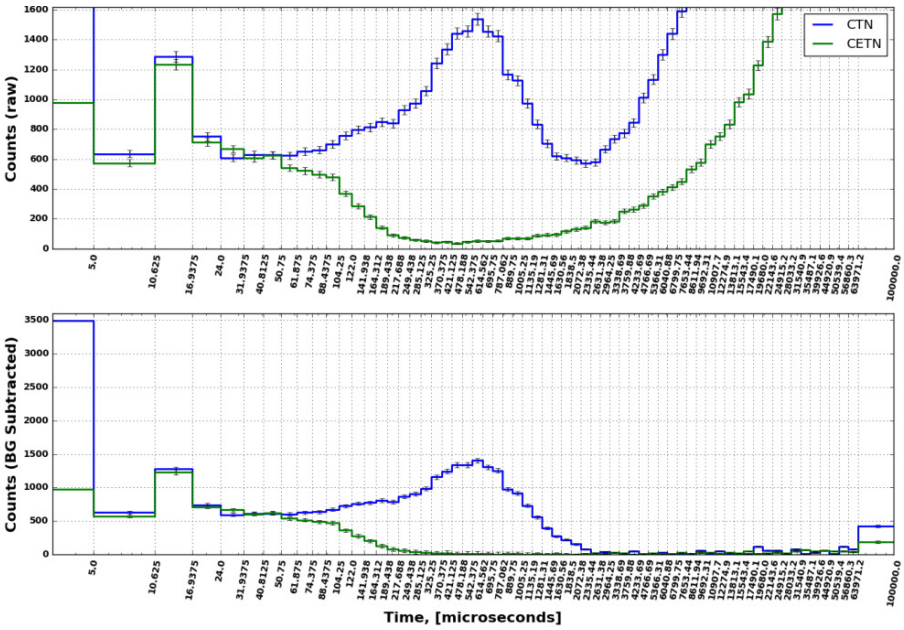

Figure S2.3. Shown are raw DAN die-away data (top) and background subtracted die-away data (bottom) for the coadded data from sol 1669 and 1671. Early-arriving neutrons are directly scattered from the rover body and are not diagnostic of subsurface geochemistry (Mitrofanov et al., 2014; Sanin et al., 2015). Late-arriving neutrons are successfully removed through the background subtraction procedure (bottom).

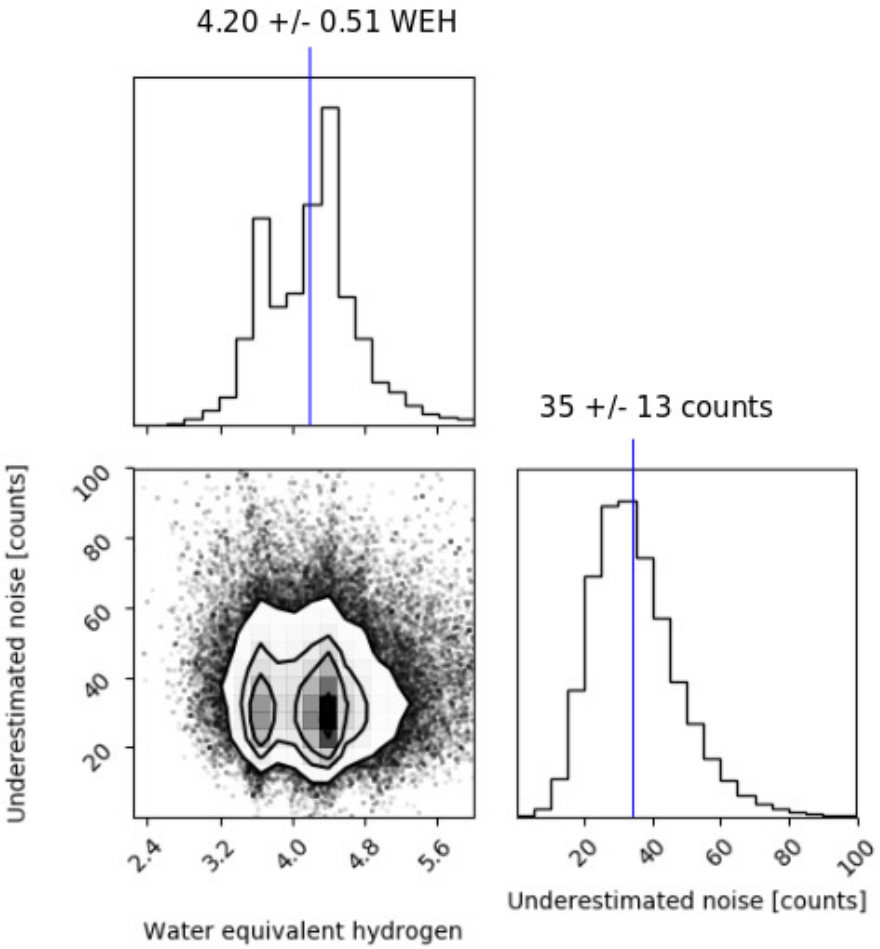

Figure S2.4. Shown are the *a posteriori* distributions of the fitted parameters determined from models of a homogeneous *Sebina* (Murray) composition. The marginalized distributions are projected as histograms along the diagonal. The mean and standard deviation of the hydrogen content is 4.20 ± 0.51 WEH and f=35 ± 13 counts, with a correlation coefficient of 0.03 between the two parameters.

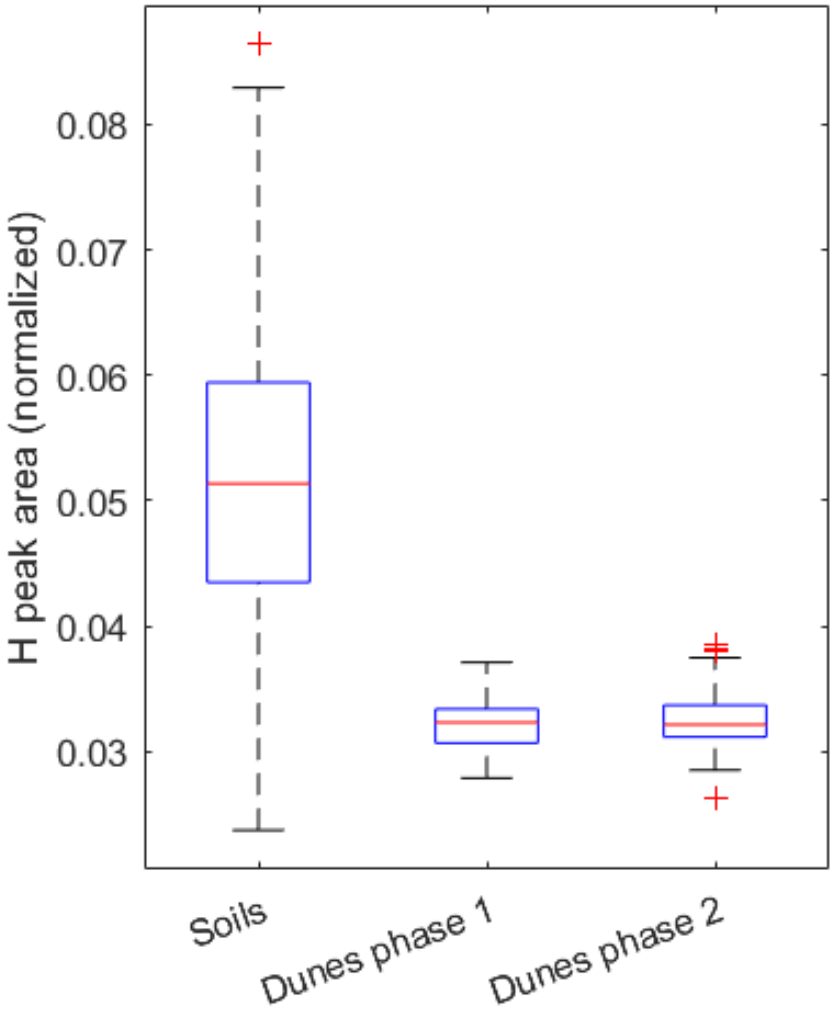

Figure S2.5. Distribution of the ChemCam hydrogen peak area (Normalized to O peak area at 778 nm) (Rapin et al., 2017a) for the soils and dune materials. Soils refers fine-grained soils analyzed using the "blind target mode" (Cousin et al., 2017). Dunes phase 1 and phase 2 correspond to all Laser Induced Breakdown Spectroscopy data obtained on Bagnold Dune sand in the phase 1 and phase 2 campaigns. Due to a number of points obtained with a poor laser focus, a threshold was applied to remove spectra with low intensity. Cousin et al. (2017) showed similar results on the hydrogen signal using the hydrogen ICA score (Forni et al., 2013) and here we extend the result to the Bagnold Dunes phase 2 measurements using the hydrogen peak fitting method.

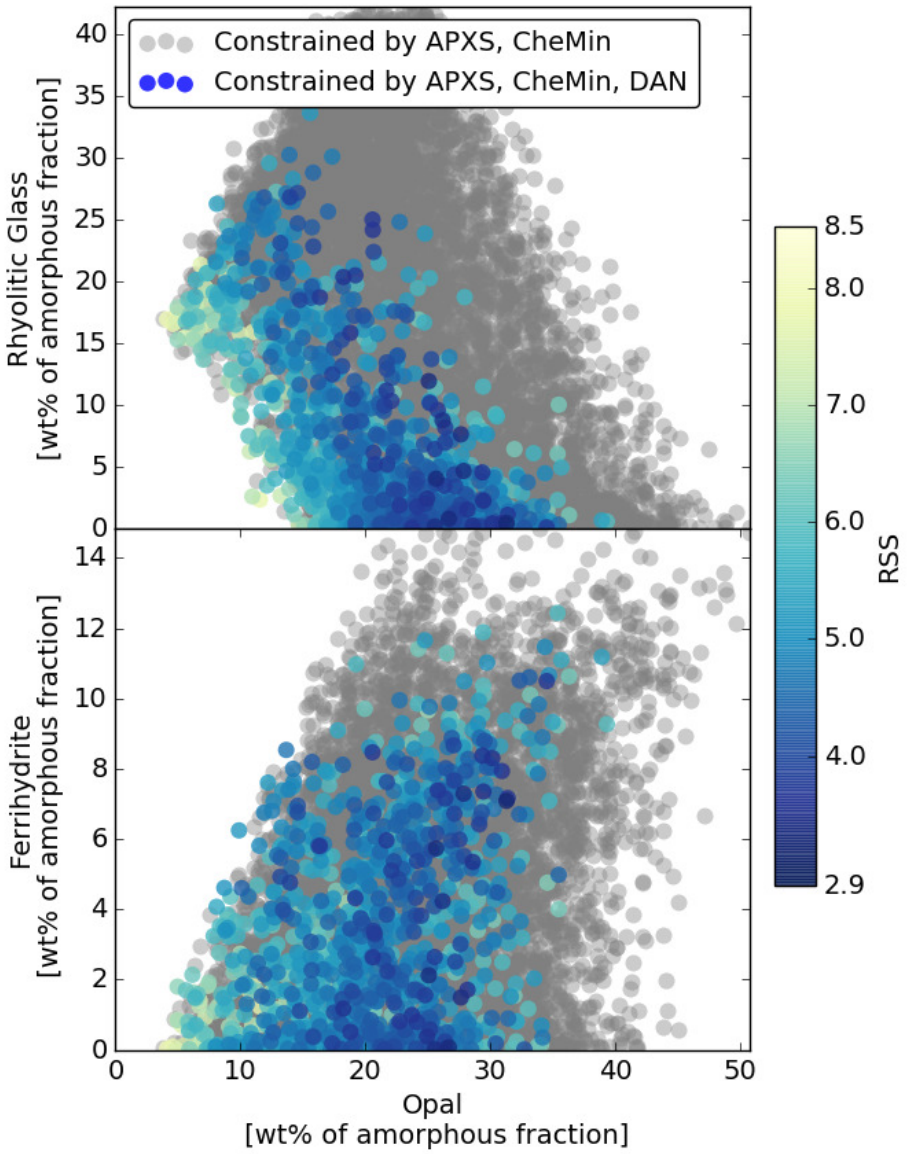

Figure S2.6. Shown are abundances of opal and rhyolitic glass (top), as well as opal and ferrihydrite (bottom) for the 10,000 amorphous composition models shown in Figure 2. Grey points represent models that do not fit the DAN-derived water abundance of the amorphous fraction and colored points represent models that all constraints. Opal and rhyolitic glass are shown to be anticorrelated whereas opal and ferrihydrite are correlated.

2.8 Acknowledgments

We acknowledge the Dynamic Albedo of Neutrons instrument team and the broader Mars Science Laboratory team. This work was supported by the Mars Science Laboratory Participating Scientist Program, award number NNN12AA01C, and by the NASA Earth and Space Exploration Fellowship, award number PLANET17F-0107. Computational support was provided in part by the Space Science and Applications group at Los Alamos National Laboratory and by the Research Computing center at Arizona State University. The authors thank Michael Line at Arizona State University for providing insight into statistical methods used herein. All data from this work is publicly accessible on the Planetary Data System, www.pds.nasa.gov.

References

Achilles, C. N. et al. (Nov. 2017). Mineralogy of an active eolian sediment from the Namib dune, Gale crater, Mars. *Journal of Geophysical Research: Planets* 122, pp. 2344–2361.

Achilles, C. N. et al. (Mar. 2018). Amorphous Phase Characterization Through X-Ray Diffraction Profile Modeling: Implications for Amorphous Phases in Gale Crater Rocks and Soils. *Lunar and Planetary Science Conference*. 49. Lunar and Planetary Inst. Technical Report, p. 2661.

Balic-zunic, T., R. Birkedal, A. Katerinopoulou, and P. Comodi (Mar. 2016). Dehydration of blödite, Na2Mg(SO4)2(H2O)4, and leonite, K2 Mg(SO4)2(H2O)4. *European Journal of Mineralogy* 28 (1), pp. 33–42.

Berglund, M. and M. E. Wieser (2011). Isotopic compositions of the elements 2009 (IUPAC Technical Report). *Pure and Applied Chemistry* 83 (2), pp. 397–410.

Bish, D. L. et al. (Nov. 2013). X-ray Diffraction Results from Mars Science Laboratory: Mineralogy of Rocknest at Gale Crater. *Science* 341, 1238932, p. 1238932.

Black, S. R. and B. M. Hynek (June 2018). Characterization of terrestrial hydrothermal alteration products with Mars analog instrumentation: Implications for current and future rover investigations. *Icarus* 307, pp. 235–259.

Blake, D. F. et al. (Sept. 2013). Curiosity at Gale Crater, Mars: Characterization and Analysis of the Rocknest Sand Shadow. *Science* 341, 1239505, p. 1239505.

Bridges, N. T. and B. L. Ehlmann (2017). The Mars Science Laboratory (MSL) Bagnold Dunes Campaign, Phase I: Overview and introduction to the special issue. *Journal of Geophysical Research: Planets* 123 (1), pp. 3–19.

Bridges, N. T. et al. (2014). The rock abrasion record at Gale Crater: Mars Science Laboratory results from Bradbury Landing to Rocknest. *Journal of Geophysical Research: Planets* 119 (6), pp. 1374–1389.

Bristow, T. F. et al. (2018). Clay mineral diversity and abundance in sedimentary rocks of Gale crater, Mars. *Science Advances* 4 (6).

Burns, R. G. (Mar. 1986). Terrestrial analogues of the surface rocks of Mars? *Nature* 320, p. 55.

Cousin, A. et al. (Mar. 2014). ChemCam Blind Targets: A Helpful way of Analyzing Soils and Rocks Along the Traverse. *Lunar and Planetary Science Conference*. 45. Lunar and Planetary Inst. Technical Report, p. 1278.

Cousin, A. et al. (Oct. 2017). Geochemistry of the Bagnold dune field as observed by ChemCam and comparison with other aeolian deposits at Gale Crater. *Journal of Geophysical Research: Planets* 122, pp. 2144–2162.

Ehlmann, B. L., D. L. Bish, S. W. Ruff, and J. F. Mustard (Oct. 2012). Mineralogy and chemistry of altered Icelandic basalts: Application to clay mineral detection and understanding aqueous environments on Mars. *Journal of Geophysical Research: Planets* 117, E00J16, E00J16.

Ehlmann, B. L. et al. (2017). Chemistry, mineralogy, and grain properties at Namib and High dunes, Bagnold dune field, Gale crater, Mars: A synthesis of Curiosity rover observations. *Journal of Geophysical Research: Planets* 122 (12), pp. 2510–2543.

Filiberto, J., A. H. Treiman, and L. Le (Oct. 2008). Crystallization experiments on a Gusev Adirondack basalt composition. *Meteoritics and Planetary Science* 43, pp. 1137–1146.

Filiberto, J. and A. H. Treiman (2009). Martian magmas contained abundant chlorine, but little water. *Geology* 37 (12), p. 1087.

Foreman-Mackey, D., D. W. Hogg, D. Lang, and J. Goodman (Mar. 2013). emcee: The MCMC Hammer. *Publications of the Astronomical Society of the Pacific* 125, p. 306. arXiv: 1202.3665.

Forni, O., S. Maurice, O. Gasnault, R. C. Wiens, A. Cousin, S. M. Clegg, J. B. Sirven, and J. Lasue (Aug. 2013). Independent component analysis classification of laser induced breakdown spectroscopy spectra. *Spectrochimica Acta* 86, pp. 31–41.

Hardgrove, C., J. Moersch, and D. Drake (2011). Effects of geochemical composition on neutron die-away measurements: Implications for Mars Science Laboratory's Dynamic Albedo of Neutrons experiment. *Nuclear Instruments and Methods in Physics Research, Section A: Accelerators, Spectrometers, Detectors and Associated Equipment* 659 (1), pp. 442–455.

Hausrath, E. M., D. C. Golden, R. V. Morris, D. G. Agresti, and D. W. Ming (Jan. 2013). Acid sulfate alteration of fluorapatite, basaltic glass and olivine by hydrothermal vapors and fluids: Implications for fumarolic activity and secondary

phosphate phases in sulfate-rich Paso Robles soil at Gusev Crater, Mars. *Journal of Geophysical Research: Planets* 118, pp. 1–13.

Herrero, M. J., J. I. Escavy, and B. C. Schreiber (2015). Thenardite after mirabilite deposits as a cool climate indicator in the geological record: lower Miocene of central Spain. *Climate of the Past* 11 (1), pp. 1–13.

Jun, I. et al. (Nov. 2013). Neutron background environment measured by the Mars Science Laboratory's Dynamic Albedo of Neutrons instrument during the first 100 sols. *Journal of Geophysical Research: Planets* 118, pp. 2400–2412.

Lapotre, M. G. A. and E. B. Rampe (2018). Curiosity's Investigation of the Bagnold Dunes, Gale Crater: Overview of the Two-Phase Scientific Campaign and Introduction to the Special Collection. *Geophysical Research Letters* 45 (19), pp. 10, 200–10, 210.

Li, Y., T. Wiliana, and K. C. Tam (2007). Synthesis of amorphous calcium phosphate using various types of cyclodextrins. *Materials Research Bulletin* 42 (5).

Litvak, M. L. et al. (2016). Hydrogen and chlorine abundances in the Kimberley formation of Gale crater measured by the DAN instrument on board the Mars Science Laboratory Curiosity rover. *Journal of Geophysical Research E: Planets* 121 (5), pp. 836–845.

McKinney, G. W., J. W. Durkee, J. S. Hendricks, M. R. James, D. B. Pelowitz, L. S. Waters, and F. X. Gallmeier (Sept. 2006). *MCNPX Overview*. Vol. LA-UR-06-6206. HSSW, FNAL. Los Alamos, NM: Los Alamos National Laboratory.

Mitrofanov, I. G., A. S. Kozyrev, D. I. Lisov, A. A. Vostrukhin, D. V. Golovin, M. L. Litvak, A. V. Malakhov, M. I. Mokrousov, S. Y. Nikiforov, and A. B. Sanin (2016). Active neutron sensing of the Martian surface with the DAN experiment onboard the NASA Curiosity Mars rover: Two types of soil with different water content in the gale crater. *Astronomy Letters* 42 (4), pp. 251–259.

Mitrofanov, I. G. et al. (Sept. 2012). Dynamic Albedo of Neutrons (DAN) Experiment Onboard NASA's Mars Science Laboratory. *Space Science Reviews* 170, pp. 559–582.

Mitrofanov, I. G. et al. (July 2014). Water and chlorine content in the Martian soil along the first 1900 m of the Curiosity rover traverse as estimated by the DAN instrument. *Journal of Geophysical Research: Planets* 119, pp. 1579–1596.

Morris, R. V. et al. (June 2016). Silicic volcanism on Mars evidenced by tridymite in high-SiO2 sedimentary rock at Gale crater. *Proceedings of the National Academy of Science* 113, pp. 7071–7076.

Newman, C. E. et al. (July 2017). Winds measured by the Rover Environmental Monitoring Station (REMS) during the Mars Science Laboratory (MSL) rover's Bagnold Dunes Campaign and comparison with numerical modeling using MarsWRF. *Icarus* 291, pp. 203–231.

O'Connell-Cooper, C. D., J. G. Spray, L. M. Thompson, R. Gellert, J. A. Berger, N. I. Boyd, E. D. Desouza, G. M. Perrett, M. Schmidt, and S. J. VanBommel (Dec. 2017). APXS-derived chemistry of the Bagnold dune sands: Comparisons with Gale Crater soils and the global Martian average. *Journal of Geophysical Research: Planets* 122, pp. 2623–2643.

O'Connell-Cooper, C. D., J. G. Spray, L. M. Thompson, R. Gellert, N. I. Boyd, J. A. Berger, E. D. Desouza, and S. J. VanBommel (2018). Chemical diversity of sands within the linear and barchan dunes of the Bagnold Dunes, Gale Crater, as revealed by APXS onboard Curiosity. *Geophysical Research Letters* 45 (18), pp. 9460–9470.

Pelowitz, D. B. (Aug. 2008). *MNCPX User's Manual, version 2.6.0*. Vol. LA-CP-07-1473. Los Alamos National Laboratory.

Rampe, E., M. Kraft, T. Sharp, D. Golden, D. Ming, and P. Christensen (Nov. 2012). Allophane detection on Mars with Thermal Emission spectrometer data and implications for regional-scale chemical weathering processes. English (US). *Geology* 40 (11), pp. 995–998.

Rampe, E. B., R. V. Morris, P. D. Archer Jr., D. G. Agresti, and D. W. Ming (2016). Recognizing sulfate and phosphate complexes chemisorbed onto nanophase weathering products on Mars using in-situ and remote observationsk. *American Mineralogist* 101 (3), p. 678.

Rampe, E. B. et al. (Aug. 2017). Mineralogy of an ancient lacustrine mudstone succession from the Murray formation, Gale crater, Mars. *Earth and Planetary Science Letters* 471, pp. 172–185.

Rampe, E. B. et al. (2018). Sand mineralogy within the Bagnold Dunes, Gale crater, as observed in situ and from orbit. *Geophysical Research Letters* 45 (18), pp. 9488–9497.

Rapin, W. et al. (2017a). Quantification of water content by laser induced breakdown spectroscopy on Mars. *Spectrochimica Acta Part B: Atomic Spectroscopy* 130, pp. 82–100.

Rapin, W. et al. (2017b). Roughness effects on the hydrogen signal in laser-induced breakdown spectroscopy. *Spectrochimica Acta Part B: Atomic Spectroscopy* 137, pp. 13–22.

Rapin, W. et al. (2018). In Situ Analysis of Opal in Gale Crater, Mars. *Journal of Geophysical Research: Planets* 123 (8), pp. 1955–1972.

Ruff, S. W. et al. (Apr. 2011). Characteristics, distribution, origin, and significance of opaline silica observed by the Spirit rover in Gusev crater, Mars. *Journal of Geophysical Research: Planets* 116, E00F23, E00F23.

Sanin, A. B. et al. (2015). Data processing of the active neutron experiment DAN for a Martian regolith investigation. *Nuclear Instruments and Methods in Physics Research, Section A: Accelerators, Spectrometers, Detectors and Associated Equipment* 789, pp. 114–127.

Sears, V. F. (1992). Neutron scattering lengths and cross sections. *Neutron News* 3 (3), pp. 26–37.

Silvestro, S., D. A. Vaz, H. Yizhaq, and F. Esposito (2016). Dune-like dynamic of Martian Aeolian large ripples. *Geophysical Research Letters* 43 (16), pp. 8384–8389.

Silvestro, S., D. Vaz, R. Ewing, A. Rossi, L. Fenton, T. Michaels, J. Flahaut, and P. Geissler (2013). Pervasive aeolian activity along rover Curiosity's traverse in Gale Crater, Mars. *Geology* 41 (4), p. 483.

Sklute, E. C., H. B. Jensen, A. D. Rogers, and R. J. Reeder (2015). Morphological, structural, and spectral characteristics of amorphous iron sulfates. *Journal of Geophysical Research: Planets* 120 (4), pp. 809–830.

Squyres, S. W. et al. (May 2008). Detection of Silica-Rich Deposits on Mars. *Science* 320, p. 1063.

Stern, J. C. et al. (2018). Major Volatiles Evolved From Eolian Materials in Gale Crater. *Geophysical Research Letters* 45 (19), pp. 10, 240–10, 248.

Sullivan, R. and J. F. Kok (Oct. 2017). Aeolian saltation on Mars at low wind speeds. *Journal of Geophysical Research: Planets* 122, pp. 2111–2143.

Sutter, B. et al. (2017). Evolved gas analyses of sedimentary rocks and eolian sediment in Gale Crater, Mars: Results of the Curiosity rover's sample analysis at Mars instrument from Yellowknife Bay to the Namib Dune. *Journal of Geophysical Research: Planets* 122 (12), pp. 2574–2609.

Thomas, P., P. Simon, A. Smallwood, and A. Ray (Apr. 2007). Estimation of the diffusion coefficient of water evolved during the non-isothermal dehydration of Australian sedimentary opal. *Journal of Thermal Analysis and Calorimetry* 88, pp. 231–235.

Vaniman, D. T., D. L. Bish, S. J. Chipera, C. I. Fialips, J. William Carey, and W. C. Feldman (Oct. 2004). Magnesium sulphate salts and the history of water on Mars. *Nature* 431, pp. 663–665.

Varela, M. E., G. Kurat, M. Bonnin-Mosbah, R. Clocchiatti, and D. Massare (Jan. 2000). Glass-bearing inclusions in olivine of the Chassigny achondrite: Heterogeneous trapping at sub-igneous temperatures. *Meteoritics and Planetary Science* 35, pp. 39–52.

Wada, K. (1990). Minerals in Soil Environments. eng. *Soil Science* 150 (2), pp. 1051–1087.

Whelan, J. A. and S. S. Goldich (1961). New data for hisingerite and neotoctite. *The American Mineralogist* 46, pp. 1412–1423.

Yen, A. S. et al. (Aug. 2017). Multiple stages of aqueous alteration along fractures in mudstone and sandstone strata in Gale Crater, Mars. *Earth and Planetary Science Letters* 471, pp. 186–198.

Chapter 3

WATER-RICH, FRACTURE-ASSOCIATED ALTERATION HALOS IN GALE CRATER, MARS

Travis S. S. Gabriel,[1*†] Craig Hardgrove,[1†] Cherie N. Achilles,[2†] Elizabeth B. Rampe,[3†] William Rapin,[4] Suzanne Nowicki,[5] Sean Czarnecki,[1†] Lucy Thompson,[6] Sergei Nikiforov,[7] Maxim litvak,[7] Igor Mitrofanov[7]

[1]School of Earth and Space Exploration, Arizona State University, Tempe, AZ 85287, USA

[2]NASA Goddard Space Flight Center, Greenbelt, MD, USA

[3]NASA Johnson Space Center, Houston, TX, USA

[4]California Institute of Technology, Pasadena, CA, USA

[5]Los Alamos National Laboratory, Los Alamos, NM 87545, USA

[6]Planetary and Space Science Centre, University of New Brunswick, Fredericton, NB E3B 5A3, Canada

[7]Institute for Space Research, Russian Academy of Sciences, Moscow, Russian Federation

[*]Corresponding author: Travis.Gabriel@asu.edu

[†]Present address: 781 E Terrace Mall, ISTB4, Room 795, Tempe, AZ 85287-6004, USA.

Citation: T. S. J. Gabriel, C. Hardgrove, C. N. Achilles, E. B. Rampe, W. Rapin, S. Nowicki, S. Czarnecki, L. Thompson, S. Nikiforov, M. Litvak, I. Mitrofanov (2018). Water-rich, fracture-associated alteration halos in Gale crater, Mars. In preparation for *The Journal of Geophysical Research: Planets.*

3.1 Abstract

We performed targeted in-situ active neutron measurements of high-silica fracture-associated halos observed throughout a sandstone unit (Stimson) in Gale crater, Mars. We find that halos in two locations to have a highly enriched water content (measured to be 5.1±0.9 wt.% H_2O-equiv. H and 5.3±0.7 wt.% H_2O-equiv. H), as compared to unaltered rocks in the unit (∼0.4–1.4 wt.% H_2O-equiv. H). Geochemical and mineralogical data are consistent with the high-silica rocks being abundant in opal-A. The silica forms examined in the Stimson and an adjacent mudstone unit (Murray) demonstrate that the post-depositional environment of high silica rocks has been relatively inactive, since it would have promoted the rapid maturation of diagenetic silica to more ordered forms, and such enhancement of ordered forms is not observed. We also report a large network of fracture halos discovered in another geologic unit (Bradbury) with similar geochemical trends and neutron spectra. Together our results indicate that one of the final fluid events in Gale crater involved an extensive ground water system that ended rather abruptly, with cold and arid conditions that followed to present day. Furthermore, the bulk water content of the halos translates to ∼4–6 kg in a single meter-long fracture halo, which can serve as a potential resource of considerable scale at equatorial Mars since the deposits are found to extend up to tens of meters laterally in the unit and are composed of opal-A which releases water through mild heating, grinding, or exposure to vacuum.

3.2 Introduction

Light-toned, high-silica rocks have been observed in several units along the Curiosity rover's traverse in Gale crater (e.g. Frydenvang et al., 2017; Morris et al., 2016; Yen et al., 2017). Geochemical analysis of these rocks showed that their amorphous fraction is consistently enriched compared country rock, in addition to the regular depletion of several metals (Frydenvang et al., 2017; Morris et al., 2016; Yen et al., 2017). In one high-silica target Buckskin, powder X-ray Diffraction (XRD) experiments showed the presence of tridymite, a high-temperature polymorph of silica, indicating a silicic volcanic sediment source for the high-silica rocks in the Murray mudstone unit (Morris et al., 2016). High-silica rocks in a sandstone unit (Stimson) that unconformably overlies the Murray are in the form of fracture-associated halos that crosscut bedding and can be tens of meters in length (See Figure 3.1). In at least one location, fracture halos crosscut the contact between the Murray and the Stimson sandstone unit that unconformably overlies the Murray (Frydenvang et al., 2017, see their Supplement). For these reasons, high-silica rocks in the Murray and Stimson are suggested to have experienced related alteration events; however, the conditions of the groundwater event posited as the source of Stimson halos are debated, particularly in terms of the pH of the fluids (Frydenvang et al., 2017; Yen et al., 2017). In any scenario, the active enrichment of silica through the transport of ground water in fractures is posited to play a role, with diagenetic silica as a suggested byproduct and the likely source of the silica enrichment (Frydenvang et al., 2017; Yen et al., 2017). The presence of detridal silica (Morris et al., 2016) in the overlying high-silica Murray provides a natural source for the active silica enrichment of Stimson fracture halos (Frydenvang et al., 2017) and neutron experiments are consistent with the existence of a laterally extensive

high-silica sequence in the Murray which would provide a widespread silica source for fracture-associated halos (Czarnecki et al., In preparation). The groundwater alteration event posited for the Stimson halos is also fundamentally distinct from the hot spring setting hypothesizes for the formation of digitate and nodular diagenetic silica features observed by Spirit rover in Gusev crater, Mars (Ruff et al., 2011; Ruff and Farmer, 2016).

Given that diagenetic silica is suggested to be present in the Stimson halos (Frydenvang et al., 2017; Rapin et al., 2018; Yen et al., 2017), the amorphous composition of light-toned rocks, which makes up ∼70-90% of the bulk rock, can provide clues into their alteration history. XRD and X-ray fluorescence (XRF) experiments from the Chemistry and Mineralogy (CheMin) and Alpha-Particle X-ray Spectrometer (APXS) instruments, respectively, demonstrate the amorphous fraction of light-toned rocks is abundant in Si, strongly suggesting the presence of either opal or rhyolitic (Si-rich) glass (Achilles et al., 2018; Morris et al., 2016). Despite a good match of silica-rich phases to the amorphous 'hump', the X-ray patterns for these materials are degenerate and discriminating between individual phases is difficult (e.g. Morris et al., 2016, see their Supplement). The water content of these rocks, however, serves as a strong indicator between Si-rich glasses and opal-A; martian glasses are understood to have less than ∼0.1 wt.% H_2O, as determined from isotopic and geochemical analysis of martian meteorites (e.g. Filiberto and Treiman, 2009; Liu et al., 2018; McCubbin et al., 2016), whereas the presence of water above ∼1 wt.% is considered essential for the mineralloid's existence (J. D. Dana and E. S. Dana, 1997). Depending on the formation conditions and maturity, among other factors, opal can have a range of water contents up to 20 wt.% H_2O (e.g. Adams et al., 1982; J. D. Dana and E. S. Dana, 1997; Huang and Vogler, 1972; Jones and Renaut, 2004). However,

measurements of the water content of high-silica rocks between the Sample Analysis at Mars (SAM) instrument and ChemCam are not commensurate (Rapin et al., 2018). SAM Evolved Gas Analysis (EGA) experiments estimate 0.9 ± 0.3 wt% H_2O and Chemistry Camera (ChemCam) experiments estimate 3.2 ± 1.0 wt% H_2O in the high-silica Greenhorn drill target in the Stimson unit (Rapin et al., 2018). Similarly, for the high-silica target Buckskin in the Murray, SAM and ChemCam estimates differ, 1.8 ± 0.6 wt% H_2O and 4.0 ± 1.3 wt% H_2O respectively (Rapin et al., 2018). Rapin et al. (2018) demonstrates that the dehydration of samples during drilling, preparation, and delivery to the SAM instrument can be a source of discrepancy between the estimates. Furthermore, Laser-Induced Breakdown Spectroscopy (LIBS) experiments by the Chemistry and Camera (ChemCam) instrument of high-silica targets in the Murray and Stimson show correlation of SiO_2 and H_2O content which may indicate the presence of opal (Rapin et al., 2018).

Understanding the relative abundance siliceous amorphous phases that dominates the amorphous component of light-toned rocks is critical to unraveling the environmental conditions during formation. Opal and rhyolitic glass have considerably different formation and solubility conditions; high-silica volcanic glasses are quenched in eruptions and necessitate the existence of a silicic volcanic magma source. Impact-generated glasses would also require a pre-existing Si-rich substrate, and therefore require a Si-rich volcanic source. On Earth, non-biogenic opal forms in low temperature (<200 ^{o}C) aqueous environments, often in arid regions where groundwater is transported through siliceous rocks due to seasonal and long-term fluctuations in the water table, as well as fluctuations in pH (e.g. Tucker, 2001). Opaline silica is also generally more soluble in fluids and is less likely to persist in a low-ordered form

through cyclic alteration events, however the detailed maturation process is contingent on the chemistry of the system among other factors (e.g. Tucker, 2001).

We provide an independent measurement of the H content of a fracture-associated halo and the surrounding, unaltered country rocks using the Dynamic Albedo of Neutrons (DAN) instrument. By implementing novel modeling techniques that provide insight into features at the sub-field-of-view-level, we can directly address the water content of high-silica rocks. Moreover, the sensitivity of DAN experiments to the top ∼45-70 cm of the martian subsurface allows us to constrain the depth of fracture halos. Specifically, we performed dedicated active neutron experiments at the Lubango and Greenhorn targets, which are associated with two fracture halos Stimson unit. We also find an extensive fracture halo network in the Bradbury unit, with strikingly similar characteristics to those in the Stimson unit. Our results are then considered in the wider context of the mineralogical and geochemical trends in the units to understand the conditions of the diagenetic fluids and the post-depositional environment. Given the significant distribution and extent of these alteration features we consider these deposits considerable resources for in-situ utilization for exploration of otherwise relatively dry equatorial Mars and we remark on the design of in-situ resource instruments for their exploitation.

3.3 Material and Methods

We performed targeted measurements over the Lubango and Greenhorn drill targets in Stimson fracture halos using the DAN instrument in 'active' mode. Untargeted active DAN experiments are performed throughout the rover traverse, often at the end of a rover drive segment, and targeted campaigns have also been conducted over

geologic sites of interest (Ehlmann et al., 2017; Gabriel et al., 2018; Litvak et al., 2016). We also make use of untargeted active and passive neutron data, as well as data from a suite of geochemical and mineralogic instruments on board Curiosity rover.

3.3.1 DAN Instrument

The DAN instrument is composed of a detector package and a Pulse Neutron Generator (PNG) (Litvak et al., 2008; Mitrofanov et al., 2012). The detector named Counter of Thermal Neutrons (CTN) is sensitive to neutrons from 0.001 eV< E<100 keV), and the Counter of Epithermal Neutrons (CETN) is Cd coated, allowing it to be sensitive only to epithermal neutrons (0.4 eV<E<100 keV). However, these ranges are statistical in nature and the detailed energy sensitivities are reported in Mitrofanov et al. (2012). In active mode the PNG internal electronics generate ∼120 kV to accelerate deuterium (^{2}D) ions, in ∼1 μs pulses, to interact with a tritium (^{3}T) target (Mitrofanov et al., 2012). This generates a deuterium-tritium nuclear reaction, ^{2}D + ^{3}T → n (14.1 MeV) + ^{4}He (3.5 MeV), that produces neutrons isotropically. Immediately after each pulse, the detectors measure neutron counts in 64 logarithmically-spaced time bins for 100 ms (0.1 s) after the pulse. Mitrofanov et al. (2014) reports the time bin widths are loosely governed by the relation $\Delta t = 5\ \mu\text{s} \cdot 1.125^i$, $i\ \epsilon$ [0, 63], however they can deviate from this relation. We provide the exact time bin extents in Table S1 for posterity. A single active DAN measurement involves coadding results in each detector over thousands of such pulses at a frequency of 10 Hz to obtain statistical convergence of the die-away curve. During an active DAN sequence the rover and rover arm are stationary, allowing the results from each pulse to be coadded.

In passive mode, DAN relies on the relatively low flux of galactic cosmic rays (GCRs) and the decay of plutonium fuel pellets in the Multi-Mission Radioisotope Thermoelectric Generator (MMRTG) as a source of neutrons. GCR spallation reactions in the martian subsurface produce secondary high-energy neutrons whereas the MMRTG produces neutrons directly. Due to the fluctuating solar activity and martian atmosphere conditions, the flux of GCR-produced neutrons at the surface of Mars can very. Tate et al. (2018) demonstrates the GCR flux at the surface, as inferred from Radiation Assessment Detector (RAD) measurements, can vary by ∼25% over a 100 sol period, but can also maintain a ∼10% dynamic range for several hundred sols. This phenomenon is accounted for in the analysis of passive DAN data by cross-calibrations with RAD (Tate et al., 2018). Passive DAN experiments are also not time resolved and thus provide only two degrees of freedom (the count rate of epithermal and thermal neutrons), whereas active experiments contain time-of-flight information in addition to the two-band energy resolution provided by the He^3 detectors. Thus passive DAN data are processed in a markedly different manner than that of active experiments. For more detailed information on processing passive DAN experiments and their sensitivities we refer the reader to Jun et al. (2013), Tate et al. (2015), and Tate et al. (2018); in this work we focus on the analysis of active DAN experiments and present only the raw count rates of passive data to show qualitative trends.

The spot size (field-of-view) of DAN experiments is markedly different from that of orbital neutron instruments. In comparison to the meter-scale spot size of DAN experiments, the orbiting passive neutron instrument Mars Odyssey Neutron Spectrometer (MONS) has a ∼550 km diameter spot size at full-width half-maximum. While orbital neutron experiments can provide regional-scale hydration and geochemical information, they provide a cumulative result of multiple geologic units and provinces. In contrast,

DAN measurements, which we determine herein to have a surface footprint of ∼2.2 m and sensing depth of ∼45-70 cm, are sensitive to changes in local-scale geology. Active neutron experiments are performed at nearly every stop along the *Curiosity* rover's traverse, providing a wealth of geochemical and stratigraphic information from the more than 930 measurements performed to-date. Beyond cadenced experiments, dedicated campaigns of geochemically or morphologically distinct areas such as sand dunes and geologic contacts have also been made (Ehlmann et al., 2017; Gabriel et al., 2018; Litvak et al., 2016). These measurements provide compositional information of the bulk rock at the meter scale that are complementary to the micron to centimeter scale sensing areas of ChemCam LIBS and APXS experiments.

Given the comparatively small footprint, DAN experiments can benefit from high-accuracy local-scale geochemical data, such as that provided by APXS, to inform data processing techniques and increase the fidelity of the results (Gabriel et al., 2018; Litvak et al., 2016). Elemental species in martian rocks reduce (moderate) the energy of high-energy neutrons via scattering interactions; these low-energy neutrons are then detected by the DAN detector package. Hydrogen is the strongest moderator of neutrons due to its similar atomic mass to a neutron. On the other hand, neutron-absorbing elements, *e.g.* Cl and Fe, diminish the number of low-energy neutrons and can have a significant effect on the arrival-time profile and energy distribution measured by the DAN detectors (e.g. Hardgrove et al., 2011). The effects of neutron absorbers on orbital neutron data at Mars have also been investigated Diez et al. (2008). To understand the absorption potential of a bulk rock, it is useful to compute the macroscopic neutron absorption cross section, ξ_{abs}. This measure provides an understanding for the interplay between the absorption cross section of an elemental species and its abundance and variability in target rocks. For example, the absorption

cross section of Br is over twice that of Fe; however, the abundance of Br can be orders of magnitude lower than that of Fe in rocks measured by APXS. The macroscopic absorption cross section of a rock is the sum of the macroscopic absorption cross section of its N elemental components,

$$\xi_{\mathrm{abs}} = \sum_{i}^{N} \xi_{\mathrm{abs},i} = \sum_{i}^{N} \frac{a_i \sigma_{\mathrm{abs}} N_{\mathrm{A}}}{m_{\mathrm{a}}}, \tag{3.1}$$

where a_i is the abundance of the element in weight fraction, N_{A} is Avogadro's number, m_{a} is the molar mass of the element. It is convention to report σ_{abs} in units of barns (10^{-24} cm^2) or in cm^2, and thus ξ_{abs} is in units of barns/g or cm^2/g. In Table 3.1 we provide the microscopic absorption cross sections, σ_{abs}, of major rock-forming and trace elements provided by APXS analysis. When considering the abundance of rock-forming elements on Mars, Fe and Cl are typically examined due to a combination of their variability and abundance, as well as their microscopic neutron absorption cross sections (Diez et al., 2008; Hardgrove et al., 2011; Mitrofanov et al., 2014). Other elemental species, however, can also play a strong role in the variability of the bulk neutron absorption cross section, as is seen in high-silica rocks examined herein.

3.3.2 Geochemistry of Halos

The light-toned rocks associated with both fracture halos in the Stimson and high-silica zones in the underlying Murray mudstones are associated with a unique geochemical signature. APXS experiments show that light-toned halos in the Stimson are systematically depleted in Cl, Mg, Al, Cr, Mn, Fe, Ni, and Zn with respect to the unaltered bedrock; systematic enrichment is seen in Si, P, S, and Ge (Yen et al., 2017). ChemCam LIBS experiments also show excesses in Si and the suppression of Fe and Mg.

Table 3.1. Absorption cross section values for 2.2 km/s neutrons from Sears (1992), normalized to the absorption cross section of Cl (33.5 barns or equivalently 3.35×10^{-23} cm^2). Values are shown for elements whose abundances are reported by the Alpha Particle X-ray Spectrometer on Curiosity rover. Terrestrial abundances of isotopes are assumed in the calculation of the elemental cross sections.

Element	Absorption cross section $[100\times\sigma_{\text{abs}}/\sigma_{\text{abs, Cl}}]$
Cl	100
Mn	39.7
Br	20.6
Ti	18.2
Ni	13.4
Cr	9.10
Fe	7.64
K	6.27
Zn	3.31
Na	1.58
S	1.58
Ca	1.28
Al	0.690
P	0.513
Si	0.510
Mg	0.188

For example, ∼85 wt% SiO_2 was measured in the high-silica target Elk in the Marias pass region of the Murray formation and 57.4 wt% SiO_2 was measured in the Lubango fracture halo target; for context, the unaltered Stimson bedrock shows 43.8 wt% SiO_2 (Rapin et al., 2018). We also report the finding of a new group of alteration halos at the 'Darwin' waypoint ('Darwin-suite halos' hereafter) that are remarkably similar in surface expression, neutron signal, and geochemical trends. APXS measurements were not performed on these features, however geochemical information is available at one target (Kukri) from relatively long distance LIBS experiments (∼4.8 m). Similar to high-silica areas upsection, the Kukri target shows elevated Si content, with a suppression of Fe and Mg, as is the case in Stimson alteration halos.

Considering the trends in neutron-absorbing elements, namely the significant depletion in Fe content, high-silica rocks produce a strong signature in DAN data. In Figure 3.2 we show the macroscopic absorption cross section of the major and trace elements from APXS analysis for Murray and Stimson targets, altered and unaltered, as well as the Kukri target at the Darwin-suite halos. The largest contribution to the macroscopic absorption cross section occurs in Fe and Cl, as well as Ni and Br depending on the target. The systematic depletion in Cl, Ni, Mn, and Cl content in high-Si rocks contribute significantly to the differences in ξ_{abs}. In Figure 3.3 we show ξ_{abs} for all drill sites thus far along Curiosity rover's traverse. The systematically lower values of ξ_{abs} in high-silica rocks should produce overall greater thermal neutron flux, and indeed we demonstrate in later sections that this is the case.

3.3.3 Mineralogy of Halos

The Darwin-suite halos in the Bradbury unit (Figure 3.1, label 'A') observed early in the mission (sol ∼380-400) were not the subject of a drill investigation and thus, there is no mineralogical data available on this material from the CheMin instrument. The next encounter of Curiosity rover with high-silica, light-toned rocks occurred at Marias pass on sol ∼980. The Buckskin drill site in high-silica Murray at Marias Pass exhibited the first finding of tridymite, a high-temperature low-pressure silica polymorph, in Gale crater (Morris et al., 2016). Morris et al. (2016) finds the abundant tridymite (17.1 ± 1.0 wt% in the bulk) is likely the product of silicic volcanism that provided a sediment source for the light-toned Murray mudstones. Other silica-rich phases exist in the Buckskin sample: cristobalite (3.0 ± 0.4 wt%),

anhydrite (0.9 ± 0.3 wt%), and opal-CT (∼6 wt%) in the bulk; however, quartz was not detected above CheMin sensing limits (Morris et al., 2016).

In the Stimson unit, the Greenhorn and Lubango fracture-associated halo showed similar mineralogical compositions to one another, but unlike the high-silica Murray, did not include the presence of tridymite or opal-CT above CheMin detection limits. The Lubango target, however, showed the presence of gypsum (0.6 ± 0.2 wt% in the bulk) above detection limits which represented the first identification of gypsum in a martian sample (Yen et al., 2017). The alteration halos in the Stimson also featured systematic enhancements in high-silica phases. The Greenhorn and Lubango fracture halo showed 0.8 ± 0.2 and 0.9 ± 0.2 wt% quartz in the bulk respectively, similar to that of unaltered Stimson targets Big Sky and Okoruso, 1.4 ± 0.3 and 0.9 ± 0.3 wt% in the bulk respectively (Yen et al., 2017). The abundance of anhydrite was significantly elevated in the Greenhorn and Lubango targets, 5.6 ± 0.3 and 3.3 ± 0.2 wt% in the bulk respectively, as compared to Big Sky and Okoruso, 1.2 ± 0.3 and 0.5 ± 0.4 wt% respectively (Yen et al., 2017). Bassanite was similarly elevated in the Greenhorn and Lubango targets, 1.4 ± 0.3 and 2.4 ± 0.3 wt% respectively, as compared to 0.8 ± 0.4 wt% in Okoruso; Bassanite was under detection limits in the Big Sky target (Yen et al., 2017). Phase abundances relevant to our analysis and their contribution to the bulk water content are reported in Table S3.1. We note that in all cases the examined Stimson and Murray samples host a minimal amount of water in the crystalline fraction (< 0.1 wt.% H_2O).

3.3.3.1 Amorphous Component of Halos

X-ray diffraction experiments performed by the CheMin instrument find that high-silica rocks exhibit an enhancement in the fraction of amorphous component from the country rock. Greenhorn and Lubango have an amorphous fraction of ∼65 and ∼73 wt% respectively, whereas Big Sky and Okoruso have an amorphous fraction of ∼20 and ∼35 wt% respectively (Yen et al., 2017). The scenario is similar for the Buckskin drill site in Marias Pass, which features an amorphous fraction of 60-65 wt% (Morris et al., 2016), whereas the Telegraph Peak sample in the Murray, ∼6 m stratigraphically lower than Buckskin, has an amorphous fraction of 27.2 ± 15 wt% (E. B. Rampe et al., 2017). In all cases, the amorphous fraction of high-silica rocks in the Murray and Stimson is associated with elevated levels of SiO_2: ∼77 wt% and ∼66 wt% SiO_2 in the amorphous fraction of Buckskin and Stimson halos respectively; XRD and geochemical model uncertainties allow for even greater abundances (Morris et al., 2016; Yen et al., 2017).

3.3.4 Passive DAN Experiments

Untargeted passive DAN experiments are performed regularly along the Curiosity rover's traverse, both during rover mobility and while stationary. During the approach to Marias Pass the passive neutron data exhibited one of the largest spikes in thermal neutron count rates since the start of the mission. This prompted the rerouting of the rover for closer contact science at the anomaly, leading to the discovery of high-silica bedrock near the Murray-Stimson contact and the drilling of the Buckskin target. Figure S3.7 provides geologic context for the high-silica material near the

Murray-Stimson contact and the overlying high-silica fracture halos in the Pahrump Hills region. In Figure 3.4 we show the raw thermal neutron count rates from sol 900 to 1500, including high-silica regions in Marias Pass and at Stimson halos in Naukluft Plateau. Since the passive count rate of thermal neutrons correlates positively with H and negatively with neutron-absorbing elements, we use this data for a qualitative understanding of geochemical trends along the traverse. Dedicated treatment of background neutrons and other effects is required to translate passive count rates into geochemical information (Jun et al., 2013; Tate et al., 2015; Tate et al., 2018). Passive experiments were also performed in the Bradbury unit and we find a spike in thermal neutron count rates between sol 383-385, well above the statistical variability in that region, which coincides with a rover stop that fortuitously resulted in an untargeted active DAN experiment directly over a Darwin-suite halo (See Figure 3.5 and Figure S3.10). We are unable to correlate other spikes in the thermal neutron data in this area as the rover was performing long, automated drives where image products are not abundant or are obscured by the extensive amount of unconsolidated material characteristic of this region in Gale crater. On sol 390 (Site 16, Drive 0), a vast network of light-toned fracture halos is observed adjacent to the rover (see Figure S3.11); however the field-of-view did not encompass light-toned material along this region of the traverse.

3.3.5 Active DAN experiments

In total, we utilize data from 30 active DAN experiments performed in the Stimson sandstone unit and one experiment performed over a Darwin-suite halo. The neutron background is subtracted from these time-resolved neutron measurements (e.g. Sanin

et al., 2015) and the data are processed in a forward modeling scheme (Gabriel et al., 2018) to determine the H content of the underlying rock and the depth extent of halos.

3.3.5.1 Forward modeling of active DAN experiments

Active DAN experiments are compared to the results of neutron transport models using the Monte Carlo N-Particle 6 code (MCNP6) developed at Los Alamos National Laboratory (McKinney et al., 2006; Pelowitz, 2008). The models simulate the active neutron experiment, complete with the PNG, detectors, electronics, and other components. The geometries of the experiment are described in MCNP6 input files. Broadly, the existing literature on DAN experiments employs one of two types of input file types: 1) “ring model" where no rover is present and the detector is modeled as a ring-type detector to speed statistical convergence (a common technique in nuclear applications) (Sanin et al., 2015), or 2) “rover model" where rover components and the DAN detectors are present (Jun et al., 2013). In the ring model, a set of constant correction factors for each time bin are applied to account for the effects of the rover components on DAN spectra. We direct the reader to (Sanin et al., 2015) for information on the development of this model and the correction factors. In the rover model, the rover, Multi-Mission Radioisotope Thermoelectric Generator (MMRTG), and the DAN detector and PNG packages are present (Jun et al., 2013). The rover composition in the MCNP6 input file was developed through in several iterations to produce the thermal neutron response in pre-flight, ground calibration tests performed at the Jet Propulsion Laboratory (Jun et al., 2013). Herein, we implement the rover model in all simulations despite the computational expense of modeling neutron interactions with rover components. The PNG is modeled as a

point source of 14.1 MeV neutrons and 2.5×10^9 particle histories are simulated to obtain <5% relative error in the die-away curve, as is required to produce dependable results when simulating non-ring type detectors in MCNP6 (Pelowitz, 2008).

Our MCNP6 models require a description of the subsurface geochemistry and geometry. Neutron spectroscopy studies often employ two geometric models: 1. 'homogeneous' models, where the geochemistry is constant in a semi-infinite space in the subsurface and 2. '2-layer' models, where the upper layer is geochemically distinct from the lower layer of semi-infinite depth. Many other geometries or layering structures can be implemented, depending on the geologic scenario and multi-layer models can generally provide better fits to data as there are more free parameters (e.g. Mitrofanov et al., 2014). The addition of free parameters must also be cautioned since degeneracies can arise, as discussed by Feldman et al. (2011) in the context of Mars Odyssey Neutron Spectrometer data. We employ the homogeneous model for areas of unaltered Stimson and use a new 'halo' model developed specifically for the Stimson halos (see Figure 3.8). Since neutron experiments are sensitive to the geochemistry of subsurface rocks, we utilize in-situ data from APXS to inform our models. Oxide abundances reported by APXS are converted to elemental abundances and then to isotopic abundances according to terrestrial fractions (see Table S3.4 for the elemental abundances used in our models and Table S3.5 for the neutron cross section libraries we use in MCNP6).

3.3.5.2 Markov-Chain Monte Carlo

Once the active DAN data has been background subtracted to remove contribution from GCR- and RTG-generated neutrons (Gabriel et al., 2018; Sanin et al., 2015)

the observation is compared to a set of synthetic spectra from the models described previously. We utilize a data processing pipeline (Gabriel et al., 2018) that implements the Markov-chain Monte Carlo (MCMC) method and makes use of the EMCEE and CORNER packages for the Python Programming Language (Foreman-Mackey, 2016; Foreman-Mackey et al., 2013). The active spectra from both the model and data are normalized to allow their shapes to be compared across a subset of time bins that exhibit sufficient dynamic range as a function of geochemical parameters (e.g. Gabriel et al., 2018; Sanin et al., 2015). In Section 3.9 we illustrate the dynamic range in the CTN and CETN time-resolved spectra for the bins commonly used in active DAN analysis and we also denote those which are dominated by rover back scatter and background radiation; we find the commonly-used ranges (e.g. Sanin et al., 2015) are reasonable choices given the dynamic range of the data in the CTN detector.

The MCMC routine is initialized with a number of 'walkers' with associated state vectors that have a length equal to the number of free parameters. The walkers are provided initial parameters (*a priori*), and through several iterations (20,000 iterations in this work), they explore the parameter space according to the affine-invarant ensemble sampler algorithm (Goodman and Weare, 2010), maximizing the negative log of the likelihood function (Gabriel et al., 2018, See their supplement for the likelihood function). Then a subset of the latter iterations are used as an estimate for the *a posteriori* distributions of the optimized parameters (the last 1,000 iterations in this work), which removes 'burn-in' effects, a common methodology in MCMC applications. This formalism does not presuppose that the *a posteriori* distribution of the free parameters are Gaussian, which we demonstrate is particularly useful in describing the depth of features in neutron data. That is, the water content or depth results, for example, may not necessarily follow a normal distribution but

may be skewed; these factors are fully accounted for under this methodology and the N-dimensional likelihood distribution of the free parameters can be reported for a complete understanding of the measurement sensitivity and results. Our formalism also benefits from the ability to identify the underestimated noise in the data, f, which is in units of counts (Gabriel et al., 2018). Small values of f (a few % of the count values) indicate a good fit to the data and minimal underestimated noise. Whereas, in instances of noisy data, poorly converged models, poor model assumptions, *et cetera* the optimization will find large values of f.

As we show in Section 3.10, the active DAN response to H content is nonlinear, so we cannot rely on the common reduced χ^2 statistic as an absolute measure of model acceptance (e.g. Andrae et al., 2010). Instead, after an optimized model is found by the MCMC scheme we examine the S value to understand the amount of variance explained by the model:

$$S = \sqrt{\sum_{i}^{N} (D_i - M_i)^2}. \tag{3.2}$$

The active DAN data and uncertainty is D_i and $\delta_{D,i}$ respectively; the modeled DAN data is M_i and the number of bins in the time-resolved spectra is N. In the case that the underlying model assumptions are invalid, such as assuming an inaccurate subsurface geochemistry or layering structure, the MCMC scheme may exhibit poor convergence and unexpected *a posteriori* distributions of the free parameters (*e.g.* unexpected results for depth, H, *et cetera*). To directly assess the validity of model assumptions, an aspect not afforded by inspection of S alone, we examine the residuals between the MCMC-optimized model and the DAN data. Models with bias or skew in the residuals are strong indications of poor model assumptions. As an example of

residuals that demonstrate good model assumptions we show the optimized model from sol 1110 (first row of Table S3.8) in Figure S3.12. The residuals are random (minimally biased) and small in magnitude ($S \approx$106 counts), demonstrating a low level of noise and that the model assumptions are reasonable. By comparison, in Figure S3.13 we intentionally implement poor model assumptions for illustration; we utilize the homogeneous Big Sky (unaltered Stimson) model with variable H content at an active DAN experiment over Murray mudstones on sol 1285 (which have a different value of Σ_{abs}) and find obvious bias in the residuals.

We perform the aforementioned MCMC optimization procedure using the homogeneous model at all Stimson locations. Using multiple localization tools available to the MSL Curiosity rover team, including the JPL OnSight virtual reality tool (Abercrombie et al., 2017), we examine images of the underlying bedrock in the field-of-view and identify contamination from altered bedrock (light-toned halos). This allows for robust estimates of the H content of unaltered Stimson identifying measurements where the model assumptions are most appropriate, *i.e.* where the unaltered Stimson geochemistry is most relevant to the subsurface rocks. At the two drill sites of altered Stimson, Greenhorn and Lubango, we implement the halo model with a variable halo H abundance and halo depth while holding all other aspects constant. The *a posteriori* of the free parameters (H content and depth) are examined to identify any cross correlations and the residuals of good-fit models are examined to understand the validity of the underlying model assumptions.

3.4 Results

3.4.1 Unaltered Stimson

Active DAN experiments at unaltered Stimson were performed near the Marias Pass area at Pahrump Hills and ∼1 km away at Naukluft Plateau. Using the homogeneous model and geochemical abundances provided by APXS measurements of drill tailings at Big Sky and Okoruso, we determined the bulk H content across the unit. Although the two Stimson regions were separated by a significant distance, we find the water content in both areas is strikingly similar (within statistical uncertainty of one another) (See Figure 3.9). Unaltered Stimson near Marias Pass has a water content of ∼1.27-1.42 wt.% H_2O-equiv. H and the unaltered Stimson roughly 1 km southwest has a water content of ∼1.18–1.31 wt.% H_2O-equiv. H (see Table S3.8 for a list of all results). We find that in models where the neutron absorption cross section varies by less than $\sim 10^{-2}$ cm^2/g (the difference between Okoruso and Big Sky), the water content is within uncertainty. Generally, these results (listed in Table S3.8) are good statistical fits. Unaltered Stimson models show a range of S values of 70-200 counts, suggesting that the average residual across the 17-bin spectra is ∼4-12 counts. We consider this a reasonable level of deviation between the model and data considering the total counts of active DAN spectra in any *single* time bin for this region of the traverse ranges from ∼100-1000, equating to less than ∼1% of the counts depending on the measurement and time bin.

3.4.2 Alteration halos

To determine the water content and depth of Stimson fracture halos we require geochemical information for the rock that surrounds and underlies the halo (see darker material in Figure 3.8). We utilized the Okoruso and Big Sky unaltered Stimson geochemistries from APXS, as well as the mean H content reported in the previous section, to reduce the number of free parameters in the halo model. For the halo geochemistry we use the Greenhorn and Lubango APXS data and allow the H content to vary. From localization tools (e.g. Abercrombie et al., 2017) we find that the Greenhorn and Lubango fracture halos have a width of ∼20 cm (see Figure 3.1), and thus hold the width of the halo constant in these models.

From the analysis of halo models at Greenhorn and Lubango, we find the fracture halos to have similar hydration states, 5.3±0.7 wt.% H_2O-equiv. H and 5.1±0.9 wt.% H_2O-equiv. H respectively. We show the *a posteriori* distribution of the free parameters for the Lubango halo model in Figure 3.10. We find the extent of the halos at depth is different between the two sites. At Greenhorn the halo extends 59^{+11}_{-20} and at Lubango the halo extends to 33^{+25}_{-8}. As we show in Section 3.8, the sensitivity of active DAN experiments drops off precipitously after a few tens of centimeters in depth, so the skewed uncertainties on the halo depth is expected, *i.e.* models with an infinitely-deep halo will look identical to those with a halo extending to ∼60-75 cm. The S values for the best-fit models at Greenhorn and Lubango are 123 and 78 counts respectively, exhibiting a good fit to the data at both locations (see Figure 3.11). Moreover, the residuals of both models exhibit minimal skew suggesting the underlying model assumptions are reasonable.

3.4.3 Comparison of Passive and Active DAN Data

The active and passive DAN results at alteration halos are qualitatively in agreement as well. Alteration halos represent low macroscopic absorption cross section (low Cl, Fe, Mn, *etc.*) and high scattering cross section material (high H, as reported in Section 3.4.2). Thus these rocks should produce ample amounts of thermal neutrons; passive DAN data in Figure 3.4 demonstrates this is indeed the case. The unaltered Stimson represents the opposite scenario: a comparatively high macroscopic absorption cross section and a low macroscopic scattering cross section (as reported in Section 3.4.1); thus the thermal neutron signal is depressed in the unaltered Stimson.

Other notable trends are also observed in the passive data that are largely consistent with active neutron experiments and geochemical data. Murray mudstones, which make up the majority of the passive DAN data in Figure 3.4, exhibit a $\sim$50% higher thermal neutron signal than unaltered Stimson and show greater intra-unit variability overall. This is likely the case for several reasons. Murray targets exhibit a comparatively low value of ξ_{abs} ($\sim$2-4 cm^2/g lower than unaltered Stimson target; see Figure 3.3), which should produce an elevated thermal neutron signature as the rocks are less efficient at absorbing low-energy neutrons. The mineralogy of Murray mudstones also includes hydrated phases (phyllosilicates) in some, but not all, drill targets (E. B. Rampe et al., 2017) which may be a source of variability. Another source of variability is the prevelant, yet unevenly dispersed Ca-sulfate veins in this region of the Murray (L'Haridon et al., 2018); Rapin et al. (2016) identifies a majority of the veins as bassanite, with a stoichiometric water abundance (6.2 wt.% H_2O). For these reasons, we consider the observation that the Murray features a relatively-high and variable thermal neutron count rate as compared to the Simson to be an expected result.

The high-silica Murray in Marias Pass in the top panel of Figure 3.4 show a significant enhancement in thermal neutron signal, well beyond the variability in the Murray. Considering the high-silica Buckskin drill target in Marias pass has the lowest value of ξ_{abs} of drill targets measured thus far (see Figure 3.2), we consider the signal observed at these rocks to be reasonable and expected. However, we do not analyze active DAN experiments at this location in this work since the variable sand/rubble cover throughout the region require detailed localization efforts, as mentioned in (Rapin et al., 2018), that are outside the scope of this work; this is covered extensively by Czarnecki et al. (In preparation). Nevertheless, both ChemCam LIBS and SAM EGA experiments were performed at Buckskin (Rapin et al., 2018; Sutter et al., 2017) and we use these studies to develop an understanding of the formation environment of high-silica rocks in the Discussion section.

Other sites along the traverse also exhibit regular behavior in the DAN passive data. The signal over Bagnold dune sands ($\sim$35 counts/second), for example, is depressed with respect to the surrounding Murray bedrock and slightly elevated over unaltered Stimson. However, we note that the value of ξ_{abs} is lower in Bagnold sands with respect to unaltered Stimson, which allows Bagnold dune sands to more efficiently moderate thermal neutrons. Bagnold dunes are also in proximity to the Murray measurements featured between sols 1180-1300 in Figure 3.4 which may also introduce the periodic depressions observed in neutron data. This effect would depend on the volume of the field-of-view encompassed by sand, but is not a factor in Stimson measurements as the Naukluft Plateau generally represents a local topographical high where unconsolidated material does not settle.

3.4.3.1 Darwin-suite halos

We find that light-toned halos were not constrained to the Murray and Stimson units, but were also observed earlier in the mission, around sol 380-390 at the Darwin waypoint, where unconsolidated groundcover (common in this region) was not present (see panel labeled 'A' in Figure 3.1). The Kukri target was the subject of ChemCam LIBS experiments, and similar to the fracture halos up section, it was also depleted in Fe and Mg potentially indicating a related or similar fluid alteration event. However, uniquely, the Kukri target was enriched in alkali content compared to high-silica materials in Stimson and Murray (See Figure 3.3 and Table S3.7). The Si content of Kukri is also enriched ($\sim$70-75 wt.%), however, given the absence of XRF and XRD analysis of these features we cannot quantify the extent to which these geochemical trends are associated with the amorphous fraction. On sol 385 the DAN field-of-view fortuitously encompassed a fracture halo (shown in Figure 3.5) which produced an elevated thermal neutron signal; this thermal neutron signal was also observed in passive neutron data during rover driving in the area (see Figure S3.10). This indicates a significant increase in either H content, decrease in neutron absorber abundance (*e.g.* Fe and Cl), or both. Through analysis of the active neutron data at this site, where we allow both H content and absorption cross section to vary (the latter is varied using Cl and Fe content, as similarly performed in (Czarnecki et al., In preparation; Litvak et al., 2016; Mitrofanov et al., 2014)), we find the *bulk* rocks in the field-of-view at this site to be consistent with homogeneous models of a low absorber content ($0.41^{+0.01}_{-0.01}$ barns) and an H content of $2.58^{+0.23}_{-0.16}$ wt.% H_2O-equiv. H. We note that absorption cross section of this site is far below the statistical deviations in the unit, indicating a unique composition from from the country rock that is depleted in

neutron absorbers (a common attribute to high-silica rocks upsection). By comparison, Mitrofanov et al. (2014) find the region between sol 370 to 400 to have a Cl-equivalent cross section (their ξ_{Cl} parameter) to have values of 0.88±0.31 wt% Cl. Mitrofanov et al. (2014) finds that the Kukri site is only consistent with their models that feature no Cl whatsoever, likely implying another major absorber is depleted (*e.g.* Fe, as seen in LIBS experiments at Kukri that indicate a low absorption cross section (See Figure 3.2). In addition, Darwin-suite halos have also been identified by anomaly detection analysis using purely data-driven methods, which strengthens the notion that they are geochemically distinct end-members in DAN data, distinct from the country rock (Kerner et al., Submitted).

3.5 Discussion

In general, we find the dark and light-toned Stimson to have markedly different levels of hydration (See Figure 3.9), consistent with the formation of fracture halos through alteration by groundwater fluids (Frydenvang et al., 2017; Yen et al., 2017). The alteration process significantly enhanced the amorphous fraction of the material and this fraction is the predominant reservoir of the hydration. Our water content for the fracture halos is entirely consistent with that estimated by ChemCam LIBS experiments (Rapin et al., 2018), and further demonstrates that the elevated H abundance and inferred opal-A-rich composition, extends at depth to tens of centimeters. Considering that LIBS measurements are sensitive to the top microns to millimeters of material (Wiens et al., 2012) and the water content is slightly lower than ours for the bulk of the halo volume, the two results are consistent with some level of dehydration at the surface; however, the uncertainty of both measurements are not

indistinguishable so this cannot be positively confirmed. The fact that DAN experiments show the *a posteriori* distribution is peaked at a halo depth of ∼30-40 cm and falls off thereafter suggests the fracture halos may be vertically zonal or variable, possibly due to localized silica concentrations in the groundwater or variable leaching conditions in the column (*i.e.* due to pH fluctuations). Though this point cannot be positively confirmed given the 'hump' in the likelihood distribution at depths greater than ∼40 cm (See Figure 3.10). Furthermore, given the exceedingly high levels of Si in the amorphous fraction of these materials (Frydenvang et al., 2017), the observed correlation with Si and H in ChemCam LIBS experiments (Rapin et al., 2018), and our confirmation of the bulk H-enrichment in the halos, we find that the Stimson fracture halos are likely abundant in opal-A throughout the halo.

The water content of the unaltered Stimson shows remarkably consistent values (between 1.0-2.0 wt.% H_2O-equiv. H) when rejecting areas where contamination by alteration halos in the field-of-view is obvious (See Figure 3.9). Furthermore, data in this range is bimodal, suggesting that some amount of the field-of-view may also be encompassed by altered, hydrated rock not identified from surface images, which sometimes provide sparse coverage. This suggests that the lower range (∼0.4–1.4 wt.% H_2O-equiv. H) is likely most representative of an unaltered end-member composition. In Table S3.1 we demonstrate that only 0.05±0.02 wt.% H_2O is held in the crystalline fraction (in bassanite) indicating that the amorphous fraction is the dominant carrier of water. Yen et al. (2017) reports that a composition of Si-rich glasses provides a good fit to the X-ray amorphous hump, however spectra of high-Si X-ray amorphous materials are subject to degeneracy: silica glass, silica gels, impact glasses, gem opal, *et cetera* are nearly indistinguishable (Morris et al., 2016, Supplemental Material). Primarily, the X-ray amorphous hump is most sensitive to the overall Si content

of the samples; the peak sharpens and shifts to lower 2θ angles with increasing Si. In any case, martian glasses are understood to have a rather low water content (<0.1 wt.% H_2O) (e.g. Filiberto and Treiman, 2009; Liu et al., 2018; McCubbin et al., 2016), so it is unlikely that they are the predominant phase in the unaltered Stimson rock. Sulfur is the second most abundant species in the amorphous fraction of the Big Sky sample, potentially indicating the presence of amorphous sulfates. To this point, SAM EGA experiments of the Big Sky target show SO_2 releases above ∼700°C that are indicative of Mg-sulfates. Mg-sulfates, can contain a considerable amount of water (∼22 wt.% H_2O) when synthesized under martian conditions (Vaniman et al., 2004), which may help explain the H_2O releases at similar temperatures in EGA data (Sutter et al., 2017). Assuming the Mg content of the amorphous fraction in unaltered Stimson (∼2-5 wt.% of the bulk (Yen et al., 2017, Supplementary Material)) is entirely attributable to Mg-sulfates, this would correspond to a contribution of 0.44–1.1 wt% H_2O to the bulk water content. Thus the presence of glasses, amorphous Mg-sulfates, and minor contributions from bassanite are consistent with the water content estimated for the unaltered end member of Stimson rocks (∼0.4–1.4 wt.% H_2O-equiv. H). Any variability in the Stimson water content beyond the unaltered end-member we describe may be due to additional contribution from amorphous opal in alteration zones, a scenario consistent with the observed correlation between H and Si signal from LIBS experiments in the Stimson (Rapin et al., 2018), and/or elevated amounts of sulfates (which are also characteristic of high-silica Stimson rocks) (Frydenvang et al., 2017).

3.5.1 Halo formation and post-depositional environment

In terms of mature diagenetic forms, Stimson halos feature a minor amount of quartz, but lack opal-CT, the intermediate diagenetic phase (Yen et al., 2017). Despite that the abundance of quartz in the *bulk* is nearly identical in the unaltered and altered Stimson, both the amorphous fraction and *crystalline* quartz abundance nearly doubles in the altered rocks (Yen et al., 2017). This is consistent with the resistance of quartz to weathering as compared to other primary volcanic minerals in unaltered Stimson rocks, *i.e.* the mineralogy does not necessitate that the observed quartz precipitated through the diaganetic process that formed the opal-A. We note though that some minor amount of solution and dissolution of quartz in the diagenetic process in these halos cannot be positively rejected. The absence of intermediate forms (opal-CT), however, does suggest the presence of fluids were not long lived or that the solubility conditions rapidly changed (Williams and George, 1985). Generally, silica maturation follows the diagenetic sequence opal-A→opal-CT → quartz (e.g. J. D. Dana and E. S. Dana, 1997; Williams and George, 1985), however several controls govern the silica solubility conditions and the maturation process (e.g. Williams and George, 1985). A rapid decrease in temperature or pH, for example, may allow for the diagenetic processes to cease, but the presence of fluids would allow for the maturation of opal-A. We posit that the retreat of groundwater then was most likely swift so as to limit the solution/dissolution reactions, which would have encouraged opal-A maturation and produce opal-CT and/or excess quartz in the altered Stimson targets.

The mere presence of opal-A on the surface of Mars, presumably stable on the order of billions of years, indicates a specific and uneventful post-depositional environment in terms of lack of overburden and fluids, as well as low temperatures (Ruff et al., 2011).

Even in the absence of overburden, the maturation of surficial opal-A deposits on Earth can be accelerated by post-depositional heat overprinting or fumarolic activity; under these active conditions maturation of New Zealand hot spring deposits (sinters), for example, occur on the order of thousands of years Lynne and Campbell, 2007. In contrast, low levels of post-depositional alteration have been shown to allow opal-A deposits to persist on Earth for $\sim 10^4$–10^5 years or longer (Rodgers et al., 2004). For pelagic and lacustrine siliceous deposits on Earth, opal-A undergoes maturation to opal-CT and quartz on the order $\sim 10^6$–10^8 years (e.g. Siever, 1983), with the specific maturation rate dependent on burial depth and temperature. Independent of other environmental considerations, temperature is widely known to correlate strongly with silica solubility (e.g. Siever, 1983) and first principles approaches show an exponential increase in solubility with temperature (e.g. Williams and Crerar, 1985); thus the lack of enhanced intermediate/mature diagenetic forms may indicate the presence of post-depositional fluids must have occurred in a low-temperature environment similar to the present day. Equatorial temperatures on Mars vary seasonally, but at most, ground temperatures in Gale crater peak around $\sim$290 K and are often well below the freezing point of water (Vasavada et al., 2017). The presence of atmospheric water on at present-day Mars is also low, as compared to Earth, which may discourage even slow diagenetic maturation through adsorption-desorption reactions. Atmospheric water vapor at the surface of Mars is $\sim$100 ppmv (e.g. Montmessin and Ferron, 2019), several orders of magnitude lower than on Earth ($\sim$10,000 ppmv) (e.g. Palchetti et al., 2008). We posit that the present-day cold and arid conditions that are posited for the Amazonion (most recent geologic era on Mars) contributed significantly towards the preservation of opal-A deposits and that the post-depositional conditions were unlikely to deviate significantly from present day in Gale crater.

3.5.1.1 Alteration downsection and the role of the Bradbury unit

The high-silica Murray observed in Marias Pass generated a significant thermal neutron signal, broadly consistent with the fracture halos upsection. These high-silica rocks and the measured silica phases are also consistent with the post-depositional formation conditions implied by the results at halos in the Stimson upsection. The Buckskin (high-silica Murray target in Marias Pass) is devoid of quartz, but XRD analysis indicates a significant presence of opal-CT and cristobalite. Furthermore, Rapin et al. (2018) suggests opal-A may also be present, as indicated by LIBS experiments. The light-toned, high-silica material is also interpreted to be primarily detrital in origin due to the significant abundance of tridymite (Morris et al., 2016). Thus, similar arguments to those made for the altered and unaltered Stimson do not apply to the light-toned and dark-toned rocks in the Murray. For example, the fact that quartz is detected in Telegraph Peak and is not detected in Buckskin (high-silica) (See Table S3.1) does not necessarily indicate that diagenetic processes weathered pre-existing quartz in the high-silica Murray; instead, it may be possible high-silica Murray had a distinct set of original mineralogic composition compared to the nominal composition of the unit.

High-silica Murray, however, is posited to be a possible source of Si in Stimson halos upsection, due to the need for some level of active enrichment of Si in the halos (Frydenvang et al., 2017; Yen et al., 2017). Thus, the silica forms in Si-rich Murray may serve as useful diagnostics of the groundwater system. The presence of opal-CT in Buckskin and absence of quartz is commensurate with a groundwater alteration scenario that swiftly ended, so as to limit the dissolution of quartz altogether; a scenario we posit to be consistent with Stimson halo phases. If we assume the same

alteration event produced both the opal-CT in the Murray and the opal-A in the Stimson fracture halos, it is likely the case that the solubility conditions in the Murray and Stimson were distinct, either due to pH or chemistry (since temperature and pressure would have been more or less identical). We must also admit the possibility that the opal-CT observed in high-silica Murray was also detrital or matured from detrital opal-A. In any case, the total integrated interaction time of high-silica Murray with water must have been limited considering the opal-CT should undergo maturation to quartz in at most ∼100–400 Ma in the presence of fluids in cold martian conditions (0°C) (Tosca and Knoll, 2009).

There are several lines of evidence that suggest the formation environment of the Darwin-suite halos downsection may have been similar, or potentially related, to the Stimson halos. The Darwin-suite halos in the Bradbury unit are, like their Stimson counterparts, at the margins of fractures that crosscut bedding and are within a few tens of centimeters in width (Figure 3.1). Geochemically, these halos show similar trends in Fe, Mg, and Si as those seen in Stimson halos (Figure 3.3), which produces a low in neutron absorption cross section (Figure 3.3. Thus Darwin-suite halos produce considerable anomalies in thermal neutron signal in passive experiments taken during and outside of rover mobility (Figure 3.5 and S10) and in active experiments which indicate an anomalously low value of ξ_{abs}. The halo networks observed in the Bradbury group are also seen to extend to great distances, beyond the field-of-view of NavCam imaging (see Figure S3.10), which potentially indicates they may be as extensive as those found in the Stimson; we demonstrate in Figure S3.7 that halo networks at the Pahrump Hills region extend across swaths of hundreds of meters of landscape. In any case, the existence of halos in the Bradbury group and their potentially similar formation environment may suggest that the groundwater event

posited for the formation of Stimson halos may have been more laterally extensive, similarly altering lakebed units with prexisting fracture networks in Gale crater. Given that the Bradbury group is laterally extensive, this may imply that event may have played a role in vast regions of Gale crater.

3.6 Conclusion

We performed a wide-spread sampling of the H content in the Stimson unit, which includes altered (light-toned) and unaltered rocks. We find that the unaltered rocks in the unit have a water content in the range of ∼0.7-2.0 wt.% H_2O-equiv. H. The lower end of this range (∼0.7-1.4 wt.% H_2O-equiv. H) likely represents an unaltered end-member composition. Using a specialized model to account for the presence of a geochemically-distinct fracture-associated halo, we found the water content of the Lubango and Greenhorn halos to be 5.1±0.9 wt.% H_2O-equiv. H and 5.3±0.7 wt.% H_2O-equiv. H, respectively. In both the unaltered and altered rocks, the hydrated crystalline phases make up a minimal fraction of the bulk water content, demonstrating that H-rich amorphous phases are the dominant carriers of water in the unit. Our result, combined with the fact that the halos are significantly enriched in amorphous fraction (∼70-85%), their amorphous fraction contains elevated silica (∼60-65%), and LIBS shots of halos show Si and H are correlated (Rapin et al., 2018), suggests altered Stimson rocks are likely abundant in opal-A (e.g. Rapin et al., 2018; Yen et al., 2017), along with amorphous sulfates inferred from their amorphous geochemistry (Yen et al., 2017) and observed in Evolved Gas Analysis experiments (Sutter et al., 2017). Furthermore, our analysis of thermal neutron die-away data indicates that the fracture halos are not surficial and extend, in at least one location, to ∼20-40 cm

depth, which is consistent with variability in the degree of alteration along the vertical Stimson fractures. Some level of dehydration at the surface is also consistent with our results and those of Rapin et al. (2018), however this effect could not be positively identified due to the uncertainties of the two measurements.

In light of the mineralogies of high-silica rocks and their unaltered counterparts, particularly in terms of the diagenetic silica phases, we find that these halos mark the products of the last groundwater even in Gale crater. The present of opal-A in fracture halos and absence of opal-CT or enhancement of quartz indicates that the diagenetic process was stunted abruptly. A range of mechanisms may be invoked for rapid changes in the solubility of silica, ranging from rapidly changing pH and temperature conditions, however, we suggest the rapid retreat of groundwater must have played a role. Futhermore, the persistence of these high-silica rocks to modern day indicate a post-depositional environment that was relatively low temperature and dry, consistent with current conditions posited to exist throughout the Amazonian era on Mars. The presence of water-rich opal-A on Mars presents itself as an ideal resource for in-situ utilization, considering the mild operating conditions at equatorial Mars (as compared to the poles), the ease of extraction of water from poorly-ordered silica through vacuum and/or moderate baking, and the fact that $\sim$4-6 kg of water is held in a single 1-meter-long halo. Even at moderate water extraction efficiency through grinding and/or low-temperature baking, these features provide a substantial resource.

We also report on the existence of light-toned fracture halos in an adjacent geologic unit (Bradbury) at the Darwin waypoint. These halos are remarkably similar in appearance and scale, and have have similar chemical trends to halos observed in the Stimson. Passive thermal neutron data, which correspond strongly with the presence

of hydrated high-silica rocks in the Stimson, is also elevated over these features. This suggests the halos in the Bradbury may have undergone an alteration event similar to those that generated Stimson halos and that the groundwater system, which is understood to have produced fracture-associated halos in the Stimson, played a more widespread role in the alteration of Gale crater rocks regionally. We encourage the examination of Bradbury halos using orbital datasets since this geologic group is laterally extensive, presenting an additional, potentially vast resource of water for future in-situ utilization. Moreover, the identification of similar Si-poor and H-rich fracture networks throughout the crater would help define the extent of the last groundwater event in Gale crater.

3.7 Supplementary Materials

This Supplementary Information includes two distinct materials: (1) a description of the data processing pipeline for active DAN measurements and (2) supporting figures and tables for the main manuscript. All data products for the DAN instrument used in the preparation of this manuscript are hosted publicly on the Planetary Data System (PDS) (www.pds.nasa.gov). Tools for preprocessing of binary data products to (raw) active DAN count data are also available as part of the PDS.

3.7.1 Active DAN Data Analysis

Measured data from the CTN and CETN detectors, $\mathbf{D}^{\mathrm{CTN}}$ and $\mathbf{D}^{\mathrm{CETN}}$ respectively, are compared to those provided by MCNP6 models of the experiment, $\mathbf{M}^{\mathrm{CTN}}$ and $\mathbf{M}^{\mathrm{CETN}}$ respectively. Using the Monte Carlo N-Particle 6 (MCNP6) transfer code,

the DAN active experiment will be modeled several times, each model will vary some aspect of the geochemistry of the martian subsurface. Often the hydrogen content will be varied, while all other elemental abundances and rover components are kept constant. The abundance of other major rock-forming elements are sourced from APXS experiments (see Table S3.2). A set of models, with variable hydrogen and other free parameters, are then compared to the measurement in order to find a 'best-fit' model (e.g. Mitrofanov et al., 2014; Sanin et al., 2015).

Unlike in the MCNP6 models for active DAN experiments, where the PNG is the only source of neutrons, the actual active DAN experiment on Mars is subject to background signal. This signal is due to both cosmic-ray bombardment that produces thermalized neutrons and the alpha decay of 238-plutonium from the Multi-Mission Radioisotope Thermoelectric Generator (MMRTG) which is the primary power source for the Curiosity Rover. This background signal is constant over the course of a ∼20-minute active DAN experiment and can be directly computed from neutron die-away curves by taking advantage of the design of the detector integration time (Sanin et al., 2015); after the decay of thermal neutrons returning from the subsurface after a single pulse, the detectors remain on for some time to detect the background signal. Although Sanin et al. (2015) describes the correction of background used herein, we outline these steps for completeness. Long after the peak arrival of thermalized neutrons, the DAN detectors continue integrating for a total time of 100,000 μs in 64 time bins. These late time bins can be used to compute a background count rate which can then be subtracted from the spectra (Sanin et al., 2015). Using the time bins from Sanin et al. (2015), b_i^{BG}=48 and b_f^{BG}=63 (counting from 1, with endpoints included),

we first compute the total number of counts in late time bins in both detectors,

$$\begin{aligned} C_{\rm BG}^{\rm CTN} &= \sum_{b_i^{\rm BG}}^{b_f^{\rm BG}} \mathbf{D}^{\rm CTN} \\ C_{\rm BG}^{\rm CETN} &= \sum_{b_i^{\rm BG}}^{b_f^{\rm BG}} \mathbf{D}^{\rm CETN}, \end{aligned}$$

and divide the count number by the total elapsed time from bin 48 to 63, $\Delta t_{\rm BG} = 54278.7\ \mu$s,

$$\begin{aligned} \dot{C}_{\rm BG}^{\rm CTN} &= \frac{C_{\rm BG}^{\rm CTN}}{\Delta t_{\rm BG}} \\ \dot{C}_{\rm BG}^{\rm CETN} &= \frac{C_{\rm BG}^{\rm CETN}}{\Delta t_{\rm BG}}. \end{aligned}$$

The uncertainty in the background count rate is also computed,

$$\begin{aligned} \delta_{\rm BG}^{\rm CTN} &= \frac{1}{\Delta t_{\rm BG}} \sqrt{\sum_{b_i^{\rm BG}}^{b_f^{\rm BG}} \left(\delta_{\mathbf{D}^{\rm CTN}}\right)^2} \\ \delta_{\rm BG}^{\rm CETN} &= \frac{1}{\Delta t_{\rm BG}} \sqrt{\sum_{b_i^{\rm BG}}^{b_f^{\rm BG}} \left(\delta_{\mathbf{D}^{\rm CETN}}\right)^2}, \end{aligned}$$

where $\delta_{\mathbf{D}}$ is the 1σ uncertainty in the DAN count data $\mathbf{D}$. We assume the count data follows the Poisson distribution, *i.e.* $\delta_{\mathbf{D}} = \sqrt{\mathbf{D}}$.

Then the contribution of background is removed from each bin according to the background count rate for the particular detector and the time elapsed in each bin, *i.e.* the width of the corresponding time bin,

$$\mathbf{D}'^{\rm CTN} = \mathbf{D}^{\rm CTN} - \dot{C}_{\rm BG}^{\rm CTN} \Delta \mathbf{t}$$

$$\mathbf{D}'^{\mathrm{CETN}} = \mathbf{D}^{\mathrm{CETN}} - \dot{C}_{\mathrm{BG}}^{\mathrm{CETN}} \Delta \mathbf{t}.$$

The uncertainty in this computation is also propagated for each time bin,

$$\delta'_{\mathbf{D}^{\mathrm{CTN}}} = \sqrt{\left(\delta_{\mathbf{D}^{\mathrm{CTN}}}\right)^2 + \left(\delta_{\mathrm{BG}}^{\mathrm{CTN}} \Delta \mathbf{t}\right)^2}$$
$$\delta'_{\mathbf{D}^{\mathrm{CETN}}} = \sqrt{\left(\delta_{\mathbf{D}^{\mathrm{CETN}}}\right)^2 + \left(\delta_{\mathrm{BG}}^{\mathrm{CETN}} \Delta \mathbf{t}\right)^2}$$

and the effect of background subtraction is demonstrated in demonstrated in (Gabriel et al., 2018; Sanin et al., 2015).

Since the overall shape of neutron die-away curves are indicative of subsurface geochemistry (Hardgrove et al., 2011) we compare the shape of die-away curves for the time bins that demonstrate the most dynamic range with respect to changing subsurface geochemistry (Sanin et al., 2015). The time bins used herein are similar to those in Sanin et al. (2015), b_i^{CTN}=18 and b_f^{CTN}=34 in the CTN detector, and b_i^{CETN}=13 and b_f^{CETN}=17 in the CETN detector (counting from 1). We first normalize the MCNP6 count tally data to that of the DAN data in the time bins of interest, effectively translating the model tally data into count space. First, we compute a sum of the detector data separately for both detectors,

$$U^{\mathrm{CTN}} = \sum_{b_i^{\mathrm{CTN}}}^{b_f^{\mathrm{CTN}}} \mathbf{D}'^{\mathrm{CTN}}$$
$$U^{\mathrm{CETN}} = \sum_{b_i^{\mathrm{CETN}}}^{b_f^{\mathrm{CETN}}} \mathbf{D}'^{\mathrm{CETN}}.$$

The uncertainty of the sum is also computed,

$$\begin{aligned}
\delta_{U^{\mathrm{CTN}}} &= \sqrt{\sum_{b_i^{\mathrm{CTN}}}^{b_f^{\mathrm{CTN}}} \left(\delta'_{\mathbf{D}^{\mathrm{CTN}}}\right)^2} \\
\delta_{U^{\mathrm{CETN}}} &= \sqrt{\sum_{b_i^{\mathrm{CETN}}}^{b_f^{\mathrm{CETN}}} \left(\delta'_{\mathbf{D}^{\mathrm{CETN}}}\right)^2}.
\end{aligned}$$

Then, we compute the same sum of the *model* data, separately for both detectors,

$$\begin{aligned}
V^{\mathrm{CTN}} &= \sum_{b_i^{\mathrm{CTN}}}^{b_f^{\mathrm{CTN}}} \mathbf{M}^{\mathrm{CTN}} \\
V^{\mathrm{CETN}} &= \sum_{b_i^{\mathrm{CETN}}}^{b_f^{\mathrm{CETN}}} \mathbf{M}^{\mathrm{CETN}}.
\end{aligned}$$

The uncertainty of the sum is also computed,

$$\begin{aligned}
\delta_{V^{\mathrm{CTN}}} &= \sqrt{\sum_{b_i^{\mathrm{CTN}}}^{b_f^{\mathrm{CTN}}} \left(\delta_{\mathbf{M}^{\mathrm{CTN}}}\right)^2} \\
\delta_{V^{\mathrm{CETN}}} &= \sqrt{\sum_{b_i^{\mathrm{CETN}}}^{b_f^{\mathrm{CETN}}} \left(\delta_{\mathbf{M}^{\mathrm{CETN}}}\right)^2}.
\end{aligned}$$

By dividing both sums, U and V, we arrive at the conversion factor X that converts tally data to count space,

$$\begin{aligned}
X^{\mathrm{CTN}} &= \frac{U^{\mathrm{CTN}}}{V^{\mathrm{CTN}}}, \\
X^{\mathrm{CETN}} &= \frac{U^{\mathrm{CETN}}}{V^{\mathrm{CETN}}},
\end{aligned}$$

with error propagated as such:

$$\begin{aligned}
\delta_{X^{\mathrm{CTN}}} &= \frac{U^{\mathrm{CTN}}}{V^{\mathrm{CTN}}}\sqrt{\left(\frac{\delta_{U^{\mathrm{CTN}}}}{U^{\mathrm{CTN}}}\right)^2+\left(\frac{\delta_{V^{\mathrm{CTN}}}}{V^{\mathrm{CTN}}}\right)^2} \\
\delta_{X^{\mathrm{CETN}}} &= \frac{U^{\mathrm{CETN}}}{V^{\mathrm{CETN}}}\sqrt{\left(\frac{\delta_{U^{\mathrm{CETN}}}}{U^{\mathrm{CETN}}}\right)^2+\left(\frac{\delta_{V^{\mathrm{CETN}}}}{V^{\mathrm{CETN}}}\right)^2}.
\end{aligned}$$

Then the tally data from MCNP6 models are normalized,

$$\begin{aligned}
\mathbf{M}'^{\mathrm{CTN}} &= \mathbf{M}^{\mathrm{CTN}}X^{\mathrm{CTN}} \\
\mathbf{M}'^{\mathrm{CETN}} &= \mathbf{M}^{\mathrm{CETN}}X^{\mathrm{CETN}}
\end{aligned}$$

and the error is propagated,

$$\begin{aligned}
\delta'^{\mathrm{CTN}}_{\mathbf{M}} &= \mathbf{M}^{\mathrm{CTN}}X^{\mathrm{CTN}}\sqrt{\left(\frac{\delta_{\mathbf{M}^{\mathrm{CTN}}}}{\mathbf{M}^{\mathrm{CTN}}}\right)^2+\left(\frac{\delta_{X^{\mathrm{CTN}}}}{X^{\mathrm{CTN}}}\right)^2} \\
\delta'^{\mathrm{CETN}}_{\mathbf{M}} &= \mathbf{M}^{\mathrm{CETN}}X^{\mathrm{CETN}}\sqrt{\left(\frac{\delta_{\mathbf{M}^{\mathrm{CETN}}}}{\mathbf{M}^{\mathrm{CETN}}}\right)^2+\left(\frac{\delta_{X^{\mathrm{CETN}}}}{X^{\mathrm{CETN}}}\right)^2}.
\end{aligned}$$

At this point, the normalized model data, $\mathbf{M}'$, can be compared to background subtracted data, $\mathbf{D}'$, from an active DAN experiment.

Instead of minimizing the χ^2 parameter as a means of finding a best-fit model, as is performed in Mitrofanov et al. (2014) and Sanin et al. (2015), we employ a Markov Chain Monte Carlo (MCMC) method (Foreman-Mackey et al., 2013) to maximize the likelihood function, or more specifically minimize the negative log of the likelihood function:

$$\mathcal{L} = -\frac{1}{2}\sum_i^N\left(\frac{(C_i-\mathcal{M}_i(p_0,p_1,...,p_N)}{\sigma_i^2}+ln(2\pi\sigma_i^2)\right),$$

where C_i is the measurement data, $\mathcal{M}_i$ an interpolant of the modeled data as a function of the free parameters, *e.g.* H abundance, and the sum is taken over the range of time bins in the CTN detector shown in Figure S3.4. We have found that the CETN detector is not diagnostic, *i.e.* lacks dynamic range over the parameters of this study, and thus it is excluded from this analysis. The variance of the data and the model in each time bin is captured by the σ_i^2 term,

$$\sigma_i^2 = \delta C_i^2 + \delta \mathcal{M}_i^2(p_0, p_1, ..., p_N) + f^2,$$

where δC_i is the uncertainty of DAN data and $\delta \mathcal{M}_i$ is the uncertainty in the modeled spectra. Our MCNP6 models simulate 2.5e9 particles which provides $<<5\%$ relative error in modeled spectra for the time bins of interest. We conservatively set $\delta \mathcal{M}_i$ to be a constant 5% relative error. A new free parameter has been introduced, f, which represents the underestimation of the count uncertainty. Larger values of this parameter indicate either poor statistical convergence in the model, poor statistical convergence in the measurement, and/or a poor overall fit of the model to the data, *i.e.* inaccurate model assumptions; however, in our study we find reasonable values of f, *i.e.* f is less than a few percent of the counts in DAN spectra. In sum, the MCMC routine will find the combination of hydrogen abundance and other free parameters, *e.g.* depth, that best fits the observed spectra, while also accounting for underestimated uncertainties.

The computational resources to generate a synthetic model of active DAN spectra using the MCNP6 code is not insignificant, on the order of several hours per model on $\sim$100 core compute clusters and on the order of days on modern desktops. Thus the generation of model data cannot occur 'in line' with the MCMC routine, but rather a 'grid' of models are generated beforehand. A model grid is composed of models that

vary the free parameters, $p_0, p_1, ..., p_N$, to discrete values for which we are trying to find a non-discrete 'best-fit' value of the free parameters. In the case of DAN, examples of free parameters include hydrogen content, depth of a geochemically-distinct top layer, bulk density, etc. In the analysis to determine the water content of the local (Murray formation) bedrock performed herein, we allowed only hydrogen content to vary, from 1 WEH to 6 WEH in increments of 0.2 WEH.

Once a model grid is simulated, an interpolant is generated, $\mathcal{M}(p_0, p_1, ..., p_N)$, which allows the MCMC routine to produce modeled active DAN spectra at non-discrete parameter values. We choose to employ a linear interpolant, which assumes the behavior of the count rate as a function of the free parameter is linear, for a given bin, between discrete increments of the parameters. This assumption is appropriate when the free parameters have sufficient resolution; we find a resolution of 0.2-0.4 WEH is an appropriate sampling resolution for bulk water content and 5-10 cm is an appropriate sampling resolution for depth.

Before comparing the model grid to data, the MCMC routine requires an *a priori* 'guess' of the free parameters for each walker. We found the results of this study are rather insensitive to the initial conditions, provided the MCMC routine is allowed sufficient iterations. The *a priori* (mean and 1 standard deviation) for the water content of the bedrock in the homogeneous model was 3.0 $\pm$ 0.3 WEH. For the two-layer models, the *a priori* for the dune hydrogen was 1.0 $\pm$ 0.3 WEH and the *a priori* for the depth was 40 $\pm$ 10 cm. In both cases the *a priori* for the parameter f was 40 $\pm$ 10 counts. We simulated $8N_p$ walkers, where N_p is the number of free parameters; $N_p = 1$ in the case of the bedrock model analysis (variable hydrogen in a single layer) and $N_p = 2$ in the case of the dune analysis (variable hydrogen in the top layer, variable thickness of the top layer). We allowed the walkers to perform

10,000 steps (iterations) in the parameter space before the routine is halted. The mean and standard deviation of the free parameters are determined using the last 9,000 positions of each of the $8N_p$ walkers.

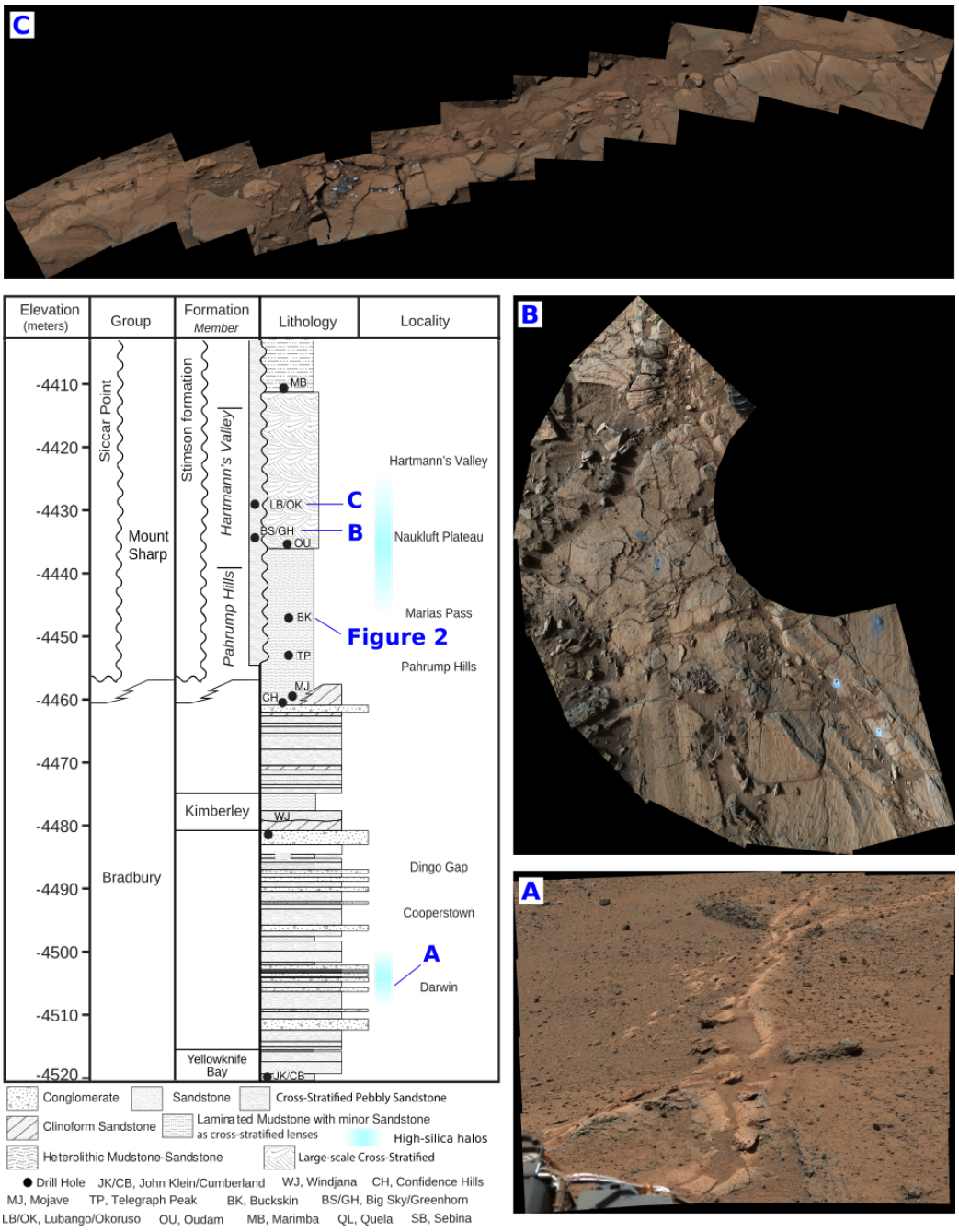

Figure 3.1. Shown is a geologic cross section of Gale crater with areas of high-silica fracture-associated halos shown. High-silica halos have been observed in the Bradbury group (A) and throughout Marias Pass and Naukluft Plateau. Two pairs of drill sites at altered and unaltered material were performed Naukluft plateau: the Greenhorn/Big Sky (B) and the Lubango/Okoruso (C) targets. Fracture halos were observed at the Stimson-Murray contact (Frydenvang et al., 2017), near regions of high-silica bedrock in the Murray.

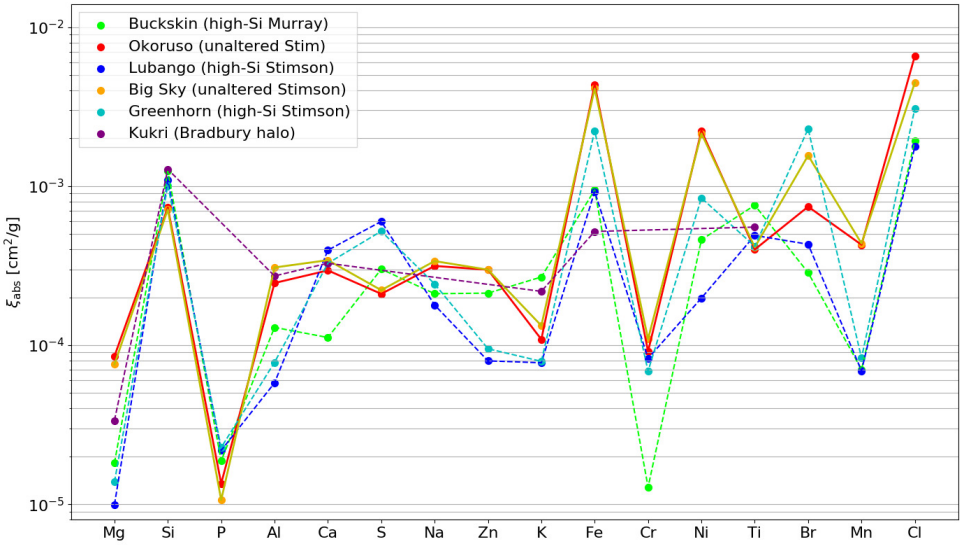

Figure 3.2. The macroscopic cross section, ξ_{abs}, for the major rock-forming elements provided by APXS measurements of drill tailings in log-space. Elemental species are shown in increasing order of their microscopic absorption cross section σ_{abs} (see Table 3.1). High-silica rocks show systematic depletion in Mg, Al, Na, Zn, K, Cr, Mn, and Cl, as well as systematic enhancement in Si and S. The geochemical trends in the halo found in the Bradbury also follows similar trends. Geochemical abundances for some of these targets are reported in Table S3.4.

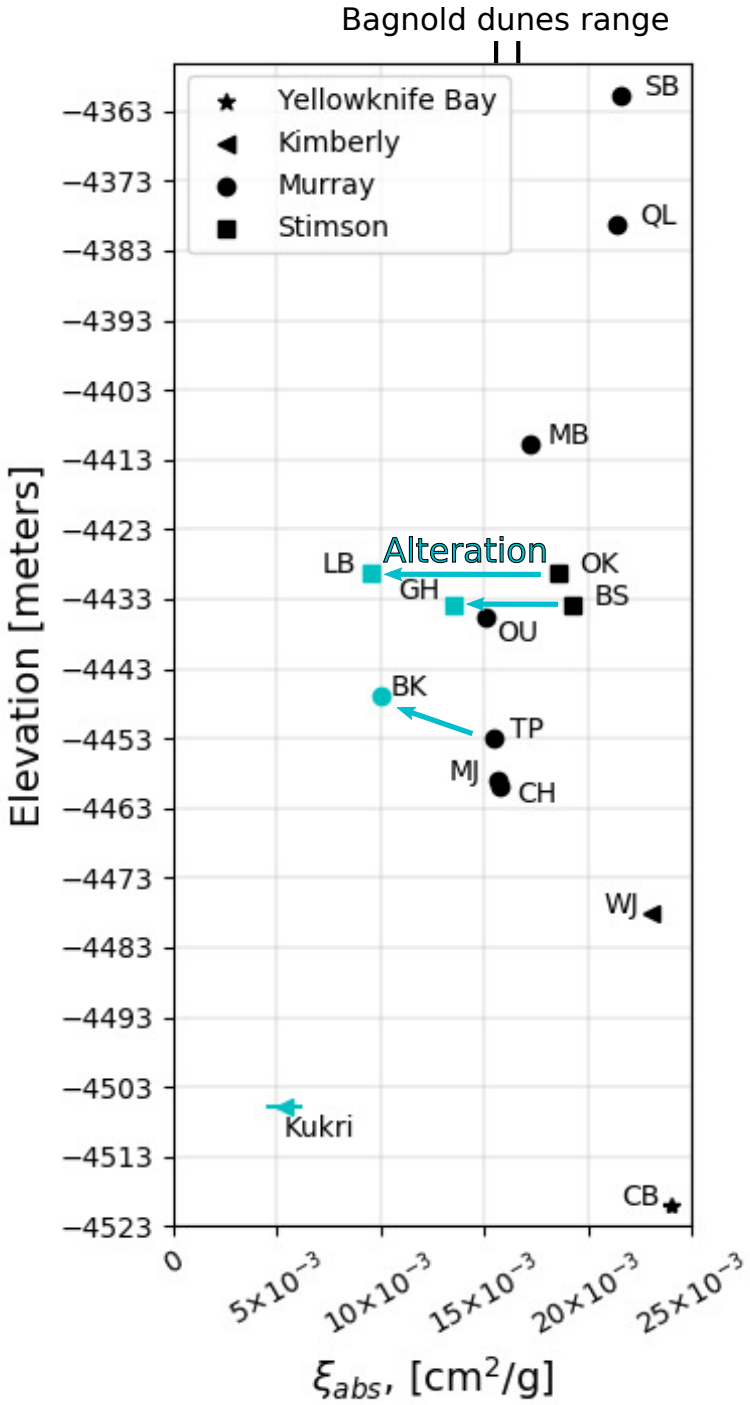

Figure 3.3. Shown is the macroscopic neutron absorption cross section, ξ_{abs}, of drill targets in Gale crater as a function of their elevation; uncertainties are on the order of $\sim 10^{-4} - 10^{-5}$ cm^2/g and are within the size of the symbol with the exception of the Kukri target. Cyan symbols represent high-silica rocks and show distinctly smaller values of ξ_{abs} due to their low Fe and Cl content. See Table S3.7 for the list of target names and APXS products used in the figure.

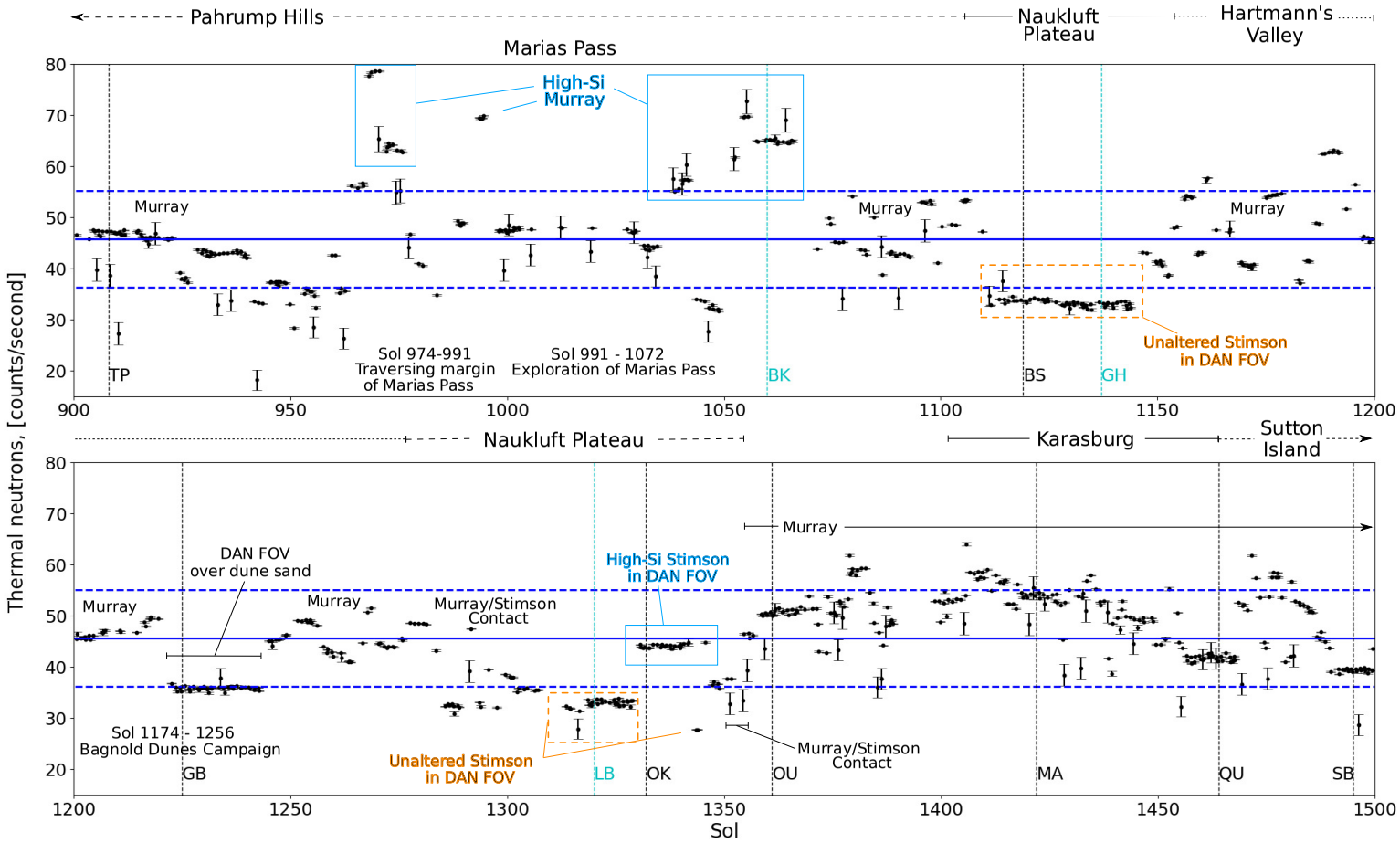

Figure 3.4. Thermal neutron (0.001 eV < E < 0.4 eV) count rates from the DAN instrument in passive mode from sol 900 to 1500; the count rate of the CETN detector (0.4 eV < E < 100 keV) was subtracted from the CTN detector (0.001 eV < E < 100 keV). Results were averaged along intervals of 0.25 sols and uncertainty in count rates (which were assumed to be Poisson-distributed) were added in quadrature. The mean and one standard deviation of the count rates between sol 900 and 1500 are shown as the blue solid and dotted lines respectively. Drilling sols are shown as vertical lines with the acronym for the target shown along the x axis. The Gobabeb (GB) scooped dune sand target is also shown. Regions of high-silica Murray in the Marias Pass region (sol∼974-1072; top panel) show significant enhancement in the thermal neutron signal (above one standard deviation). Unaltered Stimson (orange labels) has a uniquely low signal with respect to the Murray and is distinct from high-silica Stimson (sol∼1316-1344; bottom panel). Measurements made in the Murray are interspersed throughout the entire range of sols and make up most of the measurements shown.

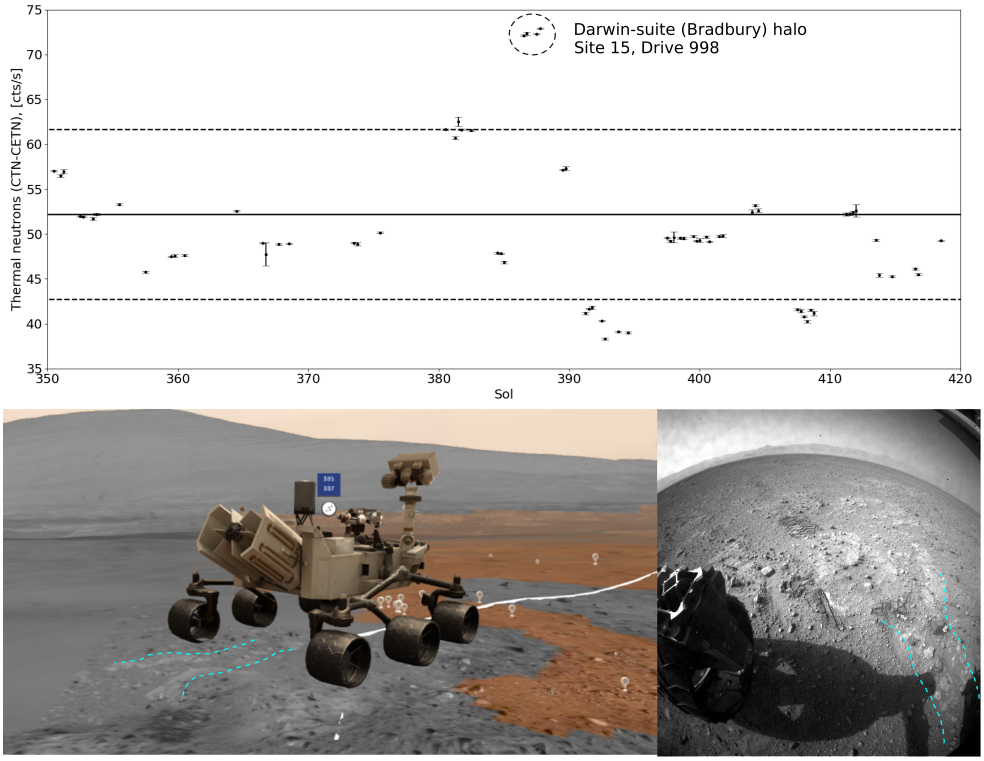

Figure 3.5. Top: Passive thermal neutron count rates at the first Darwin-suite fracture halo in the Bradbury unit; y axis is identical to Figure 3.4. Bottom left: View of site 15, drive 998 of the rover traverse in the JPL OnSight virtual reality tool (Abercrombie et al., 2017); the halo is outlined by the cyan dashed lines. Bottom right: Rear hazcam image (RLB_431684394EDR_F0150998RHAZ00311M1) at the same location.

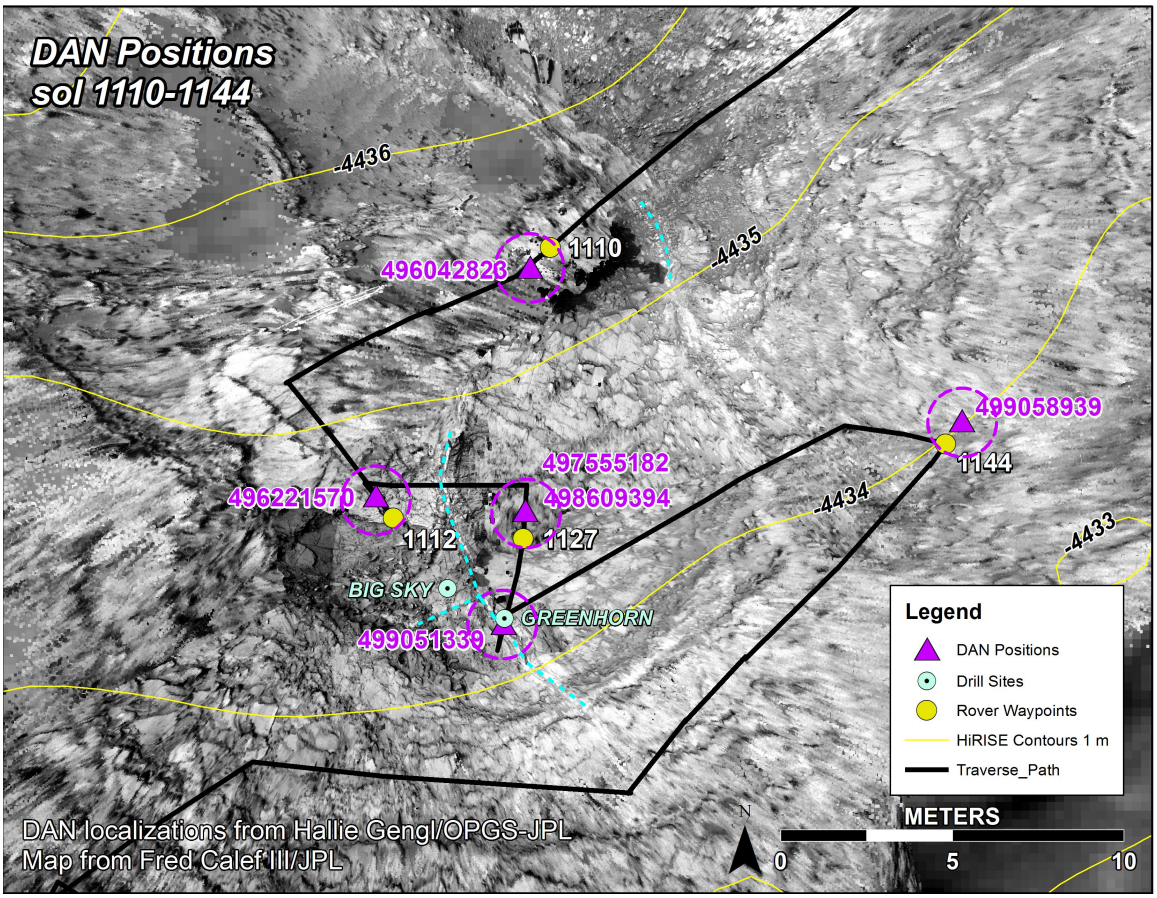

Figure 3.6. Shown is the Curiosity rover drive path (black line) from sol 1110 to 1144. The center of the active DAN field-of-view (midpoint between the rear rover wheels) is shown by purple triangle symbols and the approximate extent is shown by purple dashed lines. The Greenhorn (high-silica) and Big Sky (unaltered Stimson) drill targets are shown by blue circles. Identifiable halos are labeled by the dashed cyan line.

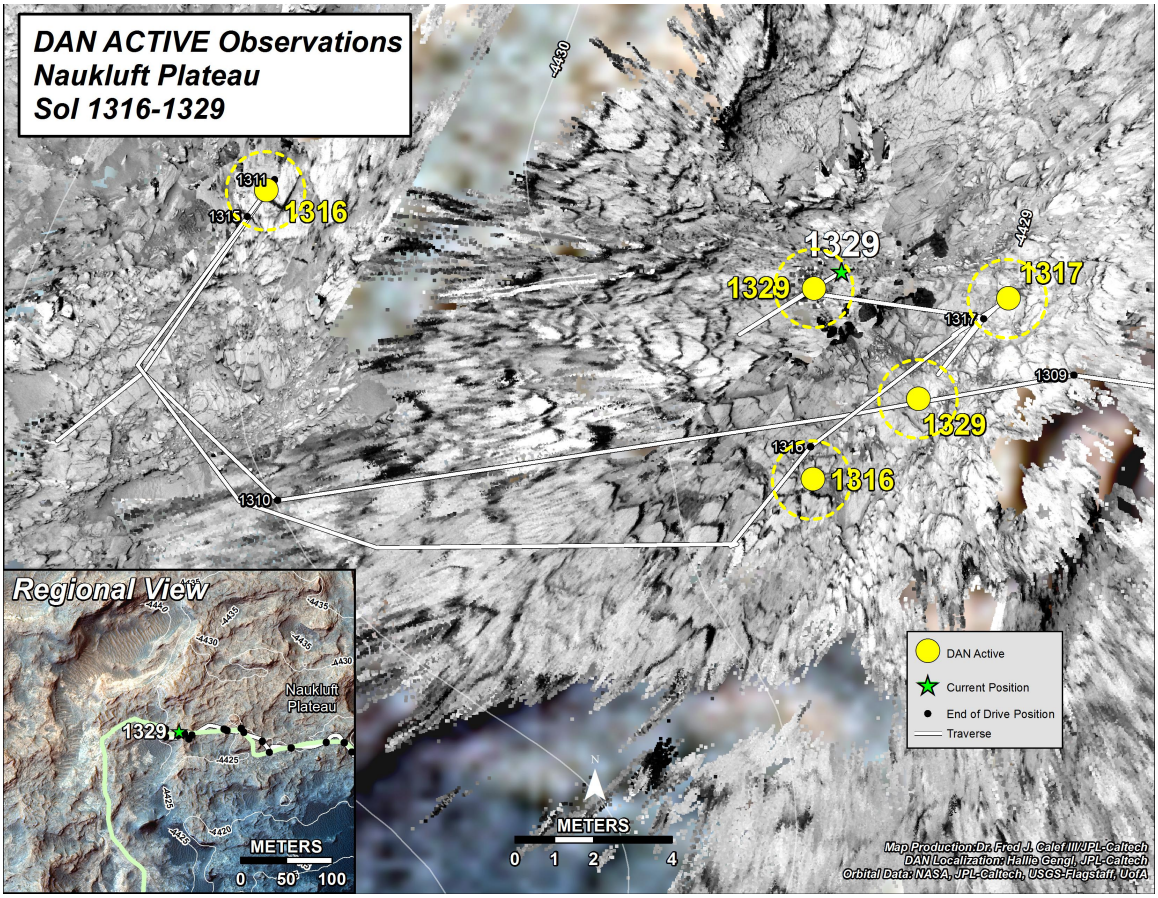

Figure 3.7. Shown is the Curiosity rover drive path (black line) from sol 1316 to 1329. The center of the active DAN field-of-view is shown by yellow circles and the approximate extent is shown by yellow dashed lines.

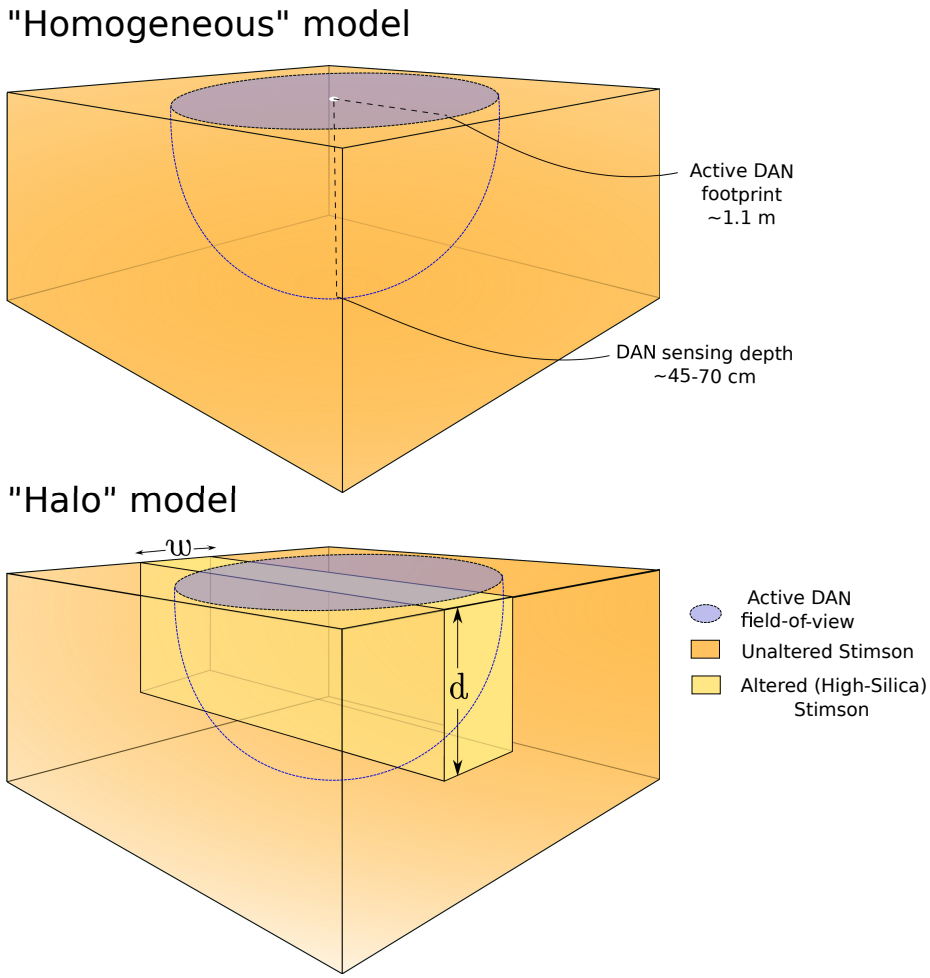

Figure 3.8. Shown is an idealized geometry of the subsurface used in the 'homogeneous' (top) and 'halo' (2-layer; top) particle transport models. Overlain is the active DAN footprint (not to scale). The halo model (bottom) shows a fracture-associated high-silica halo with a width, w, that extends down to a depth, d, and crosscuts the field-of-view.

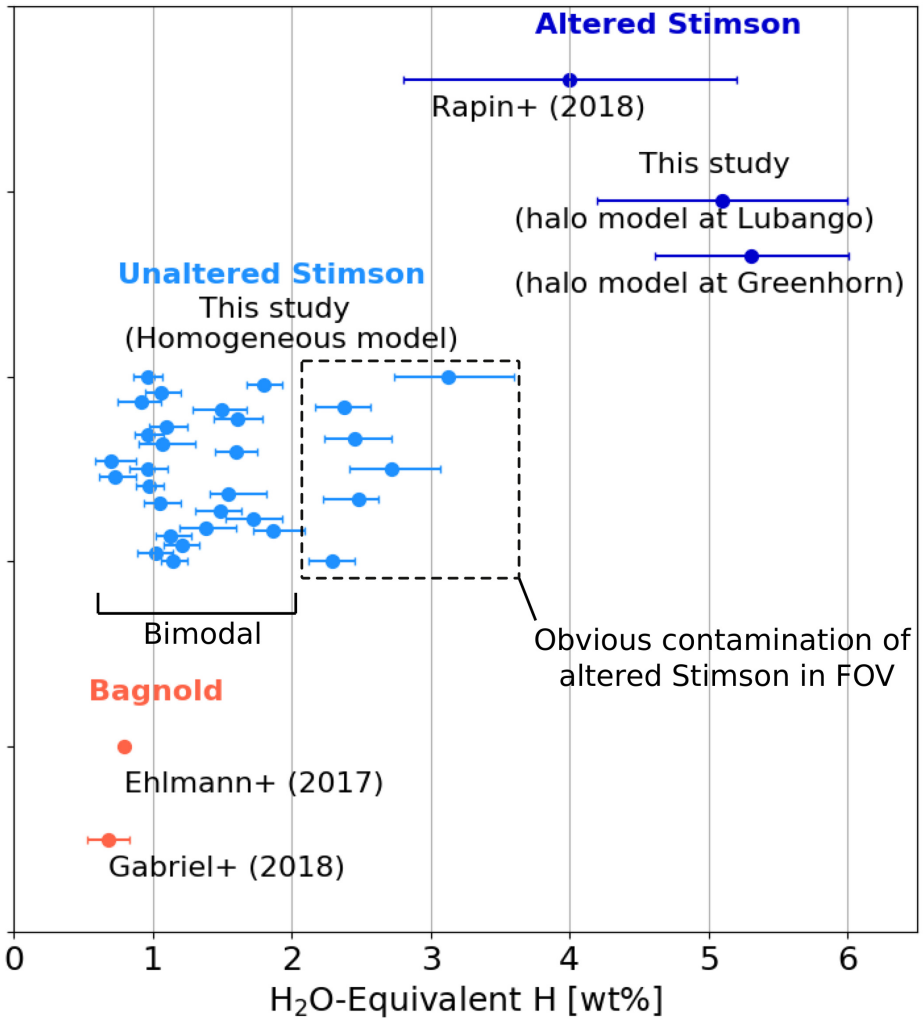

Figure 3.9. Water content of the unaltered, altered Stimson, and Bagnold dunes for comparison. Cyan points represent results where a homogeneous distribution of Okoruso-like geochemistry is assumed; areas where contamination from altered (light-toned) materials in the field-of-view are boxed and potentially bi-modally-distributed data is point labeled. The altered Stimson data shows our results using the new halo model methodology, as compared to results accumulated over many LIBS shots of high-silica targets (Rapin et al., 2018).

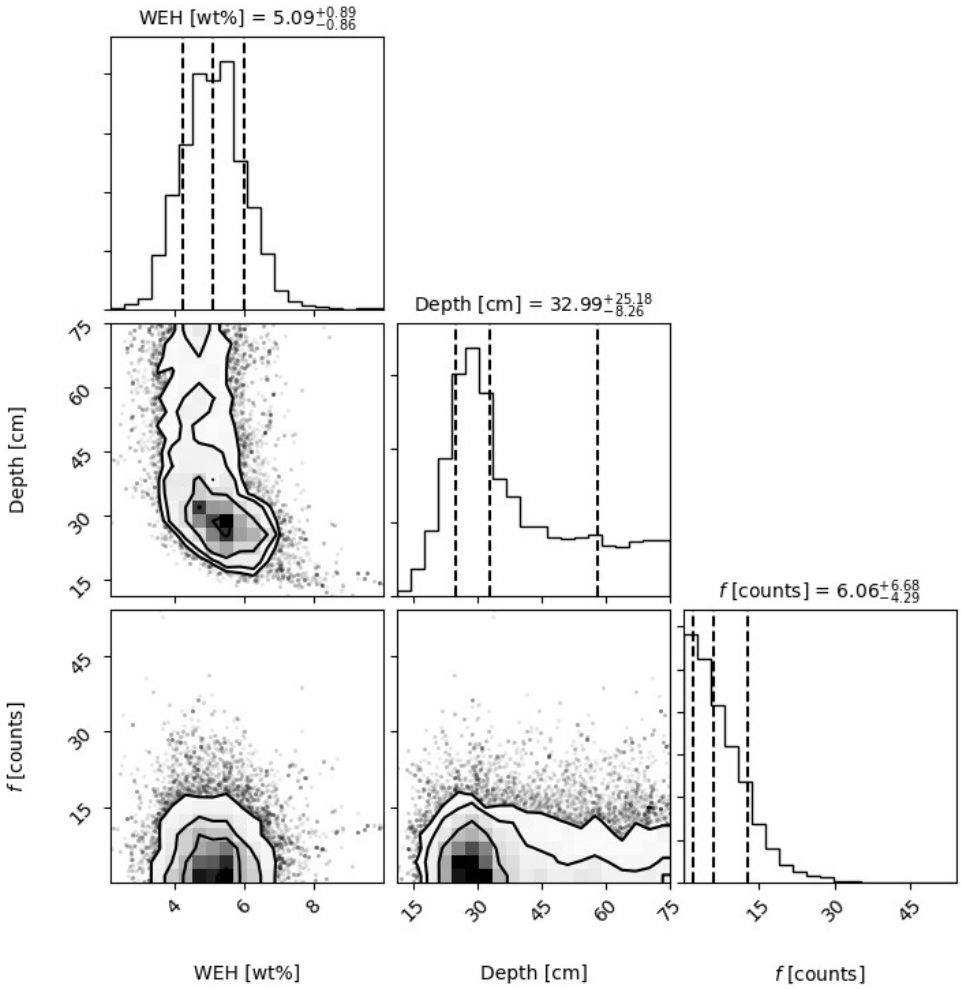

Figure 3.10. The a posteriori distribution of the halo hydrogen content, halo depth, and the f parameter provided by MCMC optimization for the active DAN observation (DNB_515473511EAC13290540812) on sol 1329 over the Lubango fracture halo (top). Diagonal frames represent the marginalized likelihood for each parameter, i.e. 1-dimensional projection of the non-diagonal frame. Dashed lines show the 16%, 50%, and 84% quantiles; 67% of the likelihood lies between the upper and lower quantile.

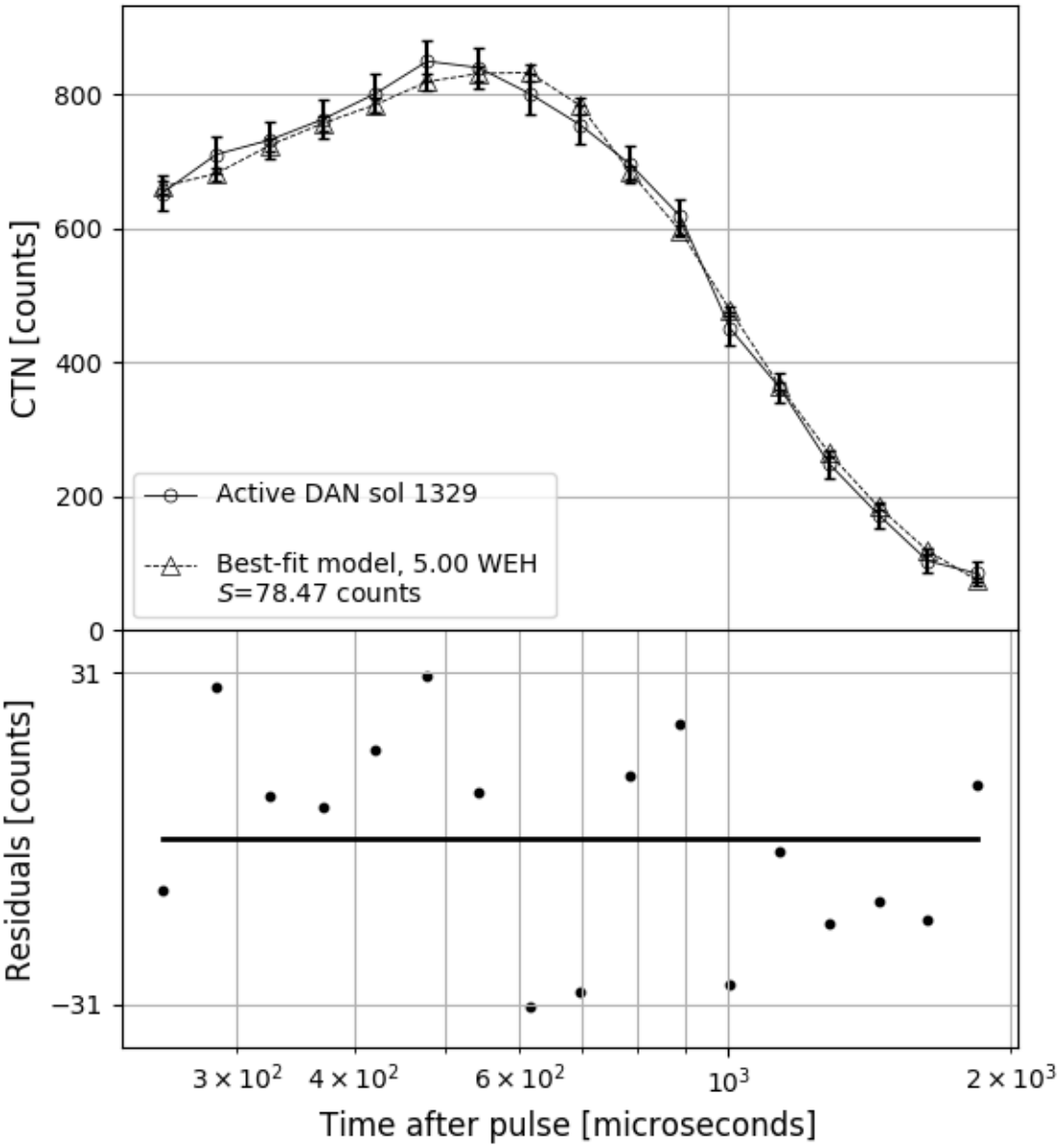

Figure 3.11. Top: The mid-drive, targeted active DAN observation on sol 1329 over the Lubango fracture-associated halo target in Naukluft Plateau compared to an MCMC-optimized model. Bottom: Corresponding data-model residuals. Both frames share the same x-axis. A value near the 50th percentile of water content (5.1±0.9 wt.% H_2O-equiv. H), depth (33 cm), and f (6 counts), as determined from the MCMC optimization, was used to generate this figure (see Figure 3.10).

Table S3.1. Top: Hydrated mineralogical abundances (in wt% of the bulk sample) determined from CheMin X-ray diffraction analysis of drill targets. The portion of the bulk water content attributed to each phase is reported in the parenthetical. Middle: Select anhydrous silica mineral abundances. Bottom: Amorphous fraction of each drill sample from FULLPAT analysis. Hyphens denote phases that are below CheMin sensing limits.

Phase	TP[a]	BK[b]	BS[c]	GH[c]	OK[c]	LB[c]
Bassanite[d]	-	-	-	1.4±0.3 (0.09±0.02)	0.8±0.4 (0.05±0.02)	2.4±0.3 (0.15±0.02)
Gypsum[d]	-	-	-	-	-	0.6±0.2 (0.13±0.04)
Opal-CT		6		-	-	-
Quartz	0.9±0.4	-	1.4±0.3	0.8±0.2	0.9±0.3	0.9±0.2
Anhydrite	-	0.7±0.2	1.2±0.3	5.6±0.3	0.5±0.4	3.3±0.2
Tridymite	-	13.6±0.8	-	-	-	-
Cristob.	7.3±1.7	2.4±0.3	-	-	-	-
Amorph.[e]	27.2±15	60–65	20±10	35±15	65±20	73±20

[a] From E. B. Rampe et al. (2017)
[b] From Morris et al. (2016)
[c] Values originally reported in Yen et al. (2017) have been corrected for APXS-derived oxide constraints.
[d] Stoichiometric abundances were used $CaSO_4 \cdot 0.5H_2O$ and $CaSO_4 \cdot 2H_2O$ for bassanite and gypsum respectively, which yields 6.20 wt% H_2O and 20.92 wt% H_2O respectively.
[e] The lower limit is derived from APXS oxide constraints and the upper limit is derived from FULLPAT analysis.

3.8 Active DAN Field-of-View

The field-of-view of planetary neutron experiments is statistical in nature. In active DAN experiments, neutrons depart from the PNG isotropically and at 14.1 MeV. However, high-energy neutrons are moderated in the subsurface through scattering and absorption interactions. Absorption cross section is inversely proportional to the neutron energy, so moderated neutrons returning to the surface are also more likely to be absorbed and thus not detected. Thus, the exact extent of the field-of-view, both laterally and at depth, is intrinsically dependent on the measured media. Sanin et al.

(2015) reports that a water-enriched lower layer at depths beyond 60 cm produced indistinguishable data from one another; however, the lateral extent of the instrument footprint was not examined, but reported as ∼1.5 m. Since our study is estimating features at the sub-footprint scale we find it prudent to examine the statistical nature of the active DAN field of view. We note that the field of view is sensitive to the composition of the underlying bedrock, so we focus here on end-member compositions relevant to our study.

We performed four simulations with a homogeneous subsurface geochemistry using the Lubango (low neutron absorption cross section; altered Stimson) and Okoruso (moderate neutron absorption cross section; unaltered Stimson) base geochemistries provided by APXS, each with 1 WEH and 5 WEH. We track the flux of neutrons through virtual surfaces placed at different locations in the simulated martian environment. Only particles that arrive at the detectors contribute to the flux through these surfaces.

First, we examine the flux of neutrons as a function of depth. We placed horizontal surfaces from 2.5 cm to 67.5 cm below the surface in increments of 5 cm. For reference, the DAN detector and PNG are ∼80 cm above the martian surface. Figure S3.1 shows the flux of neutrons arriving in both DAN detectors for the four cases. Hydrogen-rich rocks (blue circles, orange triangles) show distinct enhancements in thermal neutron production at all depths compared to their hydrogen-poor counterparts (black circles, red triangles); this an intuitive result since hydrogen is an efficient neutron moderator. The sensitivity as a function of depth is also strongly dependent on the hydrogen content. The epithermal neutron flux for hydrogen-poor models is reduced by a factor of ∼10 at depths of ∼60 cm, whereas in hydrogen-rich models the threshold occurs at ∼35 cm. Thermal neutron flux is similarly sensitive to hydrogen content; the

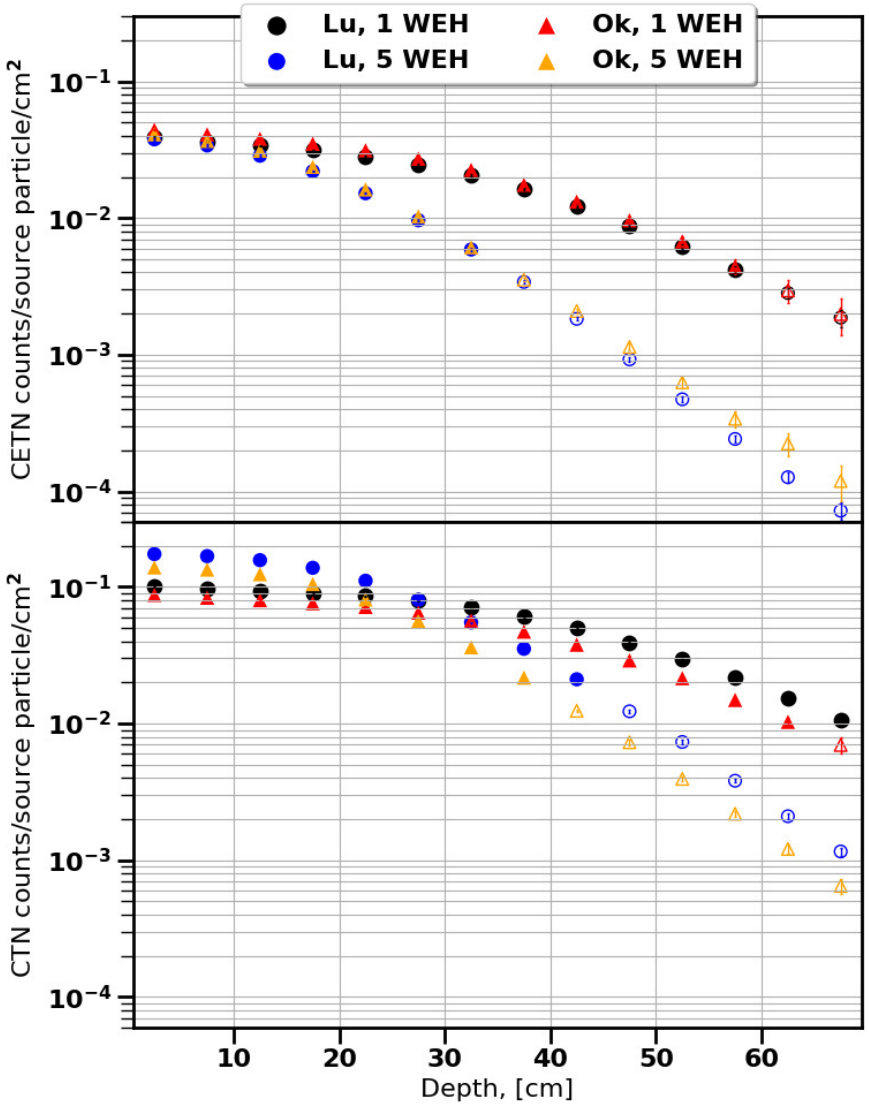

Figure S3.1. Shown is the modeled flux of neutrons in the CETN (top) and CTN (bottom) energy ranges, measured at regularly-space horizontal surfaces below the rover; 1σ uncertainties in the flux tally are provided. Unfilled markers denote flux that is 10 times less than the maximum flux for the simulation.

epithermal neutron flux for hydrogen-poor models is reduced by a factor of ∼10 at depths of ∼65-70 cm, whereas in hydrogen-rich models the threshold occurs at ∼40–45 cm. The change in depth sensitivity is comparably muted between models with similar hydrogen contents (scattering cross sections) and disparate absorption cross sections.

To examine the sensitivity of the DAN experiment in the lateral directions we place vertical tally surfaces in regular increments of 25 cm along the short and long axis of the rover. Figure S3.2 shows that the epithermal and thermal neutron flux decreases in a similar manner across all cases. However, the peak neutron flux lies between the DAN detectors and PNG, not directly below the detectors. The situation is similar along the length of the rover (see Figure S3.3; the field of view in this direction is insensitive to differences in geochemistry.

In sum, the field of view of active DAN measurements can be approximated by a spherical cap, reaching ∼40-70 cm in depth and ∼1 m in radius. The field of view is centered between the rear rover wheels, at the midpoint between the detector and PNG which are located on opposite sides of the rear of the rover. Changes in hydrogen hydrogen content predominantly effect the source depth of thermal and epithermal neutrons neutrons; the lateral extent of the field of view is relatively unchanged by changes in geochemistry. In the context of our active neutron investigation of the Lubango fracture halo, the feature is well within the instrument's sensing area. The apparent smearing of marginalized likelihood of the halo depth at 50 cm (see middle panel of Figure 3.10) is commensurate with the fact that the DAN sensing depth falls off precipitously (roughly by a factor of 10) at these depths, for representative subsurface geochemistries.

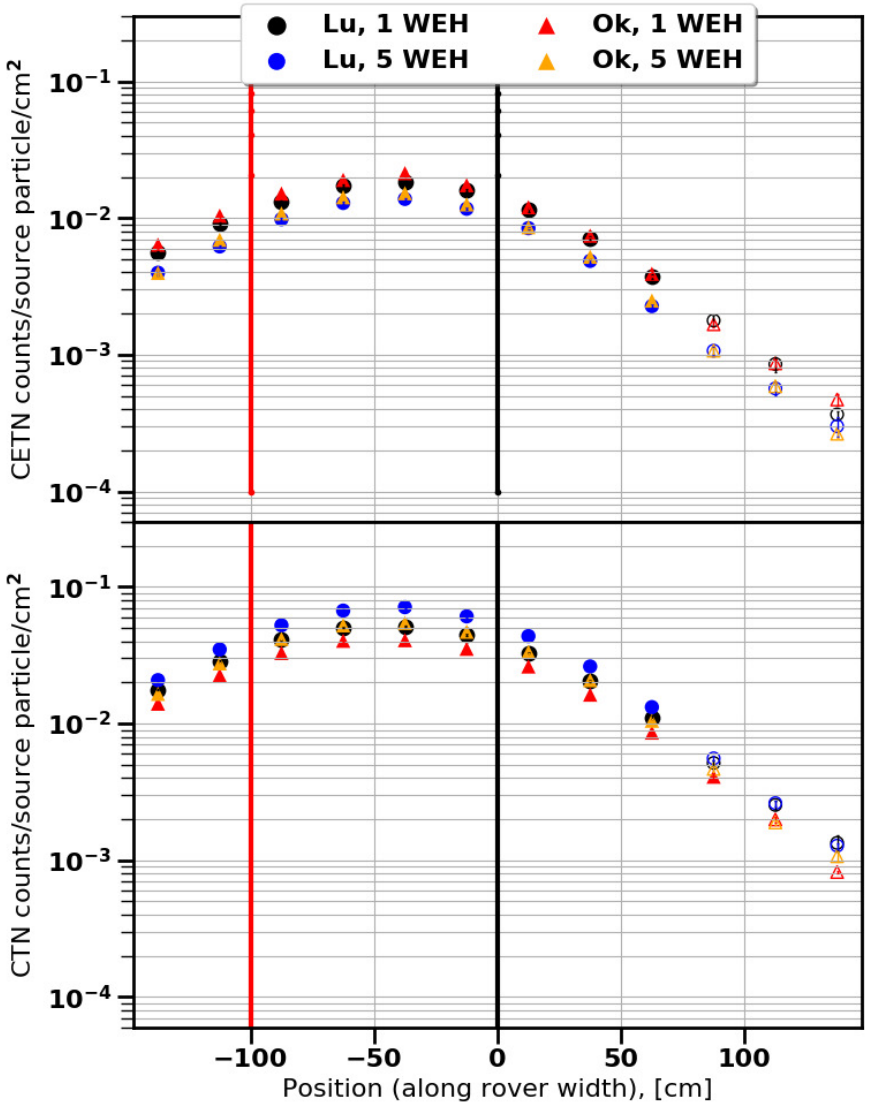

Figure S3.2. Shown is the modeled flux of neutrons in the CETN (top) and CTN (bottom) energy ranges, measured at regularly-spaced vertical surfaces placed along the short edge of the rover; 1σ uncertainties in the flux tally are provided and are generally smaller than the size of the symbol. The detectors are centered at 0 cm (black vertical line) and the point-source of neutrons used to represent the PNG is located at -100 cm (red line). Unfilled markers denote flux that is 10 times less than the maximum flux for the simulation.

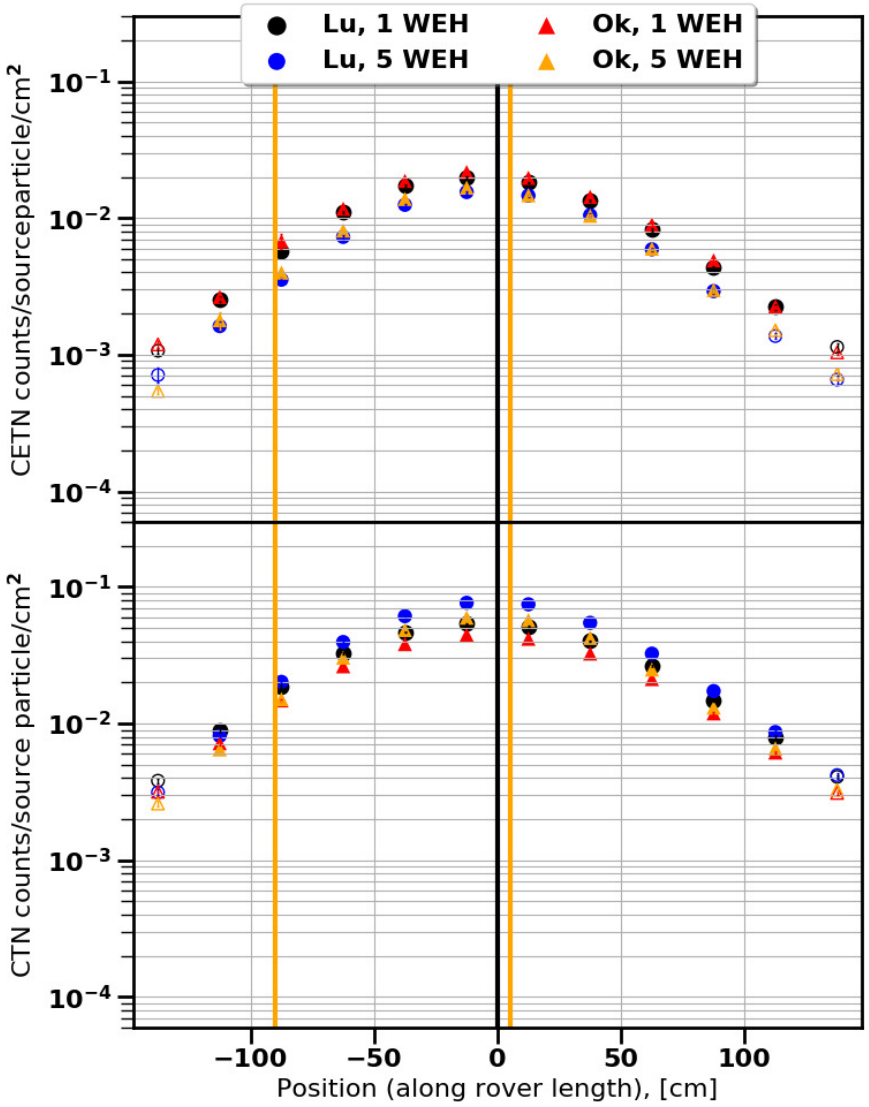

Figure S3.3. Shown is the modeled flux of neutrons in the CETN (top) and CTN (bottom) energy ranges, measured at regularly-spaced vertical surfaces placed along the long edge of the rover; 1σ uncertainties in the flux tally are provided and are generally smaller than the size of the symbol. The detectors are centered at 0 cm (blue vertical line), the rear rover wheel and middle wheel are centered at 5 cm and -85 cm respectively (yellow vertical lines). Unfilled markers denote flux that is 10 times less than the maximum flux for the simulation.

3.9 Dynamic Range of Active DAN Models

Previous studies have examined the response of active (time-resolved) DAN spectra to changes in the underlying geochemistry (e.g. Hardgrove et al., 2011). However, it prudent to demonstrate the dynamic range of DAN spectra (from models) in at least a simple case to demonstrate discernability in the shapes of die-away profiles. In Figure S3.4 we provide a heatmap of DAN count data for both detectors which demonstrates fundamental differences between the response of the two detectors. The CTN detector (sensitive to thermal and epithermal neutrons) shows a relatively large region where the subsurface chemistry shows appreciable differences in counts as a function of bulk H content. The dynamic range in the CETN detector (sensitive only to epithermal neutrons) is much more muted comparatively and the range of bins examined in MCMC optimization is smaller (e.g. Gabriel et al., 2018; Sanin et al., 2015). In Figure S3.5 we show the same data for select values of bulk H content to illustrate the dynamic range as compared to active DAN data in unaltered Stimson. When considering the worst-case model error, the CETN detector (bottom panel) exhibits more degeneracy for large values of bulk H content, whereas the shapes of die-away profiles in the CTN detector can be discerned. Nevertheless, Figure S3.5 demonstrates the potential usefulness of the CETN detector in identifying low-H geochemistries, especially given that the model errors are much smaller in practice, and thus, unlike in Gabriel et al. (2018), we include data from this detector in our MCMC optimization.

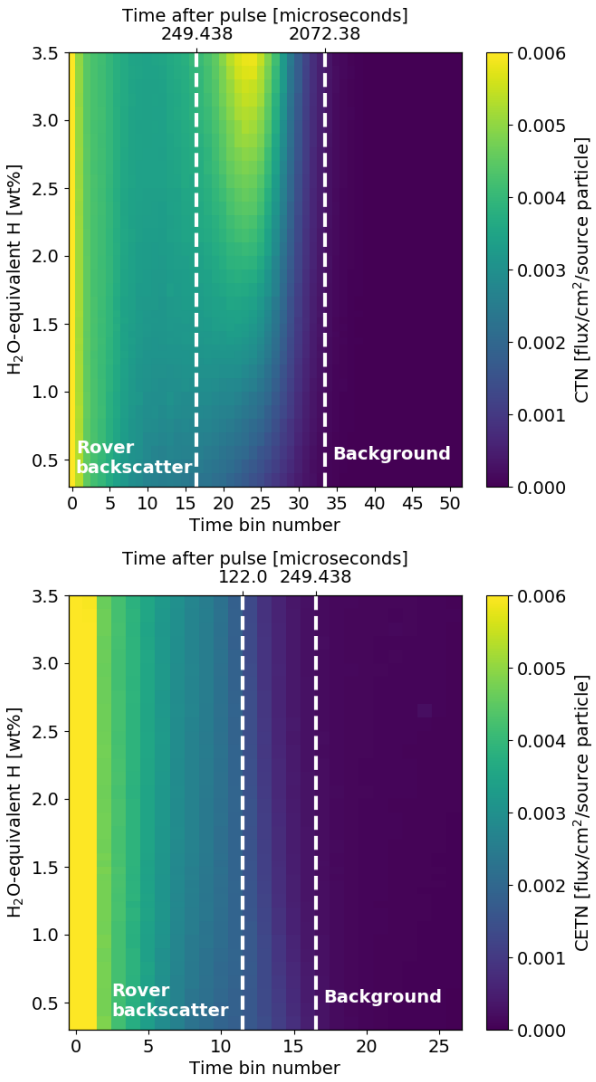

Figure S3.4. Time-resolved CTN (top) and CETN (bottom) detector count values (colors) as a function of H_2O-equivalent H (y axis) for the homogeneous MCNP6 model of Okoruso geochemistry. The 'F4' tally from MCNP6 was used and the results are proportional to counts. White lines denote the bins used in the analysis of active neutron data. Early time bins are dominated by rover backscatter and late time bins do not include contribution from PNG-generated neutrons. Since background (GCR and MMRTG) neutrons are readily subtracted from active DAN data, background sources are not modeled in MCNP6 and thus late time bins show zero flux.

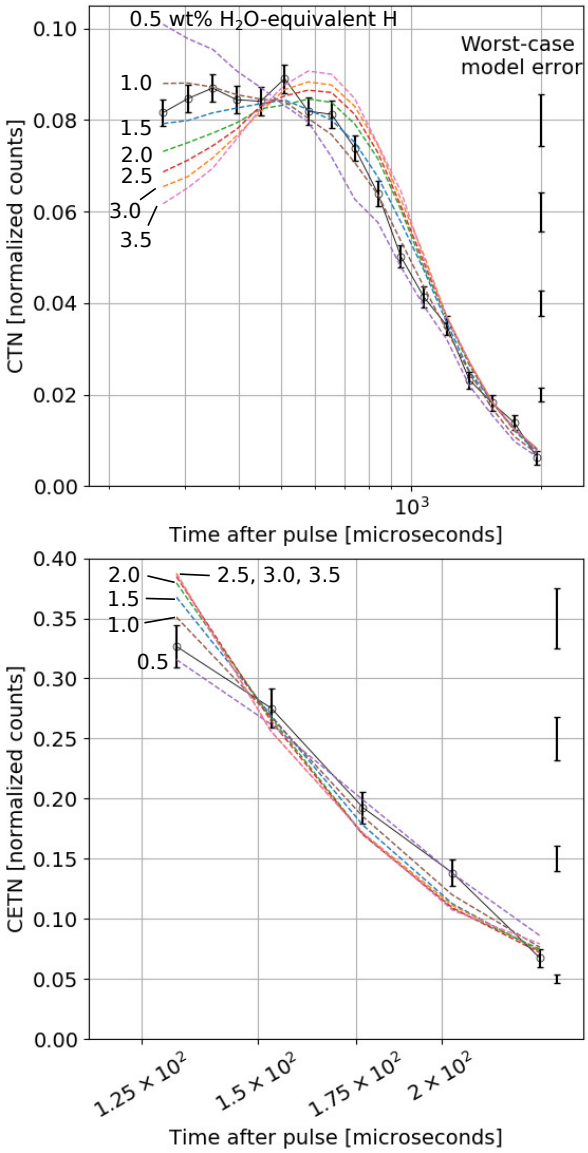

Figure S3.5. Time-resolved, normalized CTN (top) and CETN (bottom) count values (colors) for the homogeneous MCNP6 model of Okoruso geochemistry; x axis is in log space. Models with 0.5-3.5 H_2O-equivalent H in increments of 0.5 are shown. The data shown corresponds to the bins between the dashed white lines in Figure S3.4. The worst-case model errors (5% relative error propagated through the normalization) are shown on the right to illustrate the uncertainty in the models as compared to the dynamic range in their shape. Normalized count data from the active DAN experiment on sol 1110 (DNB_496042823EAC11100500448) is also shown (black solid line with error bars). The best-fit model from MCMC optimization is 1.14±0.08 H_2O-equivalent H.

3.10 Linearity of DAN Spectra

Use of the common reduced χ^2 parameter necessitates that the model response to the free parameters is linear (e.g. Anderson et al., 2015). If the model is linear, the number of degrees of freedom, D, in our case would be equal to the number of examined bins in the die-away spectrum N (16 in CTN and 5 in CETN; 21 in total), less the number of free parameters p; where p is 1 for a homogeneous model since H content is the only free parameter in that case. In the case where the model response is nonlinear, the degrees of freedom inherent to the problem is difficult to estimate and can vary as a function of the free parameters (Anderson et al., 2015). We examine the variability in different time bins of the DAN spectra as a function of a common free parameter (H content) in the homogeneous model with an Okoruso geochemistry to understand whether the concept of reduced χ^2 is well-posed for use in DAN analysis. In Figure S3.6 we perform a linear least squares fit to data in each time bin, then subtract the straight-line fit from the data to examine the shape of the residuals; residuals with a mean of zero and no bias indicate the response can reasonably be modeled as linear, whereas bias indicates a higher-order (non-linear) function is necessary to model the response. Several bins in each detector were chosen to illustrate the linearity at different points in the die-away data. We find that the thermal neutron detector shows non-linearity across the entirety of the spectra; however, for a middle range of H values, the spectra may indeed demonstrate a linear response to the free parameter (within the statistical noise of the data). The CETN detector on the other hand exhibits different responses depending on the time bin. Nevertheless, the non-linearity is strong, particularly in the later time bins. Thus we caution the use of the reduced χ^2 parameter as a strict guideline for determining the

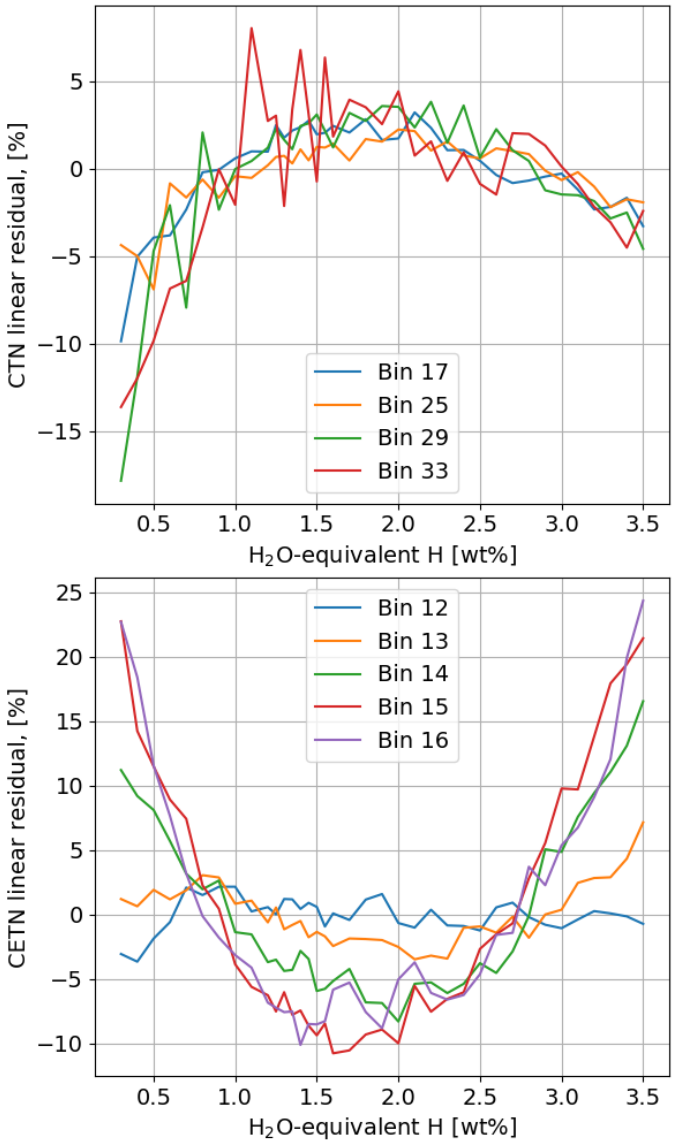

Figure S3.6. Shown are the residuals of normalized DAN model counts from a linear fit as a function of H_2O-equivalent-H in the homogeneous Okoruso geochemistry model; only a few of the analyzed bins are shown in the CTN detector for illustration; all bins used in analysis are shown for the CETN detector.

threshold for a 'good-fit' model, but instead the parameter may simply be used as a qualitative gauge for the goodness-of-fit between synthetic and measured spectra.

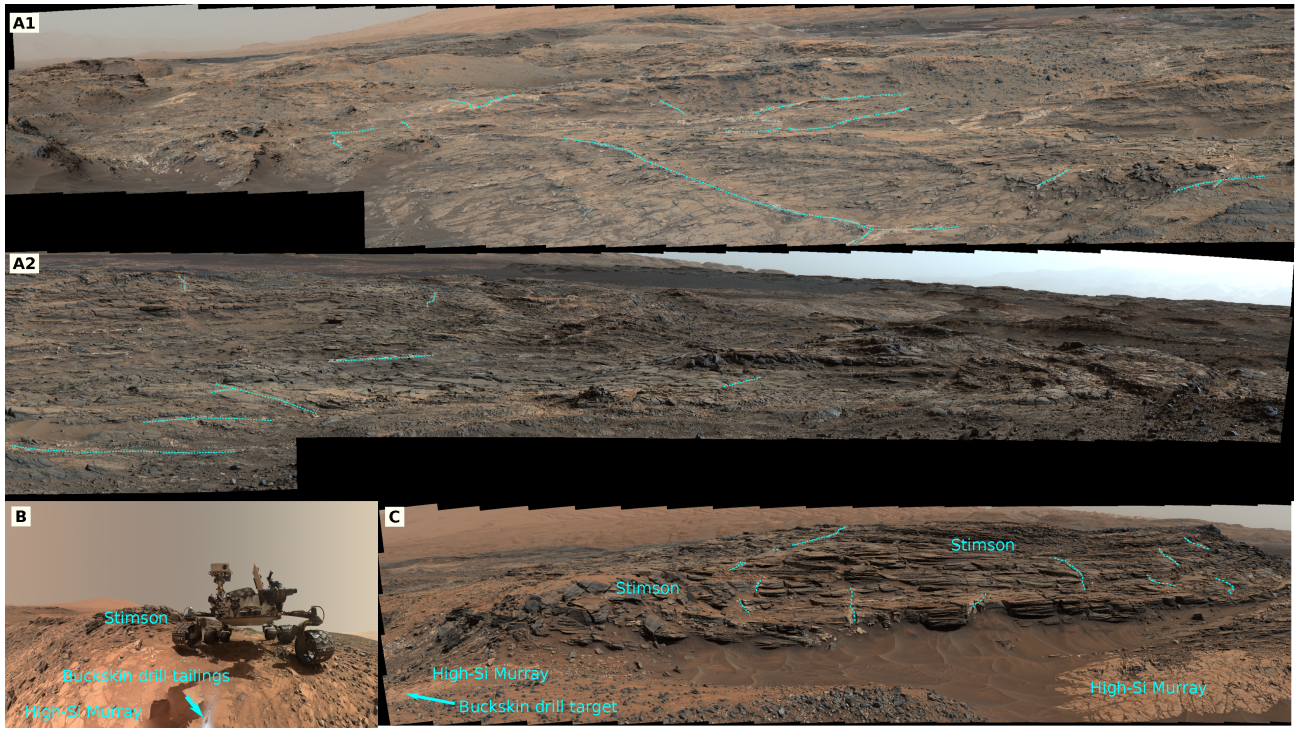

Figure S3.7. Collage of halos throughout the Marias Pass and Pahrump Hills region (See Figure 3.1 for context with stratigraphic column). A1 and A2: Left and right halves, respectively, of a large Mastcam (34 mm) mosaic (sequence: mcam04761) taken on sol 1082 of the rover drive direction, with several halos traced with cyan dashed lines. Figure S3.8 shows a top-down view of the orientation of this mosaic with respect to the Marias pass region and cardinal direction. B: Rover 'selfie' image over exposed high-silica Murray bedrock (foreground) below the Stimson (background). The Buckskin drill site is just outside of the image in the foreground direction. C: Cropped Mastcam (34 mm) mosaic (sequence: mcam04395) of the Marias Pass region taken on sol 992. Figure S3.9 shows a viewshed for context with A1 and A2.

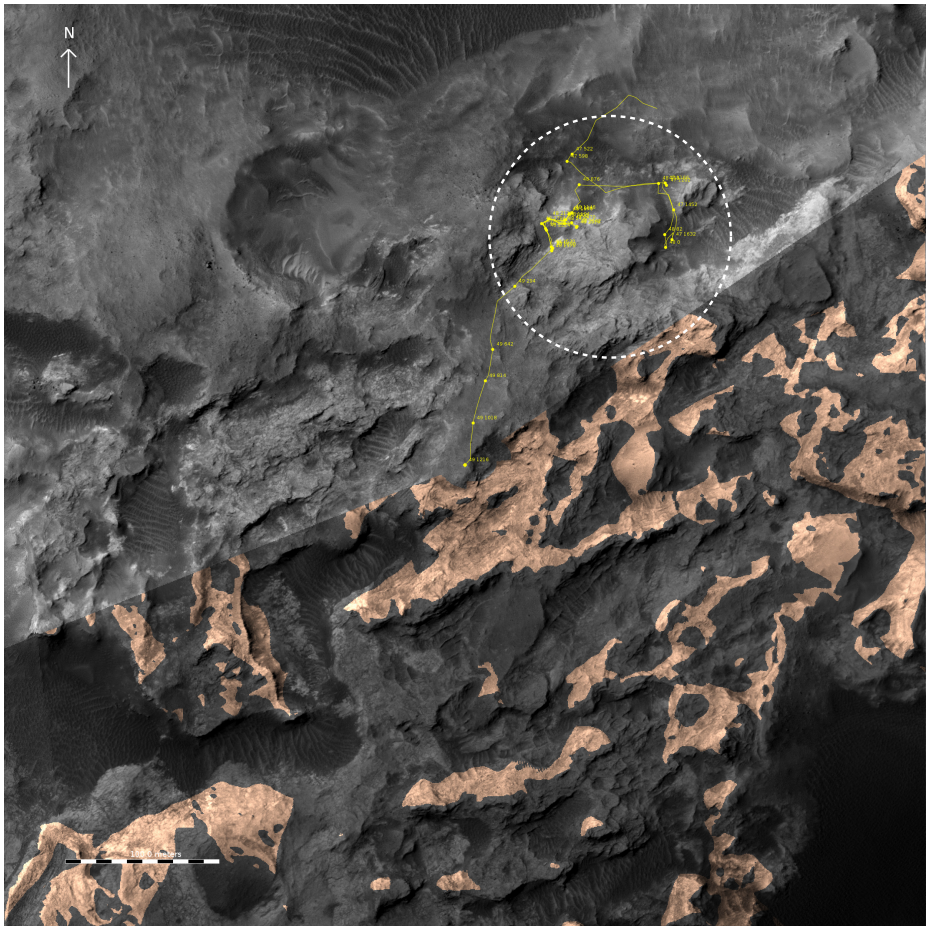

Figure S3.8. Viewshed of the Mastcam mosaic labeled 'A1' and 'A2' in Figure S3.7. The rover traverse, up to sol 1082, is represented by the yellow line and rover stops are labeled with their respective site and drive locations. The Marias Pass region is encircled by the dashed white line. The traverse before the Marias Pass region (before site 47) is not shown.

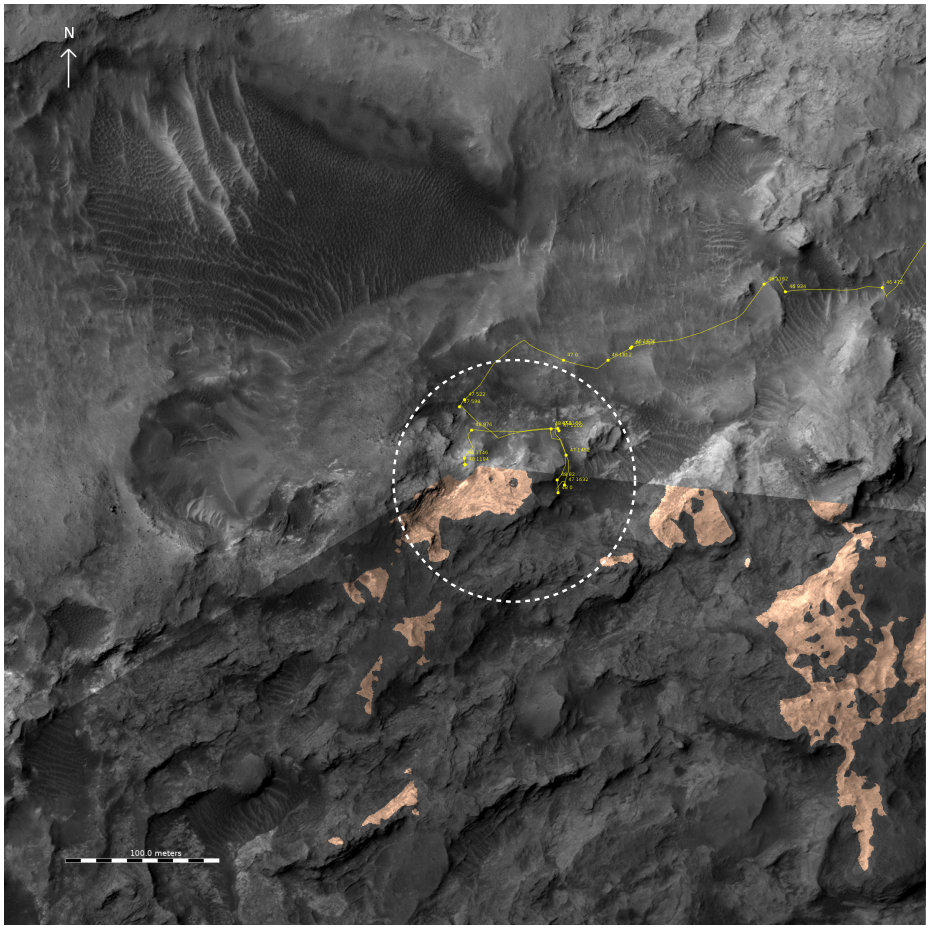

Figure S3.9. Viewshed of the Mastcam mosaic labeled 'C' in Figure S3.7. Labels are the same as Figure S3.8. The scale and location of the dashed circle in Figure S3.8 is the same in this map.

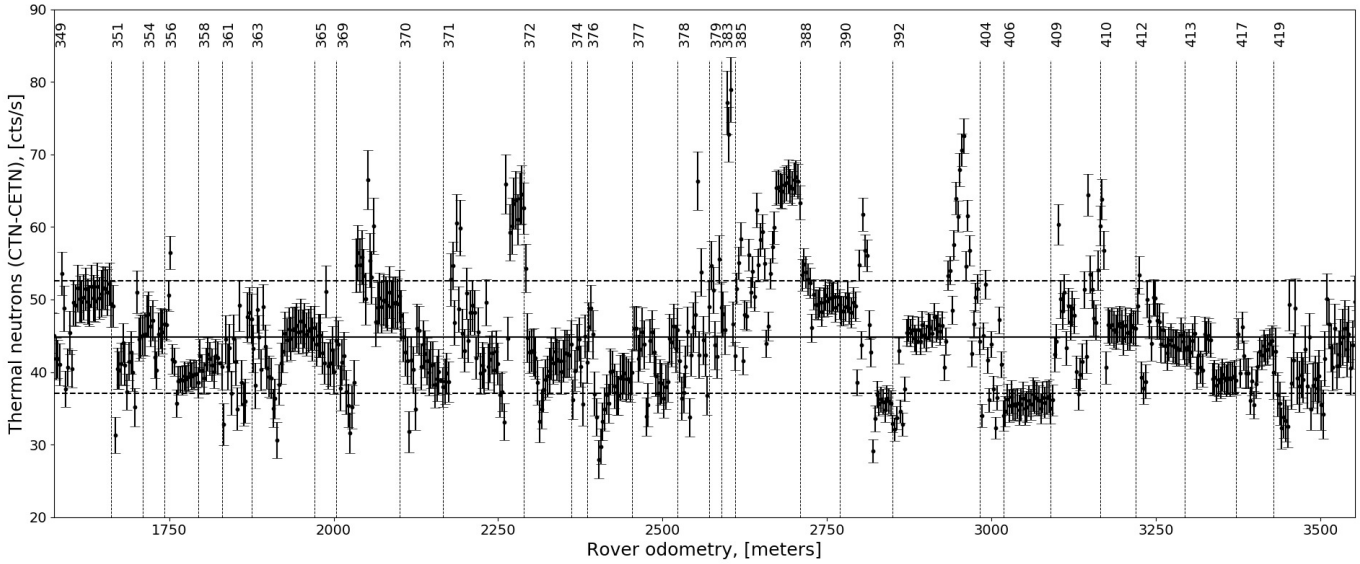

Figure S3.10. Raw count rates from the Counter of Thermal Neutrons (CTN) detector in passive mode during rover mobility. The lower x-axis is the rover odometry in meters and the first measurement with a unique sol is labeled. The mean of the count rates is shown as a solid horizontal line. The dashed horizontal lines show the standard deviation of the data added and subtracted from the mean. Measurements were taken in the vicinity of the first encounter of fracture-associated halos on the mission near the 'Darwin' waypoint. The fracture halo, shown in Figure 5, is the source of the spike in thermal neutrons between sol 383 and 385.

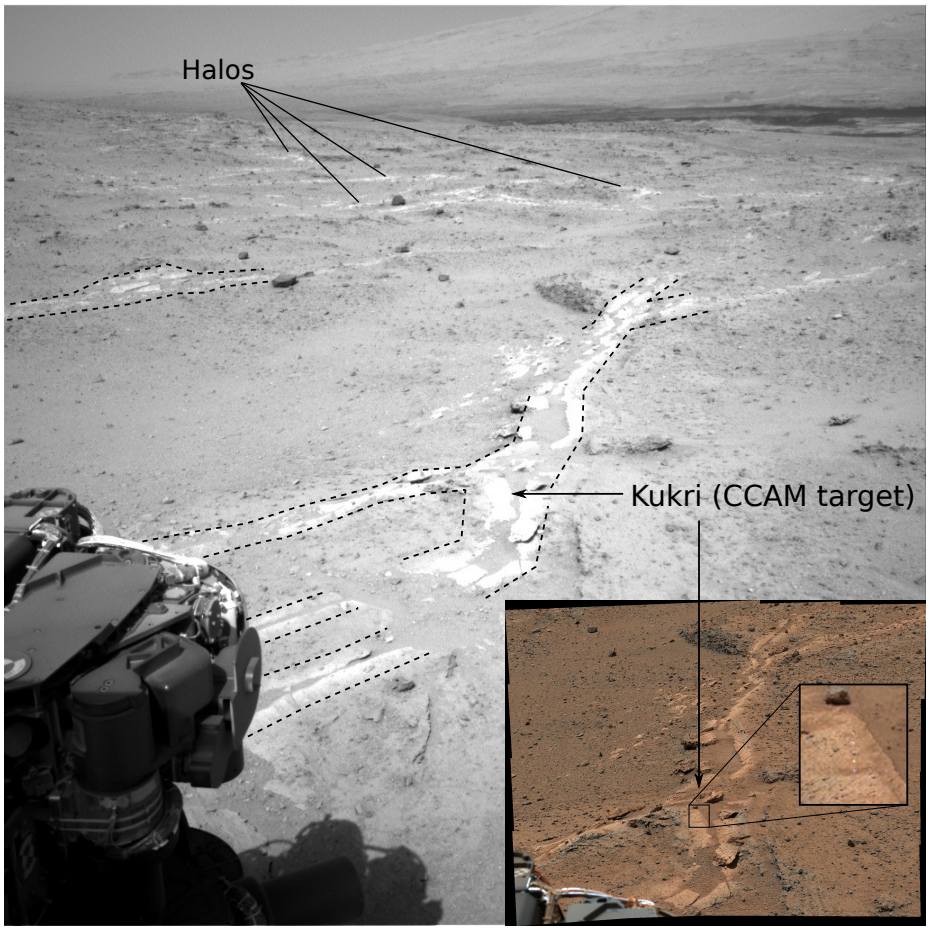

Figure S3.11. Navcam image (NRB_432125263EDR_F0160000NCAM00297M) taken on sol 390 which shows a vast network of fracture halos in the foreground and background. Inset: Mastcam image (sequence: mcam01617) taken on sol 392 which shows the Kukri target. Double inset: Zoom-in view of the inset which shows bleaching from the LIBS shots.

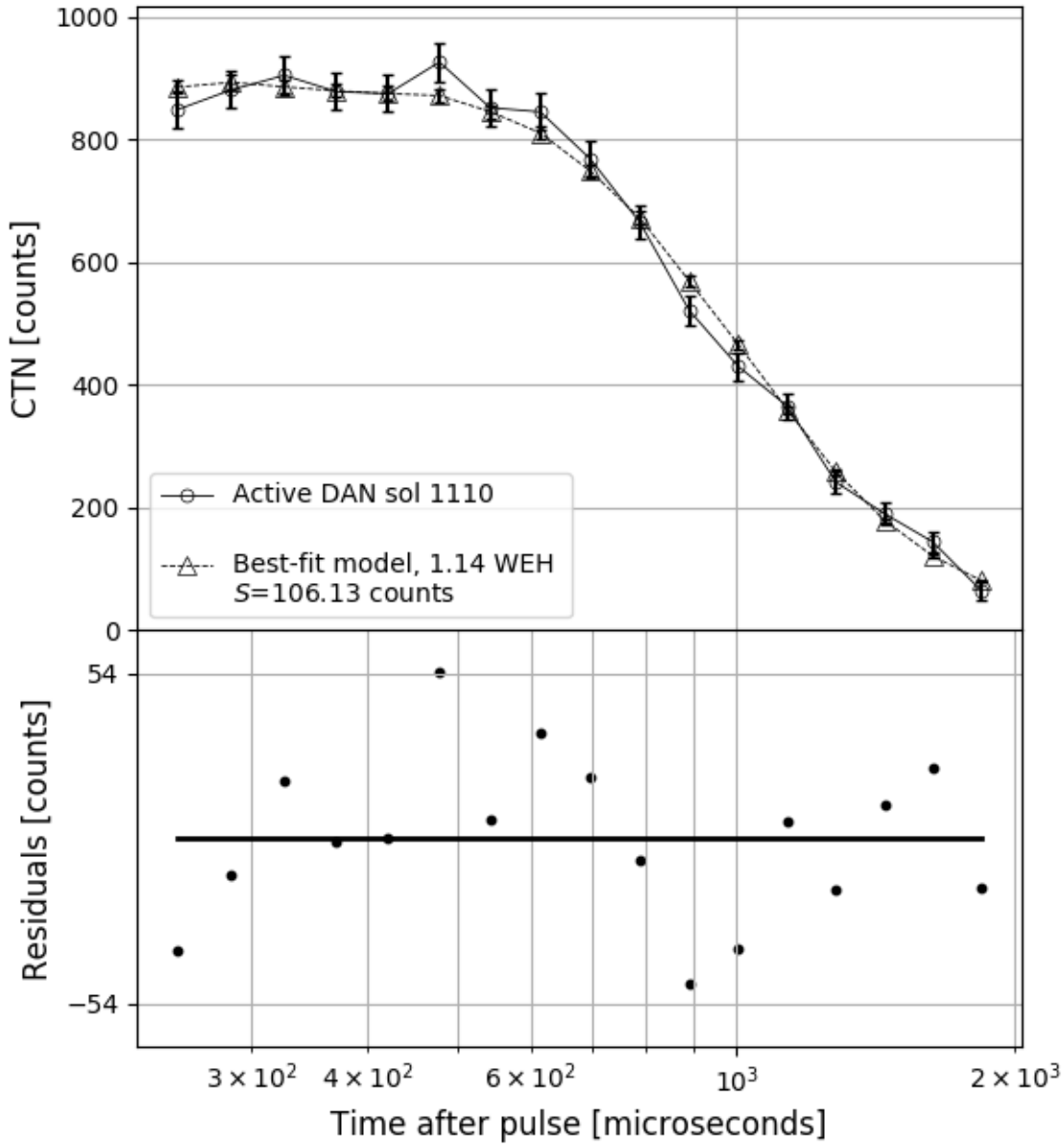

Figure S3.12. Top: The active DAN observation on sol 1110 over unaltered Stimson bedrock in Naukluft Plateau compared to the best-fit model from MCMC optimization of an unaltered Stimson base geochemistry. Bottom: Corresponding data-model residuals. Both frames share the same x-axis.

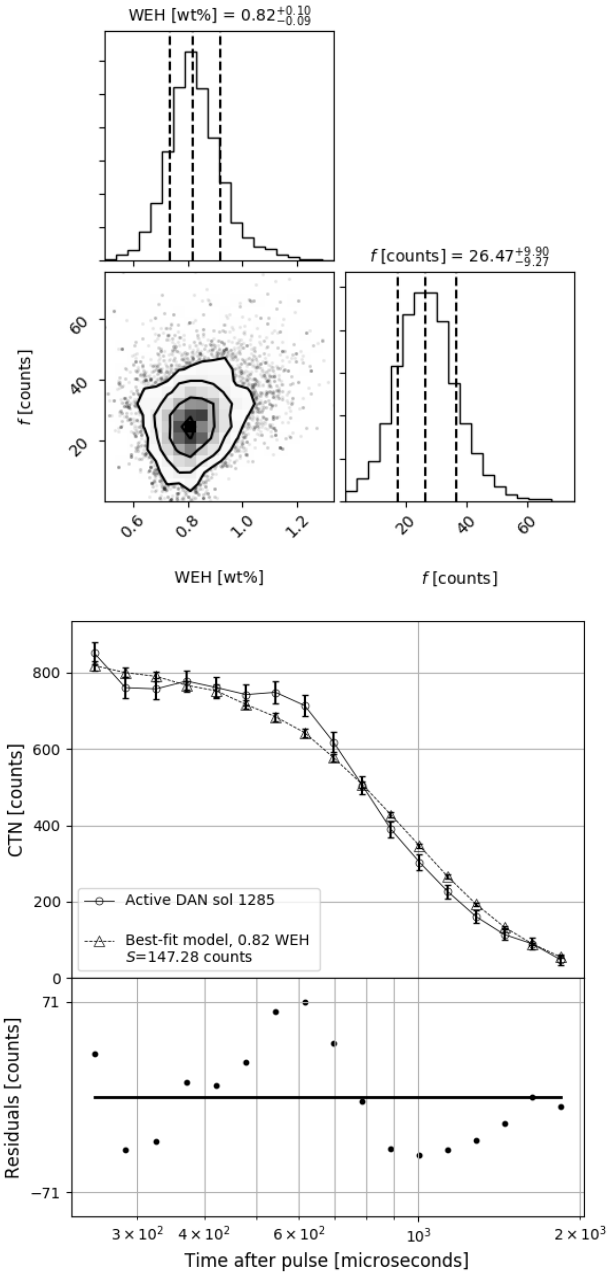

Figure S3.13. Results from MCMC optimization of the homogeneous model with a Big Sky geochemistry and variable H content at the active DAN measurement (DNB_511570880EAC12850531994) on sol 1285 over Murray rocks. Top: Posterior distributions of the optimized parameters. A non-zero value of f is shown, which is an indication of noisy data or potentially a poor fit/model assumption. Bottom: Optimized die-away model and data comparison with residuals. Obvious bias is observed in the residuals which is a strong indication of pool model assumptions.

3.11 Supplementary Tables

Table S3.2. Time bin extents and widths in microseconds for active DAN experiments

Bin number	Start	End	ΔT
0	0.000	5.000	5.000
1	5.000	10.625	5.625
2	10.625	16.938	6.312
3	16.938	24.000	7.062
4	24.000	31.938	7.938
5	31.938	40.812	8.875
6	40.812	50.750	9.938
7	50.750	61.875	11.125
8	61.875	74.375	12.500
9	74.375	88.438	14.062
10	88.438	104.250	15.812
11	104.250	122.000	17.750
12	122.000	141.938	19.938
13	141.938	164.312	22.375
14	164.312	189.438	25.125
15	189.438	217.688	28.250
16	217.688	249.438	31.750
17	249.438	285.125	35.688
18	285.125	325.250	40.125
19	325.250	370.375	45.125
20	370.375	421.125	50.750
21	421.125	478.188	57.062
22	478.188	542.375	64.188
23	542.375	614.562	72.188
24	614.562	695.750	81.188
25	695.750	787.062	91.312
26	787.062	889.750	102.688
27	889.750	1005.250	115.500
28	1005.250	1135.190	129.938
29	1135.190	1281.310	146.125
30	1281.310	1445.690	164.375
31	1445.690	1630.560	184.875
32	1630.560	1838.500	207.938
33	1838.500	2072.380	233.875
34	2072.380	2335.440	263.062
35	2335.440	2631.380	295.938
36	2631.380	2964.250	332.875
37	2964.250	3338.690	374.438

Table S3.3. Time bin extents (continued)

Bin number	Start	End	ΔT
38	3338.690	3759.880	421.188
39	3759.880	4233.690	473.812
40	4233.690	4766.690	533.000
41	4766.690	5366.310	599.625
42	5366.310	6040.880	674.562
43	6040.880	6799.750	758.875
44	6799.750	7653.440	853.688
45	7653.440	8611.940	958.500
46	8611.940	9692.310	1080.380
47	9692.310	10907.700	1215.380
48	10907.700	12274.900	1367.250
49	12274.900	13813.100	1538.120
50	13813.100	15543.400	1730.380
51	15543.400	17490.100	1946.620
52	17490.100	19680.000	2189.940
53	19680.000	22143.600	2463.620
54	22143.600	24915.200	2771.560
55	24915.200	28033.200	3118.000
56	28033.200	31540.900	3507.750
57	31540.900	35487.100	3946.190
58	35487.100	39926.600	4439.440
59	39926.600	44920.900	4994.310
60	44920.900	50539.400	5618.560
61	50539.400	56860.300	6320.880
62	56860.300	63971.200	7110.940
63	63971.200	100000.000	36028.800

Table S3.4. Shown are the elemental abundances in weight fraction for each sample used in this study. These reported values were converted from oxide abundances provided by APXS experiments of drill tailing piles.

Element	Drill Sites			
	Big Sky	Greenhorn	Okoruso	Lubango
Na	0.0222618595	0.0159842049	0.0216661437	0.0117867377
Mg	0.0485647713	0.0088544639	0.0600677968	0.0063747561
Al	0.0598017505	0.0151336946	0.0502231807	0.0112388619
Si	0.1949135927	0.2764730241	0.2088238361	0.2972187211
P	0.0031846204	0.0068030506	0.0034154910	0.0065237362
S	0.0223015592	0.0523604443	0.0026176817	0.0603584704
Cl	0.0078909999	0.0054329997	0.0062720001	0.0031209999
K	0.0041059230	0.0024489430	0.0027602496	0.0023999642
Ca	0.0530547323	0.0507291128	0.0467296756	0.0612894562
Ti	0.0053947394	0.0054720554	0.0056644465	0.0063998478
Cr	0.0030980912	0.0019465701	0.0026273565	0.0023379366
Mn	0.0029926755	0.0005696554	0.0032070464	0.0004731962
Fe	0.1488080605	0.0807865177	0.1720006474	0.0335222363
Ni	0.0465999991	0.0183000006	0.0461000018	0.0043000001
Zn	0.0292000007	0.0093000000	0.0329000019	0.0077999998
Br	0.0299999993	0.0441000015	0.0141000003	0.0082999999

Table S3.5. Terrestrial isotopic abundances used in this study determined from Sears (1992)[a] and the cross section library used in MCNP6

Element	Isotope	Abundance	Cross section library
H			
	^{1}H	1.0	1001.70c
O			
	^{16}O	1.0	8016.70c
Na			
	^{23}Na	1.0	11023.70c
Mg			
	^{24}Mg	0.7899	12024.70c
	^{25}Mg	0.1000	12024.70c
	^{26}Mg	0.1101	12026.70c
Al			
	^{27}Al	1.0	13027.70c
Si			
	^{28}Si	0.92223	14028.70c
	^{29}Si	0.04685	14029.70c
	^{30}Si	0.03092	14030.70c
P			
	^{31}P	1.0	15031.70c
S			
	^{32}S	0.9499	16032.70c
	^{33}S	0.0075	16033.70c
	^{34}S	0.0425	16034.70c
	^{36}S	0.0001	16036.70c
K			
	^{39}K	0.932581	19039.70c
	^{40}K	0.000117	19040.70c
	^{41}K	0.067302	19041.70c
Ca			
	^{40}Ca	0.96941	20040.70c
	^{42}Ca	0.00647	20042.70c
	^{43}Ca	0.00135	20043.70c
	^{44}Ca	0.02086	20044.70c
	^{46}Ca	0.00004	20046.70c
	^{48}Ca	0.00187	20048.70c
Ti			
	^{46}Ti	0.0825	22046.70c
	^{47}Ti	0.0744	22047.70c
	^{48}Ti	0.7372	22048.70c
	^{49}Ti	0.0541	22049.70c
	^{50}Ti	0.0518	22050.70c

Table S3.6. Listed are the terrestrial isotopic abundances used in this study determined from Sears (1992)[a] and the cross section library used in MCNP6.

Element	Isotope	Abundance	Cross section library
Cr			
	^{50}Cr	0.04345	24050.70c
	^{52}Cr	0.83789	24052.70c
	^{53}Cr	0.09501	24053.70c
	^{54}Cr	0.02365	24054.70c
Mn			
	^{55}Mn	1.0	25055.70c
Fe			
	^{54}Fe	0.05845	26054.70c
	^{56}Fe	0.91754	26056.70c
	^{57}Fe	0.02119	26057.70c
	^{58}Fe	0.00282	26058.70c
Ni			
	^{58}Ni	0.68077	28058.70c
	^{60}Ni	0.26223	28060.70c
	^{61}Ni	0.011399	28061.70c
	^{62}Ni	0.036346	28062.70c
	^{64}Ni	0.009255	28064.70c
Zn			
	^{64}Zn	0.4917	30064.80c
	^{66}Zn	0.2773	30066.80c
	^{67}Zn	0.0404	30067.80c
	^{68}Zn	0.1845	30068.80c
	^{70}Zn	0.0061	30070.80c
Br			
	^{79}Br	0.5069	35079.70c
	^{81}Br	0.4931	35081.70c
Cl			
	^{35}Cl	0.7576	17035.70c
	^{37}Cl	0.2424	17037.70c

aIsotopes with abundances $< 10^{-5}$ are not considered. The abundance of these isotopes are added to the most abundant isotope for a given element to ensure a sum of unity.

Table S3.7. List of targets used to generate Figure 3.3 in the main manuscript and the associated information necessary to locate the specific geochemistry files in the Planetary Data Service (pds-geosciences.wustl.edu). The associated macroscopic absorption cross section is provided in the last column.

Target	Instrument	Measurement	Sol/Site/Drive	ξ_{abs} [cm^2/g]
Cumberland (CB)	APXS	440781134	0488/24/0366	$2.4 \times 10^{-2} \pm 3.9 \times 10^{-4}$
Kukri	CCAM	-	-	$5.3 \times 10^{-3} \pm 9.0 \times 10^{-4}$
Windjana (WJ)	APXS	452752443	0622/31/1330	$2.3 \times 10^{-2} \pm 2.3 \times 10^{-4}$
Confidence Hills (CH)	APXS	465618955	0767/42/1020	$9.3 \times 10^{-3} \pm 8.6 \times 10^{-5}$
Mojave (MJ)	APXS	476006877	0884/45/0000	$1.6 \times 10^{-2} \pm 1.3 \times 10^{-4}$
Telegraph Peak (TP)	APXS	479382097	0922/45/0450	$1.5 \times 10^{-2} \pm 1.4 \times 10^{-4}$
Buckskin (BK)	APXS	492003117	1065/48/2542	$1.0 \times 10^{-2} \pm 1.3 \times 10^{-4}$
Oudam (OU)	APXS	518631778	1365/54/2280	$1.5 \times 10^{-3} \pm 1.3 \times 10^{-4}$
Big Sky (BS)	APXS	497241544	1124/50/0592	$1.9 \times 10^{-2} \pm 2.1 \times 10^{-4}$
Greenhorn (GH)	APXS	498927876	1143/50/0676	$1.3 \times 10^{-3} \pm 1.3 \times 10^{-4}$
Okoruso (OK)	APXS	516238368	1338/54/0938	$1.9 \times 10^{-2} \pm 2.2 \times 10^{-4}$
Lubango (LB)	APXS	515081203	1325/54/0746	$9.6 \times 10^{-3} \pm 2.1 \times 10^{-4}$
Marimba (MB)	APXS	524136016	1427/56/1236	$1.7 \times 10^{-2} \pm 2.1 \times 10^{-4}$
Quela (QL)	APXS	527686815	1467/57/2798	$1.3 \times 10^{-2} \pm 2.0 \times 10^{-4}$
Sebina (SB)	APXS	530425697	1497/58/2046	$2.2 \times 10^{-2} \pm 2.1 \times 10^{-4}$

Table S3.8. Table of the water content of Stimson bedrock in wt.% H_2O-equiv. H. The APXS-derived geochemical abundances from the Okoruso (ξ_{abs}=0.019 cm^2/g) and Big Sky drill targets (ξ_{abs}=0.01860 cm^2/g) were used in homogeneous MCNP6 models (See Figure 8). Measurements that have altered Stimson in the field of view, as determined from surface images, were excluded from the calculation of the mean. We provide the 16%, 50%, and 84% quantiles for the water and f values, in units of wt% and counts respectively. We also report the standard error S as a goodness-of-fit measure.

			Okoruso			**Big Sky**		
Sol	Pulses	Site/Drive	H_2O	f	S	H_2O	f	S
1110	12000	050/0448	$1.15^{+0.10}_{-0.09}$	11^{+9}_{-8}	106	$1.27^{+0.15}_{-0.08}$	10^{+8}_{-7}	99
1112	12000	050/0592	$1.02^{+0.13}_{-0.13}$	32^{+11}_{-9}	168	$1.09^{+0.13}_{-0.10}$	21^{+12}_{-11}	149
1127	12000	050/0676	$1.21^{+0.13}_{-0.13}$	13^{+9}_{-8}	106	$1.32^{+0.12}_{-0.10}$	7^{+7}_{-5}	90
1139	12000	050/0676	$1.13^{+0.15}_{-0.11}$	26^{+12}_{-11}	164	$1.22^{+0.09}_{-0.09}$	15^{+11}_{-9}	140
1144†*	12000	050/0700	$2.29^{+0.16}_{-0.17}$	11^{+10}_{-8}	121	$2.65^{+0.15}_{-0.15}$	13^{+10}_{-8}	122
1144	12000	050/0848	$1.38^{+0.22}_{-0.19}$	46^{+13}_{-11}	216	$1.66^{+0.15}_{-0.19}$	37^{+14}_{-11}	189
1148†	12000	050/1116	$1.87^{+0.22}_{-0.15}$	27^{+11}_{-11}	161	$2.06^{+0.16}_{-0.14}$	23^{+12}_{-10}	143
1151	12000	050/1222	$1.72^{+0.21}_{-0.19}$	31^{+11}_{-9}	167	$1.97^{+0.17}_{-0.16}$	23^{+10}_{-9}	144
1289	12000	053/2138	$1.49^{+0.15}_{-0.18}$	50^{+15}_{-12}	240	$1.73^{+0.13}_{-0.14}$	39^{+15}_{-12}	208
1290†	12000	053/2298	$2.48^{+0.14}_{-0.25}$	15^{+11}_{-10}	127	$2.75^{+0.15}_{-0.27}$	18^{+11}_{-11}	128
1292	12000	053/2406	$1.05^{+0.15}_{-0.11}$	25^{+11}_{-10}	142	$1.15^{+0.14}_{-0.11}$	15^{+10}_{-9}	126
1294	12000	053/2578	$1.54^{+0.18}_{-0.13}$	16^{+10}_{-9}	121	$1.75^{+0.12}_{-0.12}$	11^{+10}_{-8}	107
1296	12000	053/2644	$0.98^{+0.10}_{-0.10}$	22^{+10}_{-8}	133	$1.05^{+0.10}_{-0.08}$	12^{+10}_{-8}	118
1298†	12000	053/2980	$2.72^{+0.35}_{-0.30}$	21^{+9}_{-9}	122	$3.01^{+0.33}_{-0.25}$	26^{+10}_{-8}	138
1301†	18000	053/2980	$2.45^{+0.27}_{-0.21}$	24^{+11}_{-9}	141	$2.80^{+0.28}_{-0.36}$	33^{+12}_{-9}	159
1301	18000	053/3062	$0.73^{+0.15}_{-0.11}$	38^{+13}_{-10}	190	$0.87^{+0.09}_{-0.08}$	27^{+12}_{-11}	167
1303	12000	054/0006	$0.97^{+0.14}_{-0.14}$	26^{+10}_{-8}	130	$1.03^{+0.12}_{-0.10}$	17^{+8}_{-8}	109
1305	12000	054/0010	$0.70^{+0.18}_{-0.11}$	22^{+9}_{-7}	116	$0.85^{+0.16}_{-0.15}$	20^{+8}_{-8}	113
1309	12000	054/0088	$1.60^{+0.15}_{-0.15}$	7^{+7}_{-5}	79	$1.69^{+0.17}_{-0.17}$	6^{+6}_{-4}	74
1310	12000	054/0238	$1.07^{+0.24}_{-0.17}$	30^{+9}_{-8}	149	$1.15^{+0.18}_{-0.13}$	24^{+10}_{-9}	139
1311	12000	054/0388	$0.97^{+0.11}_{-0.10}$	5^{+6}_{-4}	80	$1.07^{+0.13}_{-0.09}$	5^{+6}_{-3}	78
1312	12000	054/0388	$1.10^{+0.15}_{-0.12}$	7^{+6}_{-4}	86	$1.28^{+0.13}_{-0.17}$	6^{+5}_{-4}	79
1315	12000	054/0412	$1.61^{+0.18}_{-0.17}$	5^{+6}_{-4}	65	$1.75^{+0.16}_{-0.14}$	5^{+5}_{-3}	58
1316	12000	054/0412	$1.50^{+0.18}_{-0.21}$	16^{+8}_{-7}	101	$1.62^{+0.16}_{-0.15}$	12^{+8}_{-7}	90
1316	12000	054/0668	$0.92^{+0.14}_{-0.17}$	22^{+8}_{-7}	114	$0.99^{+0.11}_{-0.10}$	14^{+8}_{-8}	98
1317	12000	054/0746	$1.06^{+0.14}_{-0.11}$	7^{+7}_{-5}	74	$1.24^{+0.15}_{-0.16}$	7^{+7}_{-5}	74
1329†*	18000	054/0812	$2.38^{+0.19}_{-0.21}$	6^{+6}_{-4}	71	$2.61^{+0.23}_{-0.23}$	5^{+7}_{-4}	71
1329†	12000	054/0938	$3.13^{+0.47}_{-0.39}$	24^{+9}_{-7}	118	$3.37^{+0.52}_{-0.43}$	29^{+9}_{-7}	133
1342	18000	054/0962	$1.80^{+0.13}_{-0.12}$	8^{+9}_{-6}	92	$1.98^{+0.18}_{-0.15}$	10^{+9}_{-7}	90
1342	12000	054/0992	$0.97^{+0.10}_{-0.11}$	6^{+6}_{-4}	67	$1.06^{+0.14}_{-0.10}$	6^{+6}_{-4}	59

† Sites with a field-of-view that includes altered Stimson (light-rocks). * Targeted sites where an alteration halo model was used.

3.12 Acknowledgements

We acknowledge the Dynamic Albedo of Neutrons instrument team, the broader Mars Science Laboratory team, Fred Calef, Hallie Gengl, and Jack Lightholder. This work was supported by the Mars Science Laboratory Participating Scientist Program, award number NNN12AA01C, and by the NASA Earth and Space Exploration Fellowship, award number PLANET18R-0036. The authors acknowledge Research Computing at Arizona State University for providing HPC, storage, etc. resources that have contributed to the research results reported within this paper (URL: http://www.researchcomputing.asu.edu). Computational support was also provided by the Space Science and Applications group at Los Alamos National Laboratory. All data from this work is publicly accessible on the Planetary Data System, www.pds.nasa.gov.

References

Abercrombie, S. P., A. Menzies, A. Winter, M. Clausen, B. Duran, M. Jorritsma, C. Goddard, and A. Lidawer (Dec. 2017). OnSight: Multi-platform Visualization of the Surface of Mars. *AGU Fall Meeting Abstracts*.

Achilles, C. N. et al. (Mar. 2018). Amorphous Phase Characterization Through X-Ray Diffraction Profile Modeling: Implications for Amorphous Phases in Gale Crater Rocks and Soils. *Lunar and Planetary Science Conference*. 49. Lunar and Planetary Inst. Technical Report, p. 2661.

Adams, S. J., G. E. Hawkes, and E. H. Curzon (1982). A solid state 29Si nuclear magnetic resonance study of opal and other hydrous silicas. *American Mineralogist* 76, pp. 1863–1871.

Anderson, R. et al. (2015). ChemCam results from the Shaler outcrop in Gale crater, Mars. *Icarus* 249. Special Issue: First Year of MSL, pp. 2–21.

Andrae, R., T. Schulze-Hartung, and P. Melchior (Dec. 2010). Dos and don'ts of reduced chi-squared. *arXiv e-prints*. arXiv: 1012.3754.

Czarnecki, S. et al. (In preparation). Description of a silicic volcaniclastic layer in Gale1crater, Mars using active neutron interrogation. *Journal of Geophysical Research: Planets*.

Dana, J. D. and E. S. Dana (1997). Dana's New Mineralogy, pp. 1587–1592.

Diez, B., W. C. Feldman, S. Maurice, O. Gasnault, T. H. Prettyman, M. T. Mellon, O. Aharonson, and N. Schorghofer (2008). H layering in the top meter of Mars. *Icarus* 196 (2), pp. 409–421.

Ehlmann, B. L. et al. (2017). Chemistry, mineralogy, and grain properties at Namib and High dunes, Bagnold dune field, Gale crater, Mars: A synthesis of Curiosity rover observations. *Journal of Geophysical Research: Planets* 122 (12), pp. 2510–2543.

Feldman, W. C., A. Pathare, S. Maurice, T. H. Prettyman, D. J. Lawrence, R. E. Milliken, and B. J. Travis (2011). Mars Odyssey neutron data: 2. Search for buried excess water ice deposits at nonpolar latitudes on Mars. *Journal of Geophysical Research: Planets* 116 (E11).

Filiberto, J. and A. H. Treiman (2009). Martian magmas contained abundant chlorine, but little water. *Geology* 37 (12), p. 1087.

Foreman-Mackey, D. (2016). corner.py: Scatterplot matrices in Python. *The Journal of Open Source Software* 24.

Foreman-Mackey, D., D. W. Hogg, D. Lang, and J. Goodman (Mar. 2013). emcee: The MCMC Hammer. *Publications of the Astronomical Society of the Pacific* 125, p. 306. arXiv: 1202.3665.

Frydenvang, J. et al. (2017). Diagenetic silica enrichment and late-stage groundwater activity in Gale crater, Mars. *Geophysical Research Letters* 44 (10), pp. 4716–4724.

Gabriel, T. S. J. et al. (2018). Water Abundance of Dunes in Gale Crater, Mars From Active Neutron Experiments and Implications for Amorphous Phases. *Geophysical Research Letters* 45 (23), pp. 12, 766–12, 775.

Goodman, J. and J. Weare (2010). Ensemble samplers with affine invariance. *Communications in Applied Mathematics and Computational Science* 5, pp. 65–80.

Hardgrove, C., J. Moersch, and D. Drake (2011). Effects of geochemical composition on neutron die-away measurements: Implications for Mars Science Laboratory's Dynamic Albedo of Neutrons experiment. *Nuclear Instruments and Methods in Physics Research, Section A: Accelerators, Spectrometers, Detectors and Associated Equipment* 659 (1), pp. 442–455.

Huang, W. H. and D. L. Vogler (1972). Dissolution of Opal in Water and its Water Content. *Nature Physical Science* 235 (60), pp. 157–158.

Jones, B. and R. W. Renaut (2004). Water Content of Opal-A: Implications for the Origin of Laminae in Geyserite and Sinter. *Journal of Sedimentary Research* 74 (1), pp. 117–128.

Jun, I. et al. (Nov. 2013). Neutron background environment measured by the Mars Science Laboratory's Dynamic Albedo of Neutrons instrument during the first 100 sols. *Journal of Geophysical Research: Planets* 118, pp. 2400–2412.

Kerner, H. R., C. Hardgrove, S. Czarnecki, T. S. J. Gabriel, I. Mitrofanov, M. Litvak, M. Litvak, A. Sanin, and D. Lisov (Submitted). Analysis of active neutron measurements from the Mars Science Laboratory Dynamic Albedo of Neutrons instrument: Intrinsic variability, outliers, and implications for future investigations. *Journal of Geophysical Research: Planets*.

L'Haridon, J. et al. (2018). Chemical variability in mineralized veins observed by ChemCam on the lower slopes of Mount Sharp in Gale crater, Mars. *Icarus* 311, pp. 69–86.

Litvak, M. L. et al. (2008). The Dynamic Albedo of Neutrons (DAN) Experiment for NASA's 2009 Mars Science Laboratory. *Astrobiology* 8 (3), pp. 605–612.

Litvak, M. L. et al. (2016). Hydrogen and chlorine abundances in the Kimberley formation of Gale crater measured by the DAN instrument on board the Mars Science Laboratory Curiosity rover. *Journal of Geophysical Research E: Planets* 121 (5), pp. 836–845.

Liu, Y., Y. Chen, Y. Guan, C. Ma, G. R. Rossman, J. M. Eiler, and Y. Zhang (2018). Impact-melt hygrometer for Mars: The case of shergottite Elephant Moraine (EETA) 79001. *Earth and Planetary Science Letters* 490, pp. 206–215.

Lynne, B. Y. and K. A. Campbell (2007). Morphologic and Mineralogic Transitions From Opal-A to Opal-CT in Low-Temperature Siliceous Sinter Diagenesis, Taupo Volcanic Zone, New Zealand. *Journal of Sedimentary Research* 74 (4), pp. 561–579.

McCubbin, F. M., J. W. Boyce, P. Srinivasan, A. R. Santos, S. M. Elardo, J. Filiberto, A. Steele, and C. K. Shearer (2016). Heterogeneous distribution of H2O in the Martian interior: Implications for the abundance of H2O in depleted and enriched mantle sources. *Meteoritics and Planetary Science* 51 (11), pp. 2036–2060.

McKinney, G. W., J. W. Durkee, J. S. Hendricks, M. R. James, D. B. Pelowitz, L. S. Waters, and F. X. Gallmeier (Sept. 2006). *MCNPX Overview*. Vol. LA-UR-06-6206. HSSW, FNAL. Los Alamos, NM: Los Alamos National Laboratory.

Mitrofanov, I. G. et al. (Sept. 2012). Dynamic Albedo of Neutrons (DAN) Experiment Onboard NASA's Mars Science Laboratory. *Space Science Reviews* 170, pp. 559–582.

Mitrofanov, I. G. et al. (July 2014). Water and chlorine content in the Martian soil along the first 1900 m of the Curiosity rover traverse as estimated by the DAN instrument. *Journal of Geophysical Research: Planets* 119, pp. 1579–1596.

Montmessin, F. and S. Ferron (2019). A spectral synergy method to retrieve martian water vapor column-abundance and vertical distribution applied to Mars Express SPICAM and PFS nadir measurements. *Icarus* 317 (June 2018), pp. 549–569.

Morris, R. V. et al. (June 2016). Silicic volcanism on Mars evidenced by tridymite in high-SiO2 sedimentary rock at Gale crater. *Proceedings of the National Academy of Science* 113, pp. 7071–7076.

Palchetti, L., G. Bianchini, B. Carli, U. Cortesi, and S. Del Bianco (2008). Measurement of the water vapour vertical profile and of the Earth's outgoing far infrared flux. *Atmospheric Chemistry and Physics* 8 (11), pp. 2885–2894.

Pelowitz, D. B. (Aug. 2008). *MNCPX User's Manual, version 2.6.0*. Vol. LA-CP-07-1473. Los Alamos National Laboratory.

Rampe, E. B. et al. (Aug. 2017). Mineralogy of an ancient lacustrine mudstone succession from the Murray formation, Gale crater, Mars. *Earth and Planetary Science Letters* 471, pp. 172–185.

Rapin, W. et al. (2016). Hydration state of calcium sulfates in Gale crater, Mars: Identification of bassanite veins. *Earth and Planetary Science Letters* 452, pp. 197–205.

Rapin, W. et al. (2018). In Situ Analysis of Opal in Gale Crater, Mars. *Journal of Geophysical Research: Planets* 123 (8), pp. 1955–1972.

Rodgers, K. A. et al. (2004). Silica phases in sinters and residues from geothermal fields of New Zealand. *Earth-Science Reviews* 66 (1-2), pp. 1–61.

Ruff, S. W. et al. (Apr. 2011). Characteristics, distribution, origin, and significance of opaline silica observed by the Spirit rover in Gusev crater, Mars. *Journal of Geophysical Research: Planets* 116, E00F23, E00F23.

Ruff, S. W. and J. D. Farmer (2016). Silica deposits on Mars with features resembling hot spring biosignatures at El Tatio in Chile. *Nature Communications* 7, pp. 1–10.

Sanin, A. B. et al. (2015). Data processing of the active neutron experiment DAN for a Martian regolith investigation. *Nuclear Instruments and Methods in Physics Research, Section A: Accelerators, Spectrometers, Detectors and Associated Equipment* 789, pp. 114–127.

Sears, V. F. (1992). Neutron scattering lengths and cross sections. *Neutron News* 3 (3), pp. 26–37.

Siever, R. (1983). Evolution of Chert at Active and Passive Continental Margins. Ed. by A. Iijima, J. R. Hein, and R. Siever. 36. Elsevier. Chap. 2, pp. 7–24.

Sutter, B. et al. (2017). Evolved gas analyses of sedimentary rocks and eolian sediment in Gale Crater, Mars: Results of the Curiosity rover's sample analysis at Mars instrument from Yellowknife Bay to the Namib Dune. *Journal of Geophysical Research: Planets* 122 (12), pp. 2574–2609.

Tate, C. G. et al. (2015). Water equivalent hydrogen estimates from the first 200 sols of Curiosity's traverse (Bradbury Landing to Yellowknife Bay): Results from the Dynamic Albedo of Neutrons (DAN) passive mode experiment. *Icarus* 262, pp. 102–123.

Tate, C. G. et al. (2018). Results from the dynamic albedo of neutrons (DAN) passive mode experiment: Yellowknife Bay to Amargosa Valley (Sols 201–753). *Icarus* 299, pp. 513–537.

Tosca, N. J. and A. H. Knoll (2009). Juvenile chemical sediments and the long term persistence of water at the surface of Mars. *Earth and Planetary Science Letters* 286 (3-4), pp. 379–386.

Tucker, M. E. (2001). *Sedimentary Petrology, 3rd ed.* Blackwell Publisher. Chap. 9, pp. 212–220.

Vaniman, D. T., D. L. Bish, S. J. Chipera, C. I. Fialips, J. William Carey, and W. C. Feldman (Oct. 2004). Magnesium sulphate salts and the history of water on Mars. *Nature* 431, pp. 663–665.

Vasavada, A. R., S. Piqueux, K. W. Lewis, M. T. Lemmon, and M. D. Smith (2017). Thermophysical properties along Curiosity's traverse in Gale crater, Mars, derived from the REMS ground temperature sensor. *Icarus* 284, pp. 372–386.

Wiens, R. C. et al. (Sept. 2012). The ChemCam Instrument Suite on the Mars Science Laboratory (MSL) Rover: Body Unit and Combined System Tests. *Space Science Reviews* 170 (1), pp. 167–227.

Williams, L. A. and D. A. Crerar (1985). Silica Diagenesis, II. General Mechanisms. *SEPM Journal of Sedimentary Research* Vol. 55, pp. 312–321.

Williams, L. A. and A. George (1985). Silica Diagenesis, I. Solubility Controls. *SEPM Journal of Sedimentary Research* Vol. 55 (3), pp. 301–311.

Yen, A. S. et al. (Aug. 2017). Multiple stages of aqueous alteration along fractures in mudstone and sandstone strata in Gale Crater, Mars. *Earth and Planetary Science Letters* 471, pp. 186–198.